



## **SILICON DIOXIDE MICROSTRUCTURES BASED ON MACROPOROUS SILICON FOR BIOMEDICAL APPLICATIONS.**

**María Alba Martín**

**Dipòsit Legal: T 153-2015**

**ADVERTIMENT.** L'accés als continguts d'aquesta tesi doctoral i la seva utilització ha de respectar els drets de la persona autora. Pot ser utilitzada per a consulta o estudi personal, així com en activitats o materials d'investigació i docència en els termes establerts a l'art. 32 del Text Refós de la Llei de Propietat Intel·lectual (RDL 1/1996). Per altres utilitzacions es requereix l'autorització prèvia i expressa de la persona autora. En qualsevol cas, en la utilització dels seus continguts caldrà indicar de forma clara el nom i cognoms de la persona autora i el títol de la tesi doctoral. No s'autoritza la seva reproducció o altres formes d'explotació efectuades amb finalitats de lucre ni la seva comunicació pública des d'un lloc aliè al servei TDX. Tampoc s'autoritza la presentació del seu contingut en una finestra o marc aliè a TDX (framing). Aquesta reserva de drets afecta tant als continguts de la tesi com als seus resums i índexs.

**ADVERTENCIA.** El acceso a los contenidos de esta tesis doctoral y su utilización debe respetar los derechos de la persona autora. Puede ser utilizada para consulta o estudio personal, así como en actividades o materiales de investigación y docencia en los términos establecidos en el art. 32 del Texto Refundido de la Ley de Propiedad Intelectual (RDL 1/1996). Para otros usos se requiere la autorización previa y expresa de la persona autora. En cualquier caso, en la utilización de sus contenidos se deberá indicar de forma clara el nombre y apellidos de la persona autora y el título de la tesis doctoral. No se autoriza su reproducción u otras formas de explotación efectuadas con fines lucrativos ni su comunicación pública desde un sitio ajeno al servicio TDR. Tampoco se autoriza la presentación de su contenido en una ventana o marco ajeno a TDR (framing). Esta reserva de derechos afecta tanto al contenido de la tesis como a sus resúmenes e índices.

**WARNING.** Access to the contents of this doctoral thesis and its use must respect the rights of the author. It can be used for reference or private study, as well as research and learning activities or materials in the terms established by the 32nd article of the Spanish Consolidated Copyright Act (RDL 1/1996). Express and previous authorization of the author is required for any other uses. In any case, when using its content, full name of the author and title of the thesis must be clearly indicated. Reproduction or other forms of for profit use or public communication from outside TDX service is not allowed. Presentation of its content in a window or frame external to TDX (framing) is not authorized either. These rights affect both the content of the thesis and its abstracts and indexes.

María Alba Martín

# **Silicon Dioxide Microstructures Based on Macroporous Silicon for Biomedical Applications**

Ph.D. Thesis

*Supervised by:*

Prof. Lluís Francesc Marsal Garví

Departament d'Enginyeria Electrònica, Elèctrica i Automàtica

Nanoelectronic and Photonic Systems (NePhos)



UNIVERSITAT ROVIRA I VIRGILI

Tarragona

2014

UNIVERSITAT ROVIRA I VIRGILI

SILICON DIOXIDE MICROSTRUCTURES BASED ON MACROPOROUS SILICON FOR BIOMEDICAL APPLICATIONS.

María Alba Martín

Dipòsit Legal: T 153-2015

UNIVERSITAT ROVIRA I VIRGILI

SILICON DIOXIDE MICROSTRUCTURES BASED ON MACROPOROUS SILICON FOR BIOMEDICAL APPLICATIONS.

María Alba Martín

Dipòsit Legal: T 153-2015

UNIVERSITAT ROVIRA I VIRGILI

SILICON DIOXIDE MICROSTRUCTURES BASED ON MACROPOROUS SILICON FOR BIOMEDICAL APPLICATIONS.

María Alba Martín

Dipòsit Legal: T 153-2015



Departament d'Enginyeria Electrònica, Elèctrica i Automàtica

Escola Tècnica Superior d'Enginyeria

Campus Sescelades

Avda. Països Catalans 26

43007 Tarragona, Spain

Tel. +34 977 55 96 10

Fax +34 977 55 96 05

I STATE that the present study, entitled “Silicon Dioxide Microstructures Based on Macroporous Silicon for Biomedical Applications”, presented by María Alba Martín for the award of the degree of Doctor, has been carried out under my supervision at the Department of Electrical, Electronic and Automatic Control Engineering of this University, and that it fulfils all the requirements to be eligible for the International Doctorate Award.

Tarragona, 5<sup>th</sup> of November 2014

Doctoral Thesis Supervisor

Prof. Lluís F. Marsal Garví

UNIVERSITAT ROVIRA I VIRGILI

SILICON DIOXIDE MICROSTRUCTURES BASED ON MACROPOROUS SILICON FOR BIOMEDICAL APPLICATIONS.

María Alba Martín

Dipòsit Legal: T 153-2015

## ***Acknowledgements***

This PhD thesis would have never been possible without the collaboration and support of a number of people that have helped me over the course of this journey. Hereby, I would like to acknowledge and thank all of them.

First I would like to express my gratitude and appreciation to my supervisor, Prof. Lluís Marsal, for his support, encouragement and guidance throughout this work, and for providing me the opportunity to complete my PhD thesis. I would also like to thank Dr Josep Ferré-Borrull for his valuable suggestions and advice. Financial support from Universitat Rovira i Virgili is also gratefully acknowledged.

Special thanks should also be given to Dr Pilar Formentín. Thank you for the exceptional advice and priceless assistance, for the encouragement and moral support during the hard periods, and for the invaluable discussions not limited to my research.

I am also really indebted to all those who were willing to share with me their precious research experience and to guide me in the lab: Dr Abel Santos, Dr Elisabetta Romano and Dr Agustín Mihi. Thanks for your inspiring advice, and for sharing your passion for science.

I would also like to express my gratitude to the members of Nephos group, past and present, for their collaboration, kindness and camaraderie. Specially to fellow PhD candidates Peilin, Gerard, Víctor and Pedro who have been with me almost the whole duration of this thesis, and with

---



whom I have shared so many coffees. Thanks for your continuous support in the lab and for the much appreciated discussions. It has been a pleasant and satisfying learning experience working with all of you.

I must also thank Prof. Nico Voelcker for offering me the opportunity to work and learn for three months in his research group at the Mawson Institute, Adelaide. I would like to thank him for the stimulating discussions and advice. I would also like to acknowledge Dr. Bahman Delatat for his patience, for showing me cell culture techniques and for his great contribution to the research conducted in Chapter 8. I am also grateful to all other members of Nico's groups for their help and assistance in the labs, and for their kindness and hospitality. Special thanks must go to Neka and Bea, who very much contributed to make my stay in Adelaide such an enjoyable experience.

I would like to acknowledge the staff at the Servei de Recursos Científics i Tècnics of the Universitat Rovira i Virgili, Mercé, Mariana, Lukas, Rita and Núria, for their professionalism and guidance in the numerous characterization sessions, and for their training and assistance in the cleanroom facility.

I am also grateful to Prof. Rosa Solà and her research group URLA, in particular to Úrsula and Sara, for their collaboration with the cell culture experiments that allowed me to get very inspiring results. Thank you for your contribution to the research work in Chapter 7.

My gratitude to the many good friends that contributed to make my life in Tarragona enjoyable over all these years. Thanks to all those who not only shared lunch table with me but also stories, jokes, joys and sorrows. Thanks to all my flatmates, from those who welcomed me in Tarragona, to

---

the latest residents of Villacucaracha. I should especially thank Susana, Luis, Elena, Óscar and Maria M. for their unconditional friendship and support. I am sure we will remain good friends for many years to come.

I wish to thank all my family and friends; despite the distance, they have always been an invaluable source of constant support.

Above all I would like to thank my parents and my sister for their unconditional love and encouragement throughout my entire life, and to Anthony for being by my side, encouraging, supporting and believing.

UNIVERSITAT ROVIRA I VIRGILI

SILICON DIOXIDE MICROSTRUCTURES BASED ON MACROPOROUS SILICON FOR BIOMEDICAL APPLICATIONS.

María Alba Martín

Dipòsit Legal: T 153-2015

---

## ***List of Abbreviations***

3D	—	Three-dimensional
ABS	—	Acetate buffer
APTES	—	(3-Aminopropyl)triethoxysilane
APTMS	—	(3-Aminopropyl)trimethoxysilane
ATR	—	Attenuated total reflectance
BET	—	Brunauer–Emmett–Teller
BHF	—	Buffered hydrofluoric acid
BSA	—	Bovine serum albumin
C <sub>4</sub> F <sub>8</sub>	—	Octafluorocyclobutane
CPT	—	Camptothecin
CTAC	—	Cetyltrimethylammonium chloride
CVD	—	Cardiovascular disease
DMF	—	Dimethylformamide
DMSO	—	Dimethylsulfoxide
DNA	—	Deoxyribonucleic acid
DOX	—	Doxorubicin hydrochloride
EDC	—	1-ethyl-3-(3-dimethylaminopropyl)carbodiimide
ESEM	—	Environmental scanning electron microscope
FDA	—	Food and drug administration
FITC	—	Fluorescein isothiocyanate
FT-IR	—	Fourier Transform-Infrared
GOPS	—	(3-Glycidyloxypropyl)trimethoxysilane
GRAS	—	Generally recognized as safe
GTA	—	Glutaraldehyde
H <sub>2</sub> O <sub>2</sub>	—	Hydrogen peroxide
H <sub>2</sub> SO <sub>4</sub>	—	Sulfuric acid
HAEC	—	Human aortic endothelial cells
HCl	—	Hydrochloric acid
HF	—	Hydrofluoric acid
HNO <sub>3</sub>	—	Nitric acid
ICP	—	Inductively-coupled-plasma
ICPTES	—	Isocyanatopropyltriethoxysilane

---

IUPAC	—	International Union of Pure and Applied Chemistry
IR	—	Infrared
KOH	—	Potassium hydroxide
LbL	—	Layer-by-layer
LDH	—	Lactate dehydrogenase
macro-pSi	—	Macroporous silicon
MEMS	—	Microelectromechanical systems
MPTMS	—	(3-Mercaptopropyl)trimethoxysilane
nano-pSi	—	Nanoporous silicon
NaOH	—	Sodium hydroxide
NH <sub>4</sub> OH	—	Ammonium hydroxide
NHS	—	n-Hydroxysuccinimide
NRT	—	Neurotrophin
OD	—	Optical density
PAH	—	Poly(allylamine hydrochloride)
PBS	—	Phosphate buffer saline
PEM	—	Polielectrolyte multilayers
PL	—	Photoluminescence
pSi	—	Porous
PSS	—	Sodium poly(styrene sulfonate)
PTFE	—	Polytetrafluoroethylene
PVC	—	Poly(vinyl chloride)
RIE	—	Reactive ion etching
SCR	—	Space-charge region
SD	—	Standard deviation
SEM	—	Scanning electron microscopy
Si	—	Silicon
SiO <sub>2</sub>	—	Silicon dioxide
siRNA	—	Small interfering ribonucleic acid
SMCC	—	Cyclohexane-1-carboxylate
TEM	—	Transmission electron microscopy
TMAH	—	Tetramethylammonium hydroxyde
UV	—	Ultraviolet

## List of Figures

<b>Figure 2.1.</b> Scheme of the single-tank anodization cell used for the fabrication of porous silicon layers. Adapted from reference [12].....	13
<b>Figure 2.2.</b> General current-voltage ( $I$ - $V$ ) characteristics for electrochemical etching of silicon, showing the regimes for porous silicon formation and electropolishing. Adapted from reference [14]...	14
<b>Figure 2.3.</b> Simplified mechanism for electrochemical etching of silicon in fluoride containing solutions. Adapted from reference [6].....	19
<b>Figure 2.4.</b> Proposed dissolution mechanism of crystalline silicon in hydrofluoric acid solutions. The two different reaction paths illustrate the possible 2-electron (A) and 4-electron (B) chemical dissolution paths associated with two experimental regimes: porous silicon formation and electropolishing, respectively. Adapted from reference [21].	20
<b>Figure 2.5.</b> Schematic of the equilibrium charge distribution and the electric field around pores in the electrochemical etching of low doped p-type silicon. Adapted from reference [24].	22
<b>Figure 2.6.</b> Silicon oxidation reactions at different temperatures. A) Room temperature; B) 100-200 °C and C) 300-900 °C. Adapted from reference [14].	33
<b>Figure 2.7.</b> Schematic of the general structure of a silane molecule that includes a functional group and a carbon chain spacer and three hydrolysable groups. Adapted from reference [92].	36
<b>Figure 2.9.</b> Molecular structure of two alkoxysilanes used as linkers for biomolecule attachment to SiO <sub>2</sub> surfaces.	39
<b>Figure 2.10.</b> Schematic showing the covalent immobilization of biomolecules via glutaraldehyde spacer onto amino-silanized surfaces. A) Surface silanization; B) activation with GTA; C) binding of biomolecules via amino-terminal groups on biomolecule surface and D) imine bond formation between the aldehyde-terminated surface the biomolecule.	41
<b>Figure 3.1.</b> Photograph of the electrochemical etching set-up. The wafer is mounted in the customized etching cell (A) coupled with a mechanical	

stirring system (B). The voltage-current sourcemeter Keithley 2611A applies the current and measures the resulting voltage between the electrodes (C). The system is controlled by a home-designed program run in a computer (D)..... 54

**Figure 3.2.** A) Schematic diagram of the electrochemical cell used in the pSi formation; B) photograph of the customized cell with a view of the stirrer and the Pt electrode, and the interior of the cell body with the exposed silicon at the bottom..... 55

**Figure 3.3.** Schematic representation for the sample preparation. A) Wafer oxidation; B) photoresist deposition by spin-coating; C) direct-laser lithography; D) selective removal of the oxide film by BHF etch and dissolution of the remaining photoresist layer; E) TMAH etch for the formation of inverted pyramids and F) dissolution of the residual SiO<sub>2</sub> layer..... 58

**Figure 3.4.** A, B) Tilted SEM images of the TMAH etch pits with 3 μm lattice constant formed at the silicon surface as a sample preparation for the electrochemical etching process; C) top-view of patterned silicon with 4 μm lattice constant..... 60

**Figure 3.5.** Top view SEM images of macro-pSi samples formed in HF:DMF (1:10) at 5 mA cm<sup>-2</sup> current density on substrates of resistivity A) 10-20; B) 20-30; C) 40-60; and D) 80-100 Ω cm..... 61

**Figure 3.6.** SEM images of macro-pSi samples formed on 10-20 Ω cm p-type silicon in HF:DMF (1:10) at a current density of A) 5; B) 10; C) 15 and D) 20 mA cm<sup>-2</sup>..... 62

**Figure 3.7.** Porosity versus current density for samples prepared on p-type Si of resistivity 10-20 Ω cm at a current density of 5 mA cm<sup>-2</sup>..... 63

**Figure 3.8.** SEM micrographs A) patterned Si with truncated pyramids as a result of an inadequate TMAH etch; B) macropore formation in the patterned regions; and C) tilted view of the macropore formation in depth..... 64

**Figure 3.9.** SEM images from A) top view and B) cross-sectional view of ordered macroporous silicon formed on patterned p-type Si (4 μm lattice constant) with the formation of interstitial pores; C) top view and D) cross-sectional view of ordered macroporous silicon with a good adjustment of the electrochemical parameters (3 μm lattice constant).65

**Figure 3.10.** SEM images taken from a macroporous silicon sample formed on patterned Si (4 μm lattice constant) with 40-60 Ω cm resistivity. A)

- Top view and B) detail in cross-section of the initial pyramids and subsequent electrochemical pores..... 66
- Figure 3.11.** SEM micrograph of straight pores 150  $\mu\text{m}$  in depth etched into Si with a squared pattern and 4  $\mu\text{m}$  lattice constant (left). Zoomed images at different depths display uniform pores in diameter and smooth wall surfaces (right)..... 67
- Figure 3.12.** Schematic illustration of the method for the fabrication of silicon dioxide micropillars. A) Macropore formation by electrochemical etching; B) silicon dioxide growth by thermal oxidation; C) oxide layer removal on an unmasked area of the sample backside; D) backside silicon etching in TMAH solution to release the micropillars. .... 69
- Figure 3.13.** Macro-pSi sample A) freshly anodized and B) after thermal oxidation at 1000  $^{\circ}\text{C}$  for 1.5 h. .... 70
- Figure 3.14.** SEM micrographs of  $\text{SiO}_2$  micropillars after TMAH etch of the backside bulk silicon fabricated from A) random and B) ordered macro-pSi..... 71
- Figure 3.15.** Dark-field TEM images of A) a single broken micropillar showing uniform  $\text{SiO}_2$  walls and hollow structure; B) a detail of the micropillar tip. .... 71
- Figure 3.16.** SEM top-view images of  $\text{SiO}_2$  micropillars fabricated using identical etching conditions on substrates of different resistivity: A) 10-20; B) 40-60  $\Omega\text{ cm}$ ..... 72
- Figure 3.17.** TEM micrographs of a single broken micropillar in A) dark field and B) bright field modes..... 73
- Figure 3.18.** SEM top-view micrographs of ordered  $\text{SiO}_2$  micropillar arrays from macro-pSi formed in HF:DMF (1:10) at 5  $\text{mA cm}^{-2}$  on Si substrates of A) 80-100 and B) 40-60  $\Omega\text{ cm}$  resistivity and 4  $\mu\text{m}$  lattice constant; and C) 10-20  $\Omega\text{ cm}$  resistivity and 3  $\mu\text{m}$  lattice constant. .... 74
- Figure 3.19.** SEM micrographs of micropillars with identical external diameter (1.8  $\mu\text{m}$ ) and different length of A) 5-6  $\mu\text{m}$ ; B) 10-12  $\mu\text{m}$ ; C) 13-15  $\mu\text{m}$ ; D) 16-18  $\mu\text{m}$ ; E) 20-24  $\mu\text{m}$ ; F) 25-30  $\mu\text{m}$ ; G) 35-40  $\mu\text{m}$ ; H) 50-60  $\mu\text{m}$  and I) 150-180  $\mu\text{m}$ ..... 74
- Figure 3.20.** Micropillar arrays inside microwells. A, C) Ordered micropillars protruding out of a squared area of 190  $\mu\text{m}$  side inside 100  $\mu\text{m}$  deep microwells. B, D) random micropillar on an area of 120  $\mu\text{m}$  side inside 100  $\mu\text{m}$  deep microwells. .... 75



- Figure 3.21.** Schematic illustration of the method for the fabrication of silicon dioxide microtubes. A) Macropore formation by electrochemical etching; B) silicon dioxide growth by thermal oxidation; C) oxide layer removal on the frontside surface with directional plasma ICP-RIE process; and D) bulk silicon removal by TMAH etch..... 77
- Figure 3.22.** SEM tilted micrographs of SiO<sub>2</sub> microtubes fabricated from random macroporous silicon with a protruding lengths of 9 μm..... 78
- Figure 3.23.** SEM micrographs of microtubes when the TMAH has etched most of the surrounding silicon. A) SiO<sub>2</sub> microtubes attached from the very bottom on the silicon substrate; B) collapsed and standing microtubes; C) detail of a bunch of standing microtubes..... 79
- Figure 3.24.** SEM tilted micrographs of SiO<sub>2</sub> microtubes fabricated from ordered macroporous silicon with a protruding length of 6 μm..... 80
- Figure 4.1.** Reaction and bonding mechanism of alkoxysilanes. Adapted from reference [13]..... 87
- Figure 4.2.** Schematic representation of the possible configurations for adsorbed APTES on oxidized silicon. A) APTES multilayer formation by reaction and/or interaction of dissolved silanes with the surface attached APTES; B) electrostatic attraction between the positive charged amino groups and negatively charged silicon surface amine; C) ethoxy groups are hydrolyzed to form siloxane linkages with surface silanols and to polymerize with neighboring silanes; D) hydrogen bonding between amines and surface silanols..... 89
- Figure 4.3.** Schiff base reaction for the formation of imine bond from primary amines and aldehydes (adapted from reference [3])..... 93
- Figure 4.4.** FT-IR transmission spectra of freshly anodized (blue line) and oxidized porous silicon (black line). ..... 97
- Figure 4.5.** FT-IR transmission spectra of pSi samples at selected steps of the functionalization. A) HNO<sub>3</sub>-oxidized (black line) and MPTMS-functionalized (pink line) sample and B) HNO<sub>3</sub>-oxidized (black line) and APTES-functionalized (green line) sample. Insets shown in panels A and B are expanded along the x- and y-axes in the regions of most interest. 99
- Figure 4.6.** A) FT-IR transmission spectra and B) second derivative spectra of absorbance of a pSi sample in the C-H stretching region after MPTMS-functionalization (pink line), post-treatment at pH 1 (green line); post-treatment at pH 13 (red line) and thermal curing at 120 °C for 1 h (blue

---

line). Absorption maxima appear as minima in the second derivatives .....	101
<b>Figure 4.7.</b> FT-IR transmission spectra in the N-H stretching region of a pSi sample after APTES functionalization (green line); post-treatment at pH 1 (red line); post-treatment at pH 13 (blue line) and thermal curing at 120 °C (yellow line). .....	103
<b>Figure 4.8.</b> Schematic representation of the GTA reaction onto APTES. A) Partial dehydration of the primary amine into a secondary amine; B) complete dehydration of the secondary amine into an imine group. ...	104
<b>Figure 4.9.</b> FT-IR transmission spectra of pSi samples after functionalization with APTES (green line) and subsequent GTA docking (orange line). Inset is expanded along the x- and y-axes in the region of most interest.....	105
<b>Figure 4.10.</b> FT-IR transmission spectra (A, B) and second derivative spectra of absorbance (C, D) of GTA functionalization of amino-terminated surfaces after post-treatment at pH 13 (A, C) and (B, D)...	107
<b>Figure 5.1.</b> Schematic representation of the method for the dual-side functionalization. A) Macropore formation by electrochemical etching and masked BHF etch of the oxide layer on the wafer backside; B) functionalization of the internal side of the micropillars with MPTMS; C) TMAH anisotropic etching of the bulk silicon from the backside and D) functionalization of the external side of the released micropillars with APTES, GTA and BSA-FITC.....	121
<b>Figure 5.2.</b> Tilted-view SEM micrographs of A) silicon dioxide micropillars arrays after TMAH etching of backside bulk silicon and B) microwell with released micropillars.....	124
<b>Figure 5.3.</b> Transmission FT-IR spectra of functionalized nanoporous silicon samples A) after functionalization with MPTMS; B) after functionalization with APTES (i) and subsequent GTA docking (ii). Insets shown in panels A and B are expanded along the y-axes by 20 times in the regions of most interest.....	126
<b>Figure 5.4.</b> Top-view fluorescence images of micropillar arrays A) after the labeling of the sole internal surface with rhodamine, excitation laser at 543 nm, bandpass emission filter 590 ± 30 nm; B) after the labeling of the sole external surface with BSA-FITC, excitation laser at 488 nm, bandpass emission filter 515 ± 15 nm.....	128

---

- Figure 5.5.** Top-view fluorescent image of the micropillars after dual-side functionalization under the simultaneous excitation of 488 and 543 nm lasers. Emission collected through bandpass filters of A) both  $515 \pm 15$  and  $590 \pm 30$  nm, B)  $590 \pm 30$  nm and C)  $515 \pm 15$  nm.....129
- Figure 5.6.** Cross section fluorescence images of detached micropillars collected through both  $515 \pm 15$  and  $590 \pm 30$  nm emission filters.....131
- Figure 5.7.** A) Schematic representation of the micropillars cross-section and distribution of the fluorophores on the internal and external surfaces. Cross-section view by confocal microscopy of the micropillars under the excitation of B) both 488 and 543 nm; C) 488 nm; and D) 543 nm lasers.....131
- Figure 6.1.** Layer-by-layer approach to produce thin films by using complementary charges. A) Deposition of positively charged polyelectrolyte (polycation); B) deposition of negatively charged polyelectrolyte (polyanion); C) repeat the sequence until obtaining the desired number of bilayers.....141
- Figure 6.2.** Chemical structures of the cationic and anionic polyelectrolytes, PAH and PSS, respectively, and the anticancer pharmaceutical DOX. ....142
- Figure 6.3.** Schematic of the process for the PEM coating and DOX loading and release of the SiO<sub>2</sub> micropillars. A) Polyelectrolyte pair PAH/PSS alternative deposition on the internal sidewalls of SiO<sub>2</sub> micropillars via the LbL method to construct a pH-responsive drug delivery system; B) DOX loading in the swollen PEM film at pH 2.0; C) DOX confinement due to the PEM layer contraction at pH 8.0; and D) DOX release in different media at pH 7.4 and 5.2.....145
- Figure 6.4.** Microscopy characterization of the SiO<sub>2</sub> micropillars. A) Tilted SEM image of released micropillar arrays with a 3  $\mu$ m lattice constant; B) dark-field TEM image of a detached hollow micropillar with a length of 26  $\mu$ m. ....146
- Figure 6.5.** FTIR-ATR characterization for polyelectrolyte coating. FTIR-ATR spectra of A) oxidized macroporous silicon,; B) PAH-coated,; and C) PAH/PSS-coated macroporous silicon.....147
- Figure 6.6.** Fluorescence confocal images of PEM-coated and DOX-loaded micropillars. A,B) Micropillars arrays in top view after PEM coating (eight bilayers) and DOX loading; C) detached hollow micropillars with

uniform size distribution; and D) single detached micropillar with PEM and DOX all along the walls. ....	148
<b>Figure 6.7.</b> A) Emission PL spectra of DOX 1 ng mL <sup>-1</sup> in PBS at pH 7.4; B) PL intensity vs DOX concentration at pH 5.2 and 7.4. ....	150
<b>Figure 6.8.</b> Evolution of the emission PL spectra of DOX in order to monitor the release from SiO <sub>2</sub> micropillars internally coated with eight bilayers of PAH/PSS. The photoluminescence was monitored for 4 hours at an exciting wavelength of 480 nm. ....	150
<b>Figure 6.9.</b> Drug release profile for 24 h at pH 7.4 and 5.2. A) Time evolution of pH-responsive release of DOX from PEM-coated (eight bilayers) micropillars at pH 5.2 (red squares) and 7.4 (blue triangles); B) zoomed-in plot and linear fitting of DOX release in the region between 120 and 540 min. ....	152
<b>Figure 6.10.</b> Effect of the number of bilayers in the DOX release profiles from PEM coated micropillars at pH 7.4 over a period of 24 h. ....	154
<b>Figure 6.11.</b> Effect of the number of bilayers in the DOX release. A) DOX released after 24 h and B) time to reach the 80% of the total release as a function of the number of layers. ....	154
<b>Figure 7.1.</b> Top-view SEM images of SiO <sub>2</sub> microstructures A) macro-pSi; B) random SiO <sub>2</sub> micropillars and C) ordered SiO <sub>2</sub> micropillars. ....	172
<b>Figure 7.2.</b> Schematic representation of the surface chemical treatment on silicon oxide samples to obtain a terminal collagen functionalization following the APTES-GTA-Collagen sequence. ....	172
<b>Figure 7.3.</b> Transmission FTIR spectra of A) oxidized pSi; B) APTES-functionalized pSi; C) GTA docking on APTES-functionalized pSi and D) collagen immobilization on GTA-APTES-functionalized pSi. ....	174
<b>Figure 7.4.</b> Number of HAEC cells per area unit attached to flat Si with and without collagen functionalization after 2, 7 and 9 days (left columns to right columns). ....	175
<b>Figure 7.5.</b> SEM images of HAEC on flat Si (A, B and C) and collagen-functionalized flat Si (D, E and F) after 2, 7 and 9 days incubation (left column to right column). ....	176
<b>Figure 7.6.</b> SEM images of HAEC after 2 days incubation. A) Flat Si; B) random macro-pSi; C) random micropillars and D) ordered micropillars. ....	177
<b>Figure 7.7.</b> HAEC attached to various types of SiO <sub>2</sub> microstructures. Flat silicon was used as control. Cells were counted per surface measuring	

three areas per sample. Mean values are express as cell number per mm<sup>2</sup> with error bar corresponding to standard deviation.....178

**Figure 7.8.** LDH cytotoxicity assay showing the results of HAEC cultures in different substrates after 1, 2, 4 and 7 days of incubation. Supernatants were assayed for LDH release and expressed as mean of 492 nm OD..179

**Figure 7.9.** Scanning electron microscopy of HAEC after 2 days incubation on various SiO<sub>2</sub> microstructured substrates. A,E,I) Flat Si; B,F,J) macro-pSi; C,G,K) random micropillars and D,H,L) ordered micropillars. ....181

**Figure 7.10.** A) Mean cell surface area calculated and B) mean cell circularity calculated from SEM images after 2 days of incubation. For the cell circularity 0 represents a line and 1.0 a circle. An average number of 40 cells were analyzed per sample to calculate the standard deviation. ....183

**Figure 7.11.** Fluorescence confocal microscopy images of HAEC after 2 days of incubation. Cells were stained with NucGreen for the nucleus and Phalloidin for the actin filaments. A) Flat Si; B) macro-pSi; C) random micropillars and D) ordered micropillars. ....185

**Figure 8.1.** Schematic illustration of the method for the functionalization and drug loading of silicon dioxide micropillars. A) SiO<sub>2</sub> micropillars hydroxylation; B) GOPS silanization of the external surface; C) anti-p75NTR immobilization followed by BSA incubation to prevent nonspecific binding; D) CPT loading inside the micropillars; E) mechanical detachment of SiO<sub>2</sub> micropillars; F) micropillars release in the cell medium.....199

**Figure 8.2.** SEM micrographs of A)a tilted-view of ordered silicon dioxide micropillar arrays after TMAH etching of back side bulk silicon and B) detached micropillars. ....203

**Figure 8.3.** FT-IR of A) oxidized and B) GOPS-functionalized porous silicon .....205

**Figure 8.4.** Binding of DyLight549-conjugated IgG to microtubes, analyzed by fluorescence microscopy. A) Native (unsilanized) microtubes and B) GOPS-silanized microtubes (control) were incubated with DyLight549-conjugated mouse antihuman IgG. The red chromophore ('DyLight549') indicates binding of IgG to the silanized microtubes. ....206

**Figure 8.5.** Fluorescence microscopy images of A) a top-view CPT-loaded SiO<sub>2</sub> micropillar arrays and B) individual SiO<sub>2</sub> micropillars loaded with CPT after mechanical detachment. ....207

- 
- Figure 8.6.** Release kinetics of CPT from loaded SiO<sub>2</sub> micropillars of 15 μm length.....207
- Figure 8.7.** Antibody-functionalized SiO<sub>2</sub> microtube attachment to cells. A) Brightfield microscopy image of SH-SY5Y cells after incubation with antibody-functionalized microtubes. The red arrows point to microtubes attached to cell membranes. B) Brightfield microscopy image of BSR cells after incubation with antibody-functionalized microtubes. No microtubes are visible.....208
- Figure 8.8** Viability of SH-SY5Y and BSR cells after incubation with antibody-functionalized and CPT-loaded microtubes. Cells were incubated with anti-p75NTR-functionalized microtubes for 1 h. The medium was then replaced to remove unattached microtubes releasing CPT into the cell culture medium. For each sample, viability analysis was performed in triplicate. Microtubes were applied at a final concentration of 50 μg mL<sup>-1</sup>. .....209
- Figure 8.9.** Interaction of anti-p75NTR-labelled micropillars with adherent cells. Confocal fluorescence microscopy image of SH-SY5Y neuroblastoma cells (A) and BSR cells (B). Red: actin filaments in the cytoplasm (phalloidin staining), green: nucleus (Picogreen staining), blue: micropillars (CPT fluorescence).....210
- Figure 8.10.** Time series of CPT uptake into SH-SY5Y neuroblastoma cells from CPT-loaded anti-p75NTR-labelled microtubes loaded with CPT by confocal fluorescence laser scanning microscopy. Left panels CPT fluorescence, right panels overlay (red: actin filaments in the cytoplasm (phalloidin staining), green: nucleus (Picogreen staining), blue: CPT fluorescence. ....211

UNIVERSITAT ROVIRA I VIRGILI

SILICON DIOXIDE MICROSTRUCTURES BASED ON MACROPOROUS SILICON FOR BIOMEDICAL APPLICATIONS.

María Alba Martín

Dipòsit Legal: T 153-2015

## ***List of Tables***

<b>Table 2.1.</b> Main pore morphologies and proposed formation mechanisms .....	18
-------------------------------------------------------------------------------------	----



UNIVERSITAT ROVIRA I VIRGILI

SILICON DIOXIDE MICROSTRUCTURES BASED ON MACROPOROUS SILICON FOR BIOMEDICAL APPLICATIONS.

María Alba Martín

Dipòsit Legal: T 153-2015

## ***List of Contributions***

### ***Journal Articles***

Alba, M., Delalat, B., Rogers, L.M., Marsal, L.F. & Voelcker, N.H. (2014) Silica Nanopills for Targeted Anticancer Drug Delivery (Submitted)

Formentín, P., Catalán, Ú., Fernández-Castillejo, S., Alba, M., Baranowska, M., Solà, R., Pallarès, J., & Marsal, L. F. (2014). Human aortic endothelial cell morphology influenced by topography of porous silicon substrates (Submitted).

Alba, M., Formentín, P., Ferré-Borrull, J., Pallarès, J., & Marsal, L. F. (2014). pH-responsive drug delivery system based on hollow silicon dioxide micropillars coated with polyelectrolyte multilayers. *Nanoscale research letters*, 9(1), 1-8.

Formentín, P., Alba, M., Catalán, Ú., Fernández-Castillejo, S., Pallarès, J., Solà, R., & Marsal, L. F. (2014). Effects of macro-versus nanoporous silicon substrates on human aortic endothelial cell behavior. *Nanoscale research letters*, 9(1), 1-7.

Alba, M., Romano, E., Formentín, P., Eravuchira, P. J., Ferré-Borrull, J., Pallarès, J., & Marsal, L. F. (2014). Selective dual-side functionalization of hollow SiO<sub>2</sub> micropillar arrays for biotechnological applications. *RSC Advances*, 4(22), 11409-11416.

Urteaga, R., Acquaroli, L. N., Koropecski, R. R., Santos, A., Alba, M., Pallarès, J., Marsal, L.F. & Berli, C. L. (2013). Optofluidic characterization of nanoporous membranes. *Langmuir*, 29(8), 2784-2789.

---

Alba, M., Pazos-Perez, N., Vaz, B., Formentin, P., Tebbe, M., Correa-Duarte, M. A., Granero, P., Ferré-Borrull, J., Álvarez, R., Pallarès, J., Fery, A., de Lera, A.R., Marsal, L. F. & Alvarez-Puebla, R. A. (2013). Macroscale Plasmonic Substrates for Highly Sensitive Surface-Enhanced Raman Scattering. *Angewandte Chemie International Edition*, 52(25), 6459-6463.

Santos, A., Balderrama, V. S., Alba, M., Formentín, P., Ferré-Borrull, J., Pallarès, J., & Marsal, L. F. (2012). Nanoporous anodic alumina barcodes: toward smart optical biosensors. *Advanced Materials*, 24(8), 1050-1054.

Santos, A., Alba, M., Rahman, M. M., Formentín, P., Ferré-Borrull, J., Pallarès, J., & Marsal, L. F. (2012). Structural tuning of photoluminescence in nanoporous anodic alumina by hard anodization in oxalic and malonic acids. *Nanoscale research letters*, 7(1), 1-11.

Santos, A., Vojkuvka, L., Alba, M., Balderrama, V. S., Ferré-Borrull, J., Pallarès, J., & Marsal, L. F. (2012). Understanding and morphology control of pore modulations in nanoporous anodic alumina by discontinuous anodization. *Physica Status Solidi (a)*, 209(10), 2045-2048.

Santos, A., Balderrama, V. S., Alba, M., Formentín, P., Ferré-Borrull, J., Pallarès, J., & Marsal, L. F. (2012). Tunable Fabry-Pérot interferometer based on nanoporous anodic alumina for optical biosensing purposes. *Nanoscale research letters*, 7(1), 1-4.

### **Communications to Conferences**

Alba, M., Formentin, P., Catalán, Ú., Fernández-Castillejo, S., Solà, R., Pallarès J. & Marsal, L.F. (2014) Endothelial Cell Adhesion on Macro- and Nano-Porous Silicon Substrates, *Graduate Student Meeting on Electronic Engineering*, Tarragona, Spain. (Poster presentation).

Alba, M., Formentin, P., Ferré-Borrull, J., Pallarès, J. & Marsal, L.F. (2014) pH-Responsive Drug Delivery System Based on Hollow Silicon Dioxide Micropillars Coated with Polyelectrolyte Multilayers, *Porous Semiconductors-Science and Technology (PSST)*, Benidorm, Spain (Oral presentation).

Marsal, L.F., Alba, M., Macias, G., Formentin, P., Ferré-Borrull, J., Pallarès, J. & Santos, A. (2014). Label-free and real-time Photonic sensors as analytical platforms for environmental monitoring of pollutants and Medical Diagnosis, *Electrochemical Society Meeting*, Orlando, USA (Oral presentation).

Alba, M., Formentin, P., Ferré-Borrull, J., Pallarès, J. & Marsal, L.F. (2013) Differential functionalization of the internal and external surfaces of hollow SiO<sub>2</sub> micropillars, *Graduate Student Meeting on Electronic Engineering*, Tarragona, Spain (Oral presentation).

Marsal, L.F., Alba, M., Formentín, P., Eravuchira, P.J., Pallarès, J. & Ferré-Borrull, J. (2013). Functionalization of silicon dioxide micropillars for biosensing and microarray technology. *Nanobio&Med 2013-Imaginenano 2013*, Bilbao, Spain. (Oral presentation)

Alba, M., Formentín, P., Ferré-Borrull, J., Pallarès, J. & Marsal, L.F. (2012) Label-free enzyme biosensor based on porous silicon microcavities, *Conferencia Española de Nanofotónica*, Carmona, Spain. (Poster presentation).

Alba, M., Formentín, P., Santos, A., Ferré-Borrull, J., Pallarès, J. & Marsal, L.F. (2012). Chemically modified silicon dioxide micropillars for biosensing

applications, *Graduate Student Meeting on Electronic Engineering*, Tarragona, Spain (Poster presentation).

Alba, M., Formentín, P., Santos, A., Ferré-Borrull, J., Pallarès, J. & Marsal, L.F. (2012). Silicon dioxide micro-pillars for biosensing applications, *Porous Semiconductors-Science and Technology (PSST)*, Málaga, Spain (Poster presentation).

Alba, M., Formentín, P., Santos, A., Ferré-Borrull, J., Pallarès, J. & Marsal, L.F. (2011). Optical characterization of nanoporous anodic alumina formed in oxalic acid solution, *Graduate Student Meeting on Electronic Engineering*, Tarragona, Spain (Poster presentation).

*Sapere Aude*

Horatius

UNIVERSITAT ROVIRA I VIRGILI

SILICON DIOXIDE MICROSTRUCTURES BASED ON MACROPOROUS SILICON FOR BIOMEDICAL APPLICATIONS.

María Alba Martín

Dipòsit Legal: T 153-2015

## Contents

<b>Acknowledgements</b> .....	<i>i</i>
<b>List of Abbreviations</b> .....	<i>v</i>
<b>List of Figures</b> .....	<i>vii</i>
<b>List of Tables</b> .....	<i>xv</i>
<b>List of Contributions</b> .....	<i>xvii</i>
<b>Chapter 1. Introduction</b> .....	<b>1</b>
1.1 Motivation and Background .....	2
1.2 Summary .....	5
<b>Chapter 2. Fundamentals</b> .....	<b>9</b>
2.1 Basics of the Porous Silicon Formation Process.....	11
2.1.1 An overview .....	11
2.1.2 The Electrochemical Etching of Silicon .....	12
2.1.3 Electrochemical Reactions in the Dissolution of Silicon.....	15
2.1.4 Mechanisms of the Electrochemical Dissolution and Pore Formation .....	16
2.1.5 The Physics of Macropore Formation on Low Doped p-Type Silicon .....	21
2.2 SiO <sub>2</sub> Based Materials for the Life Sciences.....	23
2.2.1 Biocompatibility of SiO <sub>2</sub> Microstructures .....	23
2.2.2 Useful Forms of Microstructured Silicon in Biomedicine ...	28
2.3 Chemical Modification of Microstructured Silicon .....	31
2.3.1 Thermal Oxidation of Silicon .....	32
2.3.2 Functionalization Methods for Silicon Dioxide .....	34
2.3.3 Interfacing Silicon Dioxide with Biomolecules.....	37
2.4 References.....	43



<b>Chapter 3. Fabrication of Three-Dimensional Microstructures based on Macroporous Silicon.....</b>	<b>51</b>
3.1 <i>Electrochemical Etching of Silicon. Experimental.....</i>	53
3.1.1 Set-up.....	53
3.1.2 Sample Preparation. Lithography.....	57
3.1.3 Pore Morphology and Process Parameters.....	60
3.3 <i>Silicon Dioxide Microstructures Based on Macroporous Silicon .....</i>	67
3.2.1 Silicon Dioxide Micropillars.....	68
3.2.2 Silicon Dioxide Microtubes .....	76
3.3 <i>Conclusions .....</i>	81
3.4 <i>References .....</i>	82
<b>Chapter 4. Functionalization Methods for Silicon Dioxide and Their Optimization towards Bioligand Conjugation.....</b>	<b>83</b>
4.1 <i>Introduction .....</i>	85
4.1.1 Silanization .....	86
4.1.2 Bioligand Conjugation to Amino-Functionalized Surfaces .	91
4.2 <i>Experimental.....</i>	94
4.2.1 Porous Silicon Sample Fabrication.....	94
4.2.2 Silanization .....	94
4.2.3 Glutaraldehyde Coupling .....	95
4.2.4 Infrared Spectroscopy.....	95
4.3 <i>Results and Discussion.....</i>	96
4.3.1 Silanization with Mercapto- and Aminosilanes.....	97
4.3.2 Post-Silanization Treatments .....	98
4.3.3 Generation of Aldehyde Group Using Glutaraldehyde Linker .....	104
4.4. <i>Conclusions.....</i>	107
4.5 <i>References .....</i>	109

## **Chapter 5. Dual-Side Functionalization of Silicon Dioxide Hollow**

<b>Micropillars</b> .....	<b>115</b>
5.1 Introduction.....	117
5.2 Experimental Section.....	119
5.2.1 Fabrication of SiO <sub>2</sub> Micropillars.....	119
5.2.2 Functionalization.....	120
5.2.3 Fluorescence Confocal Microscopy.....	123
5.3 Results and Discussion.....	123
5.4 Conclusions.....	130
5.5 References.....	132

## **Chapter 6. SiO<sub>2</sub> Micropillars Coated with Polyelectrolyte Multilayers**

<b>for pH-Responsive Drug Release</b> .....	<b>137</b>
6.1 Introduction.....	139
6.2 Experimental Methods.....	143
6.2.1 Fabrication of SiO <sub>2</sub> Micropillars.....	143
6.2.2 Polyelectrolyte Multilayer Coating.....	143
6.2.3 Characterization Techniques.....	144
6.2.4 DOX Loading and pH-Responsive Drug Release.....	144
6.3 Results and Discussion.....	145
6.4 Conclusions.....	154
6.5 References.....	156

## **Chapter 7. Cell Adhesion and Morphology of Endothelial Cells on SiO<sub>2</sub>**

<b>Microstructures</b> .....	<b>161</b>
7.1 Introduction.....	163
7.2 Experimental methods.....	167
7.2.1. Fabrication of SiO <sub>2</sub> Microstructured Substrates.....	167
7.2.2 Functionalization of the SiO <sub>2</sub> Microstructures.....	168
7.2.3 Cell Seeding and Culture.....	168
7.3 Results and Discussion.....	171

7.3.1 Surface Characterization.....	171
7.3.2 Cell Culture on Flat Si .....	174
7.3.3 Cell Growth and Cytotoxicity on Microstructured SiO <sub>2</sub> .....	176
7.3.4 Cell Morphology on SiO <sub>2</sub> Microstructures .....	179
<i>7.4 Conclusions .....</i>	<i>185</i>
<i>7.5 References .....</i>	<i>187</i>
<b>Chapter 8. Antibody-Functionalized SiO<sub>2</sub> Micropillars for Targeted Drug Delivery .....</b>	<b>193</b>
8.1 Introduction .....	195
8.2 Experimental methods .....	197
8.2.1 Micropillars fabrication.....	197
8.2.2 Modification of Outer Surface of Micropillars.....	198
8.2.3 Fourier-Transform Infrared Spectroscopy .....	200
8.2.4 Loading of the Micropillars with Camptothecin.....	200
8.2.5 Cell Culture Procedures.....	201
8.2.6 Cell Viability .....	201
8.2.7 Laser Scanning Confocal Microscopy .....	201
8.2.8 Subcellular Localization of CPT and Imaging.....	202
8.3 Results and Discussion.....	203
8.4 Conclusions .....	211
8.5 References .....	213
<b>Chapter 9. Summary and Conclusions.....</b>	<b>217</b>

# ***Chapter 1***

---

## **Introduction**

## **1.1 Motivation and Background**

The ability to nano- and microstructure materials is attracting a crescent interest from the scientific community. In a biomedical context, we should keep in mind that the complex functions occurring in our body take place in a scale that ranges from macro- to the micro- to the nanosize. Therefore, modulating the architectural features of the material to the nanoscale may bring huge benefits in controlling the physico-chemical interactions with living tissues or achieving biomimetic environments. Biomaterials are being increasingly needed for a range of applications. They can be used for short-time purposes such as surgical operations, or implanted for days to decades in long-term applications. In the pharmaceutical industry there is also a growing interest in developing drug delivery systems that are efficient for the treatment of multiple diseases, with minor side effects. Nano- and micromaterials are being currently explored in applications such as diagnostics, sensing or bone engineering.

Today, many researchers with multidisciplinary backgrounds are combining their efforts to develop advanced biomaterials and drug delivery systems. There have been important advances in these fields during the last few years. However, there are still numerous challenges to translate these systems from bench to bedside. Various questions about the possible risk to health and *in vivo* behaviors have arisen.

In this framework, silicon (Si) and its dielectric, silicon dioxide (SiO<sub>2</sub>), have rapidly emerged as biomaterials with numerous potential benefits. Silicon is the second most abundant element on earth and is present everywhere in our daily life in the form of electronic devices. In biomedicine, silicon appears in multiple commercially available

---

equipments including pacemakers, neurostimulators and many others. The biocompatibility of Si and SiO<sub>2</sub> is generally accepted. Silicon oxidizes to form SiO<sub>2</sub>, and SiO<sub>2</sub> dissolves in physiological fluids into orthosilicic acid, which is the natural form of Si found in the body. Orthosilicic acid is not only non-toxic, but also it has been recently recognized as beneficial to the bone health. In addition, silicon is the most traditional material for microfabrication due to its use historically in integrated circuit development. The precision with which it can be micromachined surpasses all other materials. By adapting microfabrication techniques to biomedical needs, novel devices for drug delivery, tissue engineering and biosensing can be engineered for *in vivo* use.

The porosification of silicon has received much interest because of its versatility to create architectures that range from sponge-like structures formed by pores of a few nanometers to tubular ordered arrays of several micrometers in diameter. Porous silicon is typically produced by the electrochemical etching of silicon in hydrofluoric acid based electrolytes. The material thus obtained is highly controllable in porosity, exhibits a convenient surface chemistry and is compatible with conventional silicon microfabrication technologies. Making the most of these unique features, porous silicon has found application in biomedicine, e.g. as drug delivery carrier, implantable device or biosensor.

Porous silicon with pores around the micron diameter size is commonly known as macroporous silicon (macro-pSi). This material is of particular interest because it can be processed following many standard techniques developed by the microelectronics industry for silicon wafers. A variety of techniques can be applied to manipulate the as-produced features of macro-pSi. Thermal oxidation of macro-pSi is a common

technique to modify the macropore shape, but also to produce a variety of novel structures in silicon. Uniform SiO<sub>2</sub> arrays such as pillars, tubes or needles can be fabricated via thermal oxidation. The resulting silicon dioxide microstructures possess a number of favorable properties that make them relevant to the field of biomaterials and drug delivery. These properties include *in vitro* and *in vivo* compatibility, and adjustable structural and functional properties. The flexibility of the chemical functionalities that can be attached onto SiO<sub>2</sub> surfaces enables the straightforward coupling of bioligands and the improvement of the surface stability. These characteristics have also motivated the use of SiO<sub>2</sub> materials in bioimaging, providing an opportunity for further application in simultaneous diagnosis and therapy (theranostics).

The association of porosification of silicon with microfabrication techniques has been explored for drug delivery applications due to their ability to combine several features such as precise shape and size into a single delivery vehicle. Clever combinations of different kinds of functional materials or multiple chemical functionalities will enable the development of multifunctional medical platforms for multimodal imaging or theranostics. As an example, combined with smart materials, microengineered platforms can be designed to be stimuli responsive. Furthermore, microparticles have shown advantages in dealing with the issues of hydrophobic drugs and undesirable pharmacokinetic profiles. In addition to delivery devices, microstructuring technologies offer exciting opportunities to create biomimetic models or flow patterns.

The field of tissue engineering has also emerged to address the need of regenerating tissues at the cellular level with the help of synthetic three-dimensional (3D) scaffolds. The matrix surrounding cells is on the micro-

and nanoscale. Therefore, in order to obtain biomimetic tissues, we must pursue the development of tunable micro-scaled architectures that are able to regulate the cell behavior. Macro-pSi and its derived structures, such as micropillars, are particularly attractive materials for this purpose due to their adjustable 3D microarchitecture and the possibility to easily process them. Micromachining these materials also allows giving arbitrary topographies that may lead to contact guidance.

Throughout this thesis we aimed the application in drug delivery and tissue engineering of 3D microstructures based on versatile macro-pSi. The adjustability of the chemical functionality was one of the foremost concerns for further design of multifunctional materials. Achieving capabilities of controlling the drug release and also of targeting specific tissues were main goals. Finally, we considered of crucial importance testing the feasibility and non-toxicity of the system *in vitro*.

## **1.2 Summary**

The major aim of this thesis is the development of SiO<sub>2</sub> microstructures based on anodically formed macro-pSi with a focus on their application in biomedicine. The electrochemical etching of silicon allows the production of 3D tubular structures in the micrometer size. This, combined with microfabrication techniques such as lithography, enables the development of ordered cylindrical arrays in the form of pores, tubes and hollow pillars. Thermal oxidation of silicon generates silicon dioxide, which is of great interest in biomedical applications due to its biocompatibility. The flexibility of the SiO<sub>2</sub> surface chemistry makes it possible to attach a variety of functionalities via the ubiquitous silanol chemistry, of special importance towards the conjugation of bioligands including proteins,



enzymes or antibodies. Tunable 3D structures, together with biomolecule conjugation, make SiO<sub>2</sub> substrates a friendly and stable material capable of interfacing and interacting with living cells. In addition, the particular architecture of hollow micropillars allows the differential functionalization of the internal and external sides. The ability to create multifunctional microstructures has been especially attractive for application in stimuli-responsive and targeted drug delivery.

The thesis is organized as follows:

Chapter 2 presents the fundamentals and a literature review as an introduction to the main techniques applied throughout this thesis. The current state-of-the-art of the electrochemical etching of silicon, reaction mechanisms and physics of the pore formation are described. A review on the possible physical forms of porous silicon for application in tissue engineering and drug delivery is also presented. The functionalization techniques for chemical modification of silicon dioxide are discussed.

Chapter 3 introduces the experimental techniques for fabricating random and ordered macro-pSi from low doped p-type Si. Methodological studies to acquire a basic understanding of the etching process and the influence of the process parameters are described. Several ordered macroporous structures obtained after optimization of parameters are presented. The fabrication techniques of inverted structures such as micropillars and microtubes from preceding macropores were described.

Chapter 4 is devoted to the chemical modification of SiO<sub>2</sub> surfaces towards bioligand conjugation. Silanization protocols to obtain an optimal silane layer with available functional sites are determined after infrared (IR) spectroscopy analysis. Post-treatments were applied to aid the

hydrolysis and condensation of the lateral alkoxy chains in order to obtain a good polymerization between neighboring silanes and avoid non-covalently bonded molecules. The terminal functionality behavior towards further crosslinking binding was also monitored.

Chapter 5 describes the methods to create dual-functionalities on the nanometrically separated sides of SiO<sub>2</sub> micropillars. Selective silanization reactions followed by fluorescent labeling with two different dyes allowed fluorescent microscopy to be used. A detailed fluorescent imaging study is presented to prove the differential inner/outer functionalization without cross-contamination.

Chapter 6 explores the use of SiO<sub>2</sub> micropillars as drug carriers combined with polyelectrolyte multilayers. These hybrid organic/inorganic delivery systems are capable of responding to external stimuli such as pH. We investigated the effect of the medium pH in the drug loading and release. The influence of the number of polyelectrolyte layers in the pharmaceutical release rate is also assessed.

The use of three-dimensional SiO<sub>2</sub> platforms (macro-pSi and ordered and random micropillars) for interfacing with living cells is detailed in Chapter 7. An adherent cell line of human aortic endothelial cells (HAEC) was used to prove the biocompatibility of the substrates. Cell adhesion and growth studies performed onto 3D microstructures are presented. Measurable results on the cell spreading and cell morphology induced by the substrates are also described.

Chapter 8 presents the application of multifunctional SiO<sub>2</sub> micropillars as targeted drug delivery systems. The ability to perform a dual-functionalization of the micropillars is exploited to externally conjugate a

specific antibody able to recognize cancer cell receptors, and to load the internal volume with an anticancer drug. Results to demonstrate the differential functionalization are presented. The targeting ability of the antibody functionalized micropillars is assessed with cancer cells. Studies to evidence selective and efficient cell killing conclude the chapter.

Finally, Chapter 9 concludes the thesis by summarizing the overall achievements of this research.

## ***Chapter 2***

---

### **Fundamentals**

Porous silicon has received increasing interest within the scientific community in the last few decades. With its unique properties, porous silicon has emerged as a very powerful material in a number of potential applications. The demonstration of its biocompatibility in the mid 1990s opened a world of possibilities in biomedicine. Its unique features, including versatile and controllable pore sizes, flexible surface chemistry and compatibility with microfabrication technologies, has led to promising advances in biotechnological and biomedical applications. There has been a particular emphasis on the applicability of porous silicon-based microstructures in drug delivery and tissue engineering.

This chapter presents a literature review and the fundamentals of (macro) porous silicon for biomedical applications, with the aim to provide an insightful background for the following chapters. The first part reviews the basics of the electrochemical etching of silicon, with a particular focus in macroporous silicon and its formation mechanisms. Several micro and nanostructured forms of porous silicon for application in biomedicine are presented. The last part of the chapter focuses on the surface modification of porous silicon by thermal oxidation and functionalization methods towards the bioconjugation of ligands.

## ***2.1 Basics of the Porous Silicon Formation Process***

### ***2.1.1 An overview***

Uhlir and Turner of Bell Laboratories accidentally discovered porous silicon (pSi) in 1956 [1] while developing a technique for polishing silicon (Si) wafers using hydrofluoric acid (HF). Under certain electrochemical conditions, it was found that a black, red or brown film was formed on the silicon surface. Therefore, the silicon did not dissolve homogenously and fine pores appeared instead, propagating primarily in the  $\langle 100 \rangle$  direction.

In the 1950s those findings were not taken further, but in the 1970s and 1980s porous silicon attracted a significant scientific interest due to its high surface area, which was thought to be useful as a model of the crystalline silicon surface in infrared spectroscopy [2, 3], as a precursor to produce thick silicon oxide layers [4] and as an electrical insulator in capacitance-based chemical sensors [5].

However, it was not until the early 1990s when the porous silicon research was seriously launched. First, Lehmann and Gösele reported a quantum confinement effect in the absorption of porous silicon [6], and almost simultaneously Leigh Canham observed bright red-orange photoluminescence properties from the material [7]. The results demonstrated efficient, tunable, room-temperature light emission at energies well above the silicon bandgap.

The photoluminescence of porous silicon stimulated the theoretical and experimental research on creating silicon-based optoelectronic devices. However, the poor chemical and mechanical stability of the material and the low electroluminescence efficiency led to a weakening interest in the

mid 1990s. At the same time, the discovery of the material unique characteristics —large surface area, flexible surface chemistry and compatibility with standard silicon microfabrication technologies— motivated the application of porous silicon beyond optoelectronics in a variety of fields such as sensing, optics, biomedicine and electronics [8-11].

The vast majority of published research on porous silicon is based upon the porosification of silicon by electrochemical etching. This process is generally referred to as “anodization” and it occurs when crystalline silicon is anodically biased in a HF-based electrolyte solution under certain anodization conditions. The final pore morphology, thickness, density and specific surface area vary in a wide range depending on the anodization conditions (electrolyte composition, current density and time of current applied), and the properties of the silicon (doping, resistivity and orientation). Therefore by varying these parameters it is possible to precisely tune the structural features of porous silicon, which makes this material advantageous in many applications.

### ***2.1.2 The Electrochemical Etching of Silicon***

In an electrochemical reaction, two electrodes are needed. One supplies electrons to the solution (the cathode) and the other removes electrons from the solution (the anode). In the case of porous silicon formation, the silicon wafer acts as the anode, and the chemical being oxidized is the silicon itself. A platinum wire, conducting and HF-resistant, constitutes the cathode. The reaction occurring here in the cathode is basically the reduction of protons to hydrogen gas. When the current flows between anode and cathode, a pore growth on the top of a wafer takes place. A schematic of a two-electrode cell for etching silicon, with the relevant half-reactions, is shown in Figure 2.1.

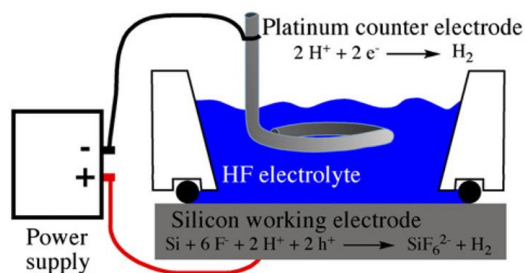


**Figure 2.1.** Scheme of the single-tank anodization cell used for the fabrication of porous silicon layers. Adapted from reference [12].

The current-voltage (I-V) characteristic of the semiconductor-electrolyte contact is determined by both the semiconducting nature of the electrode and the ionic species present in the electrolyte. The current density at the electrode for a certain potential is limited by the reaction kinetic at the interface, or by the charge supply from the electrode or the electrolyte [13].

Some of the understanding of pSi formation can be extracted from its I-V curve, shown in Figure 2.2. The curve displays characteristics common to the electrochemical semiconductor/electrolyte system: the current increases exponentially with increasing the applied potential that reaches a, decreases somewhat, and then increases slowly at increasingly positive potentials. For simplicity, the I-V curves can be divided into three distinct regions: the porous silicon formation region, a transition region and the electropolishing regime.

The dissolution and porosification of silicon occurs under low anodic overpotentials passing through the silicon electrode. There is an initial exponential rise in current with applied potential that breaks off at larger overpotentials, exhibiting a peak. Porous silicon is not formed at potentials more positive than the potential corresponding to the maximum slope of



the  $I$ - $V$  curve. The current at this point is called electropolishing current ( $J_{PS}$ ). Porous silicon forms in the exponential region at current densities below  $J_{PS}$ . This characteristic current point is assumed to divide the experimental conditions into two domains: porous silicon formation and electropolishing. The hydrogen evolution simultaneously occurs in the exponential region and its rate decreases with potential, and ceases above the current peak. If the current exceeds the electropolishing threshold current, the anodization results in a progressive, complete removal of silicon.

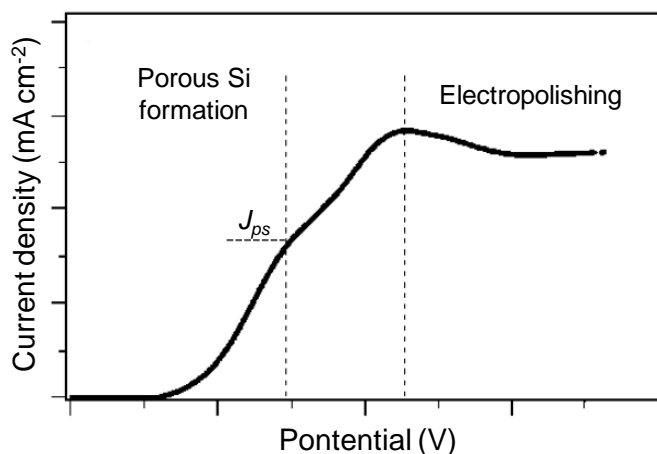


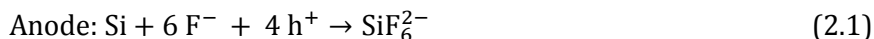
**Figure 2.2.** General current-voltage ( $I$ - $V$ ) characteristics for electrochemical etching of silicon, showing the regimes for porous silicon formation and electropolishing. Adapted from reference [14].

The quantitative values of the  $I$ - $V$  curves, as well as the values corresponding to the electropolishing peak, depend on the etching parameters and wafer doping. More details about the characteristics of the curves  $I$ - $V$  are extensively explained in references [13, 15].

### **2.1.3 Electrochemical Reactions in the Dissolution of Silicon**

In the previous section we have already mentioned that there are two regions in the current-voltage characteristic where anodic dissolution of silicon occurs.

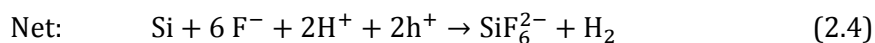
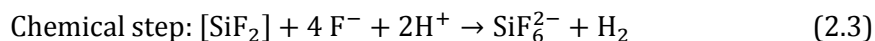
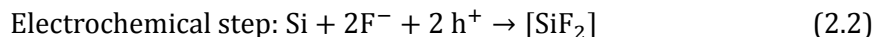
The simplest reaction occurring in the anodic dissolution of silicon in fluoride-containing solutions is the 4-electron oxidation (Equation 2.1). The electronic holes ( $h^+$ ) in the silicon valence band are used as oxidizing equivalents. The electrons provided by Si at the anode must be balanced by a reduction half-reaction that consumes electrons at the cathode. The electrochemical process carried out by these electrons is usually the reduction of water to hydrogen gas. The reaction product silicon hexafluoride ion ( $\text{SiF}_6^{2-}$ ) is a stable dianion that is highly soluble in water and stays in the solution.



This reaction, however, is predominant when the dissolution of silicon is occurring under electropolishing conditions and no porous silicon is being formed. It takes place at the more positive overpotentials depicted in Figure 2.2.

The direct dissolution of silicon atoms and reaction valence of two is the 2-electron process, which predominates at low applied potentials. Water is spontaneously reduced by silicon although the kinetics of the reaction is slow for Si in its elemental form (oxidation state 0). However, when silicon presents its +2 oxidation state, the reaction with water occurs rapidly producing the liberation of hydrogen and silicon in oxidation state +4. The 2-electron oxidation process is represented in two steps in Equations 2.2 and 2.3. At low overpotentials, the two-electron process

presented is the predominant and therefore the porous silicon formation is mainly governed by the half-reaction presented in Equation 2.4.



It should be noted that the exact chemistry of the silicon anodic dissolution is not yet completely understood. From all available data, it appears that the reaction in the 2-electron process is the main chemistry behind the formation of porous silicon. However, while this simplified chemistry can explain the dissolution of silicon atoms, it does not account for the spatial selectivity of the reaction, which results in porous formation. In effect, the resulting pore morphology does depend on the type of silicon electrode, its doping level, process conditions, etc. In the next section we shall describe some of the several models that have been proposed to explain this rich and complex morphology of porous silicon.

### ***2.1.4 Mechanisms of the Electrochemical Dissolution and Pore Formation***

A number of mechanisms have been proposed to explain the electrochemical etching of silicon in fluoride solutions. Although many details of the porous silicon formation still remain unclear, a few statements can be made. In the pore formation, Si dissolution competes with oxidation and subsequent dissolution of the oxide. Therefore, the electrolyte has to be able to dissolve silicon dioxide ( $\text{SiO}_2$ ), and in the case of silicon hydrofluoric based solutions are mandatory. Another

prerequisite for the pore formation is the existence of electronic holes since the reaction is initiated by hole capture at the surface [16]. In addition, as previously mentioned, the current must be kept between zero and the electropolishing current  $J_{ps}$ .

According to different models, initiation of the pore growth could begin at micro-cavities, structural defects, mechanically strained areas, or local perturbations [17, 18]. The dissolution takes place preferentially at the pore bottoms, where the curvature of the surface is largest, the intensity of the electric field is higher and enough holes are available. Thus, the etching of porous silicon proceeds in depth with an overall directionality which follows the anodic current paths inside silicon. The pore walls become passivated and the dissolution mainly occurs at the porous silicon/crystalline silicon interface. In addition, when adjacent pores meet each other the current flow is suddenly pinched off and further etching is blocked, avoiding pore collapse or redistribution. The practical consequence of all this is that, in stationary conditions, the porosity remains approximately constant, whereas the overall thickness of porous silicon layer grows essentially linearly in time.

The etching process leads to a self-adjusting pore growth, and a wide range of pore geometries and morphologies are accessible by modifying the electrochemical parameters and the characteristics of the silicon wafers. According to the IUPAC nomenclature for porous materials, structures with a pore width below two nanometers are called microporous [19]. The mesoporous structures range from 2 to 50 nm. Bigger pores are referred as macropores. These different features are the result of different pore formation mechanisms. Table 2.1 summarizes the types of silicon, the morphologies and the apparent operative mechanisms for the main types

of pSi formation conditions. Note that in the literature the term ‘nanoporous’ is frequently used for the microporous size regime, and ‘macroporous’ typically refers to pore diameters close to, or in, the micrometer size scale.

**Table 2.1.** Main pore sizes, morphologies and proposed formation mechanisms.

Pore type	Silicon type	Size range	Morphology	Mechanism
<b>Micropores</b>	p	2-4 nm	Sponge-like	Crystallographic face selectivity, enhanced electric field, tunneling, quantum confinement
<b>Mesopores</b>	p <sup>+</sup> , p <sup>++</sup> , n <sup>+</sup>	2-50 nm	Branchy	Enhanced electric field, tunneling
<b>Macropores</b>	n <sup>+</sup> , p <sup>+</sup> , n, p	50 nm-100 μm	Tubular	Space-charge limited, minority carrier collection, thermionic effect

Many mechanisms are thought to contribute to the electrochemical pore growth process and the final morphology. These formation mechanisms can be divided into chemical and physical phenomena.

Amongst the chemical factors governing the electrochemical dissolution of silicon, the band holes that act as oxidizing equivalents play a crucial role. These band holes are driven to the surface by the applied electric field, which tends to concentrate in sharp tips. Sharp pore tips generate electric fields that enhance the migration of holes to these areas. When a valence band hole reaches a Si atom on the surface, the atom is susceptible to nuclephilic attack by fluoride ions, and water [14].

At the silicon surface interface the species involved in the electrochemical etching (Si-O, Si-F and Si-H) compete to form new bonds. When a silicon wafer is immersed in an HF-based solution, the oxide

dissolves and the surface becomes terminated with hydrogen [20]. The dissolution of a surface Si atom involves first the replacement of a surface hydrogen atom with a fluoride ion  $F^-$  (Figure 2.3). The replacement of hydrogen with  $F^-$  requires a hole which results in a neutralized Si-F bonding. If the Si-F bond is established due to the polarizing effect of the bonded F, another ion  $F^-$  can attack and bond under generation of an  $H_2$  molecule and injection of one electron into the electrode. The silicon backbonds between the silicon atoms are weakened due to the large electronegativity of fluorine, so that the backbonds can be broken by reacting with HF in a 2-electron oxidation process (Figure 2.4A). The silicon atom is removed from the surface. The reaction product  $SiF_4$  is unstable; it reacts with 2HF and becomes  $H_2SiF_6$  (Equation 2.4), which dissociates into  $SiF_6^{2-}$  in the solution. The remaining surface silicon atoms are again hydrogenated.

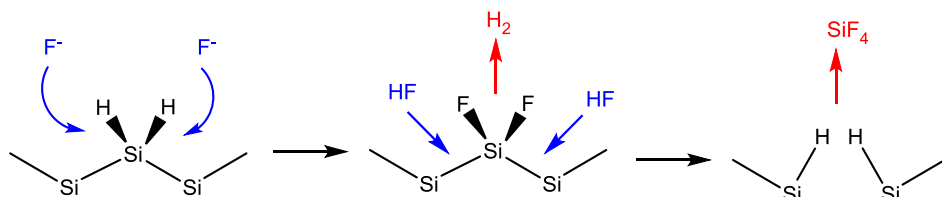


**Figure 2.3.** Simplified mechanism for electrochemical etching of silicon in fluoride containing solutions. Adapted from reference [6].

The backbonds of Si-Si-F can also be broken by reacting with  $H_2O$ , resulting in Si-O-Si bonds which are not stable in HF and the dissolution of which results in an indirect dissolution path (Figure 2.4B) through the formation of anodic oxide [21]. Si-O bonds are dissolved by  $F^-$ , and significant amounts of Si-O are only formed when the diffusion of  $F^-$  to the silicon surface is much slower than the delivery rate of valence band holes. This is the case, for instance, of the electropolishing conditions, which occurs either when a large current density is applied or when the

concentration of HF is low. Under low concentrations of HF, the Si-O bonds are formed too rapidly to be dissolved by fluoride ion and H<sub>2</sub>O molecules become the nucleophile. The insulating oxide impedes propagation of the pore since Si-O bonds cannot be dissolved due to the lack of F<sup>-</sup>. The valence band holes have to move into the porous silicon matrix to oxidize a Si atom that is accessible to the fluoride ions in the electrolyte. As a result, the silicon filaments become thinner at the pSi/bulk Si interface, undercutting the porous silicon layer.

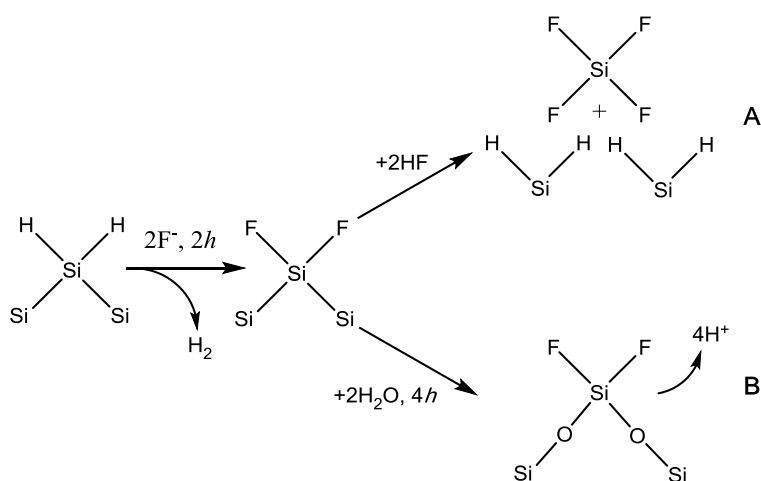


**Figure 2.4.** Proposed dissolution mechanism of crystalline silicon in hydrofluoric acid solutions. The two different reaction paths illustrate the possible 2-electron (A) and 4-electron (B) chemical dissolution paths associated with two experimental regimes: porous silicon formation and electropolishing, respectively. Adapted from reference [21].

The morphology of porous silicon is also influenced by physical factors such as the electronic properties of the semiconductor: band structure, type and concentration of the dopants, and quantum confinement effect. However, the most determining factor in the porous silicon formation is the availability of valence band holes. The doping amount plays a key role, but also the illumination (for n-type Si etch), HF concentration and applied

current density. Pores growing in the crystal direction are mainly formed under low current densities, whereas current-line-oriented pores tend to grow perpendicular to the surface plane of the wafer.

In highly doped p-type Si, the large number of valence band holes available never limits the etch. In contrast, in n-type silicon the shortage of  $h^+$  limits the density of pores. The pore and wall size in n-type silicon is determined by space-charge region (SCR), an area near the Si/electrolyte interface where the valence band holes are highly depleted. For low doped p-type silicon, the availability of holes is restricted and the SCR also plays a key role. The mechanisms of pore formation in this type of substrate are discussed in the following section in further detail, as it is a major concern throughout this thesis.

### **2.1.5 The Physics of Macropore Formation on Low Doped p-Type Silicon**

Although the formation of macroporous silicon (macro-pSi) in n-type Si under front illumination was first reported in the 1970s, it was not until 1994 that Propst and Kohl discovered the formation of macropores on low doped p-type silicon in organic HF solutions [22]. Later on, same phenomenon was also observed when aqueous HF solutions were used. Macropore formation on p-type silicon came as a surprise at first because, in contrast to n-type silicon, p-type electrodes are under forward conditions. Wehrspohn *et al.* postulated that a necessary condition for the formation of macro-pSi on low doped p-type Si is a higher resistivity of the substrate than that of the electrolyte [23]. This idea was later invalidated as macro-pSi was also found to form in electrolytes with much higher resistance than that of silicon substrate [24]. In this work, Lehmann and



Rönnebeck proposed that the macropore formation in low doped p-type silicon was governed by the thermionic emission effect, which is sensitive to the Schottky barrier height rather than the barrier width [24]. This leads to a local increase of the diffusion current, which dominates charge transfer at low doping densities. Alternatively, Lust and Clement reported a study of the conditions for macropore formation on p-type Si in different aqueous and non-aqueous solutions, and pointed out the role of the interface chemistry in the formation process of macropores [25].

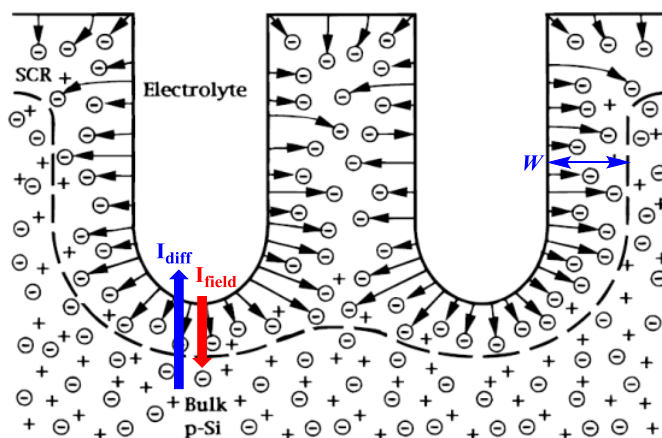


**Figure 2.5.** Schematic of the equilibrium charge distribution and the electric field around pores in the electrochemical etching of low doped p-type silicon. Adapted from reference [24].

The basic charge distribution around pores in a p-type electrode is shown in Figure 2.5. A p-type electrode is under forward conditions during macropore formation and behaves basically like a solid-state Schottky diode. The forward current of a Schottky diode is dominated by diffusion, or thermionic emission, or tunneling of holes. At zero bias, and under forward conditions, the space-charge region is not fully depleted of holes and therefore a diffusion current  $I_{diff}$  is caused by the concentration gradient of holes, according to Schottky's theory. With no applied bias,  $I_{diff}$

is compensated by the field current  $I_{\text{field}}$  and  $I_{\text{diff}}=I_{\text{field}}$  is fulfilled at the pore walls as well as the pore tip. However, the absolute values of  $I_{\text{diff}}$  and  $I_{\text{field}}$  are larger at the pore tip, because the concentration gradient of valence band holes and the electric field strength increase with decreasing the SCR width. If a forward bias  $V$  is applied,  $I_{\text{field}}$  decreases while  $I_{\text{diff}}$  increases. The higher current density values at the pore tip now become decisive. The total current density at the tip  $I_{\text{tip}} = (I_{\text{diff}} - I_{\text{field}})_{\text{tip}}$  is always higher than the current density at the wall. Therefore a depression in the electrode etches faster than a planar area, and a pore tip develops. If the distance between two neighboring pores becomes less than twice the SCR width, their SCRs overlap and the pore wall becomes passivated due to the depletion of holes [26].

The resulting morphology of macroporous films formed on p-type Si substrates can be explained as a consequence of the severe constraint for pore wall passivation in low doped p-type Si wafers: pore walls are depleted if their thickness is less than twice the SCR width  $W$ .  $W$  depends on doping density and applied bias. The relationship between the average pore wall thickness and the p-type doping density follows square root dependence, and it will be exemplified in Chapter 3.

## **2.2 SiO<sub>2</sub> Based Materials for the Life Sciences**

### **2.2.1 Biocompatibility of SiO<sub>2</sub> Microstructures**

The term “biocompatibility” was defined at a consensus conference of the European Society for Biomaterials in 1986 as “*the ability of a material to perform with an appropriate host response in a specific situation*” [27]. In terms of biocompatibility, silicon dioxide is accepted as “Generally

Recognized as Safe” (GRAS) by the United States Food and Drug Administration (FDA) [28]. Actually, materials based on silicon and particularly its oxide form, SiO<sub>2</sub>, have been used for decades in macroscale medical applications due to its unique physic-chemical properties [29]. For instance, SiO<sub>2</sub> based materials have been employed in dietary supplements [30], catheters and implants [31], dental fillers [32] and contact lenses [31]. This has motivated somewhat the development of nano- and micro-sized structured scaffolds and particles for other applications including imaging, delivery of therapeutics and tissue engineering. However, it is also known that materials with features on a sub-micron and micron scale possess characteristics that can impose their biological behaviors. Thus, it has been necessary to understand the short and long-term effects and potential hazards from nano- and micromaterials as they are exposed to the human body and the environment.

The biocompatibility of SiO<sub>2</sub> for biomedical applications is definitely a consequence of the ability to eliminate the products of the material dissolution, although it certainly depends on dosage and body site. Silicon oxide can readily dissolve in water promoting the release of silicon-containing species into solution. The hydrolysis of SiO<sub>2</sub> yields several soluble forms of silicon acid compounds, with orthosilicate (SiO<sub>4</sub><sup>4-</sup>) ion as the basic building block. The most common form of this ion is the fully protonated specie, the orthosilicic acid, Si(OH)<sub>4</sub> (see Equation 2.5). Actually, several studies performed with porous silicon and silica microparticles have shown release of orthosilicic acid [12, 33-35]



Orthosilicic acid is a nontoxic small molecule and the natural form of silicon in the bloodstream and tissues. Indeed, it is considered to be a nutrient for optimum bone health [36, 37]. Several studies have shown that silicon acid does not accumulate in the human body. Instead, it is readily absorbed by the gastrointestinal tract of humans and excreted in the urine at a rate of 1.8 mg silicon per day [35, 38]. However these oxides can be toxic in high doses, generally due to precipitation of the silicate ion in the kidneys, which leads to renal failure.

Therefore, since the body can handle and eliminate silicic acid, the important issue with SiO<sub>2</sub>-based drug delivery systems is the rate at which they degrade and resorb. This is dependent on the surface area and surface chemistry. Porosification dramatically increases the surface area. Thus, microporous and mesoporous silicon tends to dissolution and exhibit bioactivity when in contact with body fluids, whereas macroporous silicon offers higher stability and appears as bioinert material [39]. The pH also plays a key role, as the hydrolysis reaction is known to be catalyzed by OH<sup>-</sup>, being at pH 9 three times faster than at pH 2 [35]. Finally, the dosage will be crucial to eventually determine the amount of silicon oxide that the body can cope with.

The possibility of micromachining silicon into platforms of arbitrary shape with outstanding precision has motivated the use of silicon and silicon oxide based microdevices in biotechnology and biomedicine [40, 41]. Biocompatibility of silicon and silicon dioxide in micromachined devices was not addressed until only a few years ago. A pioneering work performed by Kotzar and co-workers demonstrated that neither silicon nor silicon oxide were cytotoxic *in vitro* using mouse fibroblasts [42]. These

materials were also classified as nonirritants based on 12-week rabbit muscle implantations.

The use of micromachined silicon as controlled drug-release microchip was first introduced by Langer and co-workers in 1999 when they designed a silicon-based microchip containing etched cavities. The different cavities were capped with different responsive polymers and a “sacrificial” gold membrane, thus creating a device capable of pulsatile release of its chemical loads by opening various reservoirs on command [43]. Also in 1999 Ferrari and co-workers introduced micromachined Si membranes for encapsulating pancreatic islet cells [44]. These biocapsules allow nutrients and small molecules to pass freely through the membranes while isolating transplanted cells from rejection by the patient’s immune system.

The biocompatibility of Si as a material to engineer microreservoirs for drug delivery has also been assessed *in vitro* [45]. After 21 days of subcutaneous implant in rats, adherent macrophages and foreign body giant cells were measured to determine that both Si and SiO<sub>2</sub> were biocompatible under the given conditions.

Si- and SiO<sub>2</sub>-based technology has also impacted in the development of microneedles. This use has been also tested for suitability as neural implants [46]. Si microneedles were implanted in rabbit brains for 6 months and the neuron density around the needle analyzed. It was found that the geometry is important since the recording sites must be placed along the sides of the needle and not near the tip.

Porous silicon when implanted in rat abdominal walls for up to 3 months was found to be more biocompatible than planar silicon [47]. The

porosity and pore size of silicon has been observed to affect the bioactivity of silicon [48]. Low-porosity microporous films induced hydroxyapatite growth *in vitro*, high-porosity mesoporous films exhibited substantial dissolution *in vitro*, while planar silicon was inert in the same medium [48, 49].

Apart from the use of micromachined Si and SiO<sub>2</sub> as a platform for interaction with living tissues, the low toxicity and solubility of the degradation by-products of SiO<sub>2</sub> have generated much interest for its use as nano- and micro-sized particles in an array of other biomedical applications. Owing to the nature of their composition, SiO<sub>2</sub>-based systems are more stable under various biological environments compared to many other biomaterials such as polymers. In this framework, intensive investigation has been carried out to apply this type of particles in pharmaceuticals, particularly in the delivery of drugs.

However, despite many *in vivo* and *in vitro* studies, including some animal and tissue models, the understanding of the effect of these systems still remain far from complete. It is generally accepted that particle surface area, dosage, shape and chemistry play a significant role in the cell and tissue behaviors. In addition, the size affects the cell fate and it is known that smaller SiO<sub>2</sub> particles (<100 nm) induce more harmful effects on cells than larger particles [29]. As an example, Li *et al.* found that the cytotoxicity of SiO<sub>2</sub> particles in the nanoscale were higher than that on the microscale. Nanoparticles (190–420 nm in diameter) exhibited significant cytotoxicity at concentrations above 25 µg mL<sup>-1</sup>, whereas microparticles (1220 nm in diameter) showed slight cytotoxicity over a broad concentration range of 10–480 µg mL<sup>-1</sup> [50]. They correlated this fact with the ease to endocytose nanoparticles compared to microparticles.

Porous silicon microparticles have also been used by Santos and co-workers to assess the effect of the particle concentration, surface chemistry and size in the *in vitro* cytotoxicity [51]. Smaller particles were found to be more toxic to cells, whereas thermal oxidation induced a less harmful effect than other types of surface modifications.

Some *in vivo* studies have been also conducted. Using SiO<sub>2</sub> spheres ranging 0.7-5 μm size, Godin *et al.* demonstrated that as the diameter decreased, there was less deposition of particles in the non-reticuloendothelial system organs [52]. Another relevant *in vivo* study determined that nanoporous silicon particles of 1.6 μm size introduced by intravenous administration in mice do not produce obvious changes in blood chemistry and cytokines profile [53].

Apart from the general conclusions overdrawn for Si and SiO<sub>2</sub> based scaffolds and particles, different types of cells and tissues respond differently towards the microstructured substrates or the presence of particles. Therefore, the overall interaction and eventual fate of these engineered micromaterials with biological systems are very difficult to categorize.

### **2.2.2 Useful Forms of Microstructured Silicon in Biomedicine**

One of the challenges relating to Si and SiO<sub>2</sub> based microstructures for applications in personalized medicine, is obtaining optimal structural shapes and sizes capable to adapt to each necessity. The desired but exigent forms of the biomaterials applied in biomedical devices include spherical microparticles, flexible substrates or three-dimensional (3D) architectures.

In recent years numerous studies have been conducted to demonstrate the feasibility of a number of physical architectures of pSi-based materials. As an example, pSi microparticles have been engineered by stain etching in pSiMedica labs and tested in brachytherapy [54]. Henstock and co-workers have also developed a polycaprolactone-pSi composite for orthopaedic purposes [37].

In addition, adapting microfabrication techniques originally developed in the microelectronics industry has enabled the development of novel Si and SiO<sub>2</sub>-based structures for drug delivery, tissue engineering and biosensing. The most common microfabrication method is the lithography process behind integrated circuits (IC) and microelectromechanical systems (MEMS). Lithography and other microfabrication techniques have been used in recent years to produce micromachined structures with nano- to micrometrical features in applications where 3D architectures or precise shapes were required [55].

Many biomedical applications increasingly require the benefit from the continuously improving micro- and nanofabrication protocols that are able to produce devices with a high degree of precision and accuracy in the semiconductor industry. The ability of producing monodispersed features in the nanoscale is crucial for eliminating architectural randomness as a source of experimental variation, for incorporating ever advancing capability at lower functional cost, for creating personalized treatments and, ultimately, for achieving clinical translation [55].

Cylindrical structures such as pores, walls, tubes or combination of these can be fabricated from silicon employing electrochemical etching. Combined with lithography techniques, regular, precisely shaped and



monodispersed structures can be produced. These 3D structures grow on planar silicon propagating into the substrate, and are characterized by their remarkable vertical walls, constant porosity and pore depths (up to 500  $\mu\text{m}$ ). Typically, these architectures have found applications in microfluidics [56], photovoltaics [57] and electrochemical sensing [58].

Post-anodization treatments have widely been used to modify the as-produced characteristics of these arrays by coating the walls with a film of a metal in insulator [59], changing the properties of the inner surface of pores [60], obtaining membranes [61] or infiltrating pores with various fillers [62]. Compared with micro- and meso-pSi, macro-pSi is the closest in its properties to the starting single-crystal material and, therefore, it can be subjected to standard technological procedures in microelectronics: thermal oxidation, high-temperature annealing, thin-film deposition or photolithography. These treatments have enabled the development of novel 3D architectures and also endowed macro-pSi with remarkable properties that can be exploited in biotechnology and biomedicine.

Macro-pSi substrates are attractive substrates for a variety of bioapplications. As an example, Michaelis and co-workers performed a post-anodization sputtering to form a thin gold layer that enabled the use of macro-pSi chips as a platform to determine the permeability and transport characteristics of 2D tissues using impedance analysis [63]. Cells were cultured on the macroporous surface and the pore volume was used as femtolitre-size cuvette in which the permeating probe accumulated at the site of permeation. In another study, Yoo *et al.* used 3D macro-pSi substrates as a fluorescence quencher platform to detect adenosine [64]. The superior protein adsorption capacity together with the effective fluorescence quenching enabled the protein to be detected at lower levels.

The feasibility of growing a conformal oxide layer around the macropores and dissolving the bulk Si by anisotropic etching has enabled the formation hollow structures such as microtubes or microneedles [65, 66]. Rodríguez and co-workers fabricated microneedles based on the fabrication of macro-pSi combined with oxidation and anisotropic etching [66]. The resulting microneedles of tunable dimensions were assessed for flow delivery systems. More recently, Strambini *et al.* have developed a microneedle chip for transdermal injection with integrated reservoirs. The performance of the needles was tested in skin-like polymers and with different liquids of biomedical interest [67]. A combination of different micromachining techniques and the electrochemical etching of silicon were used by Tsutsumi and co-workers to produce arrays of SiO<sub>2</sub> micropillars [68]. They proposed the device for DNA separation.

### **2.3 Chemical Modification of Microstructured Silicon**

The electrochemical etching of silicon yields a surface terminated with hydrogen. This surface of freshly prepared porous silicon is strongly unstable, as the Si-H groups are highly reactive and susceptible to attack by hydrolytic species in air or aqueous environments [14, 69]. This limits its capability for further application in biotechnology and medicine. Frequently, each application will require a different chemical functionality and a different level of stability. Fortunately, the hydride-terminated surface can be easily modified with a simple oxidation treatment and subsequently introduced a variety of functionalities [70-73]. The growth of a silicon oxide layer is the most common approach to stabilize and passivate the porous silicon surface due to its simplicity and good control over the oxide thickness [74]. Starting from an oxidized silicon surface,

there are a number of strategies to modify the surface chemistry, but undoubtedly silanization is the most popular one. The hydroxyl-terminated surface can be modified with alkyl silanes to form a covalently linked organosilane layer [75]. Thus, the reactive groups at the functional end provide attachment points for biomolecules.

### **2.3.1 Thermal Oxidation of Silicon**

Native silicon dioxide forms spontaneously on the bare surfaces of silicon when it is exposed to oxygen air or aqueous environments [76, 77]. The thickening of this layer by thermal treatment up to a few tens of nanometers provides a protective layer that effectively passivates the surface and prevents further oxidation. In addition, the possibility of exquisitely control the thickness of the  $\text{SiO}_2$  layer together with the simplicity of the method has been pivotal in the outstanding development of microelectronics industry in the last decades. Silicon oxidation is a key step in the formation of insulating or sacrificial layers involved in the fabrication of integrated circuits, microfluidic devices, optical MEMS systems and BioMEMS [78-80].

Thermal oxidation is the oldest and most commonly used thermal method to stabilize the silicon surface. A variety of oxidizing atmospheres can be used for this purpose, although the simplest oxidant is air. Air oxidation produces different types of surface species, depending on the temperature at which the reactions is performed and the humidity of the air [77]. Figure 2.6 shows the predominant oxidation reactions at different temperatures in air or oxygen. The oxidation rate is also highly dependent on the temperature. The lowest temperature process is called back-bond oxidation, which takes place at room temperature [76]. A silicon oxide layer is formed within a few hours and it continues growing for several

months. The back-bond oxidation means that the oxygen atoms selectively attack the Si-Si back-bonds of the most superficial Si atoms but do not replace hydrogen atoms on the surface (see Figure 2.6A). Higher temperatures at around 200 °C promote the formation of oxygen bridges between the surface Si atoms and the second atomic Si layer [81]. Oxidation at around this temperature also changes the surface properties from hydrophobic to hydrophilic, although the majority of the hydrogen atoms remain on the surface (see Equation 2.6B). Here, the presence of water vapor is a very important factor to determine the extension of the surface coverage of hydroxy group [82]. Temperatures above 800 °C yield the complete oxidation of silicon, where the hydrogen termination is replaced with hydroxyl groups and the thickness of the oxidized layer increases [74]. The growth rate is very dependent on the silicon structure and can vary from a few tens of minutes to several hours [14, 83].

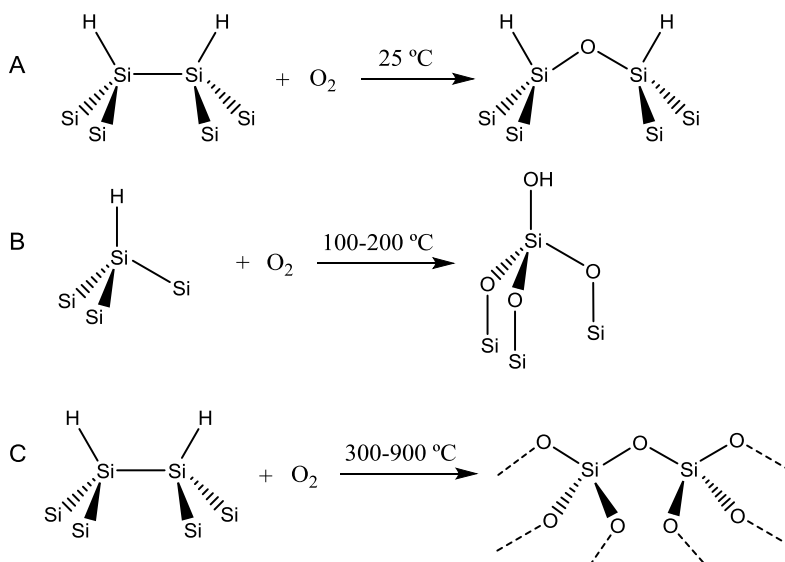


**Figure 2.6.** Silicon oxidation reactions at different temperatures. A) Room temperature; B) 100-200 °C and C) 300-900 °C. Adapted from reference [14].

In the specific case of macroporous silicon, thermal oxidation is one of the most common post-treatments applied to these tubular arrays. It is a frequent method used to manipulate macropore shape and generate a variety of structures in silicon such as SiO<sub>2</sub> micropillars, microtubes or microneedles [66, 67, 84]. SiO<sub>2</sub> on the surface of macropores has been widely used as a sacrificial layer for enlarging the pore diameter or smoothing the surface irregularities [26, 60, 85].

Temperatures ranging 800-1200 °C and oxygen or water vapor atmospheres are commonly used to thermally grow silicon dioxide layers [83]. This process goes along with an increase in volume that leads to large stresses at the interface Si/SiO<sub>2</sub>. It follows from the relationship between one gram-atom of Si and one gram-atom of SiO<sub>2</sub>, which occupy a volume of 12 and 27 cm<sup>3</sup>, respectively. Therefore, SiO<sub>2</sub> suffers a volume expansion of 2.27 times with respect to that of Si [83]. The arising compressive stresses in a silicon dioxide film and tensile stresses in silicon itself relax via viscous flow of the oxide at T > 960 °C. Thus, the main factor leading to the appearance of stresses in oxidized silicon after cooling to room temperature is the difference between the thermal expansion coefficients [86]. While these stresses are negligible in the flat silicon oxidation due to the expansion of the SiO<sub>2</sub> film in the perpendicular direction of the interface, they are known to affect the oxidation kinetics of non-planar structures [87, 88]. For instance, the oxide thickness has been observed to be thinner where the radius of the silicon surface is smaller [89]. These results are applicable to macropores [83].

### ***2.3.2 Functionalization Methods for Silicon Dioxide***

Many biomedical applications of SiO<sub>2</sub> based materials require a surface modification that is suitable to interface the biological systems in a

controlled way. For instance, in some cases the surface should prevent biofouling. Conversely, in other occasions, the surface should provide coupling points for the immobilization of biomolecules. For these reasons, silicon dioxide surfaces must be appropriately modified with organic layers that possess the requisite functionality. Reactive functional groups such as primary or secondary amino, carboxyl, hydroxyl, alkyl halogen or azide can be introduced onto the SiO<sub>2</sub> surface by different routes of chemical modification by coupling with functional moieties such as amines, carboxylic acids or aldehydes [75].

The covalent attachment of functional groups on oxidized silicon surfaces is undoubtedly dominated by the ubiquitous silanol chemistry. Silanization of SiO<sub>2</sub> surfaces allows formation of molecular layers with a very high surface coverage that improves the surface stability and reduce degradability [90, 91]. The popularity of this method relies on its straightforwardness, as it can be performed at moderate temperatures with inexpensive equipment. Furthermore, the simplicity to perform silanization reactions together with their high reproducibility are remarkable advantages over other methods of SiO<sub>2</sub> functionalization. However, the oxidized silicon is biodegradable due to the possible hydrolysis of Si-O-Si bonds, and this makes the silanized SiO<sub>2</sub> surface moderately unstable in aqueous solutions [14].

A silane compound is a monomeric silicon-based molecule containing four constituents. The general structure is depicted in Figure 2.7. The organic arm normally has a structure that terminates in a functional group or reactive component, which facilitates the covalent linkage to another organic molecule. The other part consists of the hydrolysable groups (typically alkoxy or chlorine groups) attached directly to the silicon atom.

Then, in a silanization reaction, the hydroxyl group of the SiO<sub>2</sub> surface is replaced by hydrolyzed silanols in the organofunctional silane, and a covalent Si-O-Si bond is formed through a condensation reaction [92].

The silanization procedure is the most commonly used method to add functional amine groups on the silicon oxide surface, to which different biofunctional compounds can be further attached [92-95]. Amino-functionalized SiO<sub>2</sub> surfaces can be conjugated with small organic molecules, proteins, peptides, nucleic acid, etc. A standard coupling reaction with the commonly used APTES is shown in Figure 2.8.

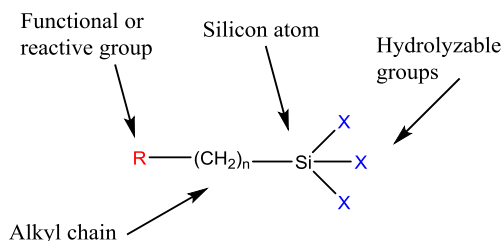


**Figure 2.7.** Schematic of the general structure of a silane molecule that includes a functional group and a carbon chain spacer and three hydrolysable groups. Adapted from reference [92].

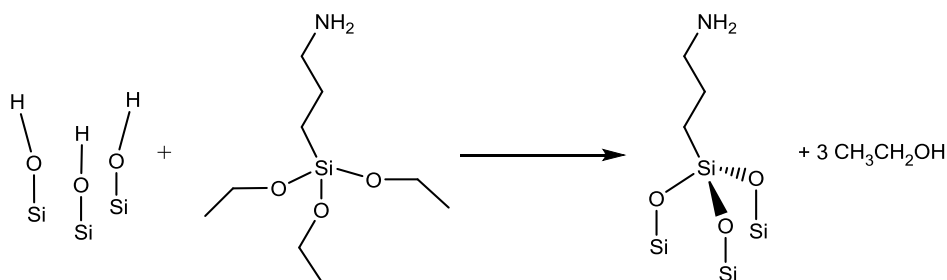


**Figure 2.8.** Scheme for the silanization reaction of silicon dioxide surfaces with the commonly used aminosilane APTES.

Besides covalent attachment, functional moieties can also be introduced onto SiO<sub>2</sub>-based surfaces through electrostatic interactions

[96]. The layer-by-layer functionalization approach can effectively cover  $\text{SiO}_2$  surfaces with controllable thickness by alternative layering of positive and negative charged polyelectrolytes on the surface. This usually makes use of the negative charges from the free  $\text{SiO}^-$  groups on the silicon oxide surface. For example, cationic polymers (such as polyethylenimine) can be electrostatically adsorbed onto the  $\text{SiO}_2$  surfaces to provide nucleic acid binding properties [97].

### ***2.3.3 Interfacing Silicon Dioxide with Biomolecules***

When choosing a linker for interfacing  $\text{SiO}_2$  surfaces with a specific bioligand, a number of considerations must be taken into account. The first consideration is the chemical functionality desired on the surface, which will influence the incorporation of molecules in further modification steps and also the type of biomolecules able to interact with the surface. Furthermore, bioligand conjugation can be performed via direct attachment to the surface or through a spacer that links the activated surface and the desired biomolecule. Therefore, we should consider the strategy to follow for the biomolecule attachment. However, the most important concern to be considered is the characteristics of the bioligand that should be attached. The possible conjugation sites and chemistries must be taken into account along with surface orientation and nonspecific binding factors, which may lead to unstable and reversible binding, and eventually to protein denaturation and bioactivity alteration.

One of the strategies to conjugate biomolecules onto  $\text{SiO}_2$  is their direct attachment via silane linkers. Silanes can range in a variety of terminal functionalities from simple amine terminated compounds to complex silanes designed for highly specific surface functionalizations [71]. The appropriate selection of the functional group for a particular application



can allow the attachment of proteins, oligonucleotides, whole cells, organelles or even tissue sections to substrates in a selective manner, which is critical to assure a proper orientation and bioactivity of the bioligand [98-102]. The organosilanes used for these applications include functional groups such as amino, epoxy, thiol, aldehyde or isocyanate groups [92].

Among silanes, the most popular coupling agents are  $\text{NH}_2$ -terminated molecules, such as APTES or aminopropyltrimethoxy silane (APTMS) [94]. The aminosilane-modified surface can be further modified to incorporate specific crosslinkers, or be readily used for direct coupling with biomolecules. For instance, Ducker *et al.* have used amino-functionalized silica surfaces for peptide synthesis [98].

Other very useful silane modification agents are glycidoxo compounds containing reactive epoxy groups. Surfaces covalently coated with these silane coupling agents can be used to conjugate thiol-, amine- or hydroxyl-containing ligands. The most frequently used glydicoxysilane is 3-glycidoxyplopyltriethoxysilane (GOPS), which can be used to link inorganic  $\text{SiO}_2$  surfaces with biological molecules containing any three of these major functional groups. One practical example using this type of silane has been demonstrated by Voelcker *et al.* where epoxy functionalized glass was used for immobilization of extracellular matrix proteins to create cells microarrays [101].

Isocyanate groups are extremely reactive toward nucleophiles and can attach biomolecules forming linkages with amines and hydroxyls. Isocyanate will hydrolyze rapidly in aqueous solution, thus they are particularly useful for covalent coupling to hydroxyl groups under non-

aqueous conditions. Isocyanatopropyltriethoxysilane (ICPTES) contains an isocyanate group at the end of a short propyl spacer that is very useful to conjugate biomolecules to inorganic substrates under anhydrous conditions [91]. For instance, this type of functionalization has been employed by Fu *et al.* to develop a glucose biosensor by immobilizing an enzyme on ICPTES.

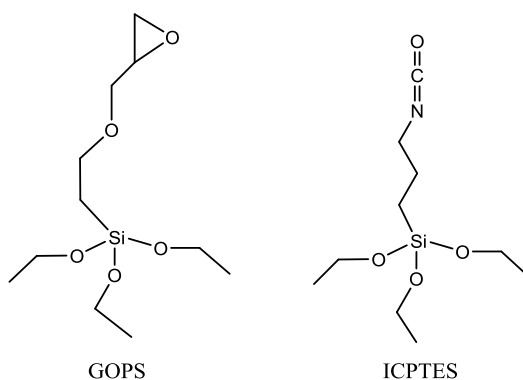


**Figure 2.9.** Molecular structure of two alkoxysilanes used as linkers for biomolecule attachment to  $\text{SiO}_2$  surfaces.

Alternatively, surfaces derivatized with organosilanes can be further modified to incorporate specific crosslinkers or spacers compounds. Actually, a two-step process is frequently preferred [103]. While the first step stabilizes the surface and introduces the desired chemical functionality, the second step allows selective and controlled attachment of biomolecules through a crosslinker. Crosslinkers or spacers are molecules with terminal reactive functional groups that are able to form covalent bonds between two compounds. In bioligand conjugation, they act as a linker between the functionalized surface and the biomolecule. These crosslinkers typically contain functional groups reactive towards amines, thiols or carboxylic acids through a covalent bond [91].

The use of heterobifunctional spacers to link thiol terminated surfaces with biomolecules is a common route for bioligand conjugation. For instance, Tinsley-Brown *et al.* demonstrated that 3-mercaptopropyl trimethoxysilane (MPTMS) can be used for conjugation with the heterobifunctional crosslinker succinimidyl 1-4-(N-maleimidomethyl) cyclohexane-1-carboxylate (SMCC) to immobilize rabbit IgG antibody [104]. This linker can therefore react with thiol functional groups, allowing it to be attached to a thiol-functionalized surface and facilitating the conjugation of an amine-containing biomolecule such as an antibody.

Amino functionalized surfaces can also be further modified with spacer arms or crosslinkers to create reactive groups for coupling affinity with ligands or biomolecules. The aminosilated surface can be used for coupling with carboxyl-containing bioligands using a carbodiimide (EDC) reaction [102, 105]. EDC activates the carboxylic acid groups and facilitates their reaction with amino groups present in the biological molecules. It is generically used along with succinimide (NHS) compounds in order to enhance the reaction rate and to achieve a better binding. Norris *et al.* have used this chemical modification to develop a silica-based photonic crystal biosensor capable of detecting DNA oligonucleotides, proteins and antibodies [98].

Aminosilanized surfaces also may be activated by use of a homobifunctional crosslinker to contain reactive groups for subsequent coupling to biomolecules. Amongst the numerous *bis*-aldehyde reagents that have been used for the conjugation of biomolecules, the five-carbon glutaraldehyde (GTA) is by far the most popular. By using GTA, proteins, enzymes or amino-modified DNA molecules can be irreversibly

immobilized on the activated surfaces via the covalent bond between the amino group on the

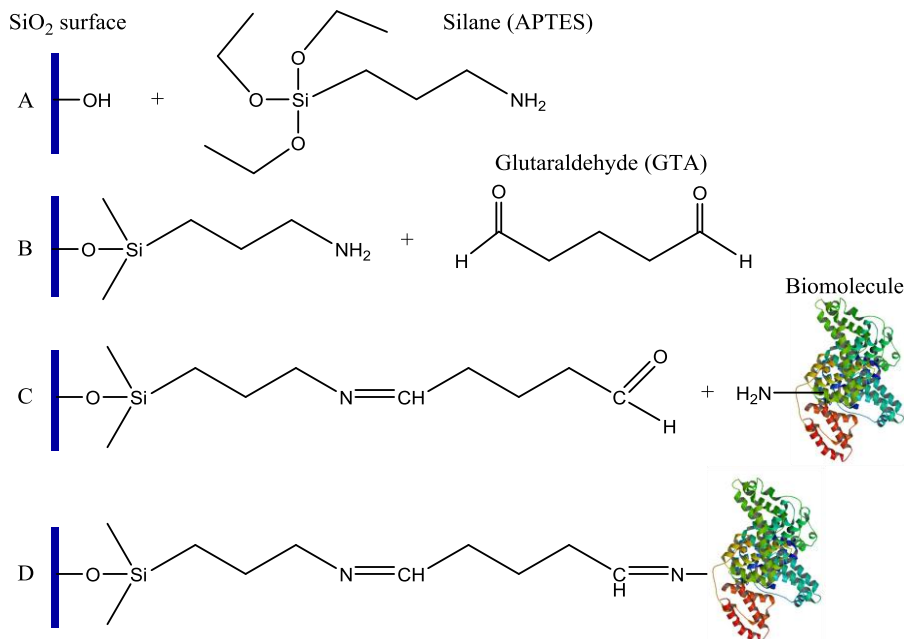


**Figure 2.10.** Schematic showing the covalent immobilization of biomolecules via glutaraldehyde spacer onto amino-silanized surfaces. A) Surface silanization; B) activation with GTA; C) binding of biomolecules via amino-terminal groups on biomolecule surface and D) imine bond formation between the aldehyde-terminated surface the biomolecule.

biomolecule and the aldehyde [105-107]. The basic reaction for biomolecule immobilization following this route is schematically shown in Figure 2.10. Although it has been repeatedly demonstrated that glutaraldehyde is an effective crosslinker, recent studies have found that GTA can undergo intra- and intermolecular transformations that may lead to undesired crosslinking and aggregation, especially in aqueous media [108]. Despite its potential shortcoming, glutaraldehyde is still being used to immobilize many different ligands onto a wide range of surfaces and

particles. For instance, very recently Agrawal *et al.* have used APTES-GTA functionalization to immobilize peroxidase enzyme onto pSi and therefore improve its activity [109]. A silicon nanowire biosensor has also been developed by Hashin *et al.* using glutaraldehyde-based chemistry to detect single-stranded DNA molecules [110].

## 2.4 References

- [1] Uhlir, A., *Electrolytic Shaping of Germanium and Silicon*. Bell System Technical Journal, 1956. **35**(2): p. 333-347.
- [2] Gupta, P., A.C. Dillon, A.S. Bracker, and S.M. George, *FTIR studies of H<sub>2</sub>O and D<sub>2</sub>O decomposition on porous silicon surfaces*. Surface Science, 1991. **245**(3): p. 360-372.
- [3] Dillon, A.C., M.B. Robinson, M.Y. Han, and S.M. George, *Diethylsilane Decomposition on Silicon Surfaces Studied Using Transmission FTIR Spectroscopy*. Journal of The Electrochemical Society, 1992. **139**(2): p. 537-543.
- [4] Imai, K., *A new dielectric isolation method using porous silicon*. Solid-State Electronics, 1981. **24**(2): p. 159-164.
- [5] Erson, R.C., R.S. Muller, and C.W. Tobias, *Investigations of porous silicon for vapor sensing*. Sensors and Actuators A: Physical, 1990. **23**(1-3): p. 835-839.
- [6] Lehmann, V. and U. Gösele, *Porous silicon formation: A quantum wire effect*. Applied Physics Letters, 1991. **58**(8): p. 856-858.
- [7] Canham, L.T., *Silicon quantum wire array fabrication by electrochemical and chemical dissolution of wafers*. Applied Physics Letters, 1990. **57**(10): p. 1046-1048.
- [8] Lin, V.S.-Y., K. Moteshareei, K.-P.S. Dancil, M.J. Sailor, and M.R. Ghadiri, *A Porous Silicon-Based Optical Interferometric Biosensor*. Science, 1997. **278**(5339): p. 840-843.
- [9] Arrand, H.F., T.M. Benson, P. Sewell, A. Loni, R.J. Bozeat, R. Arens-Fischer, M. Kruger, M. Thonissen, and H. Luth, *The application of porous silicon to optical waveguiding technology*. Selected Topics in Quantum Electronics, IEEE Journal of, 1998. **4**(6): p. 975-982.
- [10] Coffey, J.L., M.A. Whitehead, D.K. Nagesha, P. Mukherjee, G. Akkaraju, M. Totolici, R.S. Saffie, and L.T. Canham, *Porous silicon-based scaffolds for tissue engineering and other biomedical applications*. physica status solidi (a), 2005. **202**(8): p. 1451-1455.
- [11] Létant, S.E., S. Content, T.T. Tan, F. Zenhausern, and M.J. Sailor, *Integration of porous silicon chips in an electronic artificial nose*. Sensors and Actuators B: Chemical, 2000. **69**(1-2): p. 193-198.
- [12] Anglin, E.J., L. Cheng, W.R. Freeman, and M.J. Sailor, *Porous silicon in drug delivery devices and materials*. Advanced Drug Delivery Reviews, 2008. **60**(11): p. 1266-1277.
- [13] Lehmann, V., *The Semiconductor-Electrolyte Junction*, in *Electrochemistry of Silicon*. 2002, Wiley-VCH Verlag GmbH. p. 39-50.
- [14] Sailor, M.J., *Porous silicon in practice: preparation, characterization and applications*. 2012: John Wiley & Sons.

- [15] Zhang, X.G., S.D. Collins, and R.L. Smith, *Porous Silicon Formation and Electropolishing of Silicon by Anodic Polarization in HF Solution*. Journal of The Electrochemical Society, 1989. **136**(5): p. 1561-1565.
- [16] Korotcenkov, G. and B.K. Cho, *Silicon Porosification: State of the Art*. Critical Reviews in Solid State and Materials Sciences, 2010. **35**(3): p. 153-260.
- [17] Zhang, X.G., *Mechanism of Pore Formation on n-Type Silicon*. Journal of The Electrochemical Society, 1991. **138**(12): p. 3750-3756.
- [18] Corbett, J.W., D.I. Shereshevskii, and I.V. Verner, *Changes in the Creation of Point Defects Related to the Formation of Porous Silicon*. physica status solidi (a), 1995. **147**(1): p. 81-89.
- [19] Rouquerol, J., D. Avnir, D.H. Everett, C. Fairbridge, M. Haynes, N. Pernicone, J.D.F. Ramsay, K.S.W. Sing, and K.K. Unger, *Guidelines for the Characterization of Porous Solids*, in *Studies in Surface Science and Catalysis*, F.R.-R.K.S.W.S. J. Rouquerol and K.K. Unger, Editors. 1994, Elsevier. p. 1-9.
- [20] Chabal, Y.J., G.S. Higashi, K. Raghavachari, and V.A. Burrows, *Infrared spectroscopy of Si(111) and Si(100) surfaces after HF treatment: Hydrogen termination and surface morphology*. Journal of Vacuum Science & Technology A, 1989. **7**(3): p. 2104-2109.
- [21] Zhang, X.G., *Morphology and Formation Mechanisms of Porous Silicon*. Journal of The Electrochemical Society, 2004. **151**(1): p. C69-C80.
- [22] Propst, E.K. and P.A. Kohl, *The Electrochemical Oxidation of Silicon and Formation of Porous Silicon in Acetonitrile*. Journal of The Electrochemical Society, 1994. **141**(4): p. 1006-1013.
- [23] Wehrspohn, R.B., F. Ozanam, and J.N. Chazalviel, *Nano- and Macropore Formation in p-Type Silicon*. Journal of The Electrochemical Society, 1999. **146**(9): p. 3309-3314.
- [24] Lehmann, V. and S. Ronnebeck, *The Physics of Macropore Formation in Low-Doped p-Type Silicon*. Journal of The Electrochemical Society, 1999. **146**(8): p. 2968-2975.
- [25] Lust, S. and C. Lévy-Clément, *Chemical Limitations of Macropore Formation on Medium-Doped p-Type Silicon*. Journal of The Electrochemical Society, 2002. **149**(6): p. C338-C344.
- [26] Lehmann, V., *Macroporous Silicon*, in *Electrochemistry of Silicon*. 2002, Wiley-VCH Verlag GmbH. p. 183-205.
- [27] Williams, D.F., *A model for biocompatibility and its evaluation*. Journal of Biomedical Engineering, 1989. **11**(3): p. 185-191.
- [28] Lee, J.E., N. Lee, T. Kim, J. Kim, and T. Hyeon, *Multifunctional Mesoporous Silica Nanocomposite Nanoparticles for Theranostic Applications*. Accounts of Chemical Research, 2011. **44**(10): p. 893-902.
- [29] Jaganathan, H. and B. Godin, *Biocompatibility assessment of Si-based nano- and micro-particles*. Advanced Drug Delivery Reviews, 2012. **64**(15): p. 1800-1819.
- [30] Van Dyck, K., R. Van Cauwenbergh, H. Robberecht, and H. Deelstra, *Bioavailability of silicon from food and food supplements*. Fresenius' Journal of Analytical Chemistry, 1999. **363**(5-6): p. 541-544.

- [31] Braley, S., *The Chemistry and Properties of the Medical-Grade Silicones*. Journal of Macromolecular Science: Part A - Chemistry, 1970. **4**(3): p. 529-544.
- [32] Lührs, A.K. and W. Geurtsen, *The Application of Silicon and Silicates in Dentistry: A Review*, in *Biosilica in Evolution, Morphogenesis, and Nanobiotechnology*, W.G. Müller and M. Grachev, Editors. 2009, Springer Berlin Heidelberg. p. 359-380.
- [33] Chiappini, C., E. Tasciotti, J.R. Fakhoury, D. Fine, L. Pullan, Y.-C. Wang, L. Fu, X. Liu, and M. Ferrari, *Tailored Porous Silicon Microparticles: Fabrication and Properties*. ChemPhysChem, 2010. **11**(5): p. 1029-1035.
- [34] Anderson, S.H.C., H. Elliott, D.J. Wallis, L.T. Canham, and J.J. Powell, *Dissolution of different forms of partially porous silicon wafers under simulated physiological conditions*. physica status solidi (a), 2003. **197**(2): p. 331-335.
- [35] Finnie, K., D. Waller, F. Perret, A. Krause-Heuer, H. Lin, J. Hanna, and C. Barbé, *Biodegradability of sol-gel silica microparticles for drug delivery*. Journal of Sol-Gel Science and Technology, 2009. **49**(1): p. 12-18.
- [36] Jugdaohsingh, R., *Silicon and bone health*. The journal of nutrition, health & aging, 2007. **11**(2): p. 99.
- [37] Henstock, J.R., L.T. Canham, and S.I. Anderson, *Silicon: The evolution of its use in biomaterials*. Acta Biomaterialia, 2015. **11**(0): p. 17-26.
- [38] Reffitt, D.M., R. Jugdaohsingh, R.P.H. Thompson, and J.J. Powell, *Silicic acid: its gastrointestinal uptake and urinary excretion in man and effects on aluminium excretion*. Journal of Inorganic Biochemistry, 1999. **76**(2): p. 141-147.
- [39] Santos, H.A., *Porous silicon for biomedical applications*. 2014: Elsevier.
- [40] Grayson, A.C.R., R.S. Shawgo, A.M. Johnson, N.T. Flynn, L.I. Yawen, M.J. Cima, and R. Langer, *A BioMEMS review: MEMS technology for physiologically integrated devices*. Proceedings of the IEEE, 2004. **92**(1): p. 6-21.
- [41] Nuxoll, E., *BioMEMS in drug delivery*. Advanced Drug Delivery Reviews, 2013. **65**(11-12): p. 1611-1625.
- [42] Kotzar, G., M. Freas, P. Abel, A. Fleischman, S. Roy, C. Zorman, J.M. Moran, and J. Melzak, *Evaluation of MEMS materials of construction for implantable medical devices*. Biomaterials, 2002. **23**(13): p. 2737-2750.
- [43] Santini, J.T., M.J. Cima, and R. Langer, *A controlled-release microchip*. Nature, 1999. **397**(6717): p. 335-338.
- [44] Desai, T., W. Chu, G. Rasi, P. Sinibaldi-Vallebona, E. Guarino, and M. Ferrari, *Microfabricated Biocapsules Provide Short-Term Immunoisolation of Insulinoma Xenografts*. Biomedical Microdevices, 1999. **1**(2): p. 131-138.
- [45] Voskerician, G., M.S. Shive, R.S. Shawgo, H.v. Recum, J.M. Anderson, M.J. Cima, and R. Langer, *Biocompatibility and biofouling of MEMS drug delivery devices*. Biomaterials, 2003. **24**(11): p. 1959-1967.
- [46] Edell, D.J., V.V. Toi, V.M. McNeil, and L.D. Clark, *Factors influencing the biocompatibility of insertable silicon microshafts in cerebral cortex*. Biomedical Engineering, IEEE Transactions on, 1992. **39**(6): p. 635-643.



- [47] Rosengren, A., L. Wallman, N. Danielsen, T. Laurell, and L.M. Bjursten, *Tissue reactions evoked by porous and plane surfaces made out of silicon and titanium*. Biomedical Engineering, IEEE Transactions on, 2002. **49**(4): p. 392-399.
- [48] Canham, L.T., *Bioactive silicon structure fabrication through nanoetching techniques*. Advanced Materials, 1995. **7**(12): p. 1033-1037.
- [49] Canham, L.T., C.L. Reeves, J.P. Newey, M.R. Houlton, T.I. Cox, J.M. Buriak, and M.P. Stewart, *Derivatized Mesoporous Silicon with Dramatically Improved Stability in Simulated Human Blood Plasma*. Advanced Materials, 1999. **11**(18): p. 1505-1507.
- [50] He, Q., Z. Zhang, Y. Gao, J. Shi, and Y. Li, *Intracellular Localization and Cytotoxicity of Spherical Mesoporous Silica Nano- and Microparticles*. Small, 2009. **5**(23): p. 2722-2729.
- [51] Santos, H.A., J. Riikonen, J. Salonen, E. Mäkilä, T. Heikkilä, T. Laaksonen, L. Peltonen, V.-P. Lehto, and J. Hirvonen, *In vitro cytotoxicity of porous silicon microparticles: Effect of the particle concentration, surface chemistry and size*. Acta Biomaterialia, 2010. **6**(7): p. 2721-2731.
- [52] Decuzzi, P., B. Godin, T. Tanaka, S.Y. Lee, C. Chiappini, X. Liu, and M. Ferrari, *Size and shape effects in the biodistribution of intravascularly injected particles*. Journal of Controlled Release, 2010. **141**(3): p. 320-327.
- [53] Tanaka, T., B. Godin, R. Bhavane, R. Nieves-Alicea, J. Gu, X. Liu, C. Chiappini, J.R. Fakhoury, S. Amra, A. Ewing, Q. Li, I.J. Fidler, and M. Ferrari, *In vivo evaluation of safety of nanoporous silicon carriers following single and multiple dose intravenous administrations in mice*. International Journal of Pharmaceutics, 2010. **402**(1-2): p. 190-197.
- [54] Canham, L.T. and D. Ferguson, *Porous Silicon in Brachytherapy*, in *Handbook of Porous Silicon*, L. Canham, Editor. 2014, Springer International Publishing. p. 1-7.
- [55] Fine, D., A. Grattoni, R. Goodall, S.S. Bansal, C. Chiappini, S. Hosali, A.L. van de Ven, S. Srinivasan, X. Liu, B. Godin, L. Brousseau, I.K. Yazdi, J. Fernandez-Moure, E. Tasciotti, H.-J. Wu, Y. Hu, S. Klemm, and M. Ferrari, *Silicon Micro- and Nanofabrication for Medicine*. Advanced Healthcare Materials, 2013. **2**(5): p. 632-666.
- [56] Pagonis, D.N. and A.G. Nassiopoulou, *Free-standing macroporous silicon membranes over a large cavity for filtering and lab-on-chip applications*. Microelectronic Engineering, 2006. **83**(4-9): p. 1421-1425.
- [57] Jae Cheol, S., D. Chanda, W. Chern, Y. Ki Jun, J.A. Rogers, and L. Xiuling, *Experimental Study of Design Parameters in Silicon Micropillar Array Solar Cells Produced by Soft Lithography and Metal-Assisted Chemical Etching*. IEEE Journal of Photovoltaics, 2012. **2**(2): p. 129-133.
- [58] Wang, Y., S. Park, J.T.W. Yeow, A. Langner, and F. Müller, *A capacitive humidity sensor based on ordered macroporous silicon with thin film surface coating*. Sensors and Actuators B: Chemical, 2010. **149**(1): p. 136-142.
- [59] Gu, D., H. Baumgart, K. Tapily, P. Shrestha, G. Namkoong, X. Ao, and F. Müller, *Precise control of highly ordered arrays of nested semiconductor/metal nanotubes*. Nano Research, 2011. **4**(2): p. 164-170.

- [60] Trifonov, T., M. Garín, A. Rodríguez, L.F. Marsal, and R. Alcubilla, *Tuning the shape of macroporous silicon*. *physica status solidi (a)*, 2007. **204**(10): p. 3237-3242.
- [61] Thakur, M., R.B. Pernites, N. Nitta, M. Isaacson, S.L. Sinsabaugh, M.S. Wong, and S.L. Biswal, *Freestanding Macroporous Silicon and Pyrolyzed Polyacrylonitrile As a Composite Anode for Lithium Ion Batteries*. *Chemistry of Materials*, 2012. **24**(15): p. 2998-3003.
- [62] Marsal, L.F., P. Formentín, R. Palacios, T. Trifonov, J. Ferré-Borrull, A. Rodríguez, J. Pallarés, and R. Alcubilla, *Polymer microfibers obtained using porous silicon templates*. *Physica Status Solidi A*, 2008. **205**(10): p. 2437-2440.
- [63] Michaelis, S., C.E. Rommel, J. Endell, P. Goring, R. Wehrspohn, C. Steinem, A. Janshoff, H.-J. Galla, and J. Wegener, *Macroporous silicon chips for laterally resolved, multi-parametric analysis of epithelial barrier function*. *Lab on a Chip*, 2012. **12**(13): p. 2329-2336.
- [64] Yoo, L., K.-Y. Ahn, J.-Y. Ahn, T. Laurell, Y.M. Lee, P.J. Yoo, and J. Lee, *A simple one-step assay platform based on fluorescence quenching of macroporous silicon*. *Biosensors and Bioelectronics*, 2013. **41**(0): p. 477-483.
- [65] Astrova, E.V., T.N. Borovinskaya, T.S. Perova, and M.V. Zamoryanskaya, *Quartz microtubes based on macroporous silicon*. *Semiconductors*, 2004. **38**(9): p. 1084-1087.
- [66] Rodríguez, A., D. Molinero, E. Valera, T. Trifonov, L.F. Marsal, J. Pallares, and R. Alcubilla, *Fabrication of silicon oxide microneedles from macroporous silicon*. *Sensors and Actuators B-Chemical*, 2005. **109**(1): p. 135-140.
- [67] Strambini, L.M., A. Longo, A. Diligenti, and G. Barillaro, *A minimally invasive microchip for transdermal injection/sampling applications*. *Lab on a Chip*, 2012. **12**(18): p. 3370-3379.
- [68] Ohji, H., S. Izuo, P.J. French, and K. Tsutsumi, *Pillar structures with a sub-micron space fabricated by macroporous-based micromachining*. *Sensors and Actuators A: Physical*, 2002. **97-98**(0): p. 744-748.
- [69] Steinem, C., A. Janshoff, V.S.Y. Lin, N.H. Völcker, and M. Reza Ghadiri, *DNA hybridization-enhanced porous silicon corrosion: mechanistic investigations and prospect for optical interferometric biosensing*. *Tetrahedron*, 2004. **60**(49): p. 11259-11267.
- [70] Sweetman, M.J., C.J. Shearer, J.G. Shapter, and N.H. Voelcker, *Dual Silane Surface Functionalization for the Selective Attachment of Human Neuronal Cells to Porous Silicon*. *Langmuir*, 2011. **27**(15): p. 9497-9503.
- [71] Gooding, J.J. and S. Ciampi, *The molecular level modification of surfaces: from self-assembled monolayers to complex molecular assemblies*. *Chemical Society Reviews*, 2011. **40**(5): p. 2704-2718.
- [72] Chhablani, J., A. Nieto, H. Hou, E.C. Wu, W.R. Freeman, M.J. Sailor, and L. Cheng, *Oxidized porous silicon particles covalently grafted with daunorubicin as a sustained intraocular drug delivery system*. *Investigative Ophthalmology & Visual Science*, 2013. **54**(2): p. 1268-1279.

- [73] Massad-Ivanir, N., G. Shtenberg, A. Tzur, M.A. Krepker, and E. Segal, *Engineering nanostructured porous SiO<sub>2</sub> surfaces for bacteria detection via "direct cell capture"*. Analytical chemistry, 2011. **83**(9): p. 3282-9.
- [74] Riikonen, J., M. Salomäki, J. van Wonderen, M. Kemell, W. Xu, O. Korhonen, M. Ritala, F. MacMillan, J. Salonen, and V.-P. Lehto, *Surface Chemistry, Reactivity, and Pore Structure of Porous Silicon Oxidized by Various Methods*. Langmuir, 2012. **28**(28): p. 10573-10583.
- [75] Biju, V., *Chemical modifications and bioconjugate reactions of nanomaterials for sensing, imaging, drug delivery and therapy*. Chemical Society Reviews, 2014. **43**(3): p. 744-764.
- [76] Salonen, J., V.P. Lehto, and E. Laine, *The room temperature oxidation of porous silicon*. Applied Surface Science, 1997. **120**(3-4): p. 191-198.
- [77] Ogata, Y., H. Niki, T. Sakka, and M. Iwasaki, *Oxidation of Porous Silicon under Water Vapor Environment*. Journal of The Electrochemical Society, 1995. **142**(5): p. 1595-1601.
- [78] Ziaie, B., A. Baldi, M. Lei, Y. Gu, and R.A. Siegel, *Hard and soft micromachining for BioMEMS: review of techniques and examples of applications in microfluidics and drug delivery*. Advanced Drug Delivery Reviews, 2004. **56**(2): p. 145-172.
- [79] Nicollian, E.H., J.R. Brews, and E.H. Nicollian, *MOS (metal oxide semiconductor) physics and technology*. Vol. 1987. 1982: Wiley New York et al.
- [80] Lee, T.M.-H., M.C. Carles, and I.M. Hsing, *Microfabricated PCR-electrochemical device for simultaneous DNA amplification and detection*. Lab on a Chip, 2003. **3**(2): p. 100-105.
- [81] Mawhinney, D.B., J.A. Glass, and J.T. Yates, *FTIR Study of the Oxidation of Porous Silicon*. The Journal of Physical Chemistry B, 1997. **101**(7): p. 1202-1206.
- [82] Ogata, Y.H., T. Tsuboi, T. Sakka, and S. Naito, *Oxidation of Porous Silicon in Dry and Wet Environments under Mild Temperature Conditions*. Journal of Porous Materials, 2000. **7**(1-3): p. 63-66.
- [83] Astrova, E., *Oxidation of Macroporous Silicon in Handbook of porous silicon*. L. Canham, Editor. 2014, Springer International Publishing. p. 1-10.
- [84] Trifonov, T., A. Rodriguez, F. Servera, L.F. Marsal, J. Pallares, and R. Alcubilla, *High-aspect-ratio silicon dioxide pillars*. Physica Status Solidi A, 2005. **202**(8): p. 1634-1638.
- [85] Schilling, J., A. Birner, F. Müller, R.B. Wehrspohn, R. Hillebrand, U. Gösele, K. Busch, S. John, S.W. Leonard, and H.M. van Driel, *Optical characterisation of 2D macroporous silicon photonic crystals with bandgaps around 3.5 and 1.3 μm*. Optical Materials, 2001. **17**(1-2): p. 7-10.
- [86] Pap, A.E., K. Kordás, G. Tóth, J. Levoska, A. Uusimäki, J. Vähäkangas, S. Leppävuori, and T.F. George, *Thermal oxidation of porous silicon: Study on structure*. Applied Physics Letters, 2005. **86**(4): p. -.
- [87] Kao, D.B., J.P. McVittie, W.D. Nix, and K.C. Saraswat, *Two-dimensional thermal oxidation of silicon. II. Modeling stress effects in wet oxides*. Electron Devices, IEEE Transactions on, 1988. **35**(1): p. 25-37.

- [88] Dah-Bin, K., J.P. McVittie, W.D. Nix, and K.C. Saraswat, *Two-dimensional thermal oxidation of silicon*. *Experiments*. Electron Devices, IEEE Transactions on, 1987. **34**(5): p. 1008-1017.
- [89] Büttner, C.C. and M. Zacharias, *Retarded oxidation of Si nanowires*. Applied Physics Letters, 2006. **89**(26): p. -.
- [90] Zhang, F., K. Sautter, A.M. Larsen, D.A. Findley, R.C. Davis, H. Samha, and M.R. Linford, *Chemical Vapor Deposition of Three Aminosilanes on Silicon Dioxide: Surface Characterization, Stability, Effects of Silane Concentration, and Cyanine Dye Adsorption*. Langmuir, 2010. **26**(18): p. 14648-14654.
- [91] Metwalli, E., D. Haines, O. Becker, S. Conzone, and C.G. Pantano, *Surface characterizations of mono-, di-, and tri-aminosilane treated glass substrates*. Journal of Colloid and Interface Science, 2006. **298**(2): p. 825-831.
- [92] Hermanson, G.T., *Bioconjugate techniques*. 2013: Academic press.
- [93] Lee, Y., S. Park, J. Park, and W.G. Koh, *Micropatterned assembly of silica nanoparticles for a protein microarray with enhanced detection sensitivity*. Biomedical microdevices, 2010. **12**(3): p. 457-64.
- [94] Guha Thakurta, S. and A. Subramanian, *Fabrication of dense, uniform aminosilane monolayers: A platform for protein or ligand immobilization*. Colloids and Surfaces A: Physicochemical and Engineering Aspects, 2012. **414**(0): p. 384-392.
- [95] Rother, D., T. Sen, D. East, and I.J. Bruce, *Silicon, silica and its surface patterning/activation with alkoxy- and amino-silanes for nanomedical applications*. Nanomedicine, 2011. **6**(2): p. 281-300.
- [96] Li, Z., J.C. Barnes, A. Bosoy, J.F. Stoddart, and J.I. Zink, *Mesoporous silica nanoparticles in biomedical applications*. Chemical Society Reviews, 2012. **41**(7): p. 2590-2605.
- [97] Meng, H., M. Liong, T. Xia, Z. Li, Z. Ji, J.I. Zink, and A.E. Nel, *Engineered Design of Mesoporous Silica Nanoparticles to Deliver Doxorubicin and P-Glycoprotein siRNA to Overcome Drug Resistance in a Cancer Cell Line*. ACS Nano, 2010. **4**(8): p. 4539-4550.
- [98] Mosse, W.K.J., M.L. Koppens, T.R. Gengenbach, D.B. Scanlon, S.L. Gras, and W.A. Ducker, *Peptides Grafted from Solids for the Control of Interfacial Properties*. Langmuir, 2009. **25**(3): p. 1488-1494.
- [99] Baranowska, M., A.J. Slota, P.J. Eravuchira, G. Macias, E. Xifré-Pérez, J. Pallares, J. Ferré-Borrull, and L.F. Marsal, *Protein attachment to nanoporous anodic alumina for biotechnological applications: Influence of pore size, protein size and functionalization path*. Colloids and Surfaces B: Biointerfaces, 2014. **122**(0): p. 375-383.
- [100] Halliwell, C.M. and A.E.G. Cass, *A Factorial Analysis of Silanization Conditions for the Immobilization of Oligonucleotides on Glass Surfaces*. Analytical Chemistry, 2001. **73**(11): p. 2476-2483.
- [101] Rasi Ghaemi, S., F. Harding, B. Delalat, R. Vasani, and N.H. Voelcker, *Surface Engineering for Long-Term Culturing of Mesenchymal Stem Cell Microarrays*. Biomacromolecules, 2013. **14**(8): p. 2675-2683.
- [102] Treccani, L., T. Yvonne Klein, F. Meder, K. Pardun, and K. Rezwani, *Functionalized ceramics for biomedical, biotechnological and environmental applications*. Acta Biomaterialia, 2013. **9**(7): p. 7115-7150.

- [103] Gray, J.J., *The interaction of proteins with solid surfaces*. Current Opinion in Structural Biology, 2004. **14**(1): p. 110-115.
- [104] Tinsley-Bown, A.M., L.T. Canham, M. Hollings, M.H. Anderson, C.L. Reeves, T.I. Cox, S. Nicklin, D.J. Squirrell, E. Perkins, A. Hutchinson, M.J. Sailor, and A. Wun, *Tuning the Pore Size and Surface Chemistry of Porous Silicon for Immunoassays*. physica status solidi (a), 2000. **182**(1): p. 547-553.
- [105] Ducker, R.E., M.T. Montague, and G.J. Leggett, *A comparative investigation of methods for protein immobilization on self-assembled monolayers using glutaraldehyde, carbodiimide, and anhydride reagents*. Biointerphases, 2008. **3**(3): p. 59-65.
- [106] Jonkheijm, P., D. Weinrich, H. Schröder, C.M. Niemeyer, and H. Waldmann, *Chemical Strategies for Generating Protein Biochips*. Angewandte Chemie International Edition, 2008. **47**(50): p. 9618-9647.
- [107] Gunda, N.S.K., M. Singh, L. Norman, K. Kaur, and S.K. Mitra, *Optimization and characterization of biomolecule immobilization on silicon substrates using (3-aminopropyl)triethoxysilane (APTES) and glutaraldehyde linker*. Applied Surface Science, 2014. **305**(0): p. 522-530.
- [108] Migneault, I., C. Dartiguenave, M.J. Bertrand, and K.C. Waldron, *Glutaraldehyde: behavior in aqueous solution, reaction with proteins, and application to enzyme crosslinking*. Biotechniques, 2004. **37**(5): p. 790-806.
- [109] Sahare, P., M. Ayala, R. Vazquez-Duhalt, and V. Agrawal, *Immobilization of peroxidase enzyme onto the porous silicon structure for enhancing its activity and stability*. Nanoscale Research Letters, 2014. **9**(1): p. 1-9.
- [110] Adam, T. and U. Hashim, *Highly sensitive silicon nanowire biosensor with novel liquid gate control for detection of specific single-stranded DNA molecules*. Biosensors and Bioelectronics, doi:10.1016/j.bios.2014.10.005

## ***Chapter 3***

---

# Fabrication of Three-Dimensional Microstructures based on Macroporous Silicon

Macroporous silicon is material wholly convenient for the fabrication of tubular structures on the microscale. Starting from bulk silicon, regular pores can be formed in an electrochemical etching process. The macropore growth propagates in depth to form layers of constant porosity and a thickness of up to several hundreds of micrometers. The possibility of applying microfabrication technologies such as lithography enables the production, on an arbitrarily sized area, of millions of objects identically shaped with nanometric precision. The ease of growing a thermal oxide makes it possible the manipulation of the macropore morphology and the production of a variety of structures such as tubes, needles or pillars.

This chapter is devoted to the experimental techniques for producing random and ordered macroporous silicon from low doped p-type silicon. Firstly, we describe the electrochemical etching setup used for the porous silicon fabrication. The methods and etching parameters utilized for the formation of random and ordered macroporous silicon are detailed. Finally, the process sequence and process parameters for the fabrication of inverted structures from macroporous silicon, i.e. micropillars and microtubes, are presented.

### **3.1 Electrochemical Etching of Silicon. Experimental**

Herein, we describe the elements involved in the experimental etching process of silicon (Si). The system has been developed in the Department of Electronic, Electric and Automatic Engineering at the University Rovira i Virgili (URV). Some steps of the sample preparation were carried out in the cleanroom facility in the Servei de Recursos Científics i Tècnics at URV.

#### **3.1.1 Set-up**

The porous silicon (pSi) described in this report was fabricated by electrochemical anodization of silicon in a hydrofluoric acid (HF) based solution. The experimental set-up is shown in Figure 3.1. The main component of the system is a customized electrochemical single-tank cell, coupled with a current source which is also able to measure the potential difference between the two electrodes. The system is computer controlled by a program that controls the current density and etching time applied.

**Electrochemical Cell.** We used a standard two-electrode configuration: working (the Si wafer) and counter (the platinum, Pt) electrodes. A schematic diagram of our customized electrochemical cell is shown in Figure 3.2A. The cell consists of a cylindrical polytetrafluoroethylene (PTFE or Teflon®) body designed to have on the bottom an exposed anodized area of 1.54 cm<sup>2</sup>. This material was used because it is highly resistant to acids and organic solvents. The silicon sample is placed between the Teflon cylinder and a metal contact, with its polished side facing up. A mechanical stirring system is coupled to the cell cap to facilitate the renovation of the electrolyte in contact with the silicon electrode. The metal back-side contact is a copper disk that enables a uniform contact on the whole area of the wafer. Note that it should be cleaned and polished to avoid any oxide



film that might cause preferential current flows and thus an inadequate anodization. The silicon substrate is sealed and held in place by a vinylidene fluoride-hexafluoropropylene (Viton®) O-ring. Eight screws fasten together the Teflon cell and the metal contact.



**Figure 3.1.** Photograph of the electrochemical etching set-up. The wafer is mounted in the customized etching cell (A) coupled with a mechanical stirring system (B). The voltage-current sourcemeter Keithley 2611A applies the current and measures the resulting voltage between the electrodes (C). The system is controlled by a home-designed program run in a computer (D).

The HF-based solution is poured into the etching cell and this is kept in the dark by placing a poly(vinyl chloride) (PVC) cap that contains a mechanical stirrer and the platinum cathode. The reaction takes place in

the dark to prevent photogenerated currents contributing to the pore formation process. The stirring system ensures a homogenous anodization by renewing the flow of electrolyte and improving the dispersion of the hydrogen bubbles from the silicon surface. The rotation velocity is controlled by adjusting the DC voltage applied to the motor.

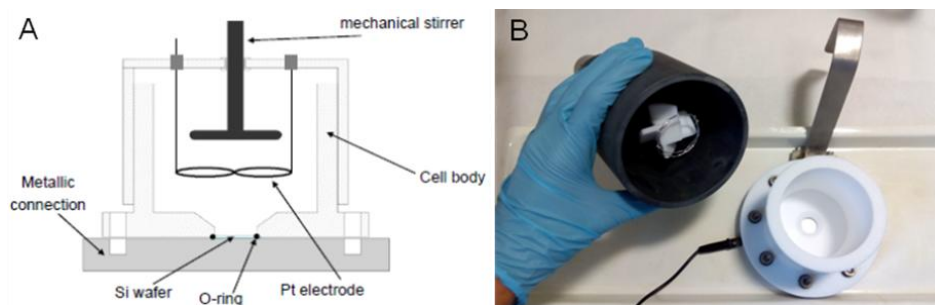


**Figure 3.2.** A) Schematic diagram of the electrochemical cell used in the pSi formation; B) photograph of the customized cell with a view of the stirrer and the Pt electrode, and the interior of the cell body with the exposed silicon at the bottom

The Pt cathode should be located not very close to the silicon surface, as relatively short distances lead to inhomogeneous pSi formation. Excessively large distances will imply the increase of the cell height and therefore greater amount of electrolyte to stir and higher resistance. The optimum distance of our cell is around 3 cm. Once the HF electrolyte is poured into the etching cell, anodization is ready to proceed.

**Current Source and Control Program.** The electrochemical process can be controlled either potentiostatically or galvanostatically. Normally cells operate in galvanostatic mode (i.e. current is the parameter set) since it assures reproducibility attaining wide ranges of porosity and thickness of

the pSi layer. In this work, we have used a constant current source (Keithley 2611A SourceMeter) for the pSi formation.

A computer program was previously designed in TestScriptBuilder (Keithley) to control the operation of the source to fabricate porous silicon. The main parameters that need to be set to carry out the anodization are:

*Output file.* The name of the forthcoming file, which will be saved in an external USB memory stick connected to the source once the anodization has finished. This will be a text file which includes applied current (in miliamperes), time (in seconds) and the measured voltage (in volts).

*Current.* The selected galvanostatic current (in miliamperes) we want to apply to our sample.

*Time.* The time the current will pass through the silicon electrode performing the anodization.

*Time between measurements.* Time between two consecutive voltage measurements.

***Electrolyte.*** The electrolyte must be an electro-active specie to be efficiently transported to the porous silicon-silicon interface where the anodization process primarily occurs. Hydrofluoric acid should be diluted due to the hydrophobic character of the clean silicon surface. Ethanol is frequently added to the hydrofluoric acid to improve uniformity and homogeneity of the porous silicon film in depth. Moreover, it is known that the addition of some surfactants that increases the viscosity of the electrolyte and reduces the surface roughness. In the macroporous silicon (macro-pSi) formation, surfactants act as wetting agents by reducing the surface tension and thus protecting the sidewalls against dissolution in order to obtain deep, regular macropores with smooth pore walls.

Surfactants that can be used in the etching of silicon include cetyltrimethylammonium chloride (CTAC), dimethylsulfoxide (DMSO), dimethylformamide (DMF) or a mixture of them. In our study, unless otherwise noted, the electrolyte was prepared by diluting commercial HF (40%) in DMF. The preferred electrolyte proportion was 1:10 (HF:DMF) as it has been repeatedly reported [1, 2] and it provides smooth surfaces and straight walls.

### **3.1.2 Sample Preparation. Lithography**

The growth of macropores in silicon is not a self-ordering process and would not form a periodic arrangement spontaneously. Nevertheless, the sites where pores should grow can be predefined by lithography and subsequent anisotropic etching in alkaline solutions such as potassium hydroxide (KOH) or tetramethyl ammonium hydroxide (TMAH). The resulting etch pits work as nucleation sites for the pore growth. The advantage of this method is that the pore arrangement and size can be tuned, and it is not restricted to hexagonal arrangements [3].

In the electrochemical etching of silicon, the resulting pores nucleate at random points on the surface. However, for a given doping density, applied voltage and electrolyte composition, an average porosity and pore diameter will arise, as a result of a self-organizing process. Therefore, the lithography has to fit with the intrinsic material parameters. The passivation of the pore walls and thus the prevention of the pore walls from being post-etched is a consequence of the space-charge region (SCR), as we discussed in Chapter 2. For a stabilized pore growth, the remaining silicon between neighboring pores should be completely depleted from charge carriers. From this requirement, a statement can be derived for the lattice constant of the lithography: the interpore distance has to be chosen

twice as large as the width of the SCR [3]. It implies that higher doped material are preferentially used for smaller interpore distances and *vice versa*.

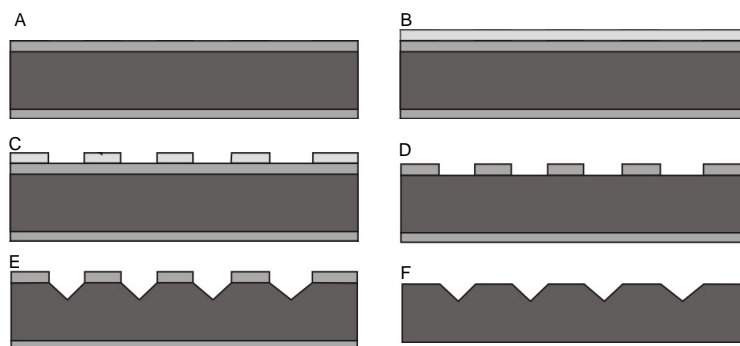


**Figure 3.3.** Schematic representation for the sample preparation. A) Wafer oxidation; B) photoresist deposition by spin-coating; C) direct-laser lithography; D) selective removal of the oxide film by BHF etch and dissolution of the remaining photoresist layer; E) TMAH etch for the formation of inverted pyramids and F) dissolution of the residual SiO<sub>2</sub> layer.

Essentially, we have adopted the sample patterning procedure that Lehmann and Föll first reported in 1990 for producing arrays of ordered macropores by electrochemical etching process [4]. A schematic representation of the sequence is shown in Figure 3.3. First, the wafers are thermally oxidized in order to grow a thin SiO<sub>2</sub> layer that will act as a mask in the anisotropic alkaline etch (Figure 3.3A). Then, a thin layer of positive photoresist is deposited onto the silicon wafer by spin-coating (Figure 3.3B). Next, the desired arrangement and period is patterned on the sample by direct-write lithography (Figure 3.3C). After developing the photoresist, the lithographic pattern is transferred onto the oxide layer by etching the silicon oxide in buffered hydrofluoric acid (BHF, Figure 3.3D). The etch pits on the surface are obtained by anisotropic etching in a TMAH solution (Figure 3.3E). The tip of the resulting inverted pyramids will act as nuclei

points for the pore growth. After the TMAH etch, the oxide is dissolved by a quick dip in HF 5% (Figure 3.3F).

**Starting Material.** Porous silicon samples were prepared on p-type (100) silicon substrates various boron doping densities and therefore different resistivities: 10-20, 20-30, 40-60, 80-100  $\Omega$  cm. This type of silicon is considered as low doped p-type silicon. 2 and 4 inch-wafers were used with a thickness of 250-300  $\mu\text{m}$ . This substrate is robust and sturdy, and allows getting flat and homogenous surfaces of porous silicon layers.

**Oxidation.** The wafers were oxidized in synthetic air at 1000  $^{\circ}\text{C}$  for 15 min. The thickness of the obtained oxide layer was about 10-12 nm. This thickness is enough to serve as a mask and protect the silicon from the anisotropic etch due to the high selectivity of TMAH towards Si versus  $\text{SiO}_2$ . This oxide layer can be removed by a few seconds dip in BHF etching mixture (ammonium fluoride etching mixture HF (6%) +  $\text{NH}_4\text{F}$  (35%)) at a rate of about 70 nm  $\text{min}^{-1}$ .

**Lithography.** This step is the most critical as any imperfection will be extended through the fabrication process and reflected as defect pores. Following standard procedures, a thin layer of positive photoresist AZ 1505 (MicroChemicals) was deposited by spin-coating on the silicon wafer at 500 rpm for 10 s then 5000 rpm for 30 s, followed by a soft bake at 100  $^{\circ}\text{C}$  for 30 s. Then the wafer was patterned by direct-write lithography (DWL 66FS, Heidelberg Instruments GmbH). This technique allows the arbitrary design of patterns on an area of adjustable dimensions. Next, the photoresist was developed by immersing the wafer in the metal ion free developer AZ 726 (MicroChemicals) for 45 s. The exposed silicon oxide was dissolved by a quick dip in BHF and thus the patterned is transferred into

the SiO<sub>2</sub> thin layer. The photoresist film is not longer needed and therefore removed with acetone.

**TMAH Etching of Silicon.** The etching of the pre-patterned silicon wafer in order to obtain the inverted pyramids was performed in 8% TMAH solution at 80 °C for 3-6 min. TMAH etch is an anisotropic process; the resulting structure is a lattice of pyramidal pits that will serve as seeds for the pore growth, as it can be observed in the scanning electron microscopy (SEM) images in Figure 3.4. The pyramid tips must be well-defined to act as nucleation points. The time for the TMAH etch to form tipped pyramids depends on the size of the lithographic pattern.

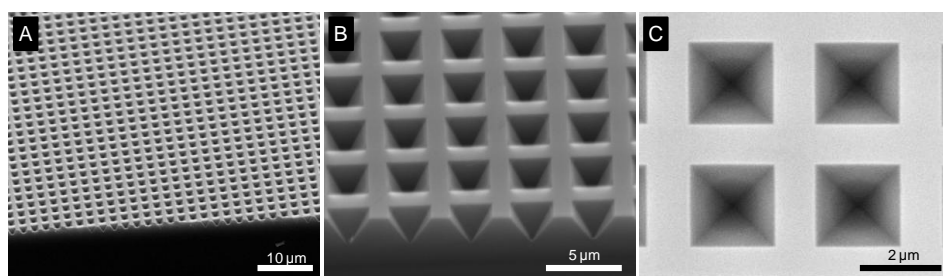


**Figure 3.4.** A, B) Tilted SEM images of the TMAH etch pits with 3 μm lattice constant formed at the silicon surface as a sample preparation for the electrochemical etching process; C) top-view of patterned silicon with 4 μm lattice constant.

### 3.1.3 Pore Morphology and Process Parameters

The morphology of macropores formed on p-type Si can be understood as a consequence of the stringent requirement for pore wall passivation in low doped p-type substrates: pore walls are depleted if their thickness is less than twice the SCR width. This thickness depends on the doping density and applied bias, thus a variety of morphologies can be obtained. Furthermore, differences in the sample preparation and lithography design

can lead to a wide range of shapes and arrangements. Undoubtedly there are a number of parameters that influence the pore formation in silicon such as type and concentration of dopant, crystal orientation, electrolyte composition, temperature and anodization regime, as we discussed in Chapter 2, section 2.1.

**Random Macropore Formation in Low Doped p-Type Silicon.** Random macro-pSi was fabricated from low doped p-type silicon wafers of orientation (1 0 0) and resistivity ranging from 10 to 100  $\Omega$  cm. Galvanostatic conditions with a low current density (5-20 mA cm<sup>-2</sup>) were used for the electrochemical etching. The electrolyte composition was 1:10 HF (40%)/DMF.

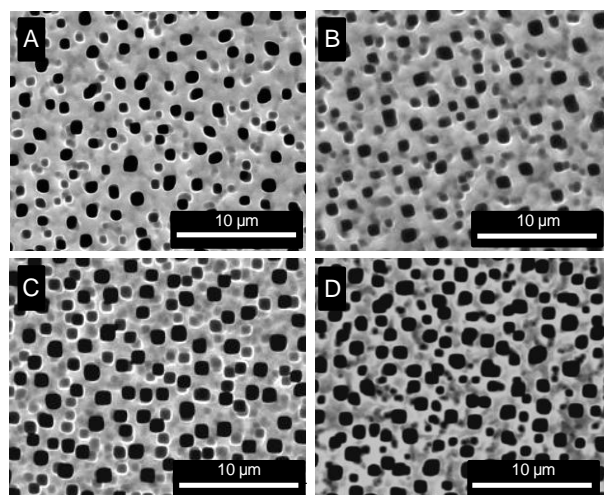


**Figure 3.5.** Top view SEM images of macro-pSi samples formed in HF:DMF (1:10) at 5 mA cm<sup>-2</sup> current density on substrates of resistivity A) 10-20; B) 20-30; C) 40-60; and D) 80-100  $\Omega$  cm.

Using this solution and a current density of 5 mA cm<sup>-2</sup>, the effect of the resistivity in the macropore morphology was analyzed. As shown in Figure 3.5, the pore morphology and density change with the p-type Si resistivity.



The average pore wall thickness and the macropore density are dependent on the substrate doping density [5]. Actually, the density of macropores in a random pore nucleation regime is linearly dependent on the doping concentration [6]. It has been also reported that in a substrate with resistivity below  $2 \Omega \text{ cm}$  the pore walls become too fragile and a roughening of the surface is produced instead of pores [5].

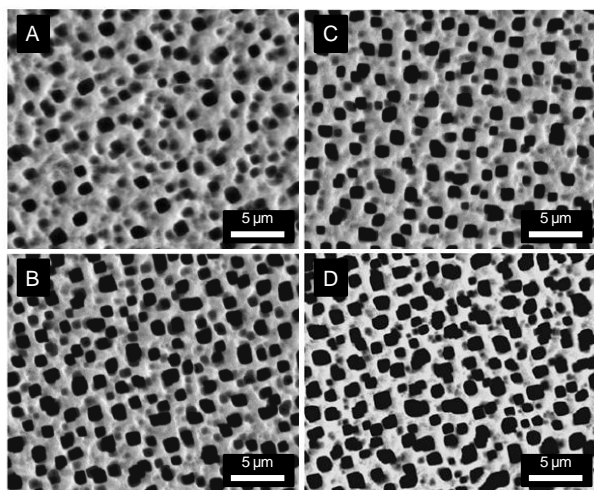


**Figure 3.6.** SEM images of macro-pSi samples formed on  $10\text{-}20 \Omega \text{ cm}$  p-type silicon in HF:DMF (1:10) at a current density of A) 5; B) 10; C) 15 and D)  $20 \text{ mA cm}^{-2}$ .

Using the same electrolyte, different macro-pSi samples were fabricated under current densities ranging from  $5$  to  $20 \text{ mA cm}^{-2}$  in a p-type substrate of resistivity  $10\text{-}20 \Omega \text{ cm}$ . The SEM micrographs shown in Figure 3.6 were analyzed using ImageJ software (NIH, USA) [7]. The etching rate and porosity versus the current density are presented in Figure 3.7 for an etching time of 10 min. The results show a pore diameter that ranges between  $1.1$  and  $1.3 \mu\text{m}$ , and porosity between 14 and 35% which increases quasi-linearly with the current density. The etching rate was also found to increase with the current density, although the linear dependence was not observed.

**Ordered Macropore Growth in Low Doped p-Type Silicon.** The previous results discussed in the section above were used as an insightful introduction to the formation of ordered macro-pSi arrays. They shed light on some electrochemical aspects such as etching conditions and lattice constant, which may be critical for growing ordered macropores. Thus, the substrates used for the formation of ordered macro-pSi were those previously investigated in the growth of random macropores: (1 0 0) p-type Si of resistivity from 10 to 100  $\Omega$  cm.

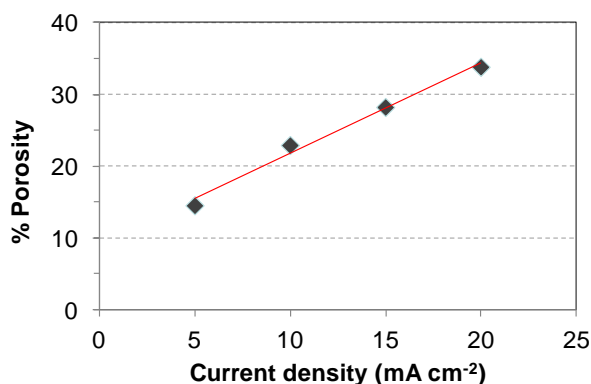


**Figure 3.7.** Porosity versus current density for samples prepared on p-type Si of resistivity 10-20  $\Omega$  cm at a current density of 5  $\text{mA cm}^{-2}$ .

The wafers were lithographically pre-patterned following the sample preparation procedure described in Section 3.1.2. Once the sample was patterned with a suitable lattice constant, the silicon substrate was ready for the formation of ordered macropore arrays. It should be noted that the pore shape and diameter are not defined by the size of the pyramidal notch but by the etching conditions and wafer resistivity. The electrochemical etching was performed using a 1:10 HF (40%)/DMF electrolyte under galvanostatic conditions.

As mentioned above, it is important that the pyramids are well-defined after the anisotropic etching in order to obtain the nuclei points for a localized pore growth. Figure 3.8A shows a micrograph where an incomplete TMAH etch led to truncated pyramids instead of tipped pyramids. The resulting macropores tended to grow in the dips of the patterned regions, but the nucleation points were not defined (see Figure 3.8B). Irregular shaped and sized macropores appear on the surface; however as the growth in depth progresses, the different superficial pores tend to regroup and form pores of very similar diameter and interpore distance (Figure 3.8C).

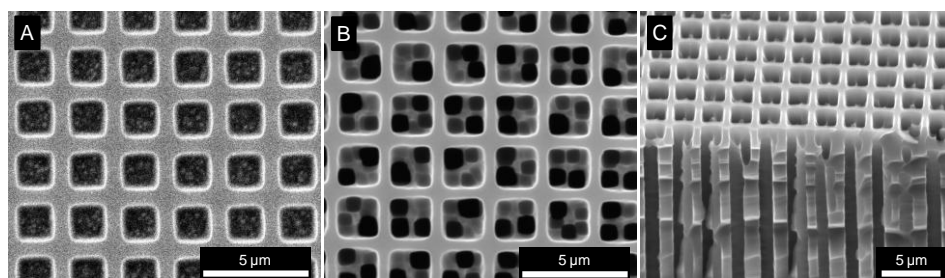


**Figure 3.8.** SEM micrographs A) patterned Si with truncated pyramids as a result of an inadequate TMAH etch; B) macropore formation in the patterned regions; and C) tilted view of the macropore formation in depth.

When the starting material is patterned with well-defined inverted pyramids, the electrochemical etching leads to deep and wide pores that penetrate into the silicon bulk following the pre-patterning arrangement, with nuclei points located at the pyramid pits. However, it may happen that the lattice constant is not appropriate for obtaining ordered macropores under the given electrochemical conditions and the specific wafer doping. This results in the uncontrolled growth of pores in some regions between neighboring pyramids, as it can be observed from Figure 3.9A. Pores in the interstitial positions appeared whenever the thickness of the wall between

two adjacent pores was larger than twice the depletion width of the electrolyte/silicon junction [8]. The diameter of the random nucleated pores is less than the pore diameter of the pores nucleated in the pits. The smoothness of the surface is also clearly affected: pores preferentially grow in the crystal direction, although some pores are also initiated on the walls, thus creating a highly rough silicon surface (Figure 3.9B). However, when we keep previous conditions but the lattice constant is reduced from 4 to 3  $\mu\text{m}$ , no random nucleation is observed in between pyramids, meaning we have now reached a lattice constant smaller than twice the depletion width (see Figures 3.9C,D).

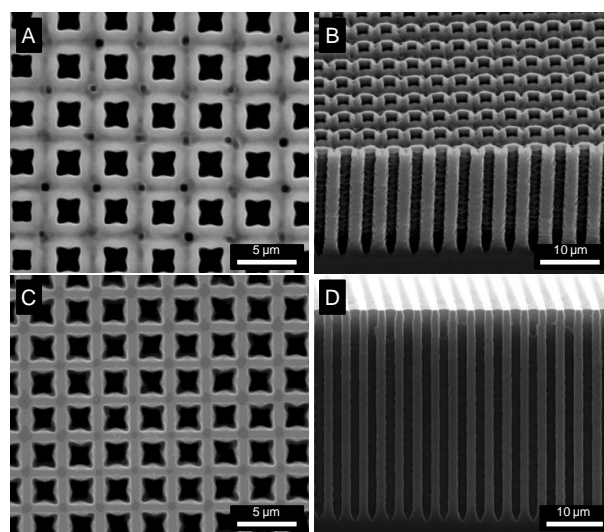


**Figure 3.9.** SEM images from A) top view and B) cross-sectional view of ordered macroporous silicon formed on patterned p-type Si (4  $\mu\text{m}$  lattice constant) with the formation of interstitial pores; C) top view and D) cross-sectional view of ordered macroporous silicon with a good adjustment of the electrochemical parameters (3  $\mu\text{m}$  lattice constant).

When the distance between pyramids is adjusted for the particular doping density, no random nucleation takes place. Regular ordered arrays

can be produced consisting of macropores of identical shape and size, and equidistant separation. Figure 3.10 shows SEM images of the macropores formed on silicon of resistivity 40-60  $\Omega$  cm at 5 mA cm<sup>-2</sup> in patterned silicon with a lattice constant of 4  $\mu$ m. As we discussed previously, the macropore dimension is determined by the etch pits in the patterned area and by the substrate resistivity. In the formation of ordered macropores, variations in the resistivity while keeping constant the lattice parameter and etching conditions resulted in different pore dimensions. The diameter of the pores was found to increase with the substrate resistivity. This is due to the dependence of the depletion width with the doping density.

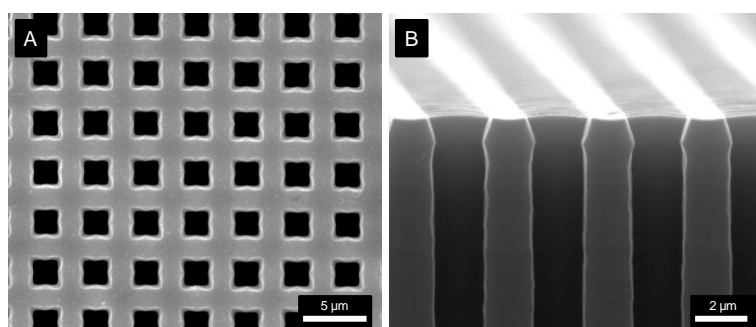


**Figure 3.10.** SEM images taken from a macroporous silicon sample formed on patterned Si (4  $\mu$ m lattice constant) with 40-60  $\Omega$  cm resistivity. A) Top view and B) detail in cross-section of the initial pyramids and subsequent electrochemical pores.

It is remarkable the feasibility to etch pores of several hundred of micrometers in depth. Thus aspect ratios of 500:1 and even more can be obtained without losing the ordering and the defined shape of the pores [9]. Figure 3.11 shows a SEM micrograph where the preservation of the ordered arrangement imparted by the lithography is kept throughout the pore growth. The etching was conducted for 3 h with a constant current density of 5 mA cm<sup>-2</sup>. The rounded-square macropores run all along the

depth of the layer (150  $\mu\text{m}$ ) without any detectable branching or obstruction. Zoomed-in images reveal the remarkable uniformity of the macropores, with regular and controlled pore size, and very smooth pore walls.

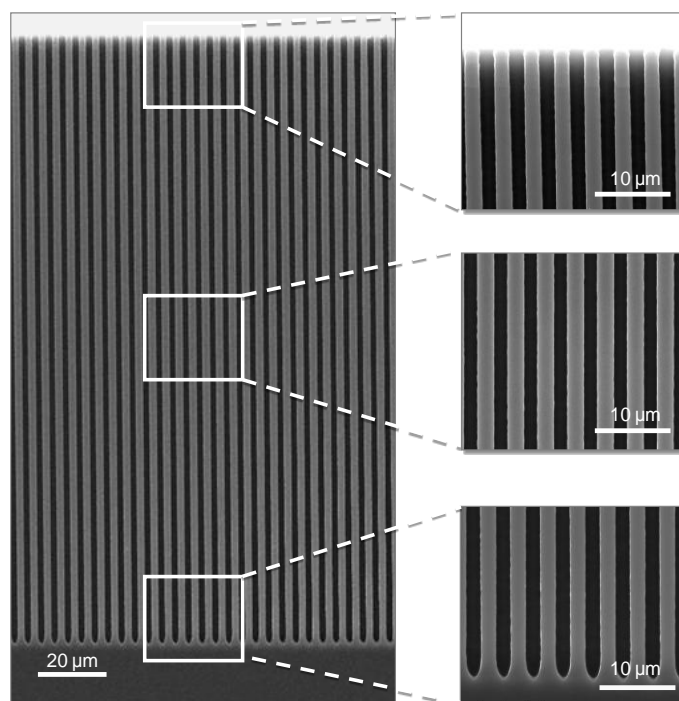


**Figure 3.11.** SEM micrograph of straight pores 150  $\mu\text{m}$  in depth etched into Si with a squared pattern and 4  $\mu\text{m}$  lattice constant (left). Zoomed images at different depths display uniform pores in diameter and smooth wall surfaces (right).

### ***3.2 Silicon Dioxide Microstructures Based on Macroporous Silicon***

As we previously described, macro-pSi is a material ideally suited for the fabrication of tubular structures on the micrometer size scale. Pores can be formed either in a random fashion or in a regular arrangement and

with controlled shape. Using macro-pSi as starting material, it is also possible to create three-dimensional (3D) structures by introducing some modifications in the standard process. For instance, by varying the pore diameter with periodic modulations, highly precise 3D photonic crystals can be fabricated [10].

Starting from macro-pSi, the manipulation of the pore shape or the fabrication of novel structures can be performed by taking advantage of one of the most precious features of silicon: the ease of growing a conformal SiO<sub>2</sub> layer by thermal oxidation [11]. This characteristic allows the fabrication of inverted structures such as hollow micropillars, microneedles or microtubes [12-14].

### **3.2.1 Silicon Dioxide Micropillars**

High-aspect-ratio hollow SiO<sub>2</sub> micropillars can be obtained from macro-pSi formed on low doped p-type Si. Following the formation of straight regular pores by electrochemical etching of silicon (Figure 3.12A), an oxide layer of thickness between 150 and 300 nm is thermally grown (Figure 3.12B). The oxidation takes place in a furnace at 1000 °C in ambient air for 1.5-2 h, depending on the desired final thickness. Next, the silicon oxide formed on the backside of the wafer was removed on an arbitrarily sized and shaped area (Figure 3.12C). This area can be defined by its selective exposure to a BHF solution. Typically, we used a customized Teflon cell that encases one side of the sample. It protects the macroporous frontside of the wafer from any contact with the solution, while the backside is exposed to the BHF on an area that is slightly smaller than the diameter of the macroporous region on the frontside. However, smaller, arbitrarily designed regions can also be lithographically selected. Finally, the backside silicon was etched off in 8-25% TMAH solutions at 85 °C. The conformal

oxide grown around the pores acts as a TMAH etch stop. As a result, the oxidized pore tips appear protruding out of the wafer backside (Figure 3.12D).

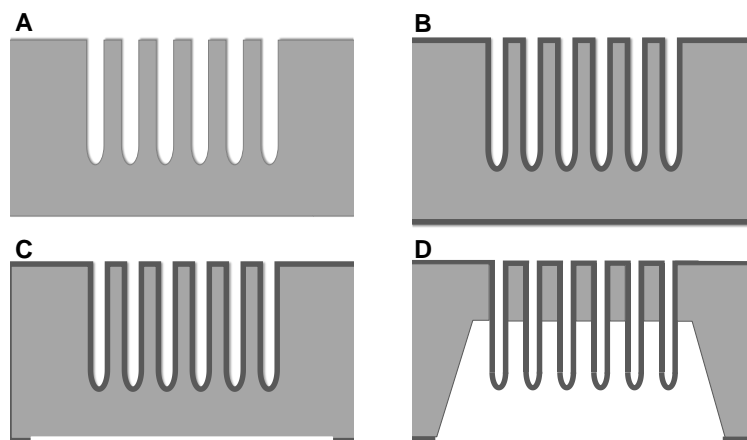


**Figure 3.12.** Schematic illustration of the method for the fabrication of silicon dioxide micropillars. A) Macropore formation by electrochemical etching; B) silicon dioxide growth by thermal oxidation; C) oxide layer removal on an unmasked area of the sample backside; D) backside silicon etching in TMAH solution to release the micropillars.

Silicon dioxide micropillars preserve the shape and arrangement of the preceding macro-pSi. This means that they can present both ordered and random arrangements, depending on whether the starting silicon substrate was patterned or not. Nevertheless, the thermal oxidation of silicon produces a material of lower molecule density that results in a volume expansion. If the volume expansion of the newly formed  $\text{SiO}_2$  takes place in one direction, the thickness of the oxide is 2.2 times the thickness of the original silicon [15]. Figure 3.13 shows the differences in morphology between a freshly etched macro-pSi sample and oxidized macro-pSi (1000 °C for 1.5 h in air). It was observed a decrease in porosity of about 20%



after the strong thermal oxidation that forms the walls of the future micropillars.

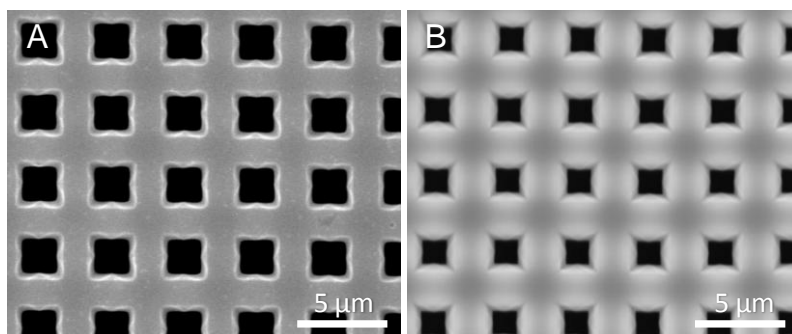


**Figure 3.13.** Macro-pSi sample A) freshly anodized and B) after thermal oxidation at 1000 °C for 1.5 h.

The geometrical characteristics of the micropillars are tunable as well as those of the previous macropores were. Modifications in the etching parameters change the macroporous silicon features and therefore the subsequent micropillars. Figure 3.14 shows SEM images SiO<sub>2</sub> micropillars after the silicon has been etched. Their geometry is that of the initial macropores, with rounded-square sections and almost hemispherical tips. Figure 3.14A shows micropillars randomly organized, whilst in Figure 3.14B ordered arrays were obtained by using lithographic patterned silicon substrates. As it can be observed, a remarkable vertical uniformity of the pillar was achieved.

The thermally grown SiO<sub>2</sub> that acts as micropillar wall is of constant thickness along the pillar axis. This attribute was first observed in SEM cross-sectional images (Figure 3.14) and then confirmed by transmission electron microscopy (TEM) for a single detached micropillar. Figure 3.15 is a cross-section-like dark field TEM image of a single broken micropillar, which confirms the hollow architecture and uniform SiO<sub>2</sub> walls. The oxide

presents a homogeneous thickness (about 200 nm) all along the protruding micropillar.

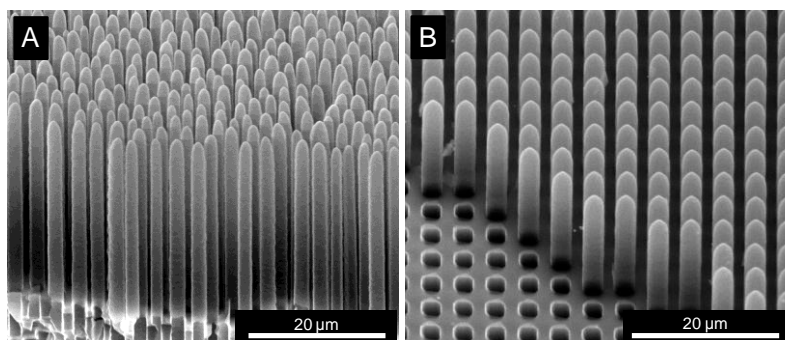


**Figure 3.14.** SEM micrographs of SiO<sub>2</sub> micropillars after TMAH etch of the backside bulk silicon fabricated from A) random and B) ordered macro-pSi.

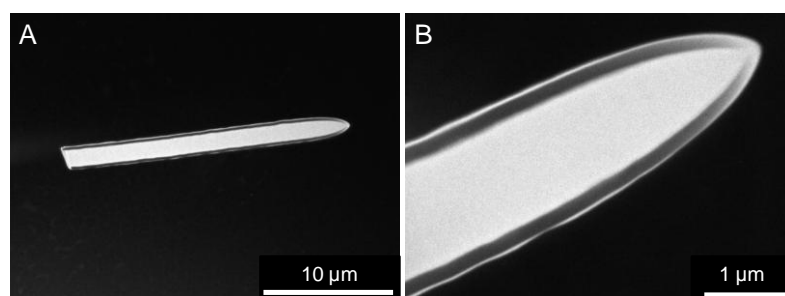


**Figure 3.15.** Dark-field TEM images of A) a single broken micropillar showing uniform SiO<sub>2</sub> walls and hollow structure; B) a detail of the micropillar tip.

As it occurred in the electrochemical formation of macro-pSi, the resistivity of the substrate plays a key role in the geometrical features of the micropillars. The diameter increases and the pore density decreases with the resistivity when keeping constant the rest of electrochemical conditions. For the silicon dioxide micropillars shown in Figure 3.16 (formed from macro-pSi fabricated in 1:10 HF/DMF at 5 mA cm<sup>-2</sup>), we observe an average diameter a little smaller for micropillars formed on Si of 10-20 Ω cm resistivity (1.8 µm, Figure 3.16A) than those formed on Si 40-60 Ω cm (2.0 µm, Figure 3.16B). However, the micropillar density is

noticeably higher for resistivity 10-20  $\Omega$  cm than for 40-60  $\Omega$  cm, with an area fraction covered of 38% and of 25%, respectively. All these data were obtained by image processing using ImageJ software [7].

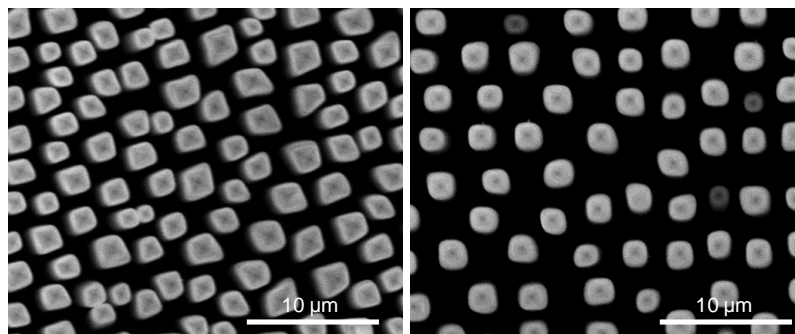


**Figure 3.16.** SEM top-view images of SiO<sub>2</sub> micropillars fabricated using identical etching conditions on substrates of different resistivity: A) 10-20; B) 40-60  $\Omega$  cm.

Micropillar arrays in a predefined arrangement can be fabricated from ordered macro-pSi. However, as we mentioned above, there are limitations in the electrochemical etching of pre-patterned silicon: not any size or arrangement can be achieved, but only those that are suitably consistent with the doping density and etching conditions. A mismatch in these parameters may result in roughly-walled, non-uniform micropillars, as it can be observed in the TEM image shown in Figure 3.17. Although high-aspect-ratio, hollow structures are obtained, the oxide wall presents a very rough surface. This indicates the electrochemical conditions were unstable during the pore growth, which can lead to branching or obstruction.

The precise control over the etching parameters, lattice constant and wafer resistivity is needed to optimize the process and consequently to be able to obtain regular, well-defined micropillars. Figure 3.18 shows three micropillar samples obtained from three differently doped substrates. The lattice constant was adjusted for the formation of regular macropores

whose geometry is transferred into the subsequent micropillars. Thus, for very low doped Si (80-100  $\Omega$  cm and 40-60  $\Omega$  cm, in Figures 3.18A and 3.18B, respectively) the lattice constant was chosen to be 4  $\mu$ m in view of previous results in randomly formed porous silicon. However, for a resistivity 10-20  $\Omega$  cm (Figure 3.18C) such a lattice constant would result in the irregular formation of pores, as we previously discussed. In that case a 3  $\mu$ m lattice constant was chosen. It is also clear that despite having used same etching parameters and lattice constant for samples in Figures 3.18A and 17B, the resistivity impart a different morphology, which is related to the SCR width for a given doping density.

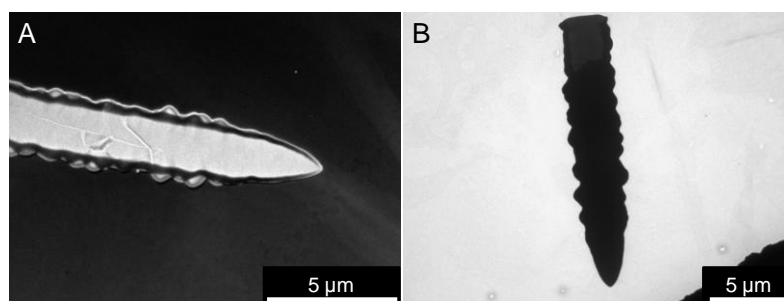


**Figure 3.17.** TEM micrographs of a single broken micropillar in A) dark field and B) bright field modes.

In the fabrication of SiO<sub>2</sub> micropillars based on p-type silicon, the pore pattern and diameter are moderately modifiable due to limitations in the macropore formation process. Complex phenomena mediate in the formation of the preceding macro-pSi, as we discussed in Chapter 2. They are influenced by the etching conditions, wafer doping and lithography indentation. However, the length can be adjusted from a few to several tens of micrometers as it only depends on the TMAH etching time. Actually, they can be as long as the thickness of the initial silicon wafer. For the anisotropic etch in TMAH 25% at 80 °C we found a Si dissolution rate of

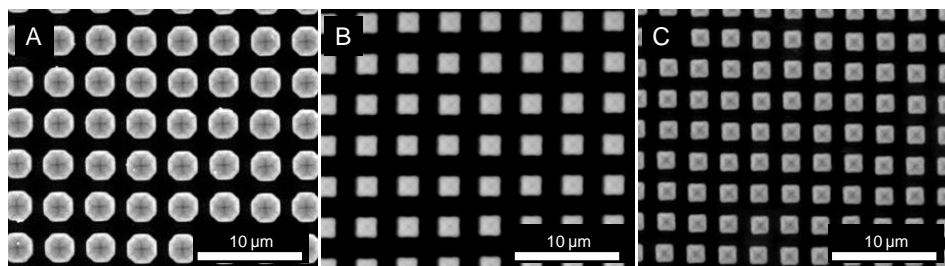


**Figure 3.18.** SEM top-view micrographs of ordered SiO<sub>2</sub> micropillar arrays from macro-pSi formed in HF:DMF (1:10) at 5 mA cm<sup>-2</sup> on Si substrates of A) 80-100 and B) 40-60 Ω cm resistivity and 4 µm lattice constant; and C) 10-20 Ω cm resistivity and 3 µm lattice constant.

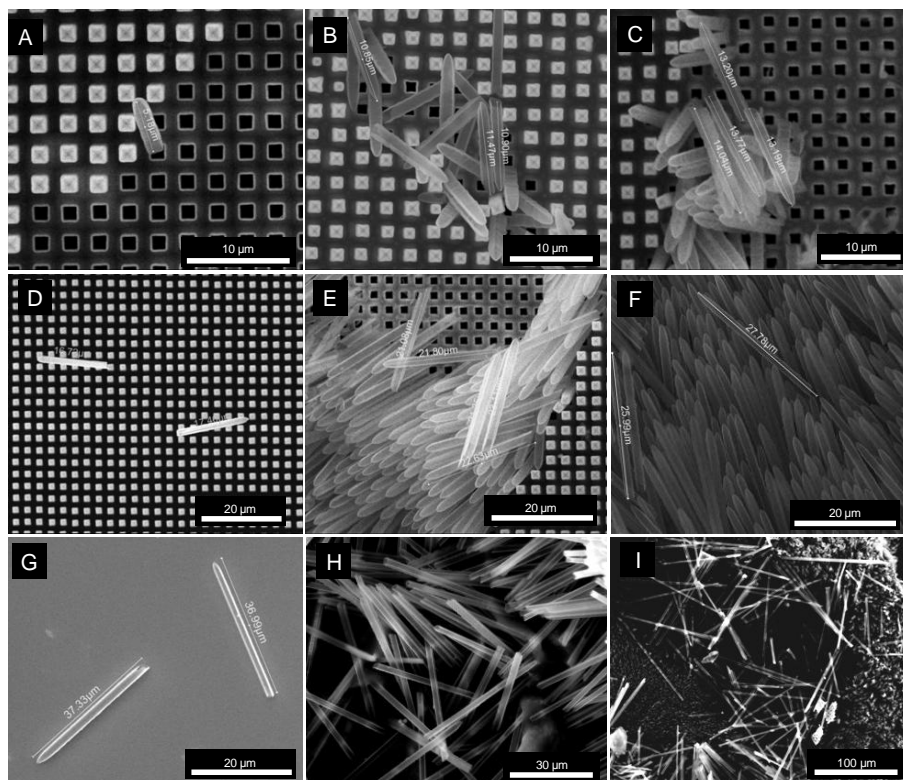


**Figure 3.19.** SEM micrographs of micropillars with identical external diameter (1.8 µm) and different length of A) 5-6 µm; B) 10-12 µm; C) 13-15 µm; D) 16-18 µm; E) 20-24 µm; F) 25-30 µm; G) 35-40 µm; H) 50-60 µm and I) 150-180 µm.

about  $0.7 \mu\text{m min}^{-1}$ . Figure 3.19 shows SEM images of micropillars of different sizes that were obtained from boron-doped Si,  $10\text{-}20 \Omega \text{ cm}$  resistivity, patterned with a  $3 \mu\text{m}$  lattice constant. These micrographs exemplify the capability of fabricating micropillars in a wide range of lengths.

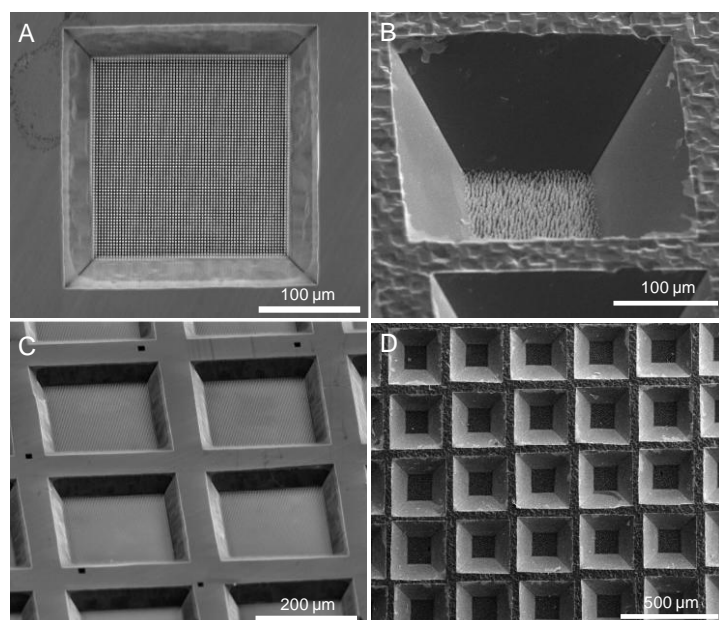


**Figure 3.20.** Micropillar arrays inside microwells. A, C) Ordered micropillars protruding out of a squared area of  $190 \mu\text{m}$  side inside  $100 \mu\text{m}$  deep microwells. B ,D) random micropillar on an area of  $120 \mu\text{m}$  side inside  $100 \mu\text{m}$  deep microwells.

The oxide removal from the backside of the silicon wafer is usually masked with a Teflon cell that exposes certain area to the BHF etching solution (see Figure 3.12D). Nevertheless, these oxide-free windows where the  $\text{SiO}_2$  micropillars will appear protruding out can be arbitrarily selected and designed using lithography techniques. We either employed direct-laser or masked photo-lithography to pattern these areas and thus choose the subsequent regions where the micropillars will protrude out of the

backside. The oxide acts as a mask and the silicon is only anisotropically etched in the oxide-free windows, thus creating microwells with SiO<sub>2</sub> micropillars inside, as shown in Figure 3.20. The dimensions of these microwells are easily adjustable by modifying the size of the photolithography mask or the direct-laser writing design. The depth of these microwells can be also tuned with the TMAH etching time.

### **3.2.2 Silicon Dioxide Microtubes**

Microtubes are hollow structures with tip diameters in the range of the micrometers. They can be fabricated by combining macroporous silicon, oxide growth and dry and wet etching techniques. The dimensions and arrangement of these microtubes depend solely on the electrochemical etching conditions, within the limits of the macroporous silicon formation.

The main process sequence for microtube fabrication is illustrated schematically in Figure 3.21. The starting material is a sample of high-aspect ratio silicon macropores (Figure 3.21A). A thermal oxidation is performed to grow a silicon dioxide layer on the surface of the macroporous silicon sample (Figure 3.21B). Typically, the oxidation is performed in a furnace at 1000 °C in ambient air for 1.5 h to obtain an oxide layer of about 150 nm thick. Then, oxide on the macroporous side of the sample was exposed to octafluorocyclobutane/oxygen (C<sub>4</sub>F<sub>8</sub>/O<sub>2</sub>) combining inductively-coupled-plasma and reactive ion etching (ICP-RIE, PlasmaLab 80 Plus, Oxford Instruments Plasma Technology) at 18 sccm C<sub>4</sub>F<sub>8</sub> and 2 sccm O<sub>2</sub>, 15 mTorr, 300 W ICP and 100 W HF power to remove the 200 nm oxide layer on the frontside surface (Figure 3.21C). The equipment is fitted with an endpoint detection system based on laser interferometry that measures etch depth and stops the SiO<sub>2</sub> dissolutions when the oxide layer has been removed. After removal of the protective

oxide layer on the frontside, a TMAH etch (8% at 80 °C) is used to obtain microtubes with a tunable protruding length, that depends on the anisotropic etching time.

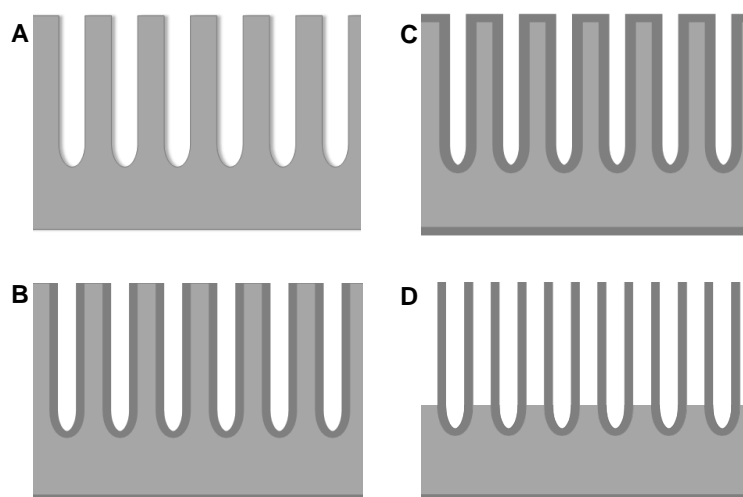


**Figure 3.21.** Schematic illustration of the method for the fabrication of silicon dioxide microtubes. A) Macropore formation by electrochemical etching; B) silicon dioxide growth by thermal oxidation; C) oxide layer removal on the frontside surface with directional plasma ICP-RIE process; and D) bulk silicon removal by TMAH etch.

The main process sequence for microtube fabrication is illustrated schematically in Figure 3.21. The starting material is a sample of high-aspect ratio silicon macropores (Figure 3.21A). A thermal oxidation is performed to grow a silicon dioxide layer on the surface of the macroporous silicon sample (Figure 3.21B). Typically, the oxidation is performed in a furnace at 1000 °C in ambient air for 1.5 h to obtain an oxide layer of about 150 nm thick. Then, oxide on the macroporous side of the sample was exposed to  $C_4F_8/O_2$  combining inductively-coupled-plasma and reactive ion etching (ICP-RIE, PlasmaLab 80 Plus, Oxford Instruments Plasma Technology) at 18 sccm  $C_4F_8$  and 2 sccm  $O_2$ , 15 mTorr, 300 W ICP



and 100 W high frequency power to remove the 200 nm oxide layer on the frontside surface (Figure 3.21C). The equipment is fitted with an endpoint detection system based on laser interferometry that measures etch depth and stops the  $\text{SiO}_2$  dissolutions when the oxide layer has been removed. After removal of the protective oxide layer on the frontside, a TMAH etch (8% at 80 °C) is used to obtain microtubes with a tunable protruding length, that depends on the anisotropic etching time.

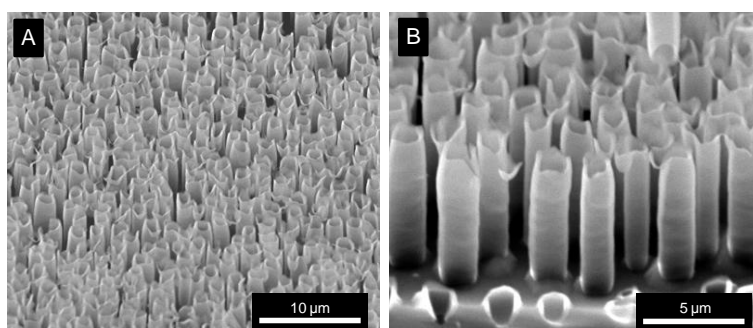


**Figure 3.22.** SEM tilted micrographs of  $\text{SiO}_2$  microtubes fabricated from random macroporous silicon with a protruding lengths of 9  $\mu\text{m}$ .

The morphology of the resulting microtubes is given by the preceding macropores. Figure 3.22 shows SEM images of the microtubes obtained following the procedure outlined above, using silicon substrates of resistivity 10-20  $\Omega$  cm. Firstly, without any sample preparation, macropores were formed and subsequently processed to create the tube structure (Figure 3.22A). The microtube density and shape is given by the electrochemical conditions. The wall thickness depends on the oxidation. We found that 150 nm is enough to give them a good mechanical stability.

Note that  $\text{SiO}_2$  layer removal occurs only on the macroporous silicon surface, since the etch rate in the direction of the plasma propagation is much faster than in the perpendicular one. This effect is more evident at

the pore bottom end. The thin oxide layer there is not completely dissolved by the plasma etch due to the high curvature of the tip, despite being partially parallel to the surface. A further dry etch will eventually lead to a complete removal of the tip, yielding  $\text{SiO}_2$  structures opened at both ends.

As previously mentioned, the protruding length depends on the time the silicon is anisotropically etched in the TMAH solution. The other limiting factor is the length of the initial macropores. If the etched depth surpasses the macropore length, the microtubes will not have any silicon around that keep them anchored to the substrate. Subsequently the microtubes will be individually transferred into the solution. Figure 3.23A shows a microtube sample where the TMAH dissolved most of the silicon acting as a support, thus they are attached to the substrate solely from the very tip. If the etching continues, the microtubes lose their anchoring to the surface and consequently some of them remain standing or collapsed on the substrate, some others may be transferred into the TMAH etching solution (see Figures 3.23B and 3.23C).

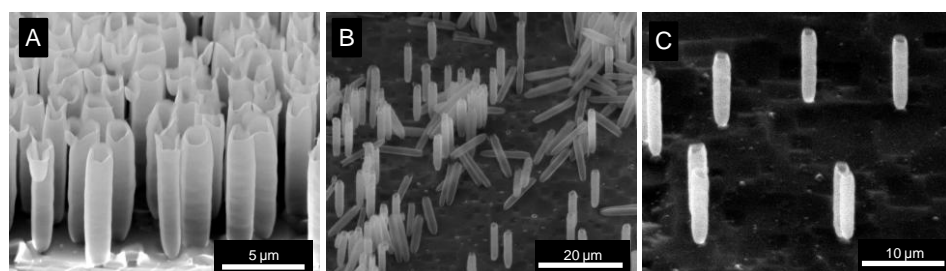


**Figure 3.23.** SEM micrographs of microtubes when the TMAH has etched most of the surrounding silicon. A)  $\text{SiO}_2$  microtubes attached from the very bottom on the silicon substrate; B) collapsed and standing microtubes; C) detail of a bunch of standing microtubes.

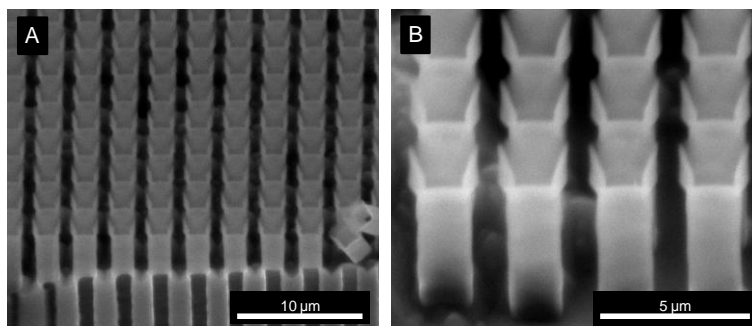


**Figure 3.24.** SEM tilted micrographs of SiO<sub>2</sub> microtubes fabricated from ordered macroporous silicon with a protruding length of 6 μm.

Starting from ordered arrays of macro-pSi, the same experimental procedure outlined above yields well-organized arrays of microtubes. Microtubes with a protruding length of about 6 μm were obtained from a macro-pSi sample with a lattice constant of 3 μm (see Figure 3.24). We have already mentioned that the diameter and geometry of the macropores and consequent micropillars is not given by the dimensions of the inverted pyramids created *via* lithography, but by the electrochemical conditions. This means that the initiating pyramid is not always embedded in the final macropore. When forming microtubes this fact is more evident, as we can observe from the SEM micrographs in Figure 3.24. The microtube opened-end, instead of having the typical square-rounded shape, it presents a squared shape, larger than the diameter of the macropore.

### **3.3 Conclusions**

In this chapter we have presented the methods to fabricate random and ordered macroporous silicon from low doped p-type Si. The anodization system has been described in detail, as well as the lithography techniques to obtain the pre-etching pits for ordered arrangement.

Morphological characterization in SEM revealed a wide size distribution in the randomly formed macropores. In contrast, lithographically patterned pits act as nuclei points for the pore growth, which results in quasi-cylindrical pores of identical size organized in an ordered arrangement. The matching conditions of lattice constant, resistivity and etching parameters were determined in order to obtain straight and stable pore growth. Strong thermal oxidation is utilized to generate inverted structures such as hollow micropillars made of silicon dioxide. Hollow micropillars generally adopted the shape and arrangement of the former macropores, i.e. random or ordered organization. Nevertheless, the length of these microstructures was found to be highly tunable, depending on the time the sample is immersed in the anisotropic etching solution. The microstructures developed in this chapter were the base material for further application in the following chapters.

### 3.4 References

- [1] Vyatkin, A.F., *Macroporous silicon: material science and technology*, in *Micro- and Nanoelectronics 2003*, K.A. Valiev and A.A. Orlikovsky, Editors. 2004. p. 187-191.
- [2] Pagonis, D.N. and A.G. Nassiopoulou, *Free-standing macroporous silicon membranes over a large cavity for filtering and lab-on-chip applications*. *Microelectronic Engineering*, 2006. **83**(4-9): p. 1421-1425.
- [3] Trifonov, T., L.F. Marsal, and Á. Rodríguez, *Photonic bandgap analysis and fabrication of macroporous silicon by electrochemical etching*. 2004.
- [4] Lehmann, V. and H. Föll, *Formation Mechanism and Properties of Electrochemically Etched Trenches in n-Type Silicon*. *Journal of The Electrochemical Society*, 1990. **137**(2): p. 653-659.
- [5] Lehmann, V., *Macroporous Silicon*, in *Electrochemistry of Silicon*. 2002, Wiley-VCH Verlag GmbH. p. 183-205.
- [6] Vyatkin, A., V. Starkov, V. Tzeitlin, H. Presting, J. Konle, and U. König, *Random and Ordered Macropore Formation in p-Type Silicon*. *Journal of The Electrochemical Society*, 2002. **149**(1): p. G70-G76.
- [7] Schneider, C.A., W.S. Rasband, and K.W. Eliceiri, *NIH Image to ImageJ: 25 years of image analysis*. *Nat Meth*, 2012. **9**(7): p. 671-675.
- [8] Bettotti, P., L. Dal Negro, Z. Gaburro, L. Pavesi, A. Lui, M. Galli, M. Patrini, and F. Marabelli, *P-type macroporous silicon for two-dimensional photonic crystals*. *Journal of applied physics*, 2002. **92**(12): p. 6966-6972.
- [9] Langner, A., F. Müller, and U. Gösele, *Macroporous Silicon*, in *Molecular-and Nano-Tubes*. 2011, Springer. p. 431-460.
- [10] Matthias, S., F. Müller, C. Jamois, R.B. Wehrspohn, and U. Gösele, *Large-Area Three-Dimensional Structuring by Electrochemical Etching and Lithography*. *Advanced Materials*, 2004. **16**(23-24): p. 2166-2170.
- [11] Astrova, E., *Oxidation of Macroporous Silicon* in *Handbook of porous silicon*. L. Canham, Editor. 2014, Springer International Publishing. p. 1-10.
- [12] Trifonov, T., A. Rodriguez, F. Servera, L.F. Marsal, J. Pallares, and R. Alcubilla, *High-aspect-ratio silicon dioxide pillars*. *Physica Status Solidi A*, 2005. **202**(8): p. 1634-1638.
- [13] Rodriguez, A., D. Molinero, E. Valera, T. Trifonov, L.F. Marsal, J. Pallares, and R. Alcubilla, *Fabrication of silicon oxide microneedles from macroporous silicon*. *Sensors and Actuators B-Chemical*, 2005. **109**(1): p. 135-140.
- [14] Astrova, E.V., T.N. Borovinskaya, T.S. Perova, and M.V. Zamoryanskaya, *Quartz microtubes based on macroporous silicon*. *Semiconductors*, 2004. **38**(9): p. 1084-1087.
- [15] Christiansen, T.L., O. Hansen, J.A. Jensen, and E.V. Thomsen, *Thermal Oxidation of Structured Silicon Dioxide*. *ECS Journal of Solid State Science and Technology*, 2014. **3**(5): p. N63-N68.

## ***Chapter 4***

---

# Functionalization Methods for Silicon Dioxide and Their Optimization towards Bioligand Conjugation

As prepared nano and micro-structures based on silicon dioxide often need surface modifications to make them suitable for applications in biosensing, drug delivery, bioimaging and cell culture. The modification of the surface chemistry not only helps to control the physico-chemical features but also the toxicological and pharmacological properties of the material. Furthermore, introduction of various reactive functional groups on its surface allows the conjugation of a variety of biological agents such as antibodies, proteins, ligands, drugs and genes. Thus, it is possible to construct multifunctional and hybrid systems based on porous silicon and its derived structures for imaging and therapy.

In this chapter we describe the functionalization methods employed in the following chapters. The silanol chemistry is briefly reviewed, and the silanization methods are described. Further attachment of crosslinking molecules for subsequent biomolecule conjugation is also detailed. Infrared spectroscopy is used to characterize attachment of the organic layers onto silicon dioxide surfaces and also to study the hydrolysis and condensation of organosilanes. The crosslinking reaction between aminosilane and glutaraldehyde is also characterized by infrared spectroscopy.

## 4.1 Introduction

The hydrophilicity [1] and biosafety [2-4] of as-produced silicon dioxide ( $\text{SiO}_2$ ) based microstructures make them one of the friendliest materials for applications in the life sciences. Despite starting from a strongly unstable, hydrogen-terminated surface in the freshly formed macroporous silicon (macro-pSi), the oxidation step allows the controlled growth of an oxide layer that stabilizes the silicon against any other surface modification. Nevertheless, silicon dioxide does not show any chemical affinity to biomolecules or cell tissues. Therefore, assorted functional groups are often necessary for employing these materials in biomedical and biotechnological applications such as biosensing, bioanalysis, bioimaging, drug delivery and therapy [3]. For instance, sometimes they should stimulate the cell-growth (prostheses) [5] or act as antifouling (artificial valves, catheters, etc) [6]. In some other cases, they may be specific for the recognition and measure of bioanalytes (disease or immunity-related, etc) [7, 8]. These attainments are strongly reliant on the surface chemistry and only possible through the grafting of appropriate molecules or set of molecules that provide the surface with a suitable terminal functionality.

The following sections discuss the functionalization strategies used to obtain  $\text{SiO}_2$  surfaces covered with different organic molecular layers. Porous silicon (pSi) samples were prepared by electrochemical etching and subsequently oxidized. pSi of high surface area was employed to obtain an enhanced signal gain in the infrared (IR) spectroscopy analysis. Two different silanization reactions were investigated and optimized to introduce suitable functional groups for the different applications that will be described in the next chapters. Silanization with (3-



mercaptopropyl)trimethoxysilane (MPTMS) was used to study the influence of post-treatments in the hydrolysis and condensation of silanes and to introduce thiol (-SH) functionality on SiO<sub>2</sub> surfaces for further coupling in subsequent experiments. Surfaces were also chemically modified with the aminosilane (3-aminopropyl)triethoxysilane (APTES) to prepare the samples for subsequent bioligand conjugation. The silanization reaction and the effect of acid and basic post-treatments were investigated by Fourier transform infrared (FT-IR) spectroscopy. Infrared analysis showed that these treatments were not only affected the number of residual alkoxy groups, but also the equilibrium between -NH<sub>2</sub> and -NH<sub>3</sub><sup>+</sup> which can be of great importance for further modification of the adsorbed layer. Thus, a following aldehyde (-CHO) functionalization was performed with glutaraldehyde (GTA). The aldehyde groups at the two opposite terminals allow condensation reactions aldehyde-amine, forming imine bridges and introducing aldehydic functionalities in the ω position to enable further coupling reactions with biomolecules [9, 10].

#### **4.1.1 Silanization**

The immobilization of biomolecules (e.g. proteins or antibodies) on silicon dioxide surfaces is of particular interest in biotechnology and biomedicine. Si and SiO<sub>2</sub> can be easily tailored using conventional silanol chemistries to form a covalent Si-O-Si-R bond [3, 11]. The use of alkoxy-silanes or chlorosilanes as precursors is the most widespread method to modify the chemical functionalities of hydroxyl-terminated surfaces [12], such as those of silicon dioxide. Silanes contain a silicon atom tetrahedrally coordinated to three similar hydrolysable groups (e.g. methoxy, ethoxy or chlorine) and to a functional group that introduces the desired chemical functionality to the substrate surface, as we thoroughly described in

Chapter 2. Silanization reactions are usually performed using organic solvents such as toluene, with reaction temperatures ranging from room temperature to 100 °C approximately. Oxidized silicon surfaces are often silanized with trialkoxy silanes, as they generate more stable layers than the corresponding mono- and chloro-silanes.

Schematically, the mechanism of monolayer formation is considered to proceed in four steps [13], which are depicted in Figure 4.1: 1) hydrolysis of the alkoxy- or chlorine- chains, favored in an acidic environment; 2) condensation of the generated silanols (Si-O-H) forming non-ramified polysiloxane chains, favored in basic ambient; 3) formation of hydrogen bonds with the surface hydroxyls; 4) final anchoring of the silane to the surface.

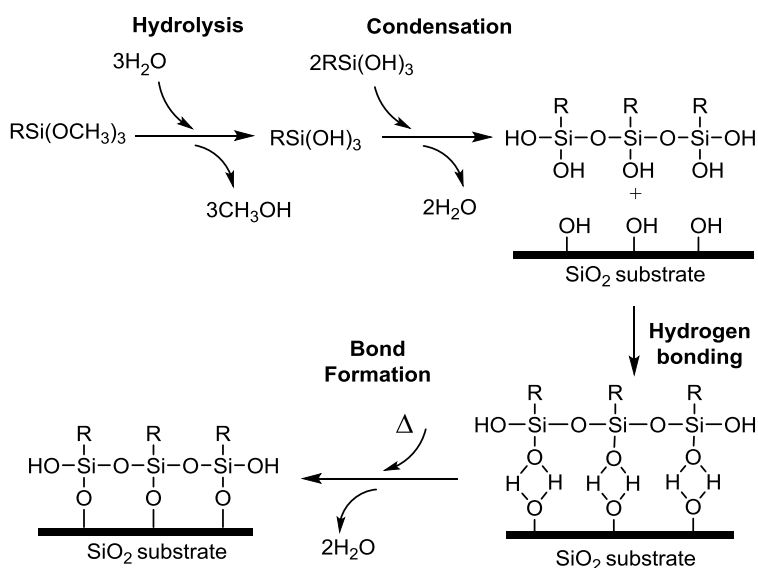


**Figure 4.1.** Reaction and bonding mechanism of alkoxy silanes. Adapted from reference [13].

These processes, though, are hard to evidence and strongly dependent on the nature of the radicals. Hence, the reactivity of alkoxy groups to

hydrolysis decreases with an increasing number of carbon atoms due to steric hindrance factors, leading to incomplete reactions [13]. Likewise, the condensation may turn into disordered oligomerization forming non-covalently bonded aggregates on the surface, especially as the number of alkoxy groups increase. An additional challenge in silanization is optimizing the amount of water in the reaction ambient, as the deposition technique is very sensitive to ambient humidity conditions, particularly considering that the surface of any oxide is always highly hydrophobic [14-16]. In absence of water no hydrolysis occurs and that results in the formation of an incomplete monolayer [17], but an overabundance of water may favor the disordered agglomeration and oligomerization [18-20]. Other parameters that have been shown to influence the degree of hydrolysis and condensation include number of alkoxy substituents [21], temperature [22], composition [23], time and concentration [24, 25], presence of water [26] and catalysts [27], condition of the surface [28] and finally the vapor-phase precursors [29-31].

It is for these reasons that much research has been undertaken to identify surface modification reactions that result in the formation of more stable functional SiO<sub>2</sub> surfaces, whilst still allowing for specific chemical functionality to be incorporated.

Aminosilanes are the most frequently used alkoxy silanes for the activation of surfaces since its terminal amino group is especially attractive for additional chemical modifications in the fields of biotechnology and biomedicine [3, 32-36]. Amongst the variety of existing aminosilanes, (3-aminopropyl)triethoxysilane (APTES) is one of the most common for the preparation of amine-terminated silicon [3]. It is relatively cheap and easy to essay, and its conjugation with silicon dioxide produces surfaces of

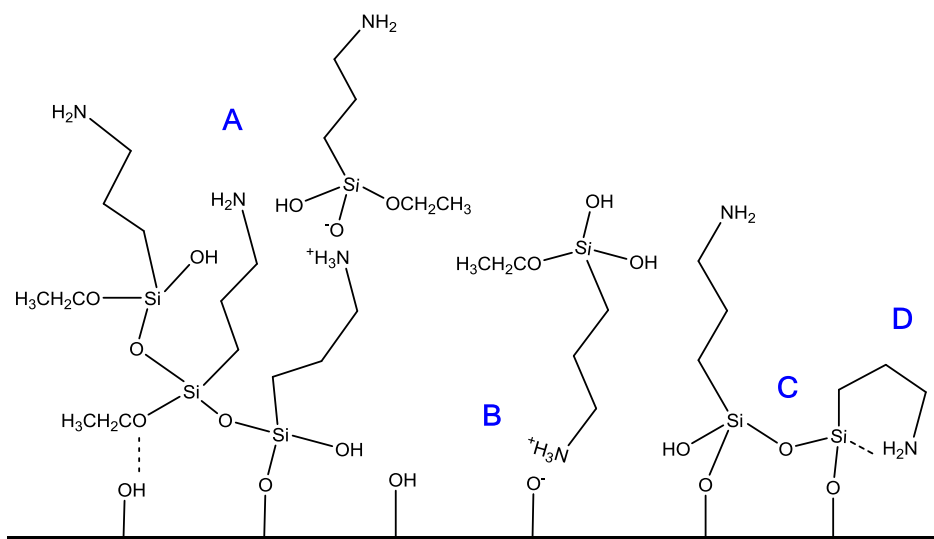


**Figure 4.2.** Schematic representation of the possible configurations for adsorbed APTES on oxidized silicon. A) APTES multilayer formation by reaction and/or interaction of dissolved silanes with the surface attached APTES; B) electrostatic attraction between the positive charged amino groups and negatively charged silicon surface amine; C) ethoxy groups are hydrolyzed to form siloxane linkages with surface silanols and to polymerize with neighboring silanes; D) hydrogen bonding between amines and surface silanols.

reproducible functional density and activity. However, the attachment site between amino groups and bioligands is often not regio-specific. And amino groups do not generally allow for direct conjugation of a bioligand. The binding between proteins or other probe biomolecules is usually performed either by non-covalent charge-charge interactions or via bifunctional crosslinkers [10, 37, 38]. Furthermore the basic character of the  $-NH_2$  group, which autocatalyzes the hydrolysis and condensation of APTES [39], prompts the reaction ambient to be as anhydrous as possible. Finally, an additional concern is that the amino groups form hydrogen bonds with surface silanols, alkoxy substituents and OH groups. Figure 4.2 summarizes some of these possible reactions and interactions that result in

a variety of configurations for an aminosilane layer. We can assert that the particular case of amino-silanes adds its own problematic to those of alkoxy-silanes, yielding layers (from mono- to multilayers) which are very disordered, rather unstable and poorly reproducible.

When using APTES, water not only influences the alkoxy group hydrolysis, but also the amine protonation, before and after grafting. There are an enormous number of studies dedicated to the optimization of the experimental conditions for APTES grafting. For instance, a pretreatment with triethylamine has been reported to double the dose of immobilized aminosilanes by enabling the direct nucleophilic attack of surface silanols onto APTES silicon atom in an anhydrous environment [39]. It has also been demonstrated that APTES in anhydrous organic solvents leads to layers predominantly grafted to the surface, while APTES in aqueous solutions provides multilayers of electrostatically bonded molecules, which are far less stable [19]. The influence of the solvent and curing treatment (water, ethanol, temperature) on the film thickness and functionality (the equilibrium between the terminal  $\text{NH}_2/\text{NH}_3^+$  groups in particular) has been thoroughly studied [40-42]. In addition, the effective availability of terminal  $-\text{NH}_2$  has been correlated with the reaction time, post-grafting thermal curing treatment, water content and silane precursor specie and concentration [40, 43-46]. More recently, the complexity of APTES reaction has been overcome by either obtaining an amino terminal group through the chemical modification of a bromine terminal functionality [47], or through vapor-phase grafting [15]. The ultimate topic about APTES involves its stability toward aqueous environments, which is particularly important for biological applications [15, 20].

Consequently, finding the optimum reaction conditions for preparing uniform thin films of aminosilanes is crucial for their successful use as surface coupling agents for applications in biotechnology and biomedicine.

#### ***4.1.2 Bioligand Conjugation to Amino-Functionalized Surfaces***

Bioligand conjugation is usually performed through a spacer that links the activated surface and the desired biomolecule. Other strategies for attaching biomolecules include the direct attachment to the surface without a crosslinker. However, this can result in a steric constraint of the protein's reactivity or a limited capability of interaction [48]. It has also been reported that the conformational changes in the protein can induce denaturation or alter the biological activity [49, 50]. These drawbacks can be minimized by introducing a crosslinker between the biomolecule and the reactive group on the surface. The linker characteristics can vary in chain length, functionality or charge, amongst others [10]. Thus a suitable choice of the molecule may potentially allow the attachment of any desired reactive group. Such crosslinkers are usually bifunctional, with equal or different terminal ends that are able to react with amine groups on surfaces generated as previously described.

One of the most common approaches to conjugate a biomolecule to an amino-functionalized surface involves the use of the coupler glutaraldehyde (GTA) [9, 34, 37, 51, 52]. The method offers a ubiquitous, inexpensive and flexible route for the biofunctionalization of silicon dioxide surfaces. GTA is a homobifunctional crosslinker with aldehyde groups at both ends with a 5-carbon chain spacer. GTA is highly reactive with amine groups at a neutral pH [53] and is more efficient than other aldehydes in generating thermally and chemically stable crosslinks [54]. Despite the widespread use of this reagent, crosslinking with GTA presents several

drawbacks. The simple structure of GTA is not indicative of the complexity of its possible reaction mechanisms. For instance, GTA can connect two neighboring aldehyde groups, thereby leading to undesired crosslinking or loss of the reactivity for further attachment of other biomolecules [10]. Moreover, the behavior of this molecule in aqueous environments is very complex and can exist as a dimer, trimer or polymer [52, 55]. The potential toxicity of GTA has also been reported [56].

Starting from an amine-terminated surface, the terminal  $\text{NH}_2$  group from the silane is transformed into an aldehyde prior to conjugation with bioligands. GTA-functionalized surfaces can react with proteins, antibodies, enzymes or amino-modified DNA via the covalent bond between the aldehyde and the amino groups present in the biomolecules [9, 10, 51, 57, 58]. In the particular case of proteins, the free amino groups is located in the lysine side chain [10]. The immobilization efficiency depends on a number of parameters including pH value, concentration and reaction time. However, the reaction is more or less spontaneous at physiological pH and between pH 7.0 and 9.0 it can be considered irreversible [52]. Glutaraldehyde activation of an amine-terminated surface has been found to yield significantly more biomolecule attachment than observed for either active ester or anhydride derivatized surfaces [51].

The reaction between amines (either in the silane layer or in the biomolecules) and aldehydes (i.e. those of GTA) ideally results in the formation of an imine bond with the elimination of a water molecule. This reaction has been typically proposed to follow a Schiff base mechanism upon nucleophilic attack (see Figure 4.3) [3]. However, Schiff bases do not present the remarkable stability under acidic conditions and extreme temperatures that proteins crosslinked with GTA exhibit, which has

motivated the investigation of alternative mechanisms [52, 59]. For instance, oligomeric or cyclic GTA derivatives may undergo vinyl addition reactions to create stable secondary amine bonds [52].

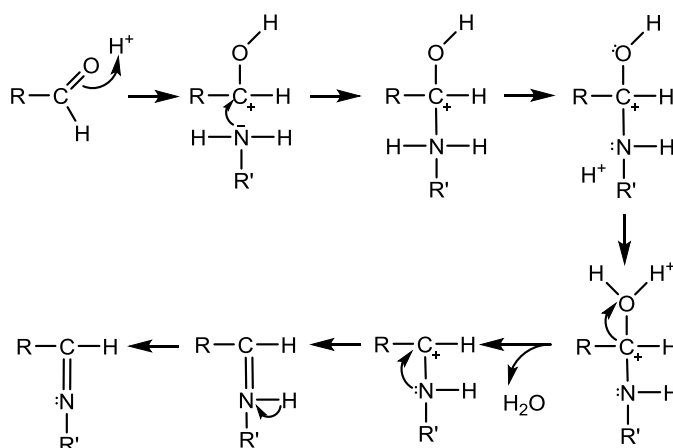


**Figure 4.3.** Schiff base reaction for the formation of imine bond from primary amines and aldehydes (adapted from reference [3]).

The pH value has been found to be a crucial factor in the reaction between amines and aldehydes. The APTES-functionalized silicon dioxide surfaces have an isoelectric point around pH 9 [60], which means most of the available  $\text{NH}_2$  are protonated at neutral pH and therefore the crosslinking reactions may be appreciably reduced [61]. By increasing the pH, more amino groups are available for the reaction with aldehydes but the polymerization of monomeric glutaraldehyde is also favored under alkaline pH [59]. Consequently, in order to obtain an optimized surface ready for bioconjugation, an acid or basic treatment to tailor the  $\text{NH}_2/\text{NH}_3^+$  functionality prior GTA coupling may be preferred over changing the medium pH.



## **4.2 Experimental**

### **4.2.1 Porous Silicon Sample Fabrication**

Vibrational investigation was performed onto nano porous silicon (nano-pSi) samples. Nano-pSi was fabricated on p-type (1 0 0) single-polished Si wafer with resistivity 11 – 16  $\Omega$  cm. The anodization was performed in aqueous hydrofluoric acid (HF, Sigma-Aldrich) solution (25%wt) for 1 h at a current density of 20 mA cm<sup>-2</sup>. These conditions provide a porous layer of a thickness around 20  $\mu$ m and average pore diameter of 5 nm (BET measurements). Prior to any functionalization with organic molecules, the samples underwent a light thermal treatment consisting in 1 h at 300 °C under nitrogen flux, followed by 1 h at 400 °C under dry air. Secondly, the amount of surface silanols were increased with a treatment in piranha (H<sub>2</sub>SO<sub>4</sub>:H<sub>2</sub>O<sub>2</sub> (30%wt) = 3:1) solution for 15 min at 80°C, followed by 10 min in aqueous (1 M) HNO<sub>3</sub> solution at room temperature. This step gives a high silanol surface coverage.

### **4.2.2 Silanization**

In view of previous reported works [18-20, 22, 62], we chose to perform surface silanization using an anhydrous organic solvent such as toluene thus avoiding the water-related oligomerization in liquid phase. We performed a series of post-treatments in aqueous solutions at pH 1 and pH 13 to maximize the hydrolysis and condensation reaction of the lateral alkoxy chains. Finally, a thermal treatment at 120 °C promotes desorption of water and non-covalently bonded molecules.

Samples were exposed to a 5 mM solution of the silane (e.g. APTES or MPTMS, Gelest) in anhydrous toluene. The reaction was allowed to proceed

for 3 h at 75 °C under nitrogen flux. At the end, the samples were washed with anhydrous toluene and ethanol, and dried under nitrogen. Afterwards, the samples underwent a post-treatment solution at pH 1 for 1 h in aqueous HCl 0.1 M, in order to assist the hydrolysis of lateral alkoxy chains. Their condensation in siloxo-bridges between vicinal grafted moieties was promoted by a treatment at pH 13 in NH<sub>4</sub>OH 0.1 M for 15 min [13]. Finally, the samples were thermally cured at 120 °C for 1 h.

Then, to compare the effect of the different terminal functionality, one sample underwent a treatment at pH 1 for 1 h to generate a positively charged aminosilated surface, then dried and thermally cured in an oven at 120 °C for 2 h.

#### **4.2.3 Glutaraldehyde Coupling**

Two different samples of APTES-functionalized pSi, one with NH<sub>2</sub> and another with NH<sub>3</sub><sup>+</sup> terminal groups, were used for GTA coupling. The reaction with glutaraldehyde was performed by exposure to 10% (v/v) solution in anhydrous ethanol (Electron Microscopy Sciences) for 30 min under N<sub>2</sub> atmosphere at room temperature. Similarly, the sample was post-treated with HCl and NH<sub>4</sub>OH, then thermally cured at 120 °C.

#### **4.2.4 Infrared Spectroscopy**

Infrared investigation was performed with a Bruker Vertex 70 (Bruker Optics), using a DTGS detector and operating in air. Each spectrum is the average of 1024 scans, collected in transmission geometry and recorded over the range 360–4500 cm<sup>-1</sup> with resolution of 4 cm<sup>-1</sup>. All the absorbance spectra were calculated using the spectrum of the empty chamber as reference, and applying both the air compensation correction and a 13-

points smoothing (Savitzky-Golay algorithm) available in OPUS software (Bruker Optics).

### **4.3 Results and Discussion**

Although most of the studies in the next Chapters are based on macroporous silicon and subsequent SiO<sub>2</sub> micropillars, electrochemically formed nano-pSi films were used for the optimization of the functionalization techniques. Due to the reduced size of its pores, nano-pSi offers a high surface area that makes it ideal for the surface chemistry investigation with transmission infrared spectroscopy. The combination of pore density, pore size and layer thickness of macro-pSi or SiO<sub>2</sub> micropillars endows them with a poor gain of internal area, being the magnifying factor between 50 and 90, which is far below the 10<sup>3</sup> factor that would provide a reliable signal in transmission geometry. Furthermore, the pore size and ordered arrangement of macropores are known to strongly reduce the transmitted infrared radiation above 1000 cm<sup>-1</sup> [63], which rules out the possibility to detect any vibrational absorption.

In nano-pSi, the combination of thickness and pore size provides a large internal area, as demonstrated by the intense clear cut absorptions due to surface silicon hydrides (Si-H<sub>x</sub> bending modes,  $\delta$ , at 600-700 cm<sup>-1</sup>, scissoring mode at 910 cm<sup>-1</sup>, stretching modes,  $\nu$ , at 2000-2150 cm<sup>-1</sup> in the IR spectrum after anodization (blue line, Figure 4.4), which makes the nanoporous samples useful also for very weak signals. After the light oxidation, the silicon hydride related peaks practically disappeared, while those related to SiO<sub>x</sub> are very intense ( $\delta$ (Si-O-Si) at 460 and 800 cm<sup>-1</sup>,  $\nu$ (Si-O) large band between 1000 and 1200 cm<sup>-1</sup> [64], black line in Figure 4.4), being the stretching absorption oversaturated. Since the oxidation is

performed via wet chemistry, the spectrum shows also a quite strong  $\nu(\text{O-H})$  band between  $2600$  and  $3800\text{ cm}^{-1}$ , related both to surface silanols and water absorbed therein, and the  $\delta(\text{H-O-H})$  mode due only to physisorbed water around  $1630\text{ cm}^{-1}$ . Considering that the thin silicon oxide is stable with respect to the silanization conditions, all these signals unavoidably appear also in the spectrum after the silanization, flattening the silane absorptions.

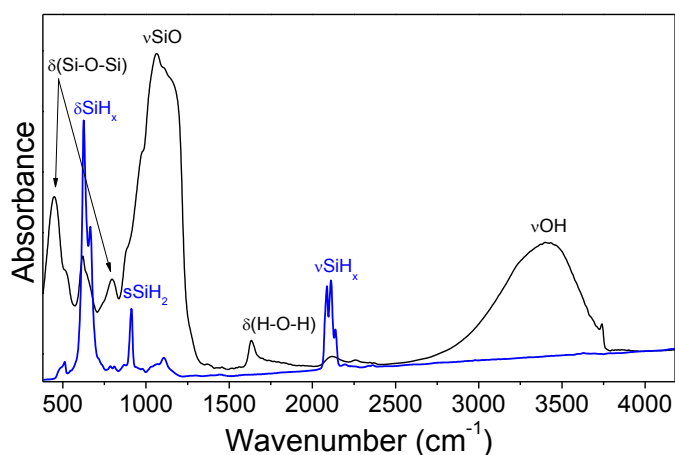


**Figure 4.4.** FT-IR transmission spectra of freshly anodized (blue line) and oxidized porous silicon (black line).

#### **4.3.1 Silanization with Mercapto- and Aminosilanes**

Figures 4.5A, B show the analytical regions for MPTMS and APTES respectively. In both cases the  $\nu\text{SiO}_x$  hides any absorptions below  $1250\text{ cm}^{-1}$ , and the stretching modes due to the propyl chain overlap with the broad  $\nu\text{OH}$  band. The  $-\text{SH}$  terminal group from the MPTMS molecule is easily recognizable by the sulphur-hydrogen stretching at  $2580\text{ cm}^{-1}$  (inset in Figure 4.5A, [65]), which falls in an otherwise clean region. However, the analysis of terminal  $-\text{NH}_2$  of the APTES molecule is considerably more complex. Since the  $\text{N-H}$  bond could participate in hydrogen bonds, its

absorptions could be broad depending on the environment (degree of molecular condensation, physisorbed water, available -OH groups). In addition, both N-H stretching and bending modes overlap with the O-H ones. Finally, it must be taken into account the spontaneous formation of  $-\text{NH}_3^+ \cdots \text{HCO}_3^-$  groups when terminal primary amines react with atmospheric  $\text{CO}_2$  upon exposure to humid air [19, 42]. Figure 4.5B and the inset therein point to a mixed termination. The two very weak peaks at 3310 and 3375  $\text{cm}^{-1}$  fall in the regions where the symmetric and antisymmetric  $\nu\text{NH}_2$  have been reported for diluted solution [65]. On the other hand, the broad and poorly structured band between 1500 and 1700  $\text{cm}^{-1}$  contains at least three absorptions (1556, 1595 and 1670  $\text{cm}^{-1}$ ), beyond the one due to physisorbed water (centered at 1625  $\text{cm}^{-1}$ ), which resemble the N-H bending modes [65] (inset in Figure 4.5B).

Both APTES- and MPTMS-functionalized pSi spectra in Figure 4.5A and B show the  $\text{CH}_x$  stretching modes between 2850 and 2990  $\text{cm}^{-1}$ , although they are strongly distorted by the overlap with the broad  $\nu\text{OH}$  band. In the spectral region between 1200 and 1800  $\text{cm}^{-1}$  there are several bands related to the  $\text{CH}_x$  bending and scissoring modes. Between 1400 and 1470  $\text{cm}^{-1}$  at least three bands appear due to the aliphatic  $\text{CH}_x$  bending modes. The  $\text{CH}_2$  wagging bands in propyl chains are spread over the range of 1200-1400  $\text{cm}^{-1}$ .

### **4.3.2 Post-Silanization Treatments**

Although the presence of the terminal group and alkoxy chain features is often considered enough to claim the surface silanization, it is rather a necessary condition than a sufficient one. The occurrence of grafting is univocally demonstrated by the appearance of signals due to the newly-born bond between the surface atoms and the reactive site at the organic

molecules. The silanization of oxidized silicon rules out such a simple experimental evidence since the docking site is a silicon-oxygen bond whose IR absorptions do not differ from those of the underlying oxide layer. However, a successful silanization implies also a good hydrolysis and condensation of the lateral alkoxy-chains [66].

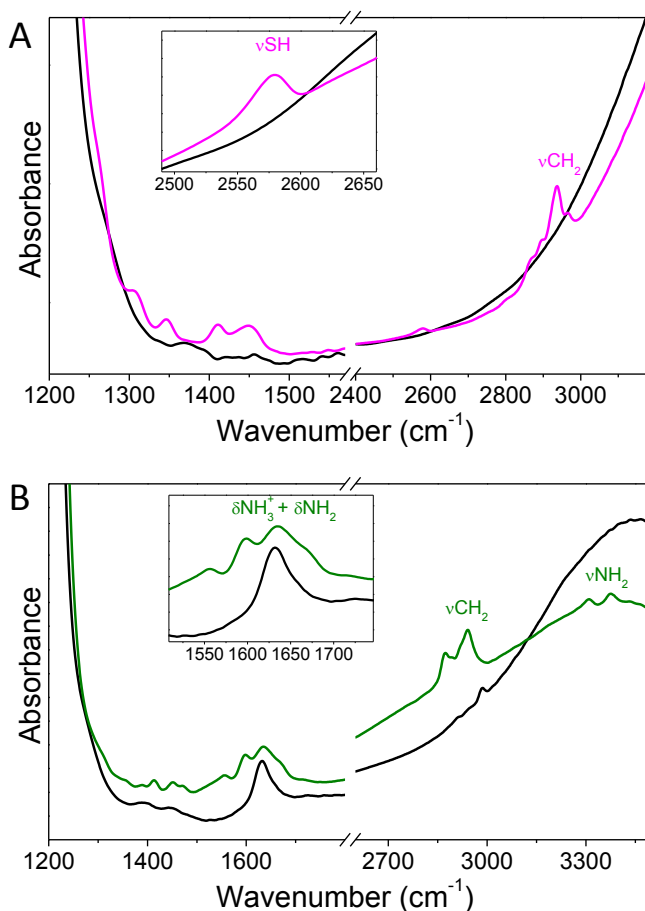


**Figure 4.5.** FT-IR transmission spectra of pSi samples at selected steps of the functionalization. A) HNO<sub>3</sub>-oxidized (black line) and MPTMS-functionalized (pink line) sample and B) HNO<sub>3</sub>-oxidized (black line) and APTES-functionalized (green line) sample. Insets shown in panels A and B are expanded along the x- and y-axes in the regions of most interest.

MPTMS molecule was employed to analyze the post-treatments effect on the hydrolysis and condensation of the lateral alkoxy chains. MPTMS, as a trimethoxysilane, was chosen over a triethoxysilane, such as APTES, because the great diversity of vibrational modes related to the multiple  $\text{CH}_x$  groups makes the spectroscopic analysis of the alkoxy chains of APTES particularly complex. For instance, the three hydrolysable ethoxy chains contain  $-\text{CH}_2$  groups whose vibration frequencies do not differ from those groups in the  $\text{NH}_2$  functional chain. Thus, the use of MPTMS is motivated by the possibility of monitoring the behavior of the hydrolysable methoxy chains by analyzing the  $-\text{CH}_3$  IR signal. Furthermore, the chemistry of the MPTMS molecule is well-known and the  $-\text{SH}$  terminal group is very stable [67, 68].

An acid post-treatment at pH 1 was applied to assist the hydrolysis of the lateral chain  $-\text{OCH}_3$  chains [69]. The infrared evidence of this hydrolysis reaction cannot be found in the formation of new  $\text{Si}-\text{OH}$  bonds, since their IR characteristics of the  $\text{O}-\text{H}$  stretching are not different from those related to adsorbed water (broad band between 2600 and 3600  $\text{cm}^{-1}$ ). However, the signals related to the  $-\text{CH}_3$  group in the lateral chains are expected to disappear or at least decrease. The effect of the post-treatments in the grafted MPTMS layer can be explained from Figure 4.6. The comparison between the spectrum after MPTMS grafting (Figure 4.6, pink line) and subsequent post-treatment at pH 1 (Figure 4.6, green line) show that the silane layer is slightly altered by the treatment. The second derivative analysis [70] shown in Figure 4.6B makes more evident these differences. In the stretching region, the bands at 2852 and 2985  $\text{cm}^{-1}$  diminish their intensity, which can be assigned to symmetric and antisymmetric vibrations associated to the  $\nu\text{OCH}_3$  of the unhydrolyzed methoxy group [67]. Conversely, the aliphatic  $\text{CH}_2$  groups give rise to a

doublet at 2894 and 2937  $\text{cm}^{-1}$  that we assign to the  $\text{CH}_2$  symmetric and asymmetric stretching modes [67], respectively, and remain unaltered after post-treatment at pH 1.

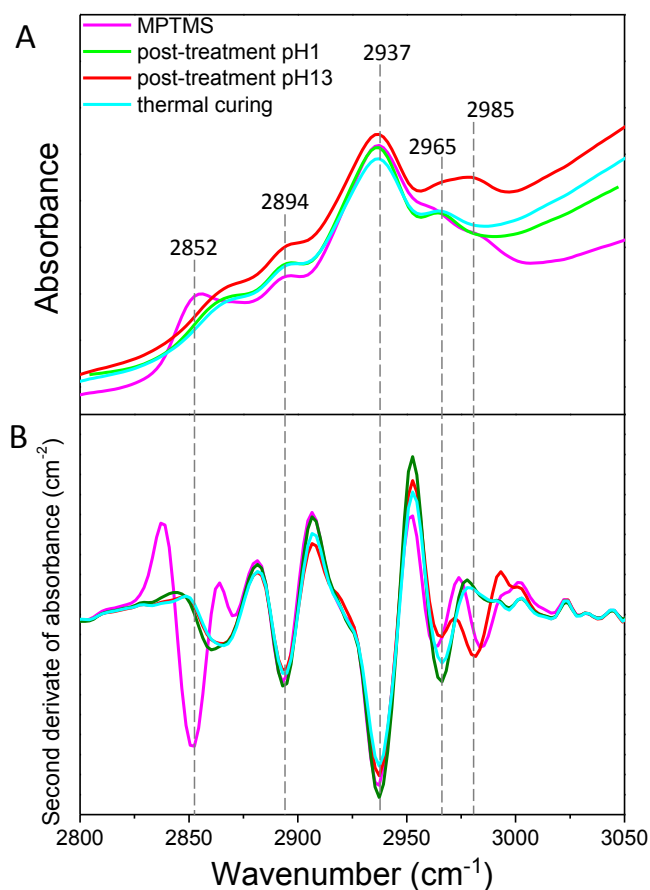


**Figure 4.6.** A) FT-IR transmission spectra and B) second derivative spectra of absorbance of a pSi sample in the C-H stretching region after MPTMS-functionalization (pink line), post-treatment at pH 1 (green line); post-treatment at pH 13 (red line) and thermal curing at 120  $^{\circ}\text{C}$  for 1 h (blue line). Absorption maxima appear as minima in the second derivatives

A condensation reaction between adjacent silanes is advantageous since the siloxane forms are more stable and less reactive than their silanol



precursors. The  $-OH$  broad band ( $2600-3800\text{ cm}^{-1}$ ) hides any significant decrease of absorption due to the loss of  $(Si)OH$  bonds. The second derivate spectrum (Figure 4.6, red line) shows an increase of a weak band at  $2985\text{ cm}^{-1}$  (assigned to the  $\nu(O)CH_3$ ), which might be due to the formation of methanol.

The state of the art advocates that curing the substrate surfaces after silanization process promotes cross-linking of adjacent silane molecules, reduces the susceptibility of hydrolysis and increases the stability of the modified surface [68]. Herein, the curing post-treatment caused a noticeable decrease in the peak at  $2985\text{ cm}^{-1}$  (see Figure 4.6, blue line).

The post-treatments effect on the APTES grafted molecule, apart from promoting the hydrolysis and condensation of the alkoxy chains, they were observed to alter the functionality of the silane layer. As we discussed in the previous section, the equilibrium  $NH_2/NH_3^+$  of the terminal amine yields a broad band between  $1500$  and  $1700\text{ cm}^{-1}$  related to the N-H bending modes, close to that of water located at  $1625\text{ cm}^{-1}$ . After the acid post treatment at pH 1, the bands centered at  $1556$  and  $1595\text{ cm}^{-1}$  reduced drastically its intensity, whereas a dominating vibrational mode arises at  $1515\text{ cm}^{-1}$ . The excess of  $H^+$  in the acid environment causes the protonation of the terminal  $-NH_2$  group, therefore we assign the band centered at  $1515\text{ cm}^{-1}$  to the symmetric  $-NH_3^+$  bending mode [22, 43]. The asymmetric  $-NH_3^+$  bending mode typically falls in the  $1610-1630\text{ cm}^{-1}$  region [22, 43], therefore overlapping with the broad, intense band at  $1625\text{ cm}^{-1}$  due to water. After a subsequent basic post-treatment at pH 13, the two vibrational modes previously observed at  $1556$  and  $1595\text{ cm}^{-1}$  arise again although with a reduced intensity. Thus, we relate them to the vibrational modes of the  $-NH_2$  terminal groups in the silane layer resulting from the

neutralization of  $-\text{NH}_3^+$  after basic post-treatment. The IR band at  $1595\text{ cm}^{-1}$  may be assigned to the  $\text{NH}_2$  bending mode [43]. The broad, poorly structured band centered at  $1556\text{ cm}^{-1}$  was considerably reduced in intensity after post-treatments. We assign this band to the  $\delta(\text{NH}_2)$  modes of amino groups with strong hydrogen bonding that may be coordinated to the Si atom in a cyclic structure (see Figure 4.3D) [43, 71]. The vibrational mode around  $1670\text{ cm}^{-1}$  that appeared after thermal treatment at  $120\text{ }^\circ\text{C}$  has been reported to be due to the formation of an imine terminal group upon the oxidation of an amine bicarbonate salt and its intensity is related to the film thickness [19]. The evident decrease in the bands intensity after post-treatment at pH 13 and thermal curing, compared to the initial APTES-functionalized sample, may be due to loss of non-covalently bonded APTES upon rinsing or thermal desorption.

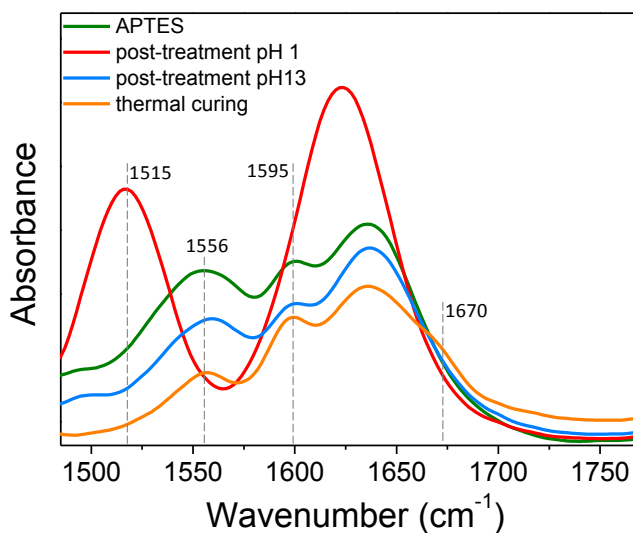


**Figure 4.7.** FT-IR transmission spectra in the N-H stretching region of a pSi sample after APTES functionalization (green line); post-treatment at pH 1 (red line); post-treatment at pH 13 (blue line) and thermal curing at  $120\text{ }^\circ\text{C}$  (yellow line).

### 4.3.3 Generation of Aldehyde Group Using Glutaraldehyde Linker

Once proved that APTES provides a good amino-functionalized surface and treatments affect the equilibrium between  $\text{-NH}_2$  and  $\text{-NH}_3^+$ , the next task is monitoring the functionalization of APTES-terminated surface with GTA linker for further biomolecule conjugation. The IR evidences of GTA successful docking on APTES can be easily drawn from Figure 4.8: (1) the IR absorptions related to the primary amine should change into those of a secondary amine, or into those of an imine group, depending on the degree of dehydration; (2) the signals related to the terminal aldehyde must appear; (3) the signals due to the propylic  $n\text{CH}_2$  should increase.

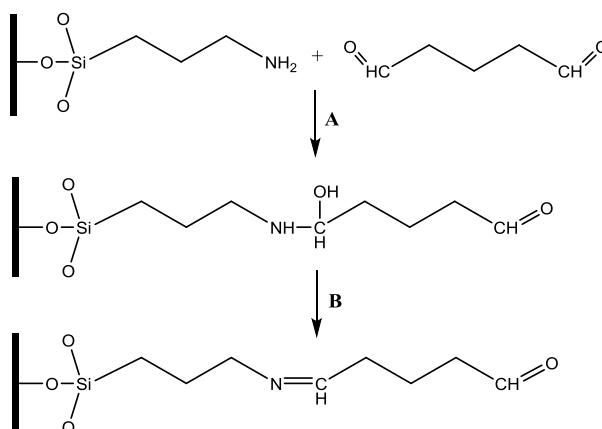


**Figure 4.8.** Schematic representation of the GTA reaction onto APTES. A) Partial dehydration of the primary amine into a secondary amine; B) complete dehydration of the secondary amine into an imine group.

The comparison between the spectrum after APTES-silanization and post-treatments (Figure 4.9, green line) and the subsequent reaction with GTA (Figure 4.9, orange line) shows that the weak absorptions at  $3310$  and  $3375\text{ cm}^{-1}$ , previously assigned to symmetric and antisymmetric  $\nu\text{NH}_2$ , extinguish, while a quite strong peak at  $1720\text{ cm}^{-1}$  appears. We assign it to

the stretching mode of the carbonyl, as we assign the weak, buried in the huge  $\nu\text{OH}$  band, absorption at  $2723\text{ cm}^{-1}$  to the aldehydic  $\nu\text{CH}$ . As far as the  $\nu\text{CH}_2$  signal is concerned, the overlap with the overwhelming  $-\text{OH}$  stretching band prevents any reliable calculation of its integral area, both before and after the reaction with GTA.

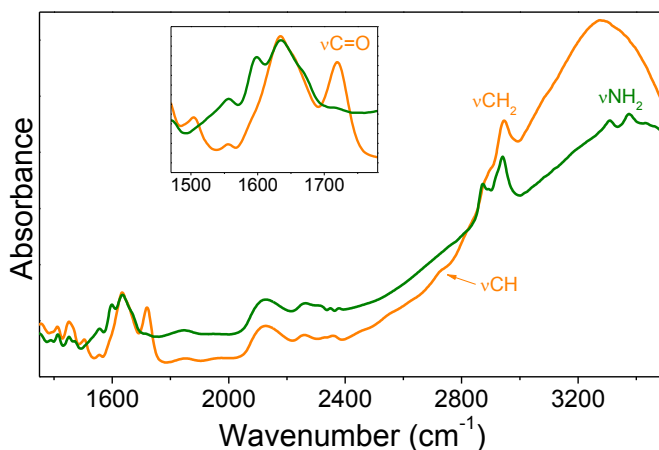


**Figure 4.9.** FT-IR transmission spectra of pSi samples after functionalization with APTES (green line) and subsequent GTA docking (orange line). Inset is expanded along the x- and y-axes in the region of most interest.

The effect of the different functional termination of the APTES layer on the GTA coupling was evaluated by performing the reaction either on  $-\text{NH}_2$  or  $-\text{NH}_3^+$  terminated surfaces. Two subsequent post-treatments at pH 1 then at pH 13 led to a mostly  $-\text{NH}_2$  terminated surface, characterized by the two bands centered at  $1556$  and  $1595\text{ cm}^{-1}$ , as shown in Figure 4.10A, green line. A following acid post-treatment in pH 1 introduced an  $-\text{NH}_3^+$  surface functionality, identified by the pronounced band centered at  $1515\text{ cm}^{-1}$ , as it can be seen in Figure 4.10B, green line.

The difference in GTA coupling between these surfaces mainly arises in the already overcrowded region where the bending modes of  $\text{NH}_2$  and  $\text{NH}_3^+$  are located. The IR analysis after GTA grafting onto  $-\text{NH}_2$  functional surfaces, shown in Figures 4.10A, C, resulted in the almost disappearance of the band centered at  $1595\text{ cm}^{-1}$ , which we assigned to  $\delta(\text{NH}_2)$ , and the arise of a peak at  $1720\text{ cm}^{-1}$ , originating from the  $\nu\text{C}=\text{O}$  mode. A presence of a shoulder around  $1667\text{ cm}^{-1}$  is assigned to the stretching mode of imine. Conversely, the GTA coupling onto  $-\text{NH}_3^+$  terminated surfaces generated the disappearance of the band at  $1515\text{ cm}^{-1}$ , associated to the symmetric  $-\text{NH}_3^+$  deformation mode (see Figure 4.10B, D, orange line). The characteristic  $\nu\text{C}=\text{O}$  mode from the aldehyde is present at  $1720\text{ cm}^{-1}$ . A band arises centered at  $1508\text{ cm}^{-1}$ , falling in the region of the secondary amine  $\delta\text{NH}$  ( $1490\text{-}1580\text{ cm}^{-1}$ ). In both surfaces, the peak at  $1556\text{ cm}^{-1}$  does not seem to significantly change after GTA grafting. We assigned this peak to  $\text{NH}_2$  hydrogen bond forming cyclic intramolecular structures, therefore impeding the availability of the amine for reaction with aldehyde groups.

Being these assignments correct, the charge of the APTES layer prior GTA attachment does not induce an alteration in the aldehyde functionality. However, the degree of dehydration in the bond formed between amines and glutaraldehyde is highly dependent on the of the APTES layer. The presence of imines is predominant in the GTA coupling on  $-\text{NH}_2$  terminated surfaces, whereas secondary amine signals dominate the spectrum after grafting on  $-\text{NH}_3^+$  terminated surfaces.

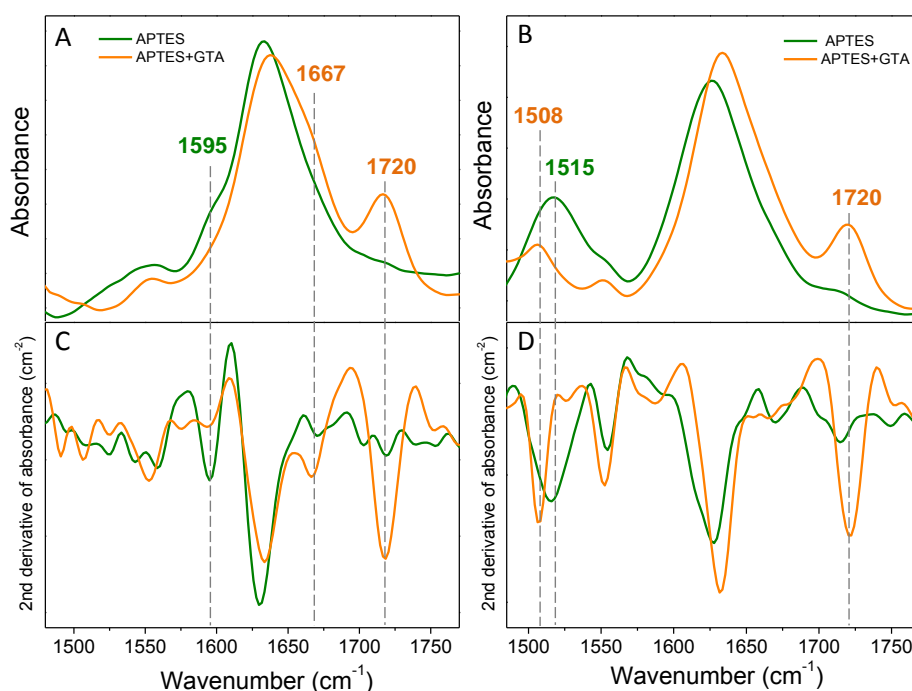


**Figure 4.10.** FT-IR transmission spectra (A, B) and second derivative spectra of absorbance (C, D) of GTA functionalization of amino-terminated surfaces after post-treatment at pH 13 (A, C) and at pH 1 (B, D).

#### 4.4. Conclusions

Oxidized pSi samples were modified via silanol chemistries and investigated using IR to obtain optimized surfaces for upcoming bioligand conjugations. Nano-pSi was fabricated by electrochemical etching in order to obtain a high surface area that enhances the signal gain in transmission FT-IR spectroscopy. Two different trialkoxysilanes were used: MPTMS and APTES. Anhydrous environments and elevated temperatures ( $\sim 75$  °C) were chosen to avoid silane oligomerization. Results for the MPTMS surface reaction showed that an acid post-treatment encourages the hydrolysis of the methoxy groups; then a basic post-treatment and thermal

curing promotes the crosslink through the formation of siloxane bonds and the desorption of non-covalently bonded, without loss of the thiol functionality. Post-treatments on APTES-functionalized samples not only affected the hydrolysis and condensation of the ethoxy chains, but also the equilibrium between the terminal functionality  $-NH_2$  and  $-NH_3^+$ . The protonation of the functional group plays a key role in subsequent coupling. Our data indicated that the glutaraldehyde crosslinking is affected by the charge of the APTES layer. The covalent bond formed between amines and aldehydes is mostly an imine when starting from a  $-NH_2$  terminated surface, whereas secondary amine bonds were observed if starting from  $-NH_3^+$  terminated samples. These results provide valuable knowledge on the  $SiO_2$  surface reactions. The optimization of these chemical modifications enables the use of oxidized pSi surfaces in various applications that require bioconjugation properties.

## 4.5 References

- [1] Biju, V., *Chemical modifications and bioconjugate reactions of nanomaterials for sensing, imaging, drug delivery and therapy*. Chemical Society Reviews, 2014. **43**(3): p. 744-764.
- [2] Canham, L.T., *Bioactive silicon structure fabrication through nanoetching techniques*. Advanced Materials, 1995. **7**(12): p. 1033-1037.
- [3] Rother, D., T. Sen, D. East, and I.J. Bruce, *Silicon, silica and its surface patterning/activation with alkoxy- and amino-silanes for nanomedical applications*. Nanomedicine, 2011. **6**(2): p. 281-300.
- [4] Malvindi, M.A., V. Brunetti, G. Vecchio, A. Galeone, R. Cingolani, and P.P. Pompa, *SiO<sub>2</sub> nanoparticles biocompatibility and their potential for gene delivery and silencing*. Nanoscale, 2012. **4**(2): p. 486-495.
- [5] Gomez-Vega, J.M., A. Hozumi, E. Saiz, A.P. Tomsia, H. Sugimura, and O. Takai, *Bioactive glass-mesoporous silica coatings on Ti6Al4V through enameling and triblock-copolymer-templated sol-gel processing*. Journal of Biomedical Materials Research, 2001. **56**(3): p. 382-389.
- [6] Banerjee, I., R.C. Pangule, and R.S. Kane, *Antifouling Coatings: Recent Developments in the Design of Surfaces That Prevent Fouling by Proteins, Bacteria, and Marine Organisms*. Advanced Materials, 2011. **23**(6): p. 690-718.
- [7] Ding, L. and H. Ju, *Biofunctionalization of nanoparticles for cytosensing and cell surface carbohydrate assay*. Journal of Materials Chemistry, 2011. **21**(45): p. 18154-18173.
- [8] Rimola, A., D. Costa, M. Sodupe, J.-F. Lambert, and P. Ugliengo, *Silica Surface Features and Their Role in the Adsorption of Biomolecules: Computational Modeling and Experiments*. Chemical Reviews, 2013. **113**(6): p. 4216-4313.
- [9] Treccani, L., T. Yvonne Klein, F. Meder, K. Pardun, and K. Rezwan, *Functionalized ceramics for biomedical, biotechnological and environmental applications*. Acta Biomaterialia, 2013. **9**(7): p. 7115-7150.
- [10] Jonkheijm, P., D. Weinrich, H. Schröder, C.M. Niemeyer, and H. Waldmann, *Chemical Strategies for Generating Protein Biochips*. Angewandte Chemie International Edition, 2008. **47**(50): p. 9618-9647.
- [11] Witucki, G.L., *A silane primer: chemistry and applications of alkoxy silanes*. Journal of coatings technology, 1993. **65**: p. 57-57.
- [12] Han, Y., D. Mayer, A. Offenhäusser, and S. Ingebrandt, *Surface activation of thin silicon oxides by wet cleaning and silanization*. Thin Solid Films, 2006. **510**(1-2): p. 175-180.
- [13] Arkles, B., J.R. Steinmetz, J. Zazyczny, and P. Mehta, *Factors contributing to the stability of alkoxy silanes in aqueous solution*. J. Adhes. Sci. Technol., 1992. **6**(1): p. 193-206.
- [14] Silberzan, P., L. Leger, D. Ausserre, and J.J. Benattar, *Silanation of silica surfaces. A new method of constructing pure or mixed monolayers*. Langmuir, 1991. **7**(8): p. 1647-1651.



- [15] Zhu, M., M.Z. Lerum, and W. Chen, *How To Prepare Reproducible, Homogeneous, and Hydrolytically Stable Aminosilane-Derived Layers on Silica*. Langmuir, 2011. **28**(1): p. 416-423.
- [16] Tripp, C.P. and M.L. Hair, *Reaction of Methylsilanols with Hydrated Silica Surfaces: The Hydrolysis of Trichloro-, Dichloro-, and Monochloromethylsilanes and the Effects of Curing*. Langmuir, 1995. **11**(1): p. 149-155.
- [17] Engelhardt, H. and P. Orth, *Alkoxy Silanes for the Preparation of Silica Based Stationary Phases with Bonded Polar Functional Groups*. Journal of Liquid Chromatography, 1987. **10**(8-9): p. 1999-2022.
- [18] Caravajal, G.S., D.E. Leyden, G.R. Quinting, and G.E. Maciel, *Structural characterization of (3-aminopropyl)triethoxysilane-modified silicas by silicon-29 and carbon-13 nuclear magnetic resonance*. Analytical Chemistry, 1988. **60**(17): p. 1776-1786.
- [19] Kim, J., P. Seidler, L.S. Wan, and C. Fill, *Formation, structure, and reactivity of amino-terminated organic films on silicon substrates*. Journal of Colloid and Interface Science, 2009. **329**(1): p. 114-119.
- [20] Asenath Smith, E. and W. Chen, *How To Prevent the Loss of Surface Functionality Derived from Aminosilanes*. Langmuir, 2008. **24**(21): p. 12405-12409.
- [21] Fadeev, A.Y. and T.J. McCarthy, *Self-Assembly Is Not the Only Reaction Possible between Alkyltrichlorosilanes and Surfaces: Monomolecular and Oligomeric Covalently Attached Layers of Dichloro- and Trichloroalkylsilanes on Silicon*. Langmuir, 2000. **16**(18): p. 7268-7274.
- [22] Pasternack, R.M., S. Rivillon Amy, and Y.J. Chabal, *Attachment of 3-(Aminopropyl)triethoxysilane on Silicon Oxide Surfaces: Dependence on Solution Temperature*. Langmuir, 2008. **24**(22): p. 12963-12971.
- [23] Cao, C., A.Y. Fadeev, and T.J. McCarthy, *Reactions of Organosilanes with Silica Surfaces in Carbon Dioxide*. Langmuir, 2001. **17**(3): p. 757-761.
- [24] Stanford, C.J., M. Dagenais, J.-H. Park, and P. DeShong, *Real-Time Monitoring of Siloxane Monolayer Film Formation on Silica Using a Fiber Bragg Grating*. Current Analytical Chemistry, 2008. **4**(4): p. 356-361.
- [25] Aissaoui, N., L. Bergaoui, J. Landoulsi, J.-F. Lambert, and S. Boujday, *Silane Layers on Silicon Surfaces: Mechanism of Interaction, Stability, and Influence on Protein Adsorption*. Langmuir, 2011. **28**(1): p. 656-665.
- [26] Krasnoslobodtsev, A.V. and S.N. Smirnov, *Effect of Water on Silanization of Silica by Trimethoxysilanes*. Langmuir, 2002. **18**(8): p. 3181-3184.
- [27] Li, H.-L., A.-P. Fu, D.-S. Xu, Guo, L.-L. Gui, and Y.-Q. Tang, *In Situ Silanization Reaction on the Surface of Freshly Prepared Porous Silicon*. Langmuir, 2002. **18**(8): p. 3198-3202.
- [28] Le Grange, J.D., J.L. Markham, and C.R. Kurkjian, *Effects of surface hydration on the deposition of silane monolayers on silica*. Langmuir, 1993. **9**(7): p. 1749-1753.
- [29] Diebold, R.M. and D.R. Clarke, *Smooth, Aggregate-Free Self-Assembled Monolayer Deposition of Silane Coupling Agents on Silicon Dioxide*. Langmuir, 2012. **28**(44): p. 15513-15520.

- [30] Dorvel, B., B. Reddy, I. Block, P. Mathias, S.E. Clare, B. Cunningham, D.E. Bergstrom, and R. Bashir, *Vapor-Phase Deposition of Monofunctional Alkoxysilanes for Sub-Nanometer-Level Biointerfacing on Silicon Oxide Surfaces*. *Advanced Functional Materials*, 2010. **20**(1): p. 87-95.
- [31] Hussein, G.A., J. Peacock, A. Sathyapalan, L.W. Zilch, M.C. Asplund, E.T. Sevy, and M.R. Linford, *Alkyl monolayers on silica surfaces prepared using neat, heated dimethylmonochlorosilanes with low vapor pressures*. *Langmuir*, 2003. **19**(12): p. 5169-5171.
- [32] Li, H., J. Zhang, X. Zhou, G. Lu, Z. Yin, G. Li, T. Wu, F. Boey, S.S. Venkatraman, and H. Zhang, *Aminosilane Micropatterns on Hydroxyl-Terminated Substrates: Fabrication and Applications*. *Langmuir*, 2009. **26**(8): p. 5603-5609.
- [33] Tanaka, M., T. Sawaguchi, M. Kuwahara, and O. Niwa, *Surface Modification of Silicon Oxide with Trialkoxysilanes toward Close-Packed Monolayer Formation*. *Langmuir*, 2013. **29**(21): p. 6361-6368.
- [34] Baranowska, M., A.J. Slota, P.J. Eravuchira, G. Macias, E. Xifré-Pérez, J. Pallares, J. Ferré-Borrull, and L.F. Marsal, *Protein attachment to nanoporous anodic alumina for biotechnological applications: Influence of pore size, protein size and functionalization path*. *Colloids and Surfaces B: Biointerfaces*, 2014. **122**(0): p. 375-383.
- [35] Lee, Y., S. Park, J. Park, and W.G. Koh, *Micropatterned assembly of silica nanoparticles for a protein microarray with enhanced detection sensitivity*. *Biomedical microdevices*, 2010. **12**(3): p. 457-64.
- [36] Wang, Y., W. Shi, W. Song, L. Wang, X. Liu, J. Chen, and R. Huang, *Tumor cell targeted delivery by specific peptide-modified mesoporous silica nanoparticles*. *Journal of Materials Chemistry*, 2012. **22**(29): p. 14608-14616.
- [37] Gunda, N.S.K., M. Singh, L. Norman, K. Kaur, and S.K. Mitra, *Optimization and characterization of biomolecule immobilization on silicon substrates using (3-aminopropyl)triethoxysilane (APTES) and glutaraldehyde linker*. *Applied Surface Science*, 2014. **305**(0): p. 522-530.
- [38] Trépout, S., S. Mornet, H. Benabdelhak, A. Ducruix, A.R. Brisson, and O. Lambert, *Membrane Protein Selectively Oriented on Solid Support and Reconstituted into a Lipid Membrane*. *Langmuir*, 2007. **23**(5): p. 2647-2654.
- [39] Kanan, S.M., W.T.Y. Tze, and C.P. Tripp, *Method to Double the Surface Concentration and Control the Orientation of Adsorbed (3-Aminopropyl)dimethylethoxysilane on Silica Powders and Glass Slides*. *Langmuir*, 2002. **18**(17): p. 6623-6627.
- [40] Howarter, J.A. and J.P. Youngblood, *Optimization of Silica Silanization by 3-Aminopropyltriethoxysilane*. *Langmuir*, 2006. **22**(26): p. 11142-11147.
- [41] Kim, J., J. Cho, P.M. Seidler, N.E. Kurland, and V.K. Yadavalli, *Investigations of Chemical Modifications of Amino-Terminated Organic Films on Silicon Substrates and Controlled Protein Immobilization*. *Langmuir*, 2010. **26**(4): p. 2599-2608.
- [42] Vandenberg, E.T., L. Bertilsson, B. Liedberg, K. Uvdal, R. Erlandsson, H. Elwing, and I. Lundström, *Structure of 3-aminopropyl triethoxy silane on*

- silicon oxide*. Journal of colloid and interface science, 1991. **147**(1): p. 103-118.
- [43] Okabayashi, H., I. Shimizu, E. Nishio, and C.J.O. Connor, *Diffuse reflectance infrared Fourier transform spectral study of the interaction of 3-aminopropyltriethoxysilane on silica gel. Behavior of amino groups on the surface*. Colloid and Polymer Science, 1997. **275**(8): p. 744-753.
- [44] Kim, J., G.J. Holinga, and G.A. Somorjai, *Curing Induced Structural Reorganization and Enhanced Reactivity of Amino-Terminated Organic Thin Films on Solid Substrates: Observations of Two Types of Chemically and Structurally Unique Amino Groups on the Surface*. Langmuir, 2011. **27**(9): p. 5171-5175.
- [45] Moon, J.H., J.W. Shin, S.Y. Kim, and J.W. Park, *Formation of Uniform Aminosilane Thin Layers: An Imine Formation To Measure Relative Surface Density of the Amine Group*. Langmuir, 1996. **12**(20): p. 4621-4624.
- [46] Zhang, F., K. Sautter, A.M. Larsen, D.A. Findley, R.C. Davis, H. Samha, and M.R. Linford, *Chemical Vapor Deposition of Three Aminosilanes on Silicon Dioxide: Surface Characterization, Stability, Effects of Silane Concentration, and Cyanine Dye Adsorption*. Langmuir, 2010. **26**(18): p. 14648-14654.
- [47] Haensch, C., S. Hoeppener, and U.S. Schubert, *Chemical modification of self-assembled silane based monolayers by surface reactions*. Chemical Society Reviews, 2010. **39**(6): p. 2323-34.
- [48] Gray, J.J., *The interaction of proteins with solid surfaces*. Current Opinion in Structural Biology, 2004. **14**(1): p. 110-115.
- [49] Baugh, L. and V. Vogel, *Structural changes of fibronectin adsorbed to model surfaces probed by fluorescence resonance energy transfer*. Journal of Biomedical Materials Research Part A, 2004. **69A**(3): p. 525-534.
- [50] Norde, W. and T. Zoungrana, *Surface-induced changes in the structure and activity of enzymes physically immobilized at solid/liquid interfaces*. Biotechnology and Applied Biochemistry, 1998. **28**(2): p. 133-143.
- [51] Ducker, R.E., M.T. Montague, and G.J. Leggett, *A comparative investigation of methods for protein immobilization on self-assembled monolayers using glutaraldehyde, carbodiimide, and anhydride reagents*. Biointerphases, 2008. **3**(3): p. 59-65.
- [52] Migneault, I., C. Dartiguenave, M.J. Bertrand, and K.C. Waldron, *Glutaraldehyde: behavior in aqueous solution, reaction with proteins, and application to enzyme crosslinking*. Biotechniques, 2004. **37**(5): p. 790-806.
- [53] Okuda, K., I. Urabe, Y. Yamada, and H. Okada, *Reaction of glutaraldehyde with amino and thiol compounds*. Journal of Fermentation and Bioengineering, 1991. **71**(2): p. 100-105.
- [54] Nimni, M.E., D. Cheung, B. Strates, M. Kodama, and K. Sheikh, *Chemically modified collagen: A natural biomaterial for tissue replacement*. Journal of Biomedical Materials Research, 1987. **21**(6): p. 741-771.
- [55] Hermanson, G.T., *Bioconjugate techniques*. 2013: Academic press.
- [56] Gough, J.E., C.A. Scotchford, and S. Downes, *Cytotoxicity of glutaraldehyde crosslinked collagen/poly(vinyl alcohol) films is by the mechanism of apoptosis*. Journal of Biomedical Materials Research, 2002. **61**(1): p. 121-130.

- [57] Wang, Q., B. Zhang, X. Lin, and W. Weng, *Hybridization biosensor based on the covalent immobilization of probe DNA on chitosan-mutiwalled carbon nanotubes nanocomposite by using glutaraldehyde as an arm linker*. *Sensors and Actuators B: Chemical*, 2011. **156**(2): p. 599-605.
- [58] Betancor, L., H.R. Luckarift, J.H. Seo, O. Brand, and J.C. Spain, *Three-dimensional immobilization of  $\beta$ -galactosidase on a silicon surface*. *Biotechnology and Bioengineering*, 2008. **99**(2): p. 261-267.
- [59] Wine, Y., N. Cohen-Hadar, A. Freeman, and F. Frolow, *Elucidation of the mechanism and end products of glutaraldehyde crosslinking reaction by X-ray structure analysis*. *Biotechnology and bioengineering*, 2007. **98**(3): p. 711-718.
- [60] Wu, Z., H. Xiang, T. Kim, M.-S. Chun, and K. Lee, *Surface properties of submicrometer silica spheres modified with aminopropyltriethoxysilane and phenyltriethoxysilane*. *Journal of colloid and interface science*, 2006. **304**(1): p. 119-124.
- [61] Farris, S., J. Song, and Q. Huang, *Alternative Reaction Mechanism for the Cross-Linking of Gelatin with Glutaraldehyde*. *Journal of Agricultural and Food Chemistry*, 2009. **58**(2): p. 998-1003.
- [62] Yadav, A.R., R. Sriram, J.A. Carter, and B.L. Miller, *Comparative study of solution-phase and vapor-phase deposition of aminosilanes on silicon dioxide surfaces*. *Materials Science and Engineering: C*, 2014. **35**(0): p. 283-290.
- [63] Garín, M., T. Trifonov, A. Rodríguez, L.F. Marsal, and R. Alcubilla, *Optical properties of 3D macroporous silicon structures*. *Materials Science and Engineering: B*, 2008. **149**(3): p. 275-280.
- [64] Lau, W., *Infrared characterization for microelectronics*. 1999: World scientific.
- [65] Socrates, G., *Infrared and Raman characteristic group frequencies: tables and charts*. 2001: Wiley Chichester.
- [66] Arkles, B., J.R. Steinmetz, J. Zazyczny, and P. Mehta, *Factors contributing to the stability of alkoxy silanes in aqueous solution*. *Journal of Adhesion Science and Technology*, 1992. **6**(1): p. 193-206.
- [67] Kurth, D.G. and T. Bein, *Surface reactions on thin layers of silane coupling agents*. *Langmuir*, 1993. **9**(11): p. 2965-2973.
- [68] Vistas, C.R., A.C.P. Águas, and G.N.M. Ferreira, *Silanization of glass chips—A factorial approach for optimization*. *Applied Surface Science*, 2013. **286**(0): p. 314-318.
- [69] Thompson, W.R. and J.E. Pemberton, *Surface Raman scattering of self-assembled monolayers of (3-mercaptopropyl)trimethoxysilane on silver: orientational effects of hydrolysis and condensation reactions*. *Chemistry of Materials*, 1993. **5**(3): p. 241-244.
- [70] Whitbeck, M.R., *Second Derivative Infrared Spectroscopy*. *Applied Spectroscopy*, 1981. **35**(1): p. 93-95.
- [71] Ishida, H., C.-h. Chiang, and J.L. Koenig, *The structure of aminofunctional silane coupling agents: 1.  $\gamma$ -Aminopropyltriethoxysilane and its analogues*. *Polymer*, 1982. **23**(2): p. 251-257.

UNIVERSITAT ROVIRA I VIRGILI

SILICON DIOXIDE MICROSTRUCTURES BASED ON MACROPOROUS SILICON FOR BIOMEDICAL APPLICATIONS.

María Alba Martín

Dipòsit Legal: T 153-2015

## ***Chapter 5***

---

### **Dual-Side Functionalization of Silicon Dioxide Hollow Micropillars**

In this chapter, we describe an approach for the fabrication and selective functionalization of the internal and external surfaces of high-aspect-ratio hollow silicon dioxide micropillar arrays. The strategy enables independent surface reactions with no cross-contamination. The dual-functionalization is carried out during the fabrication of the micropillars in four steps. First, a sample of macroporous silicon is prepared by electrochemical etching and then it is thermally oxidized to create a thin layer of silicon dioxide on the internal surface of the macropores. Next, the internal surface is functionalized with mercaptopropyl trimethoxysilane. Following, the micropillars are released anisotropically etching the backside of silicon wafers. Finally, the external surface of the micropillars is chemically modified in a multi-step biofunctionalization with aminopropyl triethoxysilane, glutaraldehyde and bovine serum albumin. The resulting structures are characterized by scanning electron microscopy and the surface reactions were confirmed by Fourier-transform infrared spectroscopy. The internal and external sides were photolabeled with tetramethyl rhodamine-5-maleimide and fluorescein isothiocyanate, respectively, and analyzed using fluorescence confocal microscopy. The peculiar three-dimensional geometry of the micropillars allows these double-active surfaces to be imaged at the same time.

## 5.1 Introduction

Three-dimensional (3D) micro- and nanostructures are promising systems for a wide range of applications in electronics [1, 2], photonics [3, 4] microfluidics [5, 6] and chemical and biological sensing [7, 8]. These 3D architectures can be fabricated in a variety of materials including silicon [9, 10], titania [11], silicon oxide [12], molybdenum alloy [13] and polymers [14, 15], and are mainly based on relatively expensive technologies such as plasma etching or reactive ion etching. In contrast, high-aspect-ratio silicon dioxide ( $\text{SiO}_2$ ) hollow micropillars can be obtained from macroporous silicon (macro-pSi) produced by the electrochemical etching of silicon [16-18]. Pre-patterned silicon wafers yield macropores in regular arrangements, whose geometrical characteristics can be tuned by modifying the anodization parameters. The ease to create a thin oxide layer allows the release of inverted structures such as hollow  $\text{SiO}_2$  micropillars or microtubes, as we described in Chapter 3.

The architecture and biocompatibility of the arrayed  $\text{SiO}_2$  micropillars point to applications in biotechnology and biomedicine. Arrays of micropillars can mimic the 3D-architected surrounding that cells experiment in their native environment [19]. The interaction between the micropillars array and the cell morphology eventually determines the cell response [20], thus making the study of *in vitro* cells as much similar as *in vivo*, increasing the reliability and reproducibility of all the in-vitro assays on microorganisms [21]. For instance, vertically aligned micropillars have been proposed to investigate the influence of topographical features on cell adhesion [22], spreading [23] and migration [24] mechanisms, and the mechanics of a single cell-substrate contact [25]. In addition, silicon dioxide is nontoxic and biodegradable [26]. The only degradation product of its



dissolution in aqueous media is orthosilicic acid, which is harmless for the body and can be excreted [27]. Based on this, silicon dioxide has been proposed as material in drug delivery [28], cell culture [29] or tissue engineering [30], as long as it is suitably surface-modified. In fact, SiO<sub>2</sub> itself has no chemical specificity towards target species, but it offers a flexible surface chemistry [31] to link interesting bioconjugators.

As far as micropillars are concerned, great attention has been put on their spatial organization when used as micro-architected substrate for cell capturing [24, 32-34], but less on their surface functionalization, though chemical interactions between the membrane and the environment affect the cell microfluidics as much as the topology of such environment [35]. In this Chapter, hollow SiO<sub>2</sub> micropillars are differently functionalized in both the external and internal surfaces without cross-contamination. The selective functionalization of nanometrically separated regions is of particular interest in the engineering of materials [36-40], but to the best of our knowledge it had not been performed in hollow micropillars prior this study.

The peculiar shape of hollow micropillar and its SiO<sub>2</sub> wall thickness (around 200 nm) allow both the internal and external sides to be monitored, at the same time, in fluorescence confocal microscopy over an area that can be as small as the size of one micropillar. This makes our micropillar layers even more attractive for potential applications in biology, since confocal microscopy that has gained popularity in recent years, being effective especially in the imaging of in-vitro living biological material [41, 42].

We chose to perform the optimized functionalization procedures detailed in Chapter 4, and standard photolabeling pathways—the internal surface was silanized with mercaptopropyl trimethoxysilane (MPTMS) and photolabeled with tetramethyl rhodamine-5-maleimide (rhodamine), whose maleimidic group reacts selectively with the thiol termination of the mercaptopropyl surface layer. The external surface was silanized with aminopropyl triethoxysilane (APTES), whose amine termination then underwent a reaction with glutaraldehyde (GTA); the third layer consisted in photolabeling with bovine serum albumin conjugated with fluorescein isothiocyanate (BSA-FITC): the amine groups on the outer shell of the protein react with the free  $\omega$ -aldehydes of the GTA layer. The silanizations and GTA docking were monitored by Fourier transform infrared (FTIR) spectroscopy. The photolabeled samples were investigated by confocal microscopy in fluorescent mode, demonstrating the occurrence of the docking reactions of rhodamine and BSA-FITC on their respective sides. Our approach leads to dual-side differentially derivatized micropillars, which opens up the possibility to conjugate an enhanced control on the interaction cell-substrate with the development of novel drug delivery systems. From a broader point of view, it is the first proof that a layer of dual-side differentially functionalized hollow micropillars can become a useful research device in biotechnology and biomedicine.

## **5.2 Experimental Section**

### **5.2.1 Fabrication of SiO<sub>2</sub> Micropillars**

**Macropore Formation.** Macro-pSi was fabricated by electrochemical etching, as described in Chapter 3 section 1.3. The starting material was a

p-type Si wafer of resistivity 40-60  $\Omega$  cm. In order to obtain periodically arranged pores, we applied the lithographic and indentation processes detailed in Chapter 3, section 1.2 with 4  $\mu\text{m}$  lattice constant. Macropores were grown perpendicular to the surface by electrochemical etching using HF(40%)/DMF 1:10 as electrolyte, under galvanostatic conditions (5 mA  $\text{cm}^{-2}$  current density). Given our experimental conditions, the pore growth rate was 0.85  $\mu\text{m min}^{-1}$ .

**Micropillar Releasing.** The process that leads to the release of bare micropillars is the one described in Chapter 3, section 2.1. After straight, regular macropores were formed, an approximately 250 nm thick  $\text{SiO}_2$  layer was grown by thermal oxidation at 1000  $^\circ\text{C}$  for 2 h in air. Then, the backside of the wafer was etched with buffered hydrofluoric acid (BHF, Sigma Aldrich). Finally, the silicon bulk was anisotropically etched in aqueous TMAH (Sigma Aldrich) (25%) at 85  $^\circ\text{C}$ .

**Scanning Electron Microscopy.** Macroporous silicon samples and the subsequent silicon dioxide micropillars were morphologically characterized by scanning electron microscopy (SEM) using a FEI Quanta 600 environmental scanning electron microscope (Hillsboro, OR, USA) operating at an accelerating voltage between 15 and 25 keV.

### 5.2.2 Functionalization

The dual-side functionalization of the micropillars required that the internal surface of the macropores undergoes silanization and photolabeling before the releasing of the micropillars, the bulk silicon acting as a protection for micropillar external surface (Figure 5.1A). Once the functionalization of the internal side was carried out (Figure 5.1B), the releasing of the micropillars was performed (Figure 5.1C). Then the

external surface was revealed and chemically modified following the APTES-GTA-BSA-FITC sequence (Figure 5.1D). In this final step the sample was mounted in a customized one-side Teflon reactor. It encases the macroporous side, protecting it from any further reaction, while lets the micropillar side exposed.

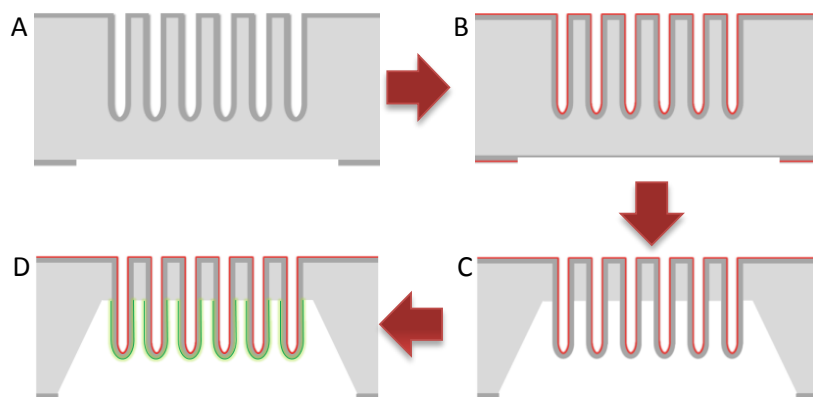


**Figure 5.1.** Schematic representation of the method for the dual-side functionalization. A) Macropore formation by electrochemical etching and masked BHF etch of the oxide layer on the wafer backside; B) functionalization of the internal side of the micropillars with MPTMS; C) TMAH anisotropic etching of the bulk silicon from the backside and D) functionalization of the external side of the released micropillars with APTES, GTA and BSA-FITC.

**Internal Functionalization.** The micropillar samples were functionalized following the optimized procedures described in Chapter 4, section 2. Here, briefly, oxidized macro-pSi was treated in potassium hydroxide (KOH) 0.1 M for 3 min and nitric acid (HNO<sub>3</sub>) 0.1 M for 10 min to ensure that the oxidized macro-pSi have a high silanol density surface [43]. Next, the samples were exposed to a 5 mM solution of MPTMS (Gelest) in anhydrous toluene [44] for 3 h. Samples were washed with anhydrous toluene and ethanol, and dried under nitrogen. Afterwards, the samples underwent 1 h

in aqueous HCl 0.1 M, in order to assist the hydrolysis of lateral  $-OCH_3$  chains. Their condensation in siloxo-bridges between vicinal grafted moieties was promoted by a treatment in  $NH_4OH$  0.1M for 15 min. Finally, the samples were thermally cured at 120 °C for 30 min. The internal surface was fluorescent-labeled using tetramethyl rhodamine-5-maleimide (Sigma Aldrich). The samples were placed for 1 h in rhodamine 100  $\mu g mL^{-1}$  in phosphate buffer saline (PBS, pH 7.4) solution, under ambient conditions. Finally, the samples were thoroughly washed with PBS and deionized water, and dried under a nitrogen flow.

**External Functionalization.** Following the same procedure outlined for the internal surface and detailed in Chapter 4, section 2, the external surface was hydroxylated and silanized in 5 mM solution of APTES (Gelest) in anhydrous toluene for 3 h at 75 °C. Afterwards, the samples were post-treated with hydrochloric acid (HCl) and ammonium hydroxide ( $NH_4OH$ ), and thermally cured. The reaction with glutaraldehyde was performed by exposure to 10% (v/v) solution in anhydrous ethanol (Electron Microscopy Sciences) for 30 min under  $N_2$  atmosphere at room temperature. The samples were rinsed in ethanol and dried with nitrogen. Finally, the samples were incubated with BSA-FITC (Sigma-Aldrich) 100  $\mu g mL^{-1}$  solution in PBS buffer (pH 7.4), for 2 h. The substrate was thoroughly washed with PBS buffer and dried with a nitrogen flow.

**Infrared Spectroscopy.** Infrared investigation was performed with a Bruker Vertex 70 (Bruker Optics), using a DTGS detector and operating in air with resolution of 4  $cm^{-1}$ . Vibrational investigation was performed onto nanoporous silicon (nano-pSi) samples.

Prior to any functionalization (carried out under the exact same conditions as for the micropillars), the samples underwent, first, a light thermal treatment consisting in 1 h at 300 °C under nitrogen flux, followed by 30 min at 400 °C under dry air. Then, the amount of surface silanols were increased with a treatment in piranha ( $\text{H}_2\text{SO}_4:\text{H}_2\text{O}_2$  (30%wt) = 3:1) solution for 15 min at 80 °C, followed by 10 min in aqueous (1 M)  $\text{HNO}_3$  solution at room temperature.

### **5.2.3 Fluorescence Confocal Microscopy**

The fluorescence images were acquired using a Nikon Eclipse TE2000-E inverted microscope, equipped with a C1 laser confocal system (EZ-C1 software, Nikon). 488 nm argon laser and 543 nm helium-neon laser were used as excitation sources for BSA-FITC and rhodamine, respectively. The emission was collected through the  $515 \pm 15$  bandpass emission filter, which gives the so-called green channel, and the  $590 \pm 30$  nm bandpass emission filter, which gives the red channel. All fluorescence images were captured using a 5-megapixel CCD.

## **5.3 Results and Discussion**

SEM was used to image the architectures of macropores and micropillars. The freshly anodized macro-pSi samples had a porosity of 25% with an average pore size of  $3.9 \mu\text{m}^2$ . Since the oxide layer grows in a conformal fashion, the released  $\text{SiO}_2$  micropillars maintain the ordering, the vertical uniformity and the shape of the initial macropores, i.e. rounded-squared sections and almost hemispherical tips (Figure 5.2A). The precision with which (1) the design is transferred from the porous layer to the micropillars, and (2) the micropillar protruding length is determined by

the reaction time in the TMAH solution, ensures that the final architecture can be quite finely tuned according to different requirements. This is an important characteristic of smart platforms for investigating cell behavior. Selecting smaller masks to pattern the backside oxide layer, micropillars arrays can be released inside microwells due to the selectivity of the TMAH etching process, as shown in Figure 5.2B. The dimensions of these microwells are easily adjustable by modifying the size of the mask and the etching time. Therefore, a large number of remarkably precise 3D structures can be fabricated on a single wafer to attain the spatial control of cells or proteins, for instance.

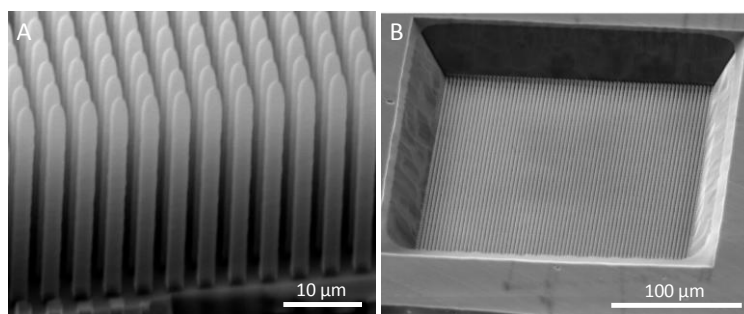


**Figure 5.2.** Tilted-view SEM micrographs of A) silicon dioxide micropillars arrays after TMAH etching of backside bulk silicon and B) microwell with released micropillars.

Infrared spectroscopy was used to confirm the functionalization of the micropillars. Nevertheless, a detailed characterization and optimization of the functionalization of silicon dioxide surface with silanes and GTA linker has been previously described in Chapter 4, section 3. Here, nano-pSi sample were used due to the limited surface area of macropores and micropillars for transmission FT-IR [45]. Nano-pSi was fabricated on p-type (1 0 0) single-polished Si wafer with resistivity 11 – 16  $\Omega$  cm etched at a 20 mA cm<sup>-2</sup> in aqueous HF (25%) solution for 1 h. However, the use of

nanoporous layers as a tool to monitor the surface functionalization was restricted to the small molecules involved in this work (silanes, glutaraldehyde), assuming that the nanometric size of the pores would have affected the surface reaction of the largest molecules (rhodamine, BSA-FITC). As consequence, the grafting of rhodamine and BSA-FITC was investigated only by fluorescence confocal microscopy.

Following same reaction procedures as those to chemically modify the internal surface of micropillars, samples silanized with MPTMS carry the -SH terminal groups which are recognizable by the sulphur-hydrogen stretching [46] at  $2580\text{ cm}^{-1}$ , as it can be seen from the FT-IR spectra shown in Figure 5.3A. Samples treated with APTES (as for the external side functionalization) presented two weak peaks around  $3310$  and  $3375\text{ cm}^{-1}$  the due to the symmetric and antisymmetric  $\text{NH}_2$  stretch modes of the amino groups [50] (see Figure 5.3B, line i). Both spectra show the stretching mode of the propylic methylenes ( $\nu\text{CH}_2$ ) between  $2800$  and  $3000\text{ cm}^{-1}$ . The GTA grafting onto APTES-functionalized was confirmed by the appearance of the characteristic bands in the range of  $1600$ - $1800\text{ cm}^{-1}$  related to the formation of amide bond between APTES and GTA (Figure 5.3B, line ii). The peak at  $1720\text{ cm}^{-1}$  corresponds to the carbonyl stretch group C=O group of the terminal aldehydes [46].

The final derivatization on both sides of the micropillars included a fluorescent dye to enable the characterization by confocal microscopy: rhodamine for the thiol-terminated internal surface, and BSA-FITC for the carbonyl-terminated external surface. These two fluorescent probes were selected because they are known to be excited at different wavelengths ( $543\text{ nm}$  for rhodamine,  $495\text{ nm}$  for BSA-FITC), and to emit at different wavelengths ( $575\text{ nm}$  for rhodamine,  $525\text{ nm}$  for BSA-FITC). By irradiating



the dual-side functionalized layer of hollow micropillars with the appropriate lasers, the collected emission contains contributions from both the surfaces—they can be visualized separately, switching the bandpass emission filter, or at the same time, relying on the fact that the emissions are different.

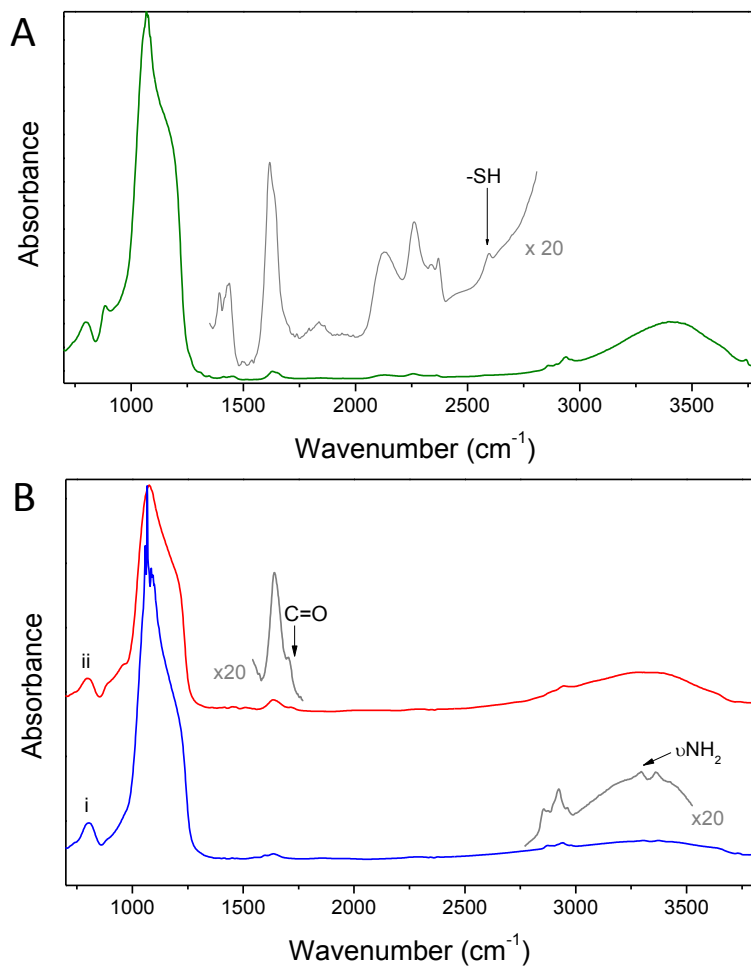


**Figure 5.3.** Transmission FT-IR spectra of functionalized nanoporous silicon samples A) after functionalization with MPTMS; B) after functionalization with APTES (i) and subsequent GTA docking (ii). Insets shown in panels A and B are expanded along the y-axes by 20 times in the regions of most interest.

In the first place, we imaged the frontside and backside of the arrays of hollow micropillars after single-side labeling. The micrograph shown in Figure 5.4A was collected exposing the labeled frontside to the laser excitation of 543 nm, using a  $590 \pm 30$  nm bandpass emission filter (red channel). Red squared-rings were observed reproducing the same pattern of the micropillars due to the rhodamine successfully attached to the micropillar internal surface (through the mercaptopropylsilane). In correspondence of each macropore, the confocal microscope collects the signal from all the rhodamine contained in the optical section (around  $1 \mu\text{m}$  thick) [47], thus the bright rings; in correspondence of the Si/SiO<sub>2</sub> bulk between macropores, the signal arrives only from the rhodamine grafted on the top flat surface, thus the black surrounding. Different intensities of the red rings suggest that the coverage degree may vary from pore to pore, sporadically being below the sensitivity of the confocal microscopy where the ring lacks. Likewise, when the labeled backside is excited with a 488 nm laser, and the emission collected through the  $515 \pm 15$  nm bandpass emission filter (green channel), strong green fluorescent rings appear (Figure 5.4B), deriving from the BSA-FITC immobilized onto the outer micropillars walls. The color intensity appeared more uniform than in case of rhodamine, suggesting that the coverage degree is more homogeneous on the external surface than on the internal surface. Those images in confocal microscope are the indirect support that the immobilization of the dyes has succeeded.

When the dual-side functionalization and subsequent labeling were performed, the fluorescence patterns from the inner and outer surfaces overlapped under the simultaneous excitation of 488 and 543 nm lasers, as shown in Figure 5.5A. The bright rings appeared in a range of intensities and colors (from green to yellow). Selecting the emission filter for

rhodamine (Figure 5.5B), we spotted that the more yellow-ish rings in Figure 5A are those in which emission of rhodamine is stronger. Figure 5C was collected selecting the emission filter for FITC. The comparison between Figure 5B and Figure 5C shows that under 488 nm excitation the emission of rhodamine in the green region is not negligible. Actually, the pattern of rhodamine in Figure 5B is repeated in Figure 5C, being the brighter green rings in correspondence to the brighter red rings. On reverse, the red emission from FITC is always negligible with respect to that from rhodamine. This emission overlap depends on the specific couple of fluorophores we chose, but it does not challenge the possibility to monitor at the same time what happens on both sides of the micropillars.

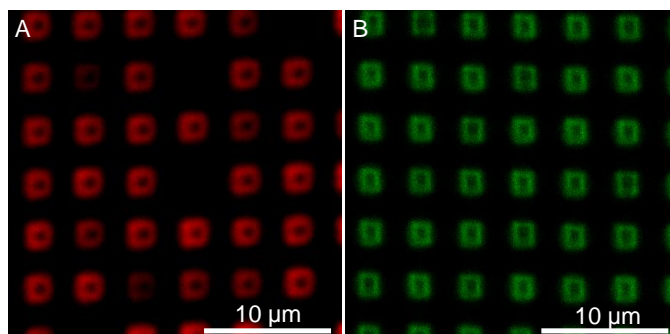


**Figure 5.4.** Top-view fluorescence images of micropillar arrays A) after the labeling of the sole internal surface with rhodamine, excitation laser at 543 nm, bandpass emission filter  $590 \pm 30$  nm; B) after the labeling of the sole external surface with BSA-FITC, excitation laser at 488 nm, bandpass emission filter  $515 \pm 15$  nm.

Figure 5.6 shows the fluorescent images of the longitudinal section of detached micropillars revealing a range of orange-ish to green-ish areas which correspondingly match the rhodamine inside the micropillar and the BSA-FITC outside. As it can be seen in Figure 5.6A, B, the very bottom of the pores (total length,  $150 \mu\text{m}$ ) were not functionalized, either with the

mercaptosilane or with the subsequent rhodamine. All the analyzed micropillar layers showed the same incomplete internal derivatization, which could depend on the macropore length. The white square frame on Figure 5.6B highlights a region of the sectioned wall where the two juxtaposed emission from the external BSA-FITC (green line on top) and the internal rhodamine (bright orange line below) are quite well separated. The faded orange region at the right-hand side of the square is the emission from the internal surface behind the section plane. We underline that the orange color is due to the fact that rhodamine under the simultaneous excitation of 488 and 543 nm lasers emits both in red and green.

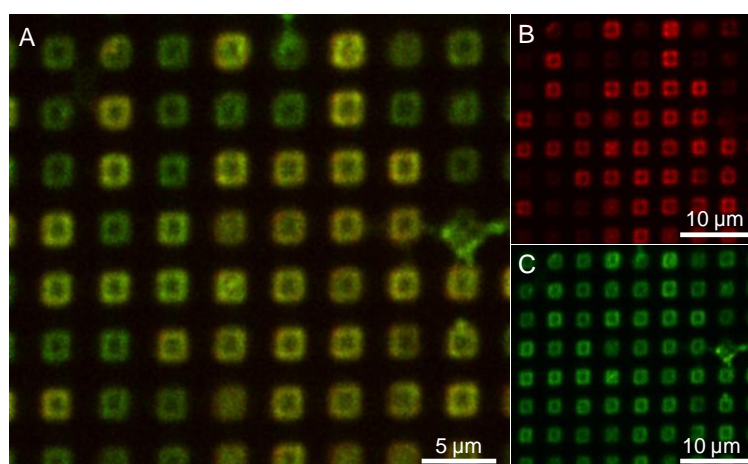


**Figure 5.5.** Top-view fluorescent image of the micropillars after dual-side functionalization under the simultaneous excitation of 488 and 543 nm lasers. Emission collected through bandpass filters of A) both  $515 \pm 15$  and  $590 \pm 30$  nm, B)  $590 \pm 30$  nm and C)  $515 \pm 15$  nm.

In order to better appreciate the dual-side functionalization, Figure 5.7 depicts the fluorescent labeled layer in cross section, including both the released micropillars and a small part of embedded macropores. In Figure 5.7B both the internal and external surfaces of the micropillars are excited

under both 488 and 523 nm excitation wavelengths. We observe that (1) where rhodamine and BSA-FITC co-exist the color is yellow-ish, exactly as in Figure 5.5A; (2) as in Figure 5.6, the tip of the micropillars appears green, since there is no rhodamine at the corresponding bottom of the macropores; and (3) where the macropores are still embedded, the color is definitely red. If the 543 nm laser is turned off and the red channel closed (Figure 5.7C), then the macropore channels barely exhibit any color, evidencing that green emission in Figure 5.7B is originated from the fluorescein. When exciting with a 543 nm laser and opening the red channel (Figure 5.7D), the walls of the micropillars are better defined than in Figure 5.7C.

## **5.4 Conclusions**

Hollow SiO<sub>2</sub> micropillar arrays were fabricated and selectively functionalized on their interior and exterior surfaces. The internal and external chemical modifications were performed before and after the micropillars release respectively, thus avoiding cross-contamination. The configuration of the vertically aligned arrays, standing on the backside of the wafer with an accessible internal surface through the pores on the frontside, made it possible the dual internal-external functionality. Since the internal and external surfaces were labeled with two different dyes, fluorescence confocal microscopy demonstrated successful dual-side functionalization. This approach enables the independent chemical activation of two nanometrically separated surfaces, which can be simultaneously imaged. 3D arrays of dual-side functionalized micropillars are a promising, flexible platform for biotechnological applications. For instance, the interior volume can be used as a smart reservoir for hosting

biochemical agents able to interact with species grafted onto the external side of the micropillars.

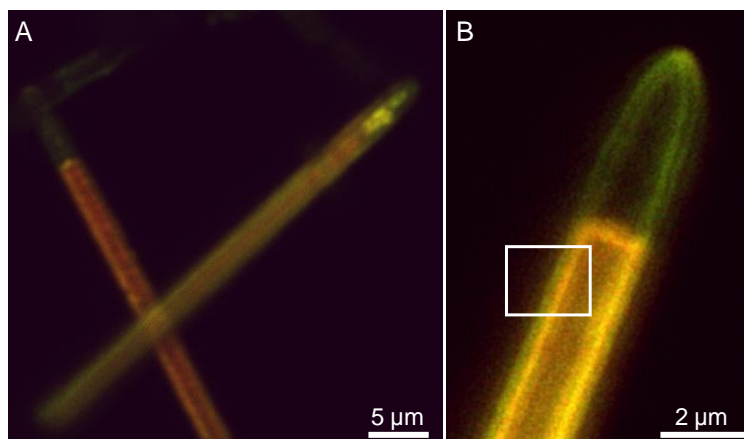


**Figure 5.6.** Cross section fluorescence images of detached micropillars collected through both  $515 \pm 15$  and  $590 \pm 30$  nm emission filters.

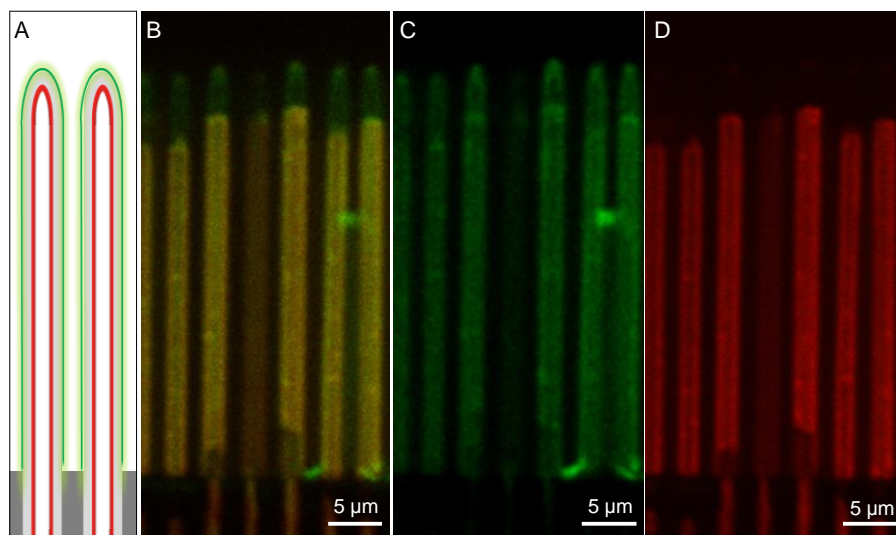


**Figure 5.7.** A) Schematic representation of the micropillars cross-section and distribution of the fluorophores on the internal and external surfaces. Cross-section view by confocal microscopy of the micropillars under the excitation of B) both 488 and 543 nm; C) 488 nm; and D) 543 nm lasers.

## 5.5 References

- [1] Ma, M., J. Cho, E. Fred Schubert, Y. Park, G. Bum Kim, and C. Sone, *Strong light-extraction enhancement in GaInN light-emitting diodes patterned with TiO<sub>2</sub> micro-pillars with tapered sidewalls*. Applied Physics Letters, 2012. **101**(14): p. 141105-141105-4.
- [2] Jae Cheol, S., D. Chanda, W. Chern, Y. Ki Jun, J.A. Rogers, and L. Xiuling, *Experimental Study of Design Parameters in Silicon Micropillar Array Solar Cells Produced by Soft Lithography and Metal-Assisted Chemical Etching*. IEEE Journal of Photovoltaics, 2012. **2**(2): p. 129-133.
- [3] Bettotti, P., L. Dal Negro, Z. Gaburro, L. Pavesi, A. Lui, M. Galli, M. Patrini, and F. Marabelli, *P-type macroporous silicon for two-dimensional photonic crystals*. Journal of applied physics, 2002. **92**(12): p. 6966-6972.
- [4] Gratson, G.M., F. García-Santamaría, V. Lousse, M. Xu, S. Fan, J.A. Lewis, and P.V. Braun, *Direct-Write Assembly of Three-Dimensional Photonic Crystals: Conversion of Polymer Scaffolds to Silicon Hollow-Woodpile Structures*. Advanced Materials, 2006. **18**(4): p. 461-465.
- [5] Shircliff, R.A., P. Stradins, H. Moutinho, J. Fennell, M.L. Ghirardi, S.W. Cowley, H.M. Branz, and I.T. Martin, *Angle-Resolved XPS Analysis and Characterization of Monolayer and Multilayer Silane Films for DNA Coupling to Silica*. Langmuir, 2013. **29**(12): p. 4057-4067.
- [6] Fryxell, G.E., *The synthesis of functional mesoporous materials*. Inorganic Chemistry Communications, 2006. **9**(11): p. 1141-1150.
- [7] De Angelis, F., F. Gentile, F. Mecarini, G. Das, M. Moretti, P. Candeloro, M. Coluccio, G. Cojoc, A. Accardo, and C. Liberale, *Breaking the diffusion limit with super-hydrophobic delivery of molecules to plasmonic nanofocusing SERS structures*. Nature Photonics, 2011. **5**(11): p. 682-687.
- [8] Tamayo, J., P.M. Kosaka, J.J. Ruz, A. San Paulo, and M. Calleja, *Biosensors based on nanomechanical systems*. Chemical Society Reviews, 2013. **42**(3): p. 1287-1311.
- [9] Feng, C., Z. Xiao, P.C.H. Chan, and I. Hsing, *Lithography-free silicon micropillars as catalyst supports for microfabricated fuel cell applications*. Electrochemistry communications, 2006. **8**(8): p. 1235-1238.
- [10] Henry, M., S. Walavalkar, A. Homyk, and A. Scherer, *Alumina etch masks for fabrication of high-aspect-ratio silicon micropillars and nanopillars*. Nanotechnology, 2009. **20**(25): p. 255305.
- [11] Dong, X., J. Tao, Y. Li, and H. Zhu, *Oriented single crystalline TiO<sub>2</sub> nanopillar arrays directly grown on titanium substrate in tetramethylammonium hydroxide solution*. Applied Surface Science, 2010. **256**(8): p. 2532-2538.
- [12] Suzuki, Y. and K. Yokoyama, *Construction of a more sensitive fluorescence sensing material for the detection of vascular endothelial growth factor, a biomarker for angiogenesis, prepared by combining a fluorescent peptide and a nanopillar substrate*. Biosensors and Bioelectronics, 2011. **26**(8): p. 3696-3699.

- 
- [13] Bei, H., S. Shim, E.P. George, M.K. Miller, E. Herbert, and G.M. Pharr, *Compressive strengths of molybdenum alloy micro-pillars prepared using a new technique*. Scripta Materialia, 2007. **57**(5): p. 397-400.
- [14] Marsal, L.F., P. Formentín, R. Palacios, T. Trifonov, J. Ferré-Borrull, A. Rodríguez, J. Pallarès, and R. Alcubilla, *Polymer microfibers obtained using porous silicon templates*. Physica Status Solidi A, 2008. **205**(10): p. 2437-2440.
- [15] Arkles, B., J.R. Steinmetz, J. Zazyczny, and P. Mehta, *Factors contributing to the stability of alkoxysilanes in aqueous solution*. Journal of Adhesion Science and Technology, 1992. **6**(1): p. 193-206.
- [16] Lehmann, V., *Macroporous Silicon*, in *Electrochemistry of Silicon*. 2002, Wiley-VCH Verlag GmbH. p. 183-205.
- [17] Trifonov, T., L.F. Marsal, A. Rodríguez, J. Pallarès, and R. Alcubilla, *Fabrication of two- and three-dimensional photonic crystals by electrochemical etching of silicon*. physica status solidi (c), 2005. **2**(8): p. 3104-3107.
- [18] Trifonov, T., A. Rodríguez, L.F. Marsal, J. Pallarès, and R. Alcubilla, *Macroporous silicon: A versatile material for 3D structure fabrication*. Sensors and Actuators A: Physical, 2008. **141**(2): p. 662-669.
- [19] Nikkhah, M., F. Edalat, S. Manoucheri, and A. Khademhosseini, *Engineering microscale topographies to control the cell-substrate interface*. Biomaterials, 2012. **33**(21): p. 5230-5246.
- [20] Su, W.-T., Y.-F. Liao, C.-Y. Lin, and L.-T. Li, *Micropillar substrate influences the cellular attachment and laminin expression*. Journal of Biomedical Materials Research Part A, 2010. **93A**(4): p. 1463-1469.
- [21] Kim, M.S., H. Hwang, Y.S. Choi, and J.K. Park, *Microfluidic micropillar arrays for 3D cell culture*. Open Biotechnology Journal, 2008. **2**: p. 224-228.
- [22] Ghibaudo, M., L. Trichet, J. Le Digabel, A. Richert, P. Hersen, and B. Ladoux, *Substrate Topography Induces a Crossover from 2D to 3D Behavior in Fibroblast Migration*. Biophysical Journal, 2009. **97**(1): p. 357-368.
- [23] Vandenberg, E.T., L. Bertilsson, B. Liedberg, K. Uvdal, R. Erlandsson, H. Elwing, and I. Lundström, *Structure of 3-aminopropyl triethoxy silane on silicon oxide*. Journal of Colloid and Interface Science, 1991. **147**(1): p. 103-118.
- [24] Acres, R.G., A.V. Ellis, J. Alvino, C.E. Lenahan, D.A. Khodakov, G.F. Metha, and G.G. Andersson, *Molecular Structure of 3-Aminopropyltriethoxysilane Layers Formed on Silanol-Terminated Silicon Surfaces*. The Journal of Physical Chemistry C, 2012. **116**(10): p. 6289-6297.
- [25] Asenath Smith, E. and W. Chen, *How To Prevent the Loss of Surface Functionality Derived from Aminosilanes*. Langmuir, 2008. **24**(21): p. 12405-12409.
- [26] Park, J.-H., L. Gu, G. von Maltzahn, E. Ruoslahti, S.N. Bhatia, and M.J. Sailor, *Biodegradable luminescent porous silicon nanoparticles for in vivo applications*. Nature materials, 2009. **8**(4): p. 331-336.
- [27] Tanaka, T., B. Godin, R. Bhavane, R. Nieves-Alicea, J. Gu, X. Liu, C. Chiappini, J.R. Fakhoury, S. Amra, A. Ewing, Q. Li, I.J. Fidler, and M. Ferrari, *In vivo evaluation of safety of nanoporous silicon carriers following single and*
-



- multiple dose intravenous administrations in mice*. International Journal of Pharmaceutics, 2010. **402**(1-2): p. 190-197.
- [28] Chhablani, J., A. Nieto, H. Hou, E.C. Wu, W.R. Freeman, M.J. Sailor, and L. Cheng, *Oxidized porous silicon particles covalently grafted with daunorubicin as a sustained intraocular drug delivery system*. Investigative Ophthalmology & Visual Science, 2013. **54**(2): p. 1268-1279.
- [29] Sweetman, M.J., C.J. Shearer, J.G. Shapter, and N.H. Voelcker, *Dual silane surface functionalization for the selective attachment of human neuronal cells to porous silicon*. Langmuir, 2011. **27**(15): p. 9497-503.
- [30] Agrawal, A.A., B.J. Nehilla, K.V. Reisig, T.R. Gaborski, D.Z. Fang, C.C. Striemer, P.M. Fauchet, and J.L. McGrath, *Porous nanocrystalline silicon membranes as highly permeable and molecularly thin substrates for cell culture*. Biomaterials, 2010. **31**(20): p. 5408-5417.
- [31] Kim, J., P. Seidler, C. Fill, and L.S. Wan, *Investigations of the effect of curing conditions on the structure and stability of amino-functionalized organic films on silicon substrates by Fourier transform infrared spectroscopy, ellipsometry, and fluorescence microscopy*. Surface Science, 2008. **602**(21): p. 3323-3330.
- [32] Fu, J., Y.-K. Wang, M.T. Yang, R.A. Desai, X. Yu, Z. Liu, and C.S. Chen, *Mechanical regulation of cell function with geometrically modulated elastomeric substrates*. Nature methods, 2010. **7**(9): p. 733-736.
- [33] Yang, M.T., J. Fu, Y.-K. Wang, R.A. Desai, and C.S. Chen, *Assaying stem cell mechanobiology on microfabricated elastomeric substrates with geometrically modulated rigidity*. Nature Protocols, 2011. **6**(2): p. 187-213.
- [34] Ross, A.M., Z. Jiang, M. Bastmeyer, and J. Lahann, *Physical Aspects of Cell Culture Substrates: Topography, Roughness, and Elasticity*. Small, 2012. **8**(3): p. 336-355.
- [35] Dickinson, L.E., D.R. Rand, J. Tsao, W. Eberle, and S. Gerecht, *Endothelial cell responses to micropillar substrates of varying dimensions and stiffness*. Journal of Biomedical Materials Research Part A, 2012. **100A**(6): p. 1457-1466.
- [36] Cauda, V., A. Schlossbauer, J. Kecht, A. Zürner, and T. Bein, *Multiple Core-Shell Functionalized Colloidal Mesoporous Silica Nanoparticles*. Journal of the American Chemical Society, 2009. **131**(32): p. 11361-11370.
- [37] Guan, B., S. Ciampi, G. Le Saux, K. Gaus, P.J. Reece, and J.J. Gooding, *Different Functionalization of the Internal and External Surfaces in Mesoporous Materials for Biosensing Applications Using "Click" Chemistry*. Langmuir, 2010. **27**(1): p. 328-334.
- [38] Wu, C.-C. and M.J. Sailor, *Selective Functionalization of the Internal and the External Surfaces of Mesoporous Silicon by Liquid Masking*. ACS Nano, 2013. **7**(4): p. 3158-3167.
- [39] Bunimovich, Y.L., G. Ge, K.C. Beverly, R.S. Ries, L. Hood, and J.R. Heath, *Electrochemically Programmed, Spatially Selective Biofunctionalization of Silicon Wires*. Langmuir, 2004. **20**(24): p. 10630-10638.
- [40] Park, I., Z. Li, A.P. Pisano, and R.S. Williams, *Selective Surface Functionalization of Silicon Nanowires via Nanoscale Joule Heating*. Nano Letters, 2007. **7**(10): p. 3106-3111.

- 
- [41] Berthing, T., S. Bonde, K.R. Rostgaard, M.H. Madsen, C.B. Sørensen, J. Nygård, and K.L. Martinez, *Cell membrane conformation at vertical nanowire array interface revealed by fluorescence imaging*. *Nanotechnology*, 2012. **23**(41): p. 415102.
- [42] Pawley, J., *Handbook of biological confocal microscopy*. 2006: Springer.
- [43] Fryxell, G.E., P.C. Rieke, L.L. Wood, M.H. Engelhard, R.E. Williford, G.L. Graff, A.A. Campbell, R.J. Wiacek, L. Lee, and A. Halverson, *Nucleophilic Displacements in Mixed Self-Assembled Monolayers*. *Langmuir*, 1996. **12**(21): p. 5064-5075.
- [44] Pasternack, R.M., S. Rivillon Amy, and Y.J. Chabal, *Attachment of 3-(Aminopropyl)triethoxysilane on Silicon Oxide Surfaces: Dependence on Solution Temperature*. *Langmuir*, 2008. **24**(22): p. 12963-12971.
- [45] Garín, M., T. Trifonov, A. Rodríguez, L.F. Marsal, and R. Alcubilla, *Optical properties of 3D macroporous silicon structures*. *Materials Science and Engineering: B*, 2008. **149**(3): p. 275-280.
- [46] Socrates, G., *Infrared and Raman characteristic group frequencies: tables and charts*. 2001: Wiley Chichester.
- [47] Pawley, J., *Fundamental Limits in Confocal Microscopy*, in *Handbook Of Biological Confocal Microscopy*, J.B. Pawley, Editor. 2006, Springer US. p. 20-42.

UNIVERSITAT ROVIRA I VIRGILI

SILICON DIOXIDE MICROSTRUCTURES BASED ON MACROPOROUS SILICON FOR BIOMEDICAL APPLICATIONS.

María Alba Martín

Dipòsit Legal: T 153-2015

## ***Chapter 6***

---

### **SiO<sub>2</sub> Micropillars Coated with Polyelectrolyte Multilayers for pH- Responsive Drug Release**

Over the past decades, the pharmaceutical industry has been facing great challenges in the development of effective and controlled drug delivery. Smart combination of different functional materials may enable the development of microstructured platforms for controlled release of encapsulated drugs that can be triggered in response to internal or external stimuli.

This chapter describes a pH-responsive drug delivery system based on polyelectrolyte multilayer coated hollow silicon dioxide micropillars. Silicon dioxide micropillars provide additional function such as drug delivery system. The polyelectrolyte multilayer is assembled by the layer-by-layer technique founded on the alternative deposition of cationic and anionic polyelectrolytes. The polyelectrolyte pair poly(allylamine hydrochloride) and sodium poly(styrene sulfonate) exhibit pH-responsive properties, therefore the loading and release of a anticancer drug doxorubicin is dependent on the medium pH. The influence of the number of layers coating the micropillars is also assessed.

## **6.1 Introduction**

The search for innovative delivery platforms for the controlled release of pharmaceuticals has been a topic of extensive research efforts since the 1960 [1-3]. Although significant milestones have been achieved since then, constructing an effective drug delivery system is still one of the most demanded challenges in biomedicine. Compared to conventional form of dosage, controlled and localized release of drugs has a number of advantages, such as reduced release rate, minimized harmful side effects and improved therapeutic efficiency [4-6]. Because of these advantages, there is a great interest of research focused on developing novel, more efficient drug delivery systems. The exceptional progress of functional micro- and nano-particles in the last few decades has given them remarkable potential to address this challenge.

The use of microstructures based on the electrochemical etching of porous silicon has attracted much attention in medical and biotechnological applications owing to its biodegradability, nontoxicity and versatile physico-chemical properties, including surface functionality, size and porosity [7-11]. The combination of electrochemical etching and microfabrication techniques have also enabled the fabrication of neatly defined and monodispersed structures with a precise control on particle dimensions and shape, which can be critical for eliminating variability, improving pharmacokinetics and adapting microscale features in several bioapplications [5, 12-14]. Particularly, hollow silicon dioxide ( $\text{SiO}_2$ ) micropillars exhibit remarkable advantages such as high chemical and mechanical stability, tunable size and functional modifiable surface [15]. The hollow volume of micropillars can be loaded with active species, such as drugs, bioactive agents, enzymes and antibiotics. Furthermore, a

differential inner/outer functionalization can activate the external surface in order to facilitate the interaction with species grafted on the external side.

In the development of novel drug delivery systems, one of the areas of greatest interest is the achievement of controlled delivery and release of drugs to avoid the drawbacks related to the premature release of active species from the cargo-loaded microparticles. Hence, a triggered and prolonged release of guest molecules upon specific stimuli may be desired. This stimulus for the drug delivery system can be induced by physical [16], chemical [17] or biogenic signals [18]. In this context, polyelectrolyte multilayers (PEM) have been widely explored to create coatings on the surface of a number of inorganic structures for the controlled delivery of drugs [19-23]. The PEM assembly is based on the layer-by-layer (LbL) approach which involves alternative adsorption of oppositely charged polyelectrolytes that will attract one another to create multilayer architectures in a conformal manner [24-26]. We refer to 'bilayer' as two oppositely charged layers. The technique is schematically depicted in Figure 6.1. By the incorporation of appropriate responsive polyelectrolytes, the PEM can allow the controlled release of active agents on the basis of stimuli such as pH [27], temperature [28] or ionic strength [29]. Particularly, pH-sensitive systems are of great interest in drug delivery due to the variations in pH that the human body exhibits. For instance, the gastrointestinal tract exhibits pH ranging from acidic in the stomach (pH 2) to basic in the intestine (pH 5-8). And compared to healthy tissues and the bloodstream (pH 7.4), most cancer and wound tissues constitute an acidic environment (pH 7.2-5.4) [30]. pH-responsive PEM films contain ionizable groups which exhibit volume changes in response to variations in pH and facilitates drug delivery control [31].

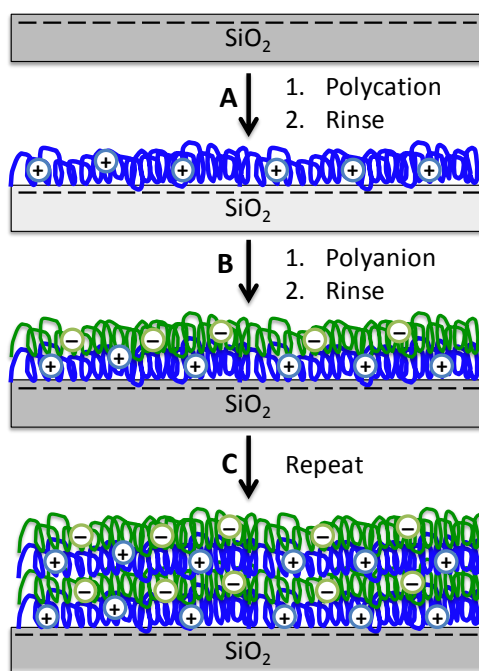


**Figure 6.1.** Layer-by-layer approach to produce thin films by using complementary charges. A) Deposition of positively charged polyelectrolyte (polycation); B) deposition of negatively charged polyelectrolyte (polyanion); C) repeat the sequence until obtaining the desired number of bilayers.

The polyelectrolyte pair comprised by poly(allylamine hydrochloride) (PAH) and sodium poly(styrene sulfonate) (PSS) has been extensively investigated for drug delivery applications due to their remarkable sensitivity to pH and improved biocompatibility [20, 32]. The deposition of the first layer of cationic polyelectrolyte PAH on the internal sidewalls of hollow micropillars is favored by the negative charge of the SiO<sub>2</sub> surface above the isoelectric point (pH 2-3) [33]. Then, the anionic PSS is deposited onto PAH by electrostatic attraction. Furthermore, to facilitate the infiltration of the polyelectrolytes inside the pores and obtain a uniform surface coating without pore blockage, a multivalent salt such as CaCl<sub>2</sub> can be added to the aqueous polyelectrolyte solution. The presence of



multivalent salts causes a much stronger shrinking of the polyelectrolyte chain owing to a higher attraction between charged monomers along the chain [34, 35]. The infiltration of the drug inside the polyelectrolyte multilayer can also be assisted by electrostatic attractive forces. The negative charge of the most external PSS layer gives extra electrostatic attraction to positively charged drugs, such as doxorubicin hydrochloride (DOX). DOX is a chemotherapeutic agent widely used in the treatment of a number of tumors, such as breast, lung or ovarian cancers [36, 37]. Its inherent fluorescence gives DOX an additional imaging capability which makes it a remarkable theranostic agent [4, 38-40].

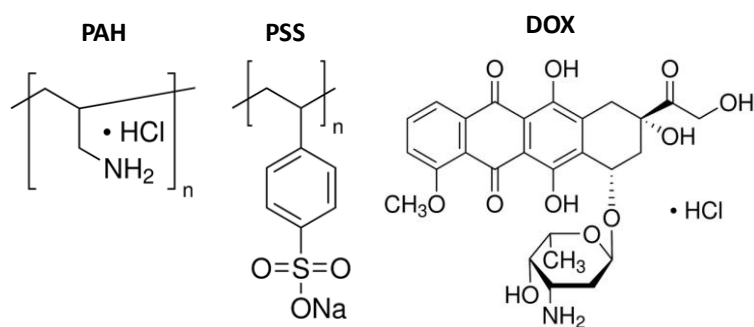


**Figure 6.2.** Chemical structures of the cationic and anionic polyelectrolytes, PAH and PSS, respectively, and the anticancer pharmaceutical DOX.

Herein, we present the combination of  $\text{SiO}_2$  micropillars with PEM coating as an approach to develop new functional materials for sustained released of drug molecules. The hollow micropillars are used as reservoirs for doxorubicin and the PAH/PSS coating as a pH-responsive switch. The polyelectrolyte multilayer on the interior surface prevents the premature release of the drug and enables an enhanced use of the hollow volume by increasing the loading capacity. The effect of the number of PAH/PSS layers in the drug loading and release is also investigated.

## **6.2 Experimental Methods**

### **6.2.1 Fabrication of SiO<sub>2</sub> Micropillars**

SiO<sub>2</sub> micropillar arrays were fabricated from macroporous silicon produced by electrochemical etching in p-type silicon wafers following the process described in Chapter 3, section 2.1. Briefly, to obtain regular pore arrays, boron-doped (p-type) silicon wafers (1 0 0) and resistivity 10-20  $\Omega$  cm (Si-Mat) were patterned with a 3  $\mu$ m lattice using a direct-write lithography system (DWL 66FS, Heidelberg Instruments GmbH). Macropores were formed under galvanostatic conditions (5 mA cm<sup>-2</sup>) in a solution of 1:10 (v:v) HF (40%, Sigma-Aldrich) to DMF (Sigma-Aldrich) for 5 h. Following, the sample was oxidized at 1000 °C for 1.5 h in air. Then, the backside of the wafer was patterned to open windows where the oxide layer was removed by BHF (Sigma-Aldrich) etching. Finally the silicon bulk was anisotropically etched in TMAH (12%, 85 °C, Sigma-Aldrich). As a result, the SiO<sub>2</sub> micropillars appear protruding out of the backside of the silicon wafer [15, 41].

### **6.2.2 Polyelectrolyte Multilayer Coating**

PAH/PSS multilayer coating was deposited by alternately exposing the internal side of the micropillar sample to solutions 1 mg mL<sup>-1</sup> in CaCl<sub>2</sub> 0.5 M of PAH (M<sub>w</sub> 58000, Sigma-Aldrich) and PSS (M<sub>w</sub> 70000, Sigma-Aldrich), for 20 min each in an ultrasonic bath (Figure 6.3A). After the deposition of each polyelectrolyte the sample was thoroughly washed twice in Mili-Q water for 5 min each. This sequence was repeated until obtaining the desired number (4, 8 or 12) of PAH/PSS bilayers.

### **6.2.3 Characterization Techniques**

The morphology and structure of the macroporous silicon and subsequent silicon dioxide micropillars were characterized by SEM using a FEI Quanta 600 environmental scanning electron microscope operating at an accelerating voltage between 15 and 25 kV. The micropillars were also morphologically characterized by TEM using a Jeol 1011 operating in dark-field mode at 80 kV. Confocal laser scanning microscopy images were taken using a Nikon Eclipse TE2000-E inverted microscope, equipped with a C1 laser confocal system (EZ-C1 software, Nikon). A 488 nm helium-neon laser was used as excitation source for DOX loaded micropillars. The emission was collected through a  $590 \pm 30$  bandpass emission filter (red channel). All fluorescence images were captured using a 5-megapixel CCD. The concentrations of DOX were determined using a spectrofluorometer (PTI Quantmaster 40) at an exciting wavelength of 480 nm.

### **6.2.4 DOX Loading and pH-Responsive Drug Release**

Doxorubicin (European Pharmacopoeia) was loaded inside the PEM-coated micropillar, as well as in bare SiO<sub>2</sub> samples. To perform the drug loading, the micropillar samples were exposed to a solution of DOX 1 mg mL<sup>-1</sup>, adjusted to pH 2.0 with HCl 1 M, for 20 h in the dark (Figure 6.3B). Then, DOX solution was adjusted to pH 8.0 with NaOH 0.1 M and further stirred for 2 h (Figure 6.3C). The drug loaded samples were washed 3 times in water at pH 8 for 10 min each. The amount of released DOX in solutions of pH 7.4 (phosphate buffer, PBS) and 5.2 (acetate buffer, ABS) was monitored over time (up to 24 h) at an exciting wavelength of 480 nm (Figure 6.3D). A calibration curve was obtained by analyzing different dilutions from a sample at a concentration of 0.1 mg mL<sup>-1</sup> of DOX.

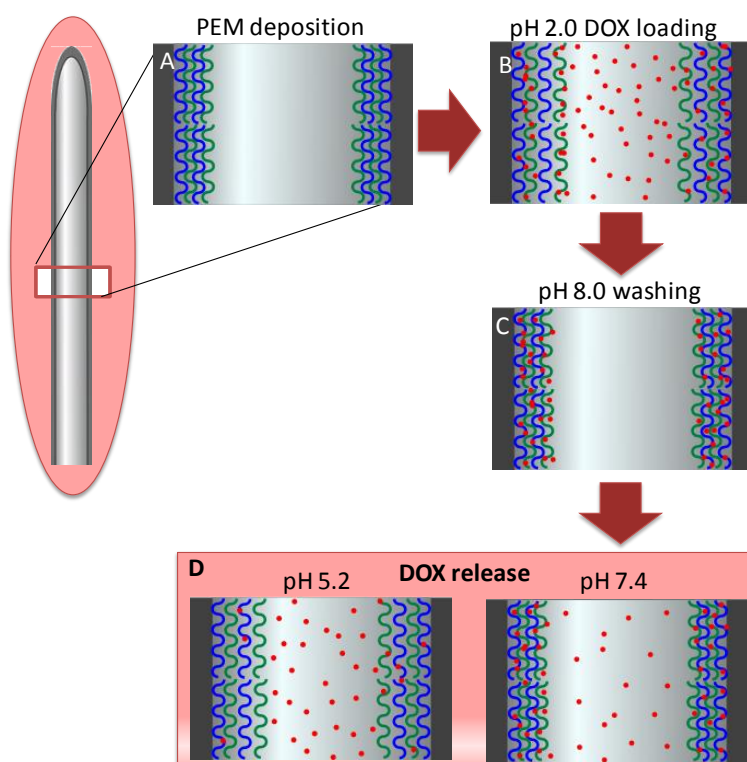


**Figure 6.3.** Schematic of the process for the PEM coating and DOX loading and release of the SiO<sub>2</sub> micropillars. A) Polyelectrolyte pair PAH/PSS alternative deposition on the internal sidewalls of SiO<sub>2</sub> micropillars via the LbL method to construct a pH-responsive drug delivery system; B) DOX loading in the swollen PEM film at pH 2.0; C) DOX confinement due to the PEM layer contraction at pH 8.0; and D) DOX release in different media at pH 7.4 and 5.2.

### 6.3 Results and Discussion

Figure 6.4A shows a SEM image of SiO<sub>2</sub> micropillars with a diameter of 1.8  $\mu\text{m}$ , protruding out of the backside of the Si wafer. The micropillar arrays retain the same arrangement and dimensions as the preceding macropores. Their nucleation points were defined by lithography-assisted indentation so that the distance between neighboring micropillars is set to

3  $\mu\text{m}$ . The thermal oxide grows in a conformal manner which preserves the ordering, morphology and uniformity of those initial macropores. The micropillar hollow structure was further investigated by TEM. Figure 6.4B shows a cross-section-like dark field TEM image of a detached micropillar with a length of 26  $\mu\text{m}$  and a regular wall thickness of approximately 150 nm all along.

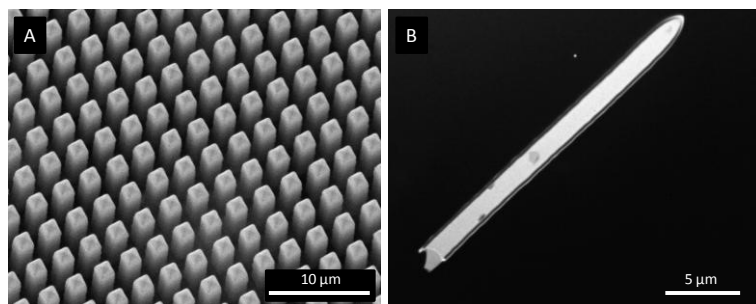


**Figure 6.4.** Microscopy characterization of the  $\text{SiO}_2$  micropillars. A) Tilted SEM image of released micropillar arrays with a 3  $\mu\text{m}$  lattice constant; B) dark-field TEM image of a detached hollow micropillar with a length of 26  $\mu\text{m}$ .

Fourier transform infrared-attenuated total reflection (FTIR-ATR) spectroscopy was employed to verify the electrostatic deposition of the polyelectrolytes on the micropillars sample. Bare  $\text{SiO}_2$  possesses a negative surface charge above the isoelectric point (pH 1.7-3.5) [42], which facilitates the cationic PAH adsorption. After PAH deposition, an absorption band appears at  $\sim 2930\text{ cm}^{-1}$  related to the  $\text{C-H}_x$  stretching vibrations, although it is distorted by the broad  $\nu\text{OH}$  band. The band centered at  $\sim 1534\text{ cm}^{-1}$  is attributed to the N-H bending modes in  $\text{NH}_3^+$  (Figure 6.5, spectrum b). These findings prove successful adsorption of the PAH on the silicon oxide. The FTIR-ATR of the sample with a bilayer of PAH/PSS shows bands related to the C-C stretching modes of the aromatic ring in the PSS molecule at 1497 and 1462  $\text{cm}^{-1}$  (Figure 6.5, spectrum c). The contribution

of the alkyl  $\text{CH}_2$  symmetric stretching components from PSS incorporates to those of PAH in the  $2800\text{-}3000\text{ cm}^{-1}$  region. However, a new intense band appears at  $2981\text{ cm}^{-1}$  which can be attributed to the C-H stretching in the PSS aromatic ring. The symmetric and asymmetric stretching regions of  $\text{SO}_3^-$  overlap with the  $\nu\text{SiO}_x$  absorption between  $900$  and  $1250\text{ cm}^{-1}$ . Nevertheless, at least two peaks can be discerned at  $1124$  and  $1160\text{ cm}^{-1}$  corresponding to the  $\text{SO}_3^-$  stretching vibrations [43, 44]. These observations confirm the successful deposition of PAH and PSS polyelectrolytes on the silicon dioxide micropillars.

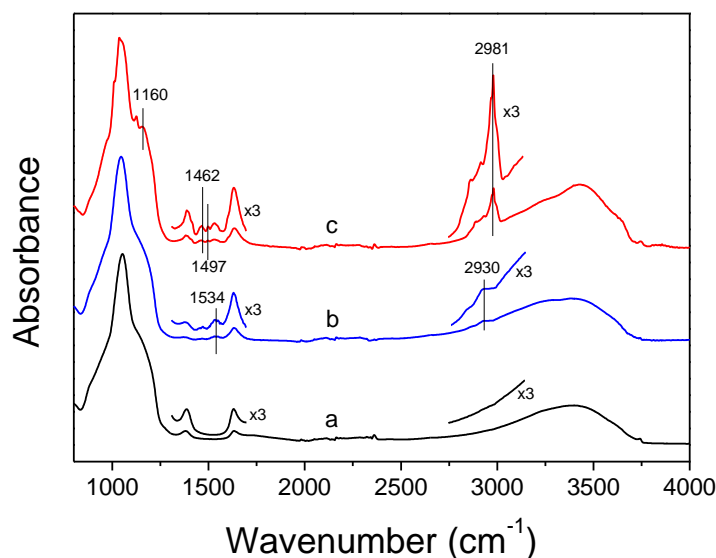


**Figure 6.5.** FTIR-ATR characterization for polyelectrolyte coating. FTIR-ATR spectra of A) oxidized macroporous silicon,; B) PAH-coated,; and C) PAH/PSS-coated macroporous silicon.

Confocal fluorescence microscopy was used to confirm drug adsorption into the polyelectrolyte multilayer, as well as to verify the PEM coating conformation inside the micropillars. Firstly, we imaged a top view of the micropillar arrays after coating with 8 bilayers PAH/PSS and loading with

DOX for 20 h at pH 2.0, then 2 h at pH 8.0 and thoroughly washed with DIW pH 8.0. At pH 2.0, the increased permeability of the PEM film facilitates the incorporation of DOX inside the PAH/PSS multilayers.

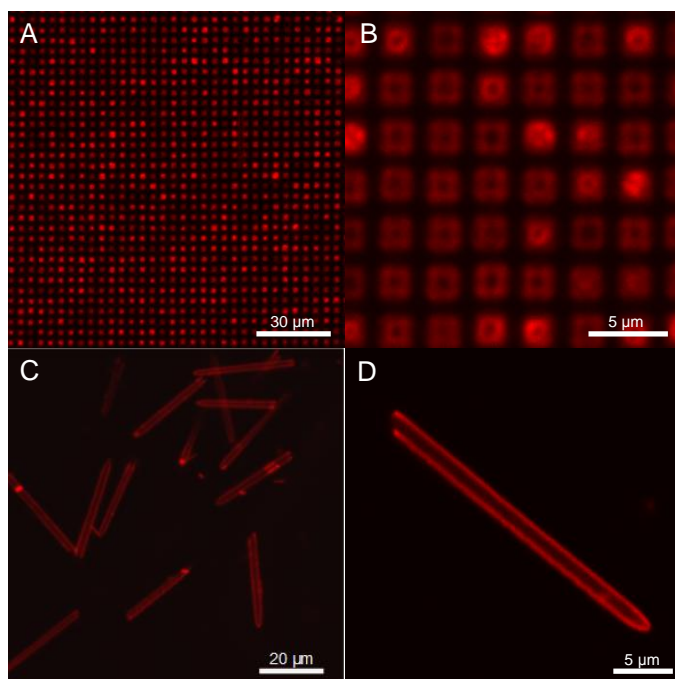


**Figure 6.6.** Fluorescence confocal images of PEM-coated and DOX-loaded micropillars. A,B) Micropillars arrays in top view after PEM coating (eight bilayers) and DOX loading; C) detached hollow micropillars with uniform size distribution; and D) single detached micropillar with PEM and DOX all along the walls.

Additionally, the negatively charged PSS outer layer promotes the electrostatic adsorption of the positively charged DOX. Then, the adjustment of pH at 8.0 causes the shrinkage of the PEM and the drug molecule is trapped inside the film. The subsequent washing will remove any non-trapped DOX molecule. Figure 6.6A was collected exposing the micropillar arrays to a laser excitation of 488 nm and using a  $590 \pm 30$  nm bandpass emission filter (red channel). Bright red dots appear in

correspondence with the micropillars pattern, which confirms the pH-controlled adsorption of DOX in the PAH/PSS multilayer. The zoomed-in micrograph shown in Figure 6.6B depicts a cross-section-like of the micropillars that reveals the distribution of the PEM film around the walls. In addition, PEM-coated and DOX-loaded micropillars were detached from the silicon substrate in order to analyze the conformation of the polyelectrolyte multilayer and subsequently, the DOX adsorption. Figure 6.6C shows a number of micropillars with uniform size and shape, exhibiting bright red fluorescence originated from the loaded DOX. This observation indicates a successful deposition of the polyelectrolyte multilayer on the micropillar sidewalls, in which no pore blockage occurred during the LbL self-assembly. The use of a multivalent salt such as  $\text{CaCl}_2$  assists the formation of the polyelectrolyte layer inside the micropillars owing to a stronger polymer-chain contraction [34]. Figure 6.6D shows a closer detail of a single hollow micropillar with a homogeneous distribution of the DOX all along their wall, confirming the conformational PEM deposition along the micropillar walls.

Prior to perform the drug release experiments from the DOX-loaded microtubes, the intrinsic photoluminescence (PL) of the DOX molecule was studied in buffer solutions in order to obtain a calibration curve that correlate the photoluminescence intensity with the known concentration. Under an excitation wavelength of 480 nm, the DOX solutions present a PL curve with two maxima peaks at 557 and 592 nm, as it can be seen in the curve shown in Figure 6.7A obtained from a DOX solution at  $1 \text{ ng mL}^{-1}$  concentration in PBS pH 7.4. The results showed no relevant difference in intensity with the change in the pH from 5.2 to 7.4. In addition, a linear relationship was found between the PL intensity at 592 nm and the DOX



concentration in a log-log scale for the range of most interest, i.e. concentrations between  $10^{-5}$  and  $10^{-2}$  mg mL $^{-1}$  (see Figure 6.7B).

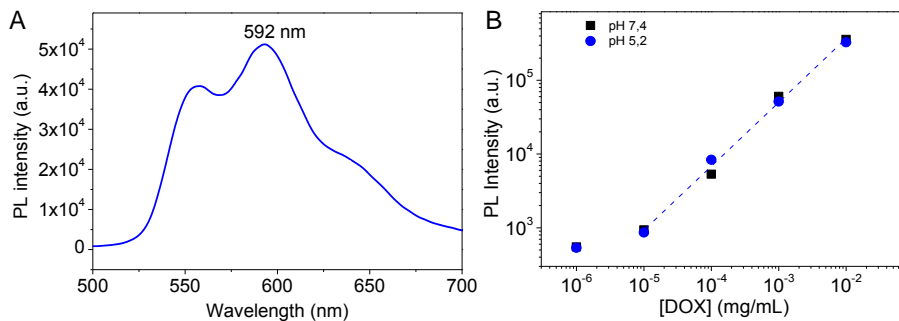


**Figure 6.7.** A) Emission PL spectra of DOX 1 ng mL $^{-1}$  in PBS at pH 7.4; B) PL intensity vs DOX concentration at pH 5.2 and 7.4.

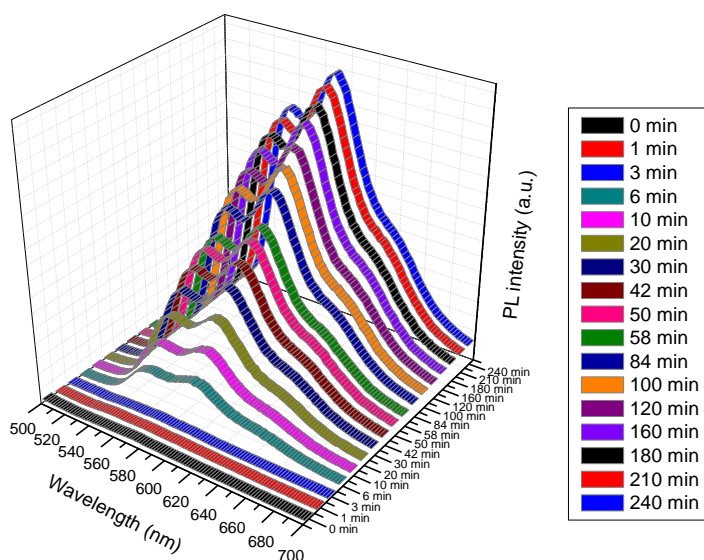


**Figure 6.8.** Evolution of the emission PL spectra of DOX in order to monitor the release from SiO $_2$  micropillars internally coated with eight bilayers of PAH/PSS. The photoluminescence was monitored for 4 hours at an exciting wavelength of 480 nm.

Following the DOX loading, the micropillars were exposed to a two different pH media to assess the pH-responsiveness. Once in contact with the aqueous medium, the PEM film swells to a certain extent, increasing its permeability and allowing the diffusion of the drug. After the DOX releasing from the PEM film, the molecule still remains inside the micropillar until it finally diffuses into the release medium through the micropillar opened-end. Figure 6.8 shows the PL curve evolution over the first 4 hours of release in PBS medium from SiO<sub>2</sub> micropillars internally coated with 8 bilayers of PAH/PSS. The maxima peaks do not shift in the wavelength axe whereas the PL intensity boosts with the time as the concentration of DOX in the buffer solution increases.

Using the calibration curves previously obtained, we can correlate the PL intensity at 592 nm with the DOX concentration in the buffer solutions. Figure 6.9A compares the release profile of DOX from the PEM-coated micropillars at pH 5.2 and 7.4 over a period of 24 h. The data indicates that the release at pH 5.2 is higher than that at pH 7.4 (4.8 and 3.2  $\mu\text{g cm}^{-2}$  after 24 h, respectively). This demonstrates the release rate is pH-dependent and increases with the decrease of pH. The swelling mechanism of PAH/PSS films is mostly related to the variation in charge density of polyelectrolyte chains induced by a change in the media pH. PAH is a weak polyelectrolyte whose amino groups become charged when the pH decreases, causing an increase in the osmotic pressure. Subsequently, water molecules diffuse into the PEM and the multilayer swells. This phenomenon, together with the electrostatic repulsion between DOX and the PAH/PSS multilayer, facilitates the permeation of the drug [45]. Furthermore, the DOX discharge from the multilayer at pH 5.2 shows a considerable burst release within the first 90 min (71.3% of the total release after 24 h), which is mitigated by the deswelling effect on the PEM

at pH 7.4 (46.97%). Considering absolute values, the DOX released after 60 min at pH 5.2 is nearly 2.5 times higher than that at pH 7.4 (3.3 and 1.3  $\mu\text{g cm}^{-2}$ , respectively). Then the release rate slows and becomes rather constant from 120 min for both pH 5.2 and 7.4, lasting approximately 7 hours (Figure 6.9B). At this point, the effect of the pH in the release rate is negligible, being these 2.38 and 2.34  $\mu\text{g cm}^{-2} \text{ min}$  at pH 5.2 and 7.4, respectively.

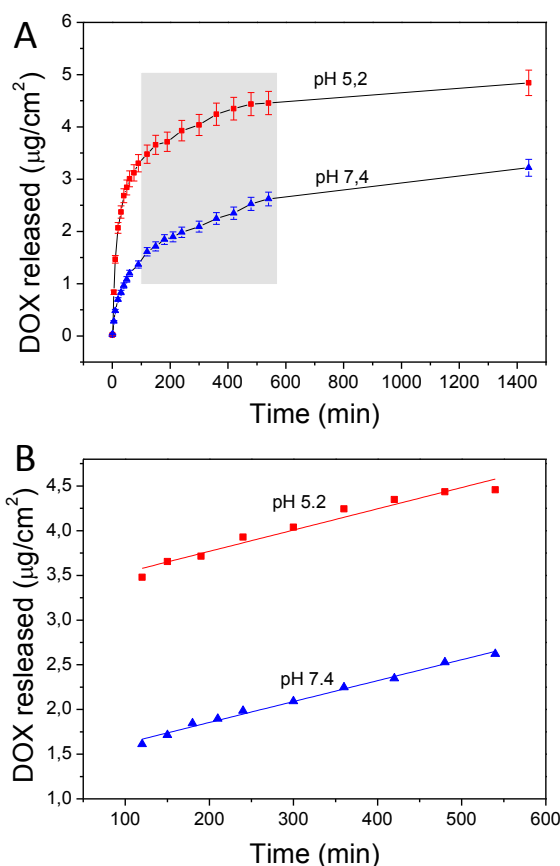


**Figure 6.9.** Drug release profile for 24 h at pH 7.4 and 5.2. A) Time evolution of pH-responsive release of DOX from PEM-coated (eight bilayers) micropillars at pH 5.2 (red squares) and 7.4 (blue triangles); B) zoomed-in plot and linear fitting of DOX release in the region between 120 and 540 min.

The effect of the number of bilayers in DOX loading and release was also investigated at pH 7.4. Figure 6.10 revealed that the loading content and release rate of DOX was layer thickness-dependent. The drug loaded was observed to be significantly higher in the PEM-coated micropillars than in those without multilayers (Figure 6.11A). Thus, the amount of DOX released after 24 h at pH 7.4 was 3 times higher in samples with 4 PAH/PSS layers compared to samples without polyelectrolyte (2.66 and 0.86  $\mu\text{g cm}^{-2}$ , respectively). Although the deposition of PEM increases the loading capacity due to an enhanced electrostatic interaction and permeability of the PEM layer, it is worth noticing that positively charged DOX molecules can still be adsorbed onto the negatively charged  $\text{SiO}_2$  micropillars walls. When further increasing the number of bilayers, the abrupt increase in the amount of DOX loaded and released was not notably improved. The release rate was also affected by the number of layers. Figure 6.11B shows that the time to reach 80% of the total DOX release after 24 h (1440 min) was delayed with the number of layers. For instance, it was found that this time was 200 min and 480 min for samples with 4 and 8 PAH/PSS layers, respectively. Thus, by adding more PEM bilayers it is possible to significantly reduce the release rate and impede the initial burst release.

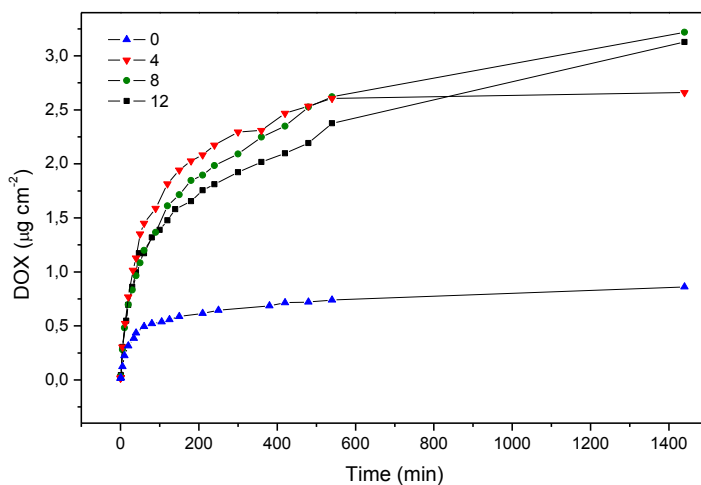


**Figure 6.10.** Effect of the number of bilayers in the DOX release profiles from PEM coated micropillars at pH 7.4 over a period of 24 h.

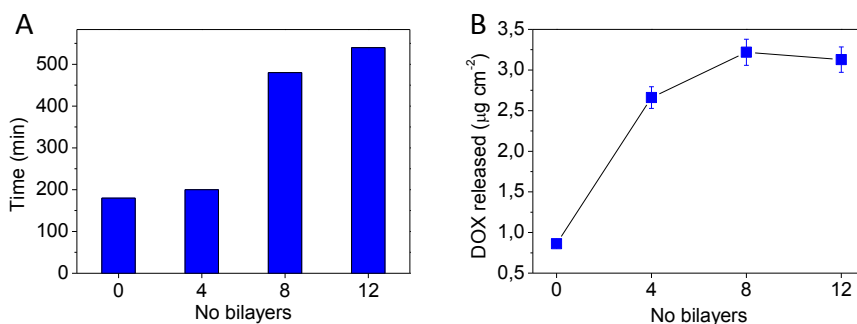


**Figure 6.11.** Effect of the number of bilayers in the DOX release. A) DOX released after 24 h and B) time to reach the 80% of the total release as a function of the number of layers.

## 6.4 Conclusions

In summary, an organic/inorganic hybrid drug delivery system was developed based on SiO<sub>2</sub> hollow micropillars internally coated with multilayers of PAH/PSS by the LbL technique. Confocal fluorescence

microscopy showed a uniform PEM coating and a successful loading of the model drug doxorubicin into the polyelectrolyte matrix. The interaction between polyelectrolyte multilayers and DOX molecules is significantly dependent on the pH for the loading and release of active agents. Thus, the release rate of DOX at pH 5.2 was found to be higher than that at pH 7.4. The effect of the number of PAH/PSS bilayers should be also consider in the loading drug. The DOX loaded was significantly higher in the PEM-coated micropillars than in those without polyelectrolytes. This system has great potential in applications of localized and targeted drug delivery.

## 6.5 References

- [1] Slowing, I.I., J.L. Vivero-Escoto, C.-W. Wu, and V.S.Y. Lin, *Mesoporous silica nanoparticles as controlled release drug delivery and gene transfection carriers*. Advanced Drug Delivery Reviews, 2008. **60**(11): p. 1278-1288.
- [2] Müller, R.H., K. Mäder, and S. Gohla, *Solid lipid nanoparticles (SLN) for controlled drug delivery – a review of the state of the art*. European Journal of Pharmaceutics and Biopharmaceutics, 2000. **50**(1): p. 161-177.
- [3] Jewell, C.M. and D.M. Lynn, *Multilayered polyelectrolyte assemblies as platforms for the delivery of DNA and other nucleic acid-based therapeutics*. Advanced Drug Delivery Reviews, 2008. **60**(9): p. 979-999.
- [4] Feng, W., X. Zhou, C. He, K. Qiu, W. Nie, L. Chen, H. Wang, X. Mo, and Y. Zhang, *Polyelectrolyte multilayer functionalized mesoporous silica nanoparticles for pH-responsive drug delivery: layer thickness-dependent release profiles and biocompatibility*. Journal of Materials Chemistry B, 2013. **1**(43): p. 5886-5898.
- [5] Godin, B., C. Chiappini, S. Srinivasan, J.F. Alexander, K. Yokoi, M. Ferrari, P. Decuzzi, and X. Liu, *Discoidal Porous Silicon Particles: Fabrication and Biodistribution in Breast Cancer Bearing Mice*. Advanced Functional Materials, 2012. **22**(20): p. 4225-4235.
- [6] Zhang, W., Z. Zhang, and Y. Zhang, *The application of carbon nanotubes in target drug delivery systems for cancer therapies*. Nanoscale Research Letters, 2011. **6**(1): p. 1-22.
- [7] Secret, E., K. Smith, V. Dubljevic, E. Moore, P. Macardle, B. Delalat, M.L. Rogers, T.G. Johns, J.O. Durand, F. Cunin, and N.H. Voelcker, *Antibody-Functionalized Porous Silicon Nanoparticles for Vectorization of Hydrophobic Drugs*. Advanced healthcare materials, 2012. **2**(5): p. 718-727.
- [8] Shtenberg, G., N. Massad-Ivanir, O. Moscovitz, S. Engin, M. Sharon, L. Fruk, and E. Segal, *Picking up the Pieces: A Generic Porous Si Biosensor for Probing the Proteolytic Products of Enzymes*. Analytical Chemistry, 2012. **85**(3): p. 1951-1956.
- [9] Park, J.-H., L. Gu, G. von Maltzahn, E. Ruoslahti, S.N. Bhatia, and M.J. Sailor, *Biodegradable luminescent porous silicon nanoparticles for in vivo applications*. Nature materials, 2009. **8**(4): p. 331-336.
- [10] Chhablani, J., A. Nieto, H. Hou, E.C. Wu, W.R. Freeman, M.J. Sailor, and L. Cheng, *Oxidized porous silicon particles covalently grafted with daunorubicin as a sustained intraocular drug delivery system*. Investigative Ophthalmology & Visual Science, 2013. **54**(2): p. 1268-1279.
- [11] Hernandez, M., G. Recio, R. Martin-Palma, J. Garcia-Ramos, C. Domingo, and P. Sevilla, *Surface enhanced fluorescence of anti-tumoral drug emodin adsorbed on silver nanoparticles and loaded on porous silicon*. Nanoscale Research Letters, 2012. **7**(1): p. 1-7.
- [12] Fine, D., A. Grattoni, R. Goodall, S.S. Bansal, C. Chiappini, S. Hosali, A.L. van de Ven, S. Srinivasan, X. Liu, B. Godin, L. Brousseau, I.K. Yazdi, J. Fernandez-

- Moure, E. Tasciotti, H.-J. Wu, Y. Hu, S. Klemm, and M. Ferrari, *Silicon Micro- and Nanofabrication for Medicine*. Advanced Healthcare Materials, 2013. **2**(5): p. 632-666.
- [13] Tanaka, T., B. Godin, R. Bhavane, R. Nieves-Alicea, J. Gu, X. Liu, C. Chiappini, J.R. Fakhoury, S. Amra, A. Ewing, Q. Li, I.J. Fidler, and M. Ferrari, *In vivo evaluation of safety of nanoporous silicon carriers following single and multiple dose intravenous administrations in mice*. International Journal of Pharmaceutics, 2010. **402**(1-2): p. 190-197.
- [14] Chiappini, C., X. Liu, J.R. Fakhoury, and M. Ferrari, *Biodegradable Porous Silicon Barcode Nanowires with Defined Geometry*. Advanced Functional Materials, 2010. **20**(14): p. 2231-2239.
- [15] Trifonov, T., A. Rodriguez, F. Servera, L.F. Marsal, J. Pallares, and R. Alcubilla, *High-aspect-ratio silicon dioxide pillars*. Physica Status Solidi A, 2005. **202**(8): p. 1634-1638.
- [16] Vasani, R.B., S.J. McInnes, M.A. Cole, A.M. Jani, A.V. Ellis, and N.H. Voelcker, *Stimulus-responsiveness and drug release from porous silicon films ATRP-grafted with poly(N-isopropylacrylamide)*. Langmuir, 2011. **27**(12): p. 7843-53.
- [17] Alvarez-Lorenzo, C., B. Blanco-Fernandez, A.M. Puga, and A. Concheiro, *Crosslinked ionic polysaccharides for stimuli-sensitive drug delivery*. Advanced Drug Delivery Reviews, 2013. **65**(9): p. 1148-1171.
- [18] Bernardos, A., L. Mondragón, E. Aznar, M.D. Marcos, R. Martínez-Máñez, F. Sancenón, J. Soto, J.M. Barat, E. Pérez-Payá, C. Guillem, and P. Amorós, *Enzyme-Responsive Intracellular Controlled Release Using Nanometric Silica Mesoporous Supports Capped with "Saccharides"*. ACS Nano, 2010. **4**(11): p. 6353-6368.
- [19] Ariga, K., M. McShane, Y.M. Lvov, Q. Ji, and J.P. Hill, *Layer-by-layer assembly for drug delivery and related applications*. Expert Opinion on Drug Delivery, 2011. **8**(5): p. 633-644.
- [20] Zhu, Y., J. Shi, W. Shen, X. Dong, J. Feng, M. Ruan, and Y. Li, *Stimuli-Responsive Controlled Drug Release from a Hollow Mesoporous Silica Sphere/Polyelectrolyte Multilayer Core-Shell Structure*. Angewandte Chemie, 2005. **117**(32): p. 5213-5217.
- [21] Deshmukh, P.K., K.P. Ramani, S.S. Singh, A.R. Tekade, V.K. Chatap, G.B. Patil, and S.B. Bari, *Stimuli-sensitive layer-by-layer (LbL) self-assembly systems: Targeting and biosensory applications*. Journal of Controlled Release, 2013. **166**(3): p. 294-306.
- [22] Feng, D., J. Shi, X. Wang, L. Zhang, and S. Cao, *Hollow hybrid hydroxyapatite microparticles with sustained and pH-responsive drug delivery properties*. RSC Advances, 2013. **3**(47): p. 24975-24982.
- [23] Wan, X., G. Zhang, and S. Liu, *pH-Disintegrable Polyelectrolyte Multilayer-Coated Mesoporous Silica Nanoparticles Exhibiting Triggered Co-Release of Cisplatin and Model Drug Molecules*. Macromolecular Rapid Communications, 2011. **32**(14): p. 1082-1089.
- [24] Delcea, M., H. Möhwald, and A.G. Skirtach, *Stimuli-responsive LbL capsules and nanoshells for drug delivery*. Advanced Drug Delivery Reviews, 2011. **63**(9): p. 730-747.



- [25] Lvov, Y., G. Decher, and H. Moehwald, *Assembly, structural characterization, and thermal behavior of layer-by-layer deposited ultrathin films of poly (vinyl sulfate) and poly (allylamine)*. *Langmuir*, 1993. **9**(2): p. 481-486.
- [26] Aliev, F.G., M.A. Correa-Duarte, A. Mamedov, J.W. Ostrander, M. Giersig, L.M. Liz-Marzán, and N.A. Kotov, *Layer-By-Layer Assembly of Core-Shell Magnetite Nanoparticles: Effect of Silica Coating on Interparticle Interactions and Magnetic Properties*. *Advanced Materials*, 1999. **11**(12): p. 1006-1010.
- [27] Yang, Y.-J., X. Tao, Q. Hou, Y. Ma, X.-L. Chen, and J.-F. Chen, *Mesoporous silica nanotubes coated with multilayered polyelectrolytes for pH-controlled drug release*. *Acta Biomaterialia*, 2010. **6**(8): p. 3092-3100.
- [28] Köhler, K. and G.B. Sukhorukov, *Heat Treatment of Polyelectrolyte Multilayer Capsules: A Versatile Method for Encapsulation*. *Advanced Functional Materials*, 2007. **17**(13): p. 2053-2061.
- [29] Gao, C., H. Möhwald, and J.C. Shen, *Enhanced Biomacromolecule Encapsulation by Swelling and Shrinking Procedures*. *ChemPhysChem*, 2004. **5**(1): p. 116-120.
- [30] Schmaljohann, D., *Thermo- and pH-responsive polymers in drug delivery*. *Advanced Drug Delivery Reviews*, 2006. **58**(15): p. 1655-1670.
- [31] Stuart, M.A.C., W.T. Huck, J. Genzer, M. Müller, C. Ober, M. Stamm, G.B. Sukhorukov, I. Szleifer, V.V. Tsukruk, and M. Urban, *Emerging applications of stimuli-responsive polymer materials*. *Nature materials*, 2010. **9**(2): p. 101-113.
- [32] Pechenkin, M.A., H. Möhwald, and D.V. Volodkin, *pH-and salt-mediated response of layer-by-layer assembled PSS/PAH microcapsules: fusion and polymer exchange*. *Soft Matter*, 2012. **8**(33): p. 8659-8665.
- [33] Kosmulski, M., *pH-dependent surface charging and points of zero charge II. Update*. *Journal of Colloid and Interface Science*, 2004. **275**(1): p. 214-224.
- [34] Cho, Y., W. Lee, Y.K. Jhon, J. Genzer, and K. Char, *Polymer Nanotubules Obtained by Layer-by-Layer Deposition within AAO-Membrane Templates with Sub-100-nm Pore Diameters*. *Small*, 2010. **6**(23): p. 2683-2689.
- [35] Liu, S., K. Ghosh, and M. Muthukumar, *Polyelectrolyte solutions with added salt: A simulation study*. *Journal of Chemical Physics*, 2003. **119**(3): p. 1813-1823.
- [36] Mohan, P. and N. Rapoport, *Doxorubicin as a Molecular Nanotheranostic Agent: Effect of Doxorubicin Encapsulation in Micelles or Nanoemulsions on the Ultrasound-Mediated Intracellular Delivery and Nuclear Trafficking*. *Molecular Pharmaceutics*, 2010. **7**(6): p. 1959-1973.
- [37] Su, J., F. Chen, V.L. Cryns, and P.B. Messersmith, *Catechol Polymers for pH-Responsive, Targeted Drug Delivery to Cancer Cells*. *Journal of the American Chemical Society*, 2011. **133**(31): p. 11850-11853.
- [38] Chen, M., X. He, K. Wang, D. He, S. Yang, P. Qiu, and S. Chen, *A pH-responsive polymer/mesoporous silica nano-container linked through an acid cleavable linker for intracellular controlled release and tumor therapy in vivo*. *Journal of Materials Chemistry B*, 2014. **2**(4): p. 428-436.

- [39] Wang, Y., W. Shi, W. Song, L. Wang, X. Liu, J. Chen, and R. Huang, *Tumor cell targeted delivery by specific peptide-modified mesoporous silica nanoparticles*. *Journal of Materials Chemistry*, 2012. **22**(29): p. 14608-14616.
- [40] Minati, L., V. Antonini, M. Dalla Serra, G. Speranza, F. Enrichi, and P. Riello, *pH-activated doxorubicin release from polyelectrolyte complex layer coated mesoporous silica nanoparticles*. *Microporous and Mesoporous Materials*, 2013. **180**(0): p. 86-91.
- [41] Alba, M., E. Romano, P. Formentin, P.J. Eravuchira, J. Ferre-Borrull, J. Pallares, and L.F. Marsal, *Selective dual-side functionalization of hollow SiO<sub>2</sub> micropillar arrays for biotechnological applications*. *RSC Advances*, 2014. **4**(22): p. 11409-11416.
- [42] Hartley, P.G., I. Larson, and P.J. Scales, *Electrokinetic and Direct Force Measurements between Silica and Mica Surfaces in Dilute Electrolyte Solutions*. *Langmuir*, 1997. **13**(8): p. 2207-2214.
- [43] Estrela-Lopis, I., J.J. Iturri Ramos, E. Donath, and S.E. Moya, *Spectroscopic Studies on the Competitive Interaction between Polystyrene Sodium Sulfonate with Polycations and the N-Tetradecyl Trimethyl Ammonium Bromide Surfactant*. *Journal of Physical Chemistry B*, 2009. **114**(1): p. 84-91.
- [44] Li, L., R. Ma, N. Iyi, Y. Ebina, K. Takada, and T. Sasaki, *Hollow nanoshell of layered double hydroxide*. *Chemical Communications*, 2006(29): p. 3125-3127.
- [45] Biesheuvel, P.M., T. Mauser, G.B. Sukhorukov, and H. Möhwald, *Micromechanical Theory for pH-Dependent Polyelectrolyte Multilayer Capsule Swelling*. *Macromolecules*, 2006. **39**(24): p. 8480-8486.

UNIVERSITAT ROVIRA I VIRGILI

SILICON DIOXIDE MICROSTRUCTURES BASED ON MACROPOROUS SILICON FOR BIOMEDICAL APPLICATIONS.

María Alba Martín

Dipòsit Legal: T 153-2015

## ***Chapter 7***

---

### Cell Adhesion and Morphology of Endothelial Cells on SiO<sub>2</sub> Microstructures

Native tissues are highly organized at the microscale, thus modulating the scaffold microarchitecture is a potent tool to mimic natural tissue structures. Furthermore, three-dimensional nano- and microtopographical features are now being used to elucidate how extracellular physical cues can direct the cell behavior and organize complex cellular processes such as cell differentiation and tissue organization. The recent advances in nano- and microtechnology have allowed the development of platforms that can be used to further understand and control the complex interactions occurring between biointerfaces and living cells.

In this chapter, we will discuss the use of three-dimensional microstructured substrates such as macroporous silicon and silicon dioxide micropillars to interface with living cells. Human aortic endothelial cells were employed to assess the biocompatibility of the different substrates. Methodological investigations were performed to determine the influence of the substrate topography on the cell adhesion and growth. The cell spreading and cell morphology induced by the substrates were quantified using scanning electron and fluorescence confocal microscopy.

## 7.1 Introduction

As *in vivo* cellular interactions occur on the nanoscale, micro- and nano-structured substrates have gained interest and attention over planar surfaces for biological studies [1-5]. Particularly, micro- and nanotechnology have provided biomaterial scientists with enormous possibilities in the fields of tissue engineering and regenerative medicine [2, 6-8]. These technologies are particularly suitable to create cell and tissue interfaces because they allow the development of well-controlled cell microenvironments to the nanoscale, mimicking the role of the *in vivo* extracellular matrix. The biomaterial surface provides geometrical, architectural and physicochemical signals that act together guiding cellular responses [9-15]. Therefore, the understanding of the influence of topography on cell behavior would be of reference to life sciences to create smart biomaterials capable to induce different effects in cells.

To date, an increasing number of studies have reported on the sensitivity of a range of cell types to micro- and nanoscale cues [1, 3, 12, 16-21]. The interactions between cells and their extracellular matrix are important in regulating many cellular functions, such as adhesion [22], proliferation [5], differentiation [23] and migration [24]. For instance, the cell adhesion is governed by the strength of the cell-material interaction [2]. This is dependent on the cell properties and the physical, geometrical, mechanical and chemical characteristics of the substrate, all of which may induce very different adhesion behaviors of human cells [7, 15, 25-28]. Cell orientation, morphology and cytoskeletal arrangements are also affected by the substrate topography [4, 18, 29]. In fact, morphology has been proven to provide critical information on cellular functions, and is an indicator of normal function in most cell types [1, 30-32]. The ability to

create various engineered micro-topographic cues can be employed to induce a pursued shape, and therefore to influence orientation, proliferation and alignment of cells [33-35].

Three-dimensional (3D) structures including grooves, wells and pillars fabricated with a variety of materials (i.e. polymers [35], titania [36], silicon [37] and silicon oxide [38, 39]) have long been employed to study cellular responses to topography [33, 35, 40]. Microstructured substrates can mimic the 3D-architected surrounding that cells experiment in their native environment [41]. For instance, vertically aligned micro- and nanopillars have been proposed to investigate the influence of topographical features on various cellular functions [22, 29, 42-44]. Furthermore, the mechanical and physical properties of the surface topography have been recognized to regulate the shapes of the cell and the cell nuclei [10], focal adhesion structures [15, 23] and cytoskeletal tension [9, 42]. Another aspect to consider is the influence of the order patterning on the cell adhesion [26], as well as the surface molecular conformations [45].

An essential principle in the development of tools for interfacing with biological systems is to minimize the use of potentially toxic materials. Silicon dioxide ( $\text{SiO}_2$ ) has been proven to be biodegradable and non-toxic, as it dissolves into harmless orthosilicic acid [46]. In addition,  $\text{SiO}_2$ -based microstructures combine an adjustable topography [39, 47] and surface chemistry [48].  $\text{SiO}_2$  microstructured substrate is a friendly material to be used in cell culture because its hydrophilicity [49], but despite of that, for many applications,  $\text{SiO}_2$  does not provide good interaction with living tissues or allow a proper cell attachment. Several surface bio-activations have been introduced to improve the substrate properties with the use of

biological components such as protein functionalization [50-52]. Collagen is attractive for biomedical applications as it is the most abundant protein in mammalian tissues and the main constituent of the extracellular matrix [53]. It provides a natural anchoring moiety for attachment and survival of cells and can be tailored into porous implantable devices [54]. Collagen stimulate cell adhesion [55], and it has been demonstrated that promotes an enhanced cell attachment in the particular case of oxidized porous silicon [56].

In the present study, we investigated cell adhesion and cell spreading behavior of human aortic endothelial cells (HAEC) on SiO<sub>2</sub>-based substrates including random macroporous silicon (macro-pSi), random micropillars and ordered micropillars. HAEC line has been one of the most commonly used models in endothelial dysfunction systems. Because of the capacity of these cells to adhere to the substrates, endothelial cells seem to be a good tool to screen new cardiovascular therapies. Indeed, cardiovascular disease (CVD) is the leading cause of morbidity and mortality in industrialized countries [57]. The causes of CVD are diverse and atherosclerosis is a common, progressive and multifactorial disease that is the clinical endpoint of an inflammatory process and endothelial dysfunction [58]. New cell culture methodological aspects need to be developed to optimize *in vitro* cellular models, and the first step is to test new substrates with different structures and with different surfaces modifications, for the growth and attachment of such human cells. Therefore, by examining the cellular behavior of HAEC cultured on various microtopographies, we can acquire a deeper understanding of the effects that the physical and chemical environment may have on the cell response. Eventually this could lead to the possible regulation of the cell fate.



In this work, the surfaces of SiO<sub>2</sub>-based microstructures were bio-activated to promote cell adhesion and surface stability. The chemical modification of the material surfaces with amino-silanes and homobifunctional aldehydes such as glutaraldehyde has been shown to efficiently immobilize proteins and antibodies [59, 60]. Flat silicon (used as control), oxidized macro-pSi and SiO<sub>2</sub> micropillars were functionalized following the APTES-GTA-Collagen sequence. APTES reacts with the hydroxylated surface and introduces an amine terminal functionality, which subsequently forms a covalent bond with GTA. Then the amine groups on the outer shell of the protein react with the free  $\omega$ -aldehyde of the GTA layer. The functionalization sequence was characterized by Fourier transform-infrared (FT-IR) spectroscopy.

We firstly studied the interaction between HAEC and flat silicon with and without collagen-functionalization to analyze the influence of the protein on the cell adhesion and growth after 2, 7 and 9 days of incubation. After analyzing the results obtained on flat Si, we used them as a control to investigate the behavior of HAEC on the different microstructures (i.e. macro-pSi, random micropillars and ordered micropillars) employing an incubation time of 2 days. SEM characterization showed the effect of the 3D-structured scaffolds on the cell adhesion, spreading and morphology compared to flat silicon. We also investigated how cellular behaviors are influenced by the arrangement of micropillars when we compared random and ordered patterns.

## 7.2 Experimental methods

### 7.2.1. Fabrication of SiO<sub>2</sub> Microstructured Substrates

**Macroporous Silicon.** Boron-doped (100) p-type Si wafers with a resistivity of 10-20  $\Omega$  cm were used for macro-pSi fabrication. Samples were prepared using the electrochemical etching process described in Chapter 3. An electrolyte of HF (40%) in DMF (1:10) was used to etch the silicon wafer at a current density of 5 mA cm<sup>-2</sup> for 1 h. Then the samples were rinsed with pentane and dried under a nitrogen flow. Subsequently, a thin layer of SiO<sub>2</sub> was grown on macro-pSi samples by thermal oxidation at 600 °C for 15 min.

**Random SiO<sub>2</sub> Micropillars.** The procedure was detailed in Chapter 3. Here, briefly, starting from p-type Si of resistivity 10-20  $\Omega$  cm, macropores were grown under galvanostatic conditions (5 mA cm<sup>-2</sup>) in a solution 1:10 of HF (40%) to DMF for 6 h. Then, an approximately 250 nm thick SiO<sub>2</sub> layer was grown by thermal oxidation at 1000 °C for 2 h in air. The oxide layer on the backside of the sample was removed by BHF etching. Next, the bulk silicon underwent anisotropic etching in aqueous TMAH (12%) at 85 °C until the pore tips appear protruding out of the sample backside.

**Ordered SiO<sub>2</sub> Micropillars.** To obtain ordered arrays of micropillars, a lithographic indentation process was performed with a 3  $\mu$ m lattice constant following to the patterning procedure explained in Chapter 3, section 1.2. Next, the patterned silicon wafers underwent the same electrochemical etching process described above to obtain random micropillars.

**Microstructure Characterization.** Random macro-pSi and SiO<sub>2</sub> micropillars were morphologically characterized by SEM using a scanning electron microscope (ESEM, FEI Quanta 600) operating at an accelerating voltage between 15 and 25 KeV.

### **7.2.2 Functionalization of the SiO<sub>2</sub> Microstructures**

Samples were treated in KOH 0.1 M for 3 min and HNO<sub>3</sub> 0.1 M for 10 min to increase the density of surface hydroxyl groups [61]. For collagen treatment of SiO<sub>2</sub> substrates, the surface was chemically modified following the APTES-GTA-Collagen sequence. Oxidized samples were silanized with APTES (Gelest) by exposure to 10% (v/v) solution in anhydrous toluene for 2 h at room temperature, then washed in succession with toluene, ethanol and deionized water and then dried under a nitrogen flow. Afterwards, the samples were thermally cured at 120 °C for 2 h. The reaction with GTA was performed by exposure to GTA 10% (v/v) solution in anhydrous ethanol (Electron Microscopy Sciences) for 1h at room temperature. The samples were rinsed in ethanol, deionized water and dried with nitrogen. Finally, the samples were incubated with collagen from bovine Achilles tendon (lyophilized, Sigma-Aldrich) 10 mg mL<sup>-1</sup> solution in PBS buffer (pH 7.4) at 4 °C overnight. Following, the substrates were thoroughly washed with PBS buffer and dried with a nitrogen flow.

### **7.2.3 Cell Seeding and Culture**

HAEC were purchased from Cascade Biologics™ (Portland, USA) and at the 5<sup>th</sup> passage were thawed and seeded on Nunclon™ Δ surface 6 or 12-well plates in the presence or absence (in the case of control conditions) of sterilized Si and SiO<sub>2</sub> substrates, at density of approximately 1.9x10<sup>4</sup> viable cells mL<sup>-1</sup> and 4x10<sup>3</sup> of viable cells cm<sup>-2</sup>. Through the whole experiment,

cells were maintained in M200 medium supplemented with 2% (v/v) low serum growth supplement (LSGS), 10 mg mL<sup>-1</sup> gentamicin, 0.25 mg mL<sup>-1</sup> amphotericin B (all from Life Technologies), 100 U mL<sup>-1</sup> penicillin and 100 mg mL<sup>-1</sup> of streptomycin (Laclinics).

Cells were seeded in complete cell culture medium and grown at 37 °C in a humidified incubator (Heracell 150) with atmosphere containing 5% CO<sub>2</sub>, and culture medium was replenished frequently with fresh medium.

**Cell Viability and Cytotoxicity.** Cell viability was assessed by morphology using phase-contrast microscopy and by trypan blue dye exclusion (Merck) in order to guarantee the viability of the cells before starting each set of experiments. The viability of the thawed HAEC was found to be >97%.

The extent of cytotoxicity of each experimental condition was determined by a colorimetric assay, which measures released lactate dehydrogenase (LDH) activity (The LDH Cytotoxicity Detection Kit, Roche Applied Science). Briefly, LDH enzyme is rapidly released into the cell culture supernatant when the plasma membrane is damaged. This result is a colorimetric reaction that can be measured at a wavelength of 492 nm. Thus, the activity of LDH released by the cells was measured in cell-free supernatants collected after different incubation times (1, 2, 4 and 7 days after thawing). Results are expressed as mean 492-optical density (OD) and standard deviation (SD: error bars) of LDH produced by the cells under each treatment condition.

**Scanning Electron Microscopy.** The morphology and shape of cells adhering to the functionalized silicon substrates were observed with a SEM (JEOL, JSM-6400). The adhered HAECs were fixed in a fixative containing 2.5% GTA / 0.1 M PBS at room temperature for 2 h. After washing twice

with 0.1 M PBS, the cells were postfixed with 1% osmium tetroxide at room temperature for 1 h. The cells were then washed twice with PBS, dehydrated through serial gradients of ethanol (10 min per each gradient), and finally dried out by the critical point dryer Baltec CPD 030. The cells along with the substrates were sputtered with gold at a current of 15 mA for 3 min by the ion sputter EMITEC K575X. SEM imaging was conducted at voltages ranging from 5-10 kV.

### ***Staining on Actin and Nuclei, and Fluorescence Confocal Microscopy.***

HAECs were cultured on functionalized and non-functionalized flat Si for 2, 7 and 9 days. SiO<sub>2</sub> microstructured substrates functionalized with collagen were incubated with HAECs for 2 days. After cell culture experiments, culture media was removed and cells were washed twice with PBS at 37 °C. The cells were fixed with a 4% (w/v) solution of paraformaldehyde in PBS for 30 min at room temperature. After washing two times more with PBS, the substrates were immersed in 0.2% Triton-X 100 in PBS for 10 min at room temperature to permeabilize the cell membrane. After rinsing with PBS two times, the actin filaments and nuclei were stained in dark at room temperature. Actin-stain 670 phalloidin (Tebu-Bio) was used to stain the actin filaments (200 nM, 30min), while NucGreen Dead 488 (Life Technologies) was used to stain the nuclei (2 drops mL<sup>-1</sup>, 10min). Each sample was washed three times with PBS, and after mounting on microscope slides using an anti-fade mounting media, the samples were kept overnight in dark at room temperature. Stained cells were kept at 4 °C in dark until microscope observations. The fluorescence images were acquired using a Nikon Eclipse TE2000-E inverted microscope, equipped with a C1 laser confocal system (EZ-C1 software, Nikon). 633 laser and 488 nm argon lasers were used as excitation sources for Phalloidin and NucGreen, respectively.

## **7.3 Results and Discussion**

### **7.3.1 Surface Characterization**

Substrates for HAEC cells culture were all based on the formation of macro-pSi via anodization of boron-doped p-type Si wafers [62]. Three different types of samples were fabricated to study the cellular response on surfaces with assorted three-dimensional geometries. The appearance of the generated microtopographical samples used in this study is shown in Figure 7.1. Macroporous silicon formed at a constant current density of 5 mA cm<sup>-2</sup> presents an average pore diameter of approximately 1.4 μm and an interpore distance of about 3 μm determined by image analysis with ImageJ [63]. Likewise, the porosity of the sample was found to be about 27% (Figure 7.1A). An identically formed macro-pSi substrate was used as precursor of randomly organized micropillars. Figure 7.1B shows micropillars of 1.9 μm diameter on average, 3 μm interpore distance and 38% surface coverage, approximately. The dissimilar geometrical features found between micropillars and their preceding macropores are due to unstable macropore formation during the first few micrometers of growth in depth. After that initial period, some nucleated pores disappear and regroup with the neighbors to grow perpendicular to the surface in a steady regime. Ordered micropillar arrays were fabricated starting from lithographically patterned silicon. A squared lattice constant of 3 μm was chosen considering the interpore separation obtained for random macropores under the given electrochemical conditions. Ordered micropillar arrays presented a surface coverage of 30% and a diameter of 1.8 μm, practically equal for all micropillars (standard deviation of 0.01 μm), as it can be seen in Figure 7.1C.

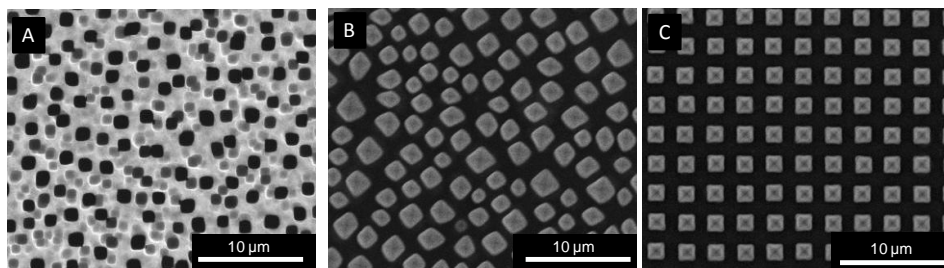


**Figure 7.1.** Top-view SEM images of SiO<sub>2</sub> microstructures A) macro-pSi; B) random SiO<sub>2</sub> micropillars and C) ordered SiO<sub>2</sub> micropillars.

A surface chemical treatment was performed on the substrates to improve cell adhesion and surface stability following the APTES-GTA-Collagen sequence. The reaction scheme is presented in Figure 7.2.

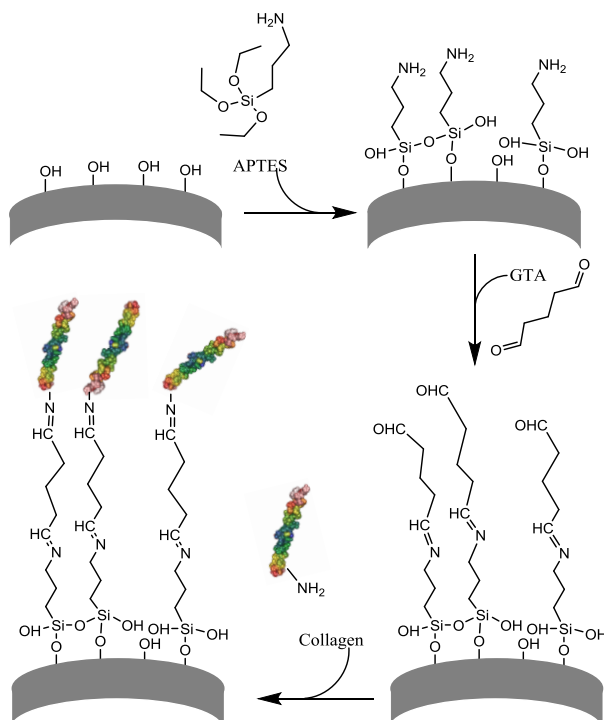


**Figure 7.2.** Schematic representation of the surface chemical treatment on silicon oxide samples to obtain a terminal collagen functionalization following the APTES-GTA-Collagen sequence.

Nano-pSi substrates of high surface area (see Chapter 4) were used to analyze the surface chemistry of the functionalized samples by transmission FT-IR. Starting from freshly-prepared porous silicon, an oxidizing pre-treatment of the surface is essential for subsequent silanization. Thus, the Si-H groups of the as-anodized sample are hydrolyzed to form an OH-terminated surface. The characteristics of silicon oxide and silanols emerge at  $800\text{ cm}^{-1}$  for (Si-O-Si) and in a saturated band between  $1000$  and  $1200\text{ cm}^{-1}$  for Si-O. A broad -OH related stretching mode appears between  $2600$  and  $3800\text{ cm}^{-1}$ , associated to both surface silanols and water absorbed by hydrogen bonding therein. And finally, the  $\delta(\text{H-O-H})$  mode at  $1630\text{ cm}^{-1}$  that is related to physisorbed water (Figure 7.3A). After APTES silanization, the  $\text{CH}_x$  stretching modes appear between  $2800$  and  $3000\text{ cm}^{-1}$ , which are assigned to the asymmetric and symmetric stretching of the  $\text{CH}_2$  aliphatic groups and also to some unhydrolyzed ethoxy groups [64]. Two peaks at  $3371$  and  $3304\text{ cm}^{-1}$  are attributed to the N-H asymmetric and symmetric stretching of the amine terminal group of the APTES molecule. The broad band between  $1500$  and  $1700\text{ cm}^{-1}$  is related to the  $\text{NH}_2$  and  $\text{NH}_3^+$  bending modes [64] (Figure 7.3B). GTA grafting on APTES is evidenced by the appearance of a peak at  $1720\text{ cm}^{-1}$  that we assign to the stretching mode of the carbonyl group. Furthermore, the absorptions previously assigned to the  $\nu(\text{N-H})$  extinguish (Figure 7.3C). Peaks in the range between  $1550$  and  $1800\text{ cm}^{-1}$  are related to the formation of amide bond between APTES and GTA. The final step is the binding of collagen to the carbonyl-terminated surface. The aldehyde groups react with amino group in the collagen molecule to form an amide covalent bond. Thus, the peak at  $1720\text{ cm}^{-1}$  previously assigned to the  $\nu(\text{C=O})$  diminishes its intensity. The band centered at  $1645\text{ cm}^{-1}$  increases



due to vibrations related to amide I groups present in the collagen molecule (Figure 7.3D).

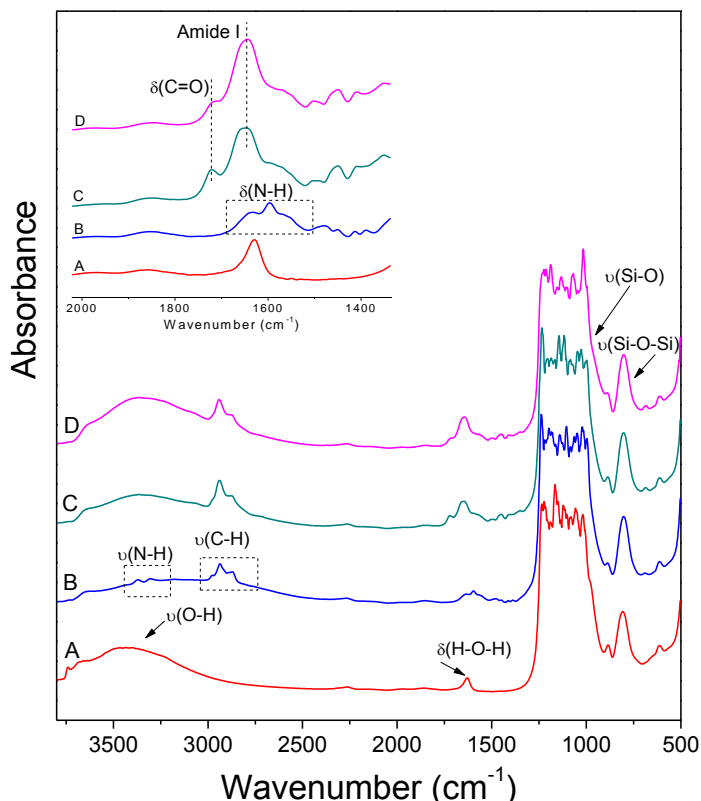


**Figure 7.3.** Transmission FTIR spectra of A) oxidized pSi; B) APTES-functionalized pSi; C) GTA docking on APTES-functionalized pSi and D) collagen immobilization on GTA-APTES-functionalized pSi.

### 7.3.2 Cell Culture on Flat Si

Firstly, we studied the cell response towards oxidized flat silicon and the biocompatibility of these substrates as a first approach to understanding the HAEC behavior. Flat silicon was thermally oxidized to create a thin layer of SiO<sub>2</sub>, and then a set of samples underwent surface modification with APTES-GTA-Collagen. Cell culture on flat Si with and

without collagen was performed and examined after 2, 7 and 9 days. At each time, the silicon substrates were washed to remove nonadherent and dead cells, and then the remaining cells were fixed. A graph summarizing the number of cells per area unit is shown in Figure 7.4.

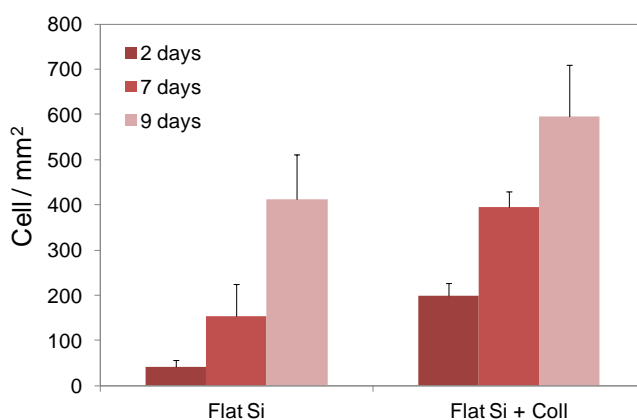


**Figure 7.4.** Number of HAEC cells per area unit attached to flat Si with and without collagen functionalization after 2, 7 and 9 days (left columns to right columns).

The experimental results show that the initial cell adhesion and growth is significantly lower on bare flat Si than on collagen-functionalized flat Si. Representative SEM images of the observable fact are shown in Figure 7.5A, D. After some days the difference in growth and proliferation of HAEC continues, and the number of cells reaches an average of 154 and 394 cells per mm<sup>2</sup> after 7 days on non-functionalized and functionalized flat Si, respectively (Figure 7.5B, E). After 9 days, about 70% confluency is observed on bare flat silicon (Figure 7.5C) whereas HAEC reaches confluence on collagen-functionalized flat silicon and therefore no more space is left for the adherent cells to grow as a monolayer (see Figure 7.5D). When the surface is modified with collagen, the number of cells is higher on flat Si substrates, as we expected. The results obtained with

collagen are in accordance with studies showing collagen promoting cell attachment, but not increasing growth and proliferation [56].

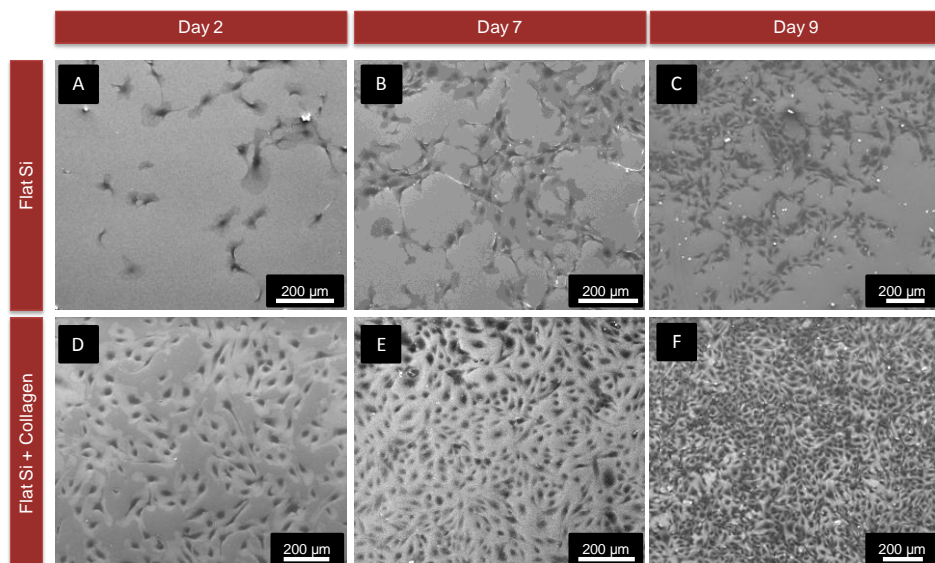


**Figure 7.5.** SEM images of HAEC on flat Si (A, B and C) and collagen-functionalized flat Si (D, E and F) after 2, 7 and 9 days incubation (left column to right column).

### 7.3.3 Cell Growth and Cytotoxicity on Microstructured $\text{SiO}_2$

After verifying the enhancement of cell adhesion and spreading on flat Si due to the functionalization with collagen, we resolved to perform the same chemical modification in the different types of microstructures to study the cell behavior following the same functionalization sequence APTES-GTA-Collagen.

An adherent human endothelial cell line was chosen to study the influence of the substrate topography on HAEC response. Figure 7.6 shows representative SEM images of cells growing on silicon oxide microstructures (i.e. macroporous silicon, random micropillars and ordered micropillars) after 2 days incubation. It can be clearly observed

from the SEM images that the shape of cells attached on microstructured substrates differs from the normal fibroblastic morphology observed on flat silicon (Figure 7.6A). Flat, well-spread cells are found on macroporous substrates (Figure 7.6B) whereas mainly round cells are observed on both random and ordered micropillars (Figures 7.6C, D).

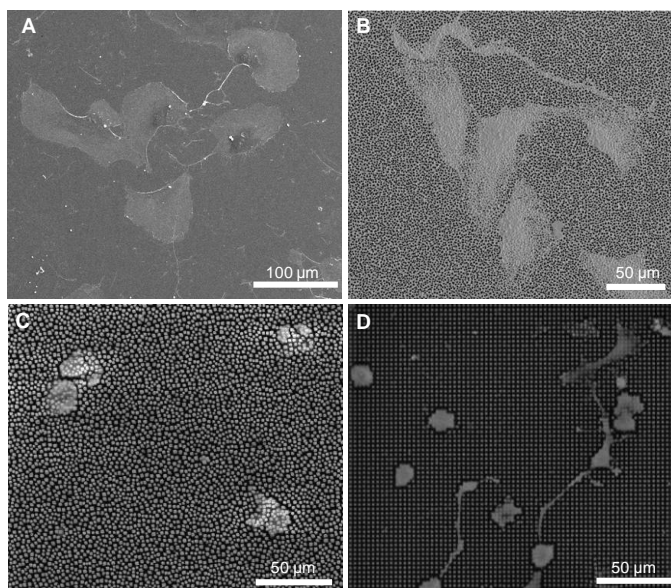


**Figure 7.6.** SEM images of HAEC after 2 days incubation. A) Flat Si; B) random macro-pSi; C) random micropillars and D) ordered micropillars.

The effect of the substrate topography over the cell growth after 2 days incubation was analyzed from the SEM images. Collagen functionalized flat silicon was used as control. As seen in the graph in Figure 7.7, the number of cells was lower on macro-pSi and random micropillars, compared to flat Si. However, in the case of ordered micropillars, the number of cells is significantly higher than on control flat silicon.

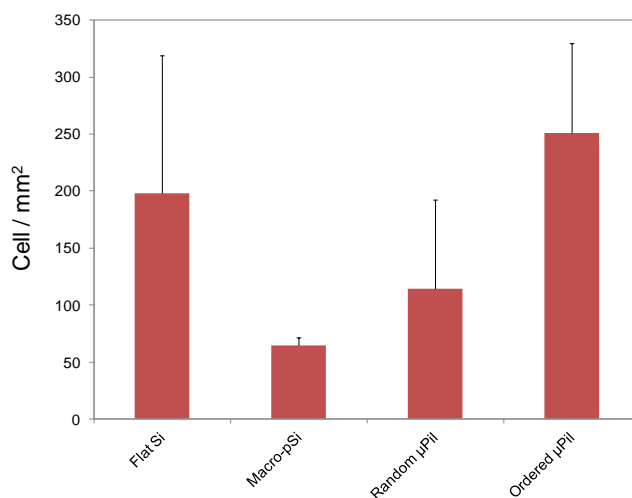


**Figure 7.7.** HAEC attached to various types of SiO<sub>2</sub> microstructures. Flat silicon was used as control. Cells were counted per surface measuring three areas per sample. Mean values are expressed as cell number per mm<sup>2</sup> with error bar corresponding to standard deviation.

Cytotoxicity was determined by a colorimetric assay, which measures the activity of released LDH (see Figure 7.8). LDH enzyme is released into the cell culture when the membrane is damaged. Thus, an increase of LDH is generally associated with a cellular injury. After a period of 7 days, the production of LDH activity released increases in all the silicon substrates and also in the blank control (cells incubated in a standard well plate without silicon substrates). These results indicate that the presence of the silicon or SiO<sub>2</sub>-based microstructures in the culture medium do not induce cytotoxicity *per se*. That suggests that cytotoxicity could be attributed to the high rate of confluency of the cells on the well plate after seven days of growing.

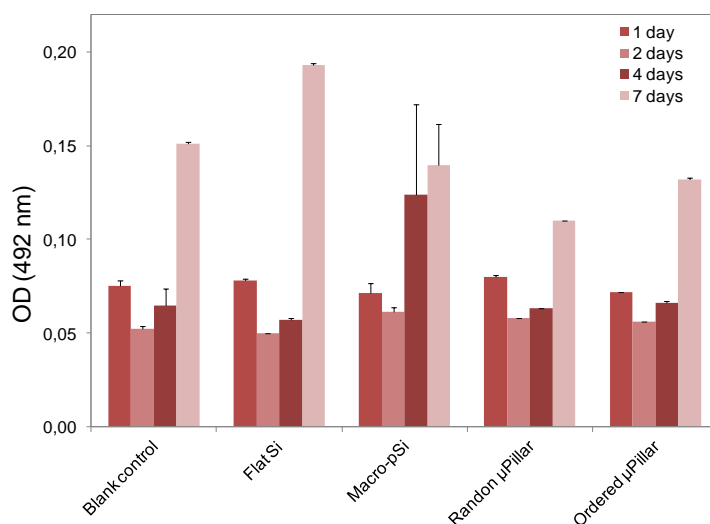


**Figure 7.8.** LDH cytotoxicity assay showing the results of HAEC cultures in different substrates after 1, 2, 4 and 7 days of incubation. Supernatants were assayed for LDH release and expressed as mean of 492 nm OD.

### 7.3.4 Cell Morphology on SiO<sub>2</sub> Microstructures

SEM microscopy was employed to study the effect of the microstructures topography on the morphology of the adhered HAEC, and to determine cell circularity and cell surface area. Representative images of HAEC cells adhered to various microstructured SiO<sub>2</sub> substrates and to flat silicon as control after 2 days of incubation are shown in Figure 7.9.

On macro-pSi with collagen the cell appears with a well spread cytoskeleton and protrusion formation outside of the cell membrane. Macro-pSi anchors the cells firmly, providing them with enough space to spread because of the abundant flat silicon surface present around the pore and the micrometer-size features in this type of structure. On this substrate, it is visible how the cell spreads on the surface and part of it penetrates inside the macropores (Figure 7.9F, J). The cells acquire a

mostly two-dimensional shape with formation of flattened large lamellipodia, which serves as anchorage points. Filopodia is not present in this type of substrate. Similar shapes were observed on collagen-functionalized flat Si, even though filopodia predominates over lamellipodia as anchoring features (Figure 7.9A, E, I). If we compare flat Si to macro-pSi, the cells on macro show two main differences. First, the pseudopods extend on the flat part of the substrate by converting the surface of the macropore in the substrate. And second, the pseudopods of the cell can grow along the macro-pSi scaffold (see magnification in Figure 7.9J). The presence of micropillars dramatically altered the cell morphology: HAEC on micropillars appeared less elongated and significantly more compact and rounded after 2 days incubation. On macro-pSi, the cell bodies were mainly localized on the top of the substrate, whereas on micropillars, cells adhered to the top of the pillars and in between them. The main part of the body appeared trapped between the pillars and in some cases suspended from pillar to pillar. The substrate topography limits the well-spread morphology observed in HAEC on macro-pSi and flat Si. Comparing random and ordered micropillars, more long and thin extensions appeared following the topographical features and anchoring around the ordered micropillars (see Figure 7.6C, D).

It was also observed that the HAEC grasping the micropillars can make them bend as an action of traction forces (see Figure 7.9K, H). Despite the stiffness of SiO<sub>2</sub> micropillars, their thin wall and hollow core lend them a relative elasticity that led to deflections due to cell contraction forces. These bending deflections are linearly proportional to the tractions forces exerted on micropillars by the adherent cells according to Hooke's law [65, 66]. Further work will be needed to control the mechanical properties of

the micropillars and determine cell attraction force acting on the substrates.

To acquire measurable understanding of HAEC surface adhesion and morphology, cell surface area and circularity studies were determined for the different substrates.

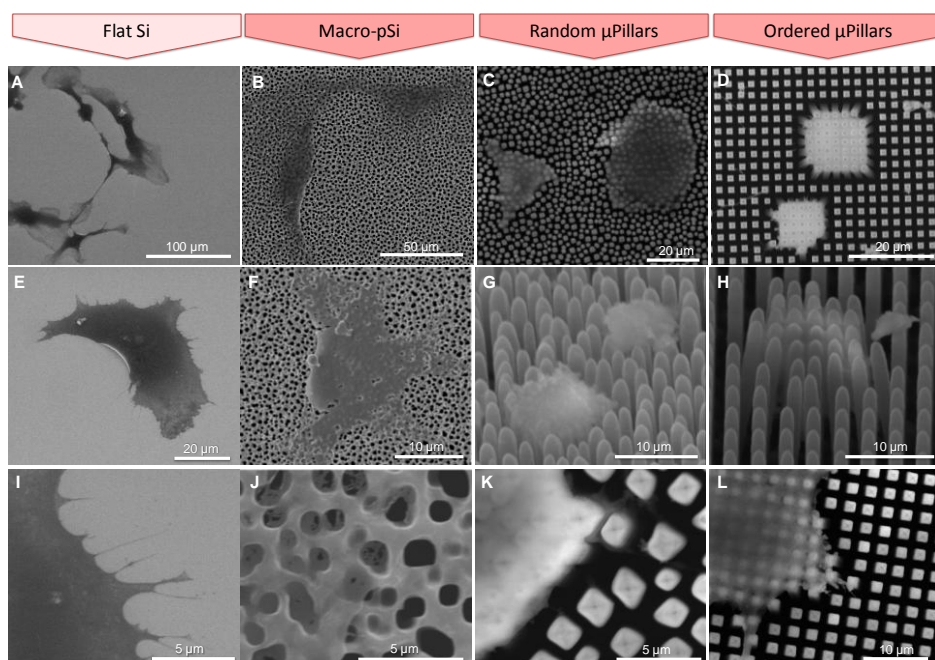


**Figure 7.9.** Scanning electron microscopy of HAEC after 2 days incubation on various SiO<sub>2</sub> microstructured substrates. A,E,I) Flat Si; B,F,J) macro-pSi; C,G,K) random micropillars and D,H,L) ordered micropillars.

We first investigated the spreading behavior by quantifying the effect of the SiO<sub>2</sub> microstructures on cell surface areas. On flat silicon the HAEC cells spread and covered a very large area ( $1347 \pm 719 \mu\text{m}^2$ ), very similar to that found for cells adhered to collagen-functionalized macro-pSi ( $1292 \pm 701 \mu\text{m}^2$ ). However, the presence of micropillars caused a noticeable modification of the cell size (Figure 7.10A). Both random and ordered



micropillars had a significantly lower cell surface area compared to the other surfaces. The mean surface area of the HAEC on the random and ordered micropillars was 528 and 331  $\mu\text{m}^2$ , respectively, showing a fold reduction in size of 2.5 for random and 4.0 for ordered micropillars compared to cells on the collagen-functionalized flat Si. The zoomed tilted images of micropillars (Figure 7.9G, H) show how the cells tend to grow in depth along the micropillars to find focal adhesion points on the vertical walls. These results suggest a three-dimensional growth pattern on micropillars, whereas on macroporous silicon the growth is mainly two-dimensional.

As a measure of cell morphology, the cell circularity was also analyzed with values between 0 and 1, where 0 represents an elongated cell in a line and 1 a perfect circular shape. HAEC had a very similar circularity on macro-pSi compared to that found on flat Si (Figure 7.10B). Slightly higher circularity values were found on random micropillars. However, it is interesting to note the significant increase in the circularity on ordered micropillars. The cell circularity shows that HAEC are significantly more elongated on macro-pSi than on micropillars, and therefore they show an analogous response on flat Si and macro-pSi. Considering that both random and ordered micropillars were very similar in diameter and surface density, the results suggest that the difference in shape is induced by the micropillar arrangement.

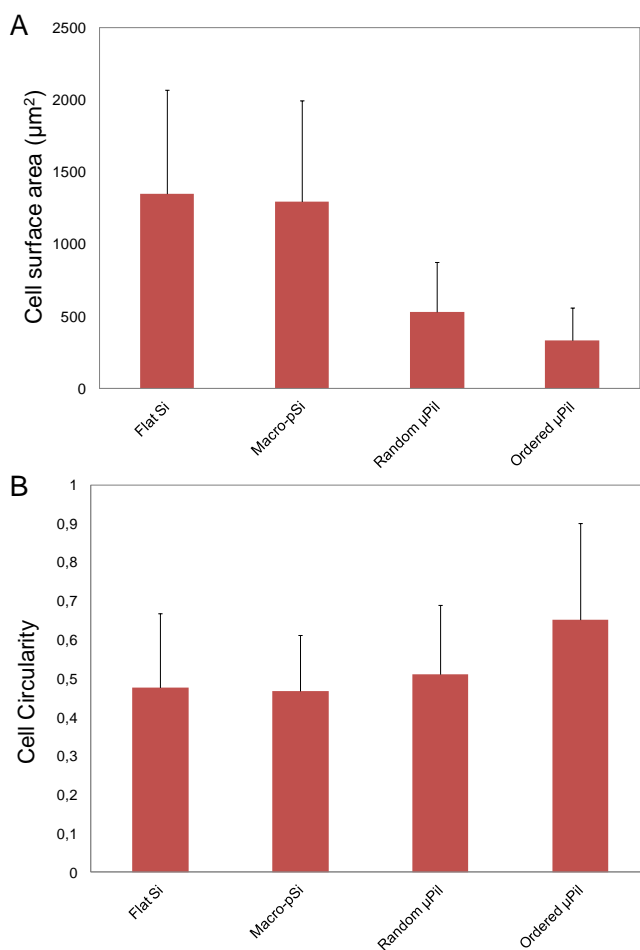


**Figure 7.10.** A) Mean cell surface area calculated and B) mean cell circularity calculated from SEM images after 2 days of incubation. For the cell circularity 0 represents a line and 1.0 a circle. An average number of 40 cells were analyzed per sample to calculate the standard deviation.

Similar morphological observations can be analyzed from the confocal microscope. We explored how the substrate morphology of the substrates influenced the cytoskeleton reorganization by focusing on actin as a structural component (red labeled). Figure 7.11 shows confocal imaging for HAEC culture on flat Si, macro-pSi and random and ordered micropillar

substrates modified with collagen after 2 days of incubation. In control flat Si and macro-pSi, the HAEC cytoskeleton appeared elongated and aligned along the major axis of the cell. Herein, characteristic strong actin filaments were distributed across the center of the cell bodies and relatively well-organized in the cell periphery (see Figure 7.11A, B). The association of actin filaments has been associated with the formation of strong focal adhesion [29]. Therefore, for cells on flat Si and macro-pSi, the focal adhesion points overlap with the ends of the actin filaments. However, the cells adhered to micropillars show actin-rich regions colocalized with the micropillars walls, although it should be noted the lack of filament formation (Figure 7.11C, D). This suggests that there is a prevalent interaction between micropillars and cell cytoskeleton. Stabilization of the actin cytoskeleton around and along the micropillars could be attributed to the increased cell adhesion through a physical entrapment of the cells. Therefore, the shape and size of the cell is closely related to the ordering and arrangement of the micropillars. The shape of the nucleus is also influenced by the morphology of the substrate. Usually the cell nuclei adopt the shape of spheres or ellipsoids, with always convex contours. That is how they predominantly appear in flat Si and macro-pSi substrates. However, on micropillars, the nuclei seem to mimic the arrangement of the attached micropillars due to a probable entrapment. Fluorescence microscopy observation also indicates that the micropillars protrude through the nucleus. Part of the nucleus seems to be extruded by the nearest neighbor micropillar, occasionally leading to a concave shape as in Figure 7.11C, D. The ordering of the micropillars also influenced the nuclei shape. On random micropillars, the shape tends to be circular or elongated, depending on the distribution of the cytoskeleton. Conversely, for ordered

micropillars the nuclei are inclined to adopt the shape of the micropillar arrangement, i.e. a rounded-square contour.

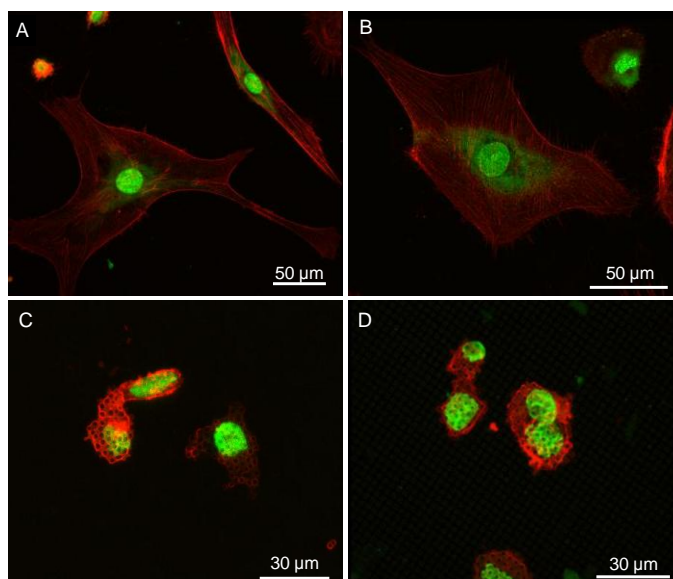


**Figure 7.11.** Fluorescence confocal microscopy images of HAEC after 2 days of incubation. Cells were stained with NucGreen for the nucleus and Phalloidin for the actin filaments. A) Flat Si; B) macro-pSi; C) random micropillars and D) ordered micropillars.

## 7.4 Conclusions

Here we have studied three different SiO<sub>2</sub>-based microstructures chemically modified with collagen to evaluate the effect of the topography and ordering on cell attachment and morphology of HAEC. First, collagen was proved to favor the adhesion of endothelial cells on flat silicon substrates. Then, HAEC were cultured on collagen-functionalized SiO<sub>2</sub> microstructures. The cytotoxicity observed after 7 days was due to the confluence of the cells and not to the SiO<sub>2</sub> substrates, as similar results

were found in the blank control. Microscopy analysis revealed significant differences in cell adhesion, spreading and morphology between the three different substrates after 2 days incubation. Cell adhesion and growth of HAEC was higher on ordered micropillars than on random micropillars or macro-pSi, with values even larger than those found on control flat Si. On macro-pSi, cells adhered firmly on the surface, and the pseudopods of the cell grow along the macro-pSi. Micropillars induced various impacts on the behavior of the HAEC *in vitro*. We observed an alteration in the cell spreading area and cell morphology including nuclei and body shapes distortion, and cytoskeletal reorganization. The cells grown on pillar substrates showed more compact and rounded morphology. The ordering of micropillar arrays was also observed to influence the cell growth and the shape of both cell body and nucleus. Patterned substrates generate cell patterns that seem to mimic the pillar arrangement. Thus, it is possible, to a certain extent, to control the adhesion, growth and morphology of HAECs. Cells adapt their molecular architecture developing a suitable morphology to feed and migrate themselves through those microstructured substrates ensuring their survival. Summarizing, these microstructured platforms offer a powerful tool to explore the complex interplay of events between biointerfaces and living cells. Nevertheless, more studies are needed to fully investigate the mechanical forces, focal adhesion formation and penetration of microstructures into the cell membrane.

## 7.5 References

- [1] Chen, C.S., M. Mrksich, S. Huang, G.M. Whitesides, and D.E. Ingber, *Geometric Control of Cell Life and Death*. Science, 1997. **276**(5317): p. 1425-1428.
- [2] Elnathan, R., M. Kwiat, F. Patolsky, and N.H. Voelcker, *Engineering vertically aligned semiconductor nanowire arrays for applications in the life sciences*. Nano Today, 2014. **9**(2): p. 172-196.
- [3] Andersson, A.-S., F. Bäckhed, A. von Euler, A. Richter-Dahlfors, D. Sutherland, and B. Kasemo, *Nanoscale features influence epithelial cell morphology and cytokine production*. Biomaterials, 2003. **24**(20): p. 3427-3436.
- [4] Choi, J.S., Y. Piao, and T.S. Seo, *Circumferential alignment of vascular smooth muscle cells in a circular microfluidic channel*. Biomaterials, 2014. **35**(1): p. 63-70.
- [5] Engler, A.J., S. Sen, H.L. Sweeney, and D.E. Discher, *Matrix Elasticity Directs Stem Cell Lineage Specification*. Cell, 2006. **126**(4): p. 677-689.
- [6] Engel, E., A. Michiardi, M. Navarro, D. Lacroix, and J.A. Planell, *Nanotechnology in regenerative medicine: the materials side*. Trends in Biotechnology, 2008. **26**(1): p. 39-47.
- [7] Collart-Dutilleul, P.-Y., E. Secret, I. Panayotov, D. Deville de Périère, R.J. Martín-Palma, V. Torres-Costa, M. Martin, C. Gergely, J.-O. Durand, F. Cunin, and F.J. Cuisinier, *Adhesion and Proliferation of Human Mesenchymal Stem Cells from Dental Pulp on Porous Silicon Scaffolds*. ACS Applied Materials & Interfaces, 2014. **6**(3): p. 1719-1728.
- [8] Zorlutuna, P., N. Annabi, G. Camci-Unal, M. Nikkha, J.M. Cha, J.W. Nichol, A. Manbachi, H. Bae, S. Chen, and A. Khademhosseini, *Microfabricated Biomaterials for Engineering 3D Tissues*. Advanced Materials, 2012. **24**(14): p. 1782-1804.
- [9] Bucaro, M.A., Y. Vasquez, B.D. Hatton, and J. Aizenberg, *Fine-Tuning the Degree of Stem Cell Polarization and Alignment on Ordered Arrays of High-Aspect-Ratio Nanopillars*. ACS Nano, 2012. **6**(7): p. 6222-6230.
- [10] Pan, Z., C. Yan, R. Peng, Y. Zhao, Y. He, and J. Ding, *Control of cell nucleus shapes via micropillar patterns*. Biomaterials, 2012. **33**(6): p. 1730-1735.
- [11] Brammer, K.S., C. Choi, C.J. Frandsen, S. Oh, and S. Jin, *Hydrophobic nanopillars initiate mesenchymal stem cell aggregation and osteo-differentiation*. Acta Biomaterialia, 2011. **7**(2): p. 683-690.
- [12] Kim, W., J.K. Ng, M.E. Kunitake, B.R. Conklin, and P. Yang, *Interfacing Silicon Nanowires with Mammalian Cells*. Journal of the American Chemical Society, 2007. **129**(23): p. 7228-7229.
- [13] Watari, S., K. Hayashi, J.A. Wood, P. Russell, P.F. Nealey, C.J. Murphy, and D.C. Genetos, *Modulation of osteogenic differentiation in hMSCs cells by submicron topographically-patterned ridges and grooves*. Biomaterials, 2012. **33**(1): p. 128-136.

- [14] Ricoult, S.G., M. Pla-Roca, R. Safavieh, G.M. Lopez-Ayon, P. Grütter, T.E. Kennedy, and D. Juncker, *Large Dynamic Range Digital Nanodot Gradients of Biomolecules Made by Low-Cost Nanocontact Printing for Cell Haptotaxis*. Small, 2013. **9**(19): p. 3308-3313.
- [15] Yang, K., K. Jung, E. Ko, J. Kim, K.I. Park, J. Kim, and S.-W. Cho, *Nanotopographical Manipulation of Focal Adhesion Formation for Enhanced Differentiation of Human Neural Stem Cells*. ACS Applied Materials & Interfaces, 2013. **5**(21): p. 10529-10540.
- [16] Flemming, R.G., C.J. Murphy, G.A. Abrams, S.L. Goodman, and P.F. Nealey, *Effects of synthetic micro- and nano-structured surfaces on cell behavior*. Biomaterials, 1999. **20**(6): p. 573-588.
- [17] Yang, L., L. Zhang, and T.J. Webster, *Nanobiomaterials: State of the Art and Future Trends*. Advanced Engineering Materials, 2011. **13**(6): p. B197-B217.
- [18] Kunzler, T.P., C. Huwiler, T. Drobek, J. Vörös, and N.D. Spencer, *Systematic study of osteoblast response to nanotopography by means of nanoparticle-density gradients*. Biomaterials, 2007. **28**(33): p. 5000-5006.
- [19] Curtis, A. and C. Wilkinson, *Topographical control of cells*. Biomaterials, 1997. **18**(24): p. 1573-1583.
- [20] Dalby, M.J., *Cellular response to low adhesion nanotopographies*. International journal of nanomedicine, 2007. **2**(3): p. 373.
- [21] Yang, M.T., N.J. Sniadecki, and C.S. Chen, *Geometric Considerations of Micro-to Nanoscale Elastomeric Post Arrays to Study Cellular Traction Forces*. Advanced Materials, 2007. **19**(20): p. 3119-3123.
- [22] Qi, S., C. Yi, S. Ji, C.-C. Fong, and M. Yang, *Cell Adhesion and Spreading Behavior on Vertically Aligned Silicon Nanowire Arrays*. ACS Applied Materials & Interfaces, 2008. **1**(1): p. 30-34.
- [23] Teo, B.K.K., S.T. Wong, C.K. Lim, T.Y.S. Kung, C.H. Yap, Y. Ramagopal, L.H. Romer, and E.K.F. Yim, *Nanotopography Modulates Mechanotransduction of Stem Cells and Induces Differentiation through Focal Adhesion Kinase*. ACS Nano, 2013. **7**(6): p. 4785-4798.
- [24] Ghibaudo, M., L. Trichet, J. Le Digabel, A. Richert, P. Hersen, and B. Ladoux, *Substrate Topography Induces a Crossover from 2D to 3D Behavior in Fibroblast Migration*. Biophysical Journal, 2009. **97**(1): p. 357-368.
- [25] Shalek, A.K., J.T. Robinson, E.S. Karp, J.S. Lee, D.-R. Ahn, M.-H. Yoon, A. Sutton, M. Jorgolli, R.S. Gertner, T.S. Gujral, G. MacBeath, E.G. Yang, and H. Park, *Vertical silicon nanowires as a universal platform for delivering biomolecules into living cells*. Proceedings of the National Academy of Sciences, 2010. **107**(5): p. 1870-1875.
- [26] Huang, J., S.V. Gräter, F. Corbellini, S. Rinck, E. Bock, R. Kemkemer, H. Kessler, J. Ding, and J.P. Spatz, *Impact of Order and Disorder in RGD Nanopatterns on Cell Adhesion*. Nano Letters, 2009. **9**(3): p. 1111-1116.
- [27] Hanson, L., Z.C. Lin, C. Xie, Y. Cui, and B. Cui, *Characterization of the Cell-Nanopillar Interface by Transmission Electron Microscopy*. Nano Letters, 2012. **12**(11): p. 5815-5820.
- [28] Piret, G., E. Galopin, Y. Coffinier, R. Boukherroub, D. Legrand, and C. Slomianny, *Culture of mammalian cells on patterned*

- superhydrophilic/superhydrophobic silicon nanowire arrays*. *Soft Matter*, 2011. **7**(18): p. 8642-8649.
- [29] So Yeon, K. and Y. Eun Gyeong, *Collective behaviors of mammalian cells on amine-coated silicon nanowires*. *Nanotechnology*, 2013. **24**(45): p. 455704.
- [30] Ingber, D.E., *Mechanical control of tissue growth: Function follows form*. *Proceedings of the National Academy of Sciences of the United States of America*, 2005. **102**(33): p. 11571-11572.
- [31] Chou, L., J.D. Firth, V.J. Uitto, and D.M. Brunette, *Substratum surface topography alters cell shape and regulates fibronectin mRNA level, mRNA stability, secretion and assembly in human fibroblasts*. *Journal of Cell Science*, 1995. **108**(4): p. 1563-1573.
- [32] Bissell, M.J. and M.H. Barcellos-Hoff, *The Influence of Extracellular Matrix on Gene Expression: Is Structure the Message?* *Journal of Cell Science*, 1987. **1987**(Supplement 8): p. 327-343.
- [33] Bettinger, C.J., R. Langer, and J.T. Borenstein, *Engineering Substrate Topography at the Micro- and Nanoscale to Control Cell Function*. *Angewandte Chemie International Edition*, 2009. **48**(30): p. 5406-5415.
- [34] Mendes, P.M., *Cellular nanotechnology: making biological interfaces smarter*. *Chemical Society Reviews*, 2013. **42**(24): p. 9207-9218.
- [35] Moraes, C., B.C. Kim, X. Zhu, K.L. Mills, A.R. Dixon, M.D. Thouless, and S. Takayama, *Defined topologically-complex protein matrices to manipulate cell shape via three-dimensional fiber-like patterns*. *Lab on a Chip*, 2014. **14**(13): p. 2191-2201.
- [36] Popat, K.C., L. Leoni, C.A. Grimes, and T.A. Desai, *Influence of engineered titania nanotubular surfaces on bone cells*. *Biomaterials*, 2007. **28**(21): p. 3188-3197.
- [37] Su, W.-T., Y.-F. Liao, C.-Y. Lin, and L.-T. Li, *Micropillar substrate influences the cellular attachment and laminin expression*. *Journal of Biomedical Materials Research Part A*, 2010. **93A**(4): p. 1463-1469.
- [38] Ainslie, K.M., S.L. Tao, K.C. Popat, H. Daniels, V. Hardev, C.A. Grimes, and T.A. Desai, *In vitro inflammatory response of nanostructured titania, silicon oxide, and polycaprolactone*. *Journal of Biomedical Materials Research Part A*, 2009. **91A**(3): p. 647-655.
- [39] Trifonov, T., A. Rodriguez, F. Servera, L.F. Marsal, J. Pallares, and R. Alcubilla, *High-aspect-ratio silicon dioxide pillars*. *Physica Status Solidi A*, 2005. **202**(8): p. 1634-1638.
- [40] Leclerc, A., D. Tremblay, S. Hadjiantoniou, N.V. Bukoreshtliev, J.L. Rogowski, M. Godin, and A.E. Pelling, *Three dimensional spatial separation of cells in response to microtopography*. *Biomaterials*, 2013. **34**(33): p. 8097-8104.
- [41] Nikkhah, M., F. Edalat, S. Manoucheri, and A. Khademhosseini, *Engineering microscale topographies to control the cell-substrate interface*. *Biomaterials*, 2012. **33**(21): p. 5230-5246.
- [42] Fu, J., Y.-K. Wang, M.T. Yang, R.A. Desai, X. Yu, Z. Liu, and C.S. Chen, *Mechanical regulation of cell function with geometrically modulated elastomeric substrates*. *Nature methods*, 2010. **7**(9): p. 733-736.



- [43] Kim, D.-J., G. Lee, G.-S. Kim, and S.-K. Lee, *Statistical analysis of immuno-functionalized tumor-cell behaviors on nanopatterned substrates*. *Nanoscale Research Letters*, 2012. **7**(1): p. 1-8.
- [44] Wang, S., H. Wang, J. Jiao, K.-J. Chen, G.E. Owens, K.-i. Kamei, J. Sun, D.J. Sherman, C.P. Behrenbruch, H. Wu, and H.-R. Tseng, *Three-Dimensional Nanostructured Substrates toward Efficient Capture of Circulating Tumor Cells*. *Angewandte Chemie*, 2009. **121**(47): p. 9132-9135.
- [45] Cho, E.C., H. Kong, T.B. Oh, and K. Cho, *Protein adhesion regulated by the nanoscale surface conformation*. *Soft Matter*, 2012. **8**(47): p. 11801-11808.
- [46] Canham, L.T., *Bioactive silicon structure fabrication through nanoetching techniques*. *Advanced Materials*, 1995. **7**(12): p. 1033-1037.
- [47] Trifonov, T., A. Rodríguez, L.F. Marsal, J. Pallarès, and R. Alcubilla, *Macroporous silicon: A versatile material for 3D structure fabrication*. *Sensors and Actuators A: Physical*, 2008. **141**(2): p. 662-669.
- [48] Biju, V., *Chemical modifications and bioconjugate reactions of nanomaterials for sensing, imaging, drug delivery and therapy*. *Chemical Society Reviews*, 2014. **43**(3): p. 744-764.
- [49] Frieser, R.G., *Characterization of Thermally Grown SiO<sub>2</sub> Surfaces by Contact Angle Measurements*. *Journal of The Electrochemical Society*, 1974. **121**(5): p. 669-672.
- [50] Tang, X., M. Yakut Ali, and M.T.A. Saif, *A novel technique for micro-patterning proteins and cells on polyacrylamide gels*. *Soft Matter*, 2012. **8**(27): p. 7197-7206.
- [51] Pastorino, L., E. Dellacasa, S. Scaglione, M. Giulianelli, F. Sbrana, M. Vassalli, and C. Ruggiero, *Oriented collagen nanocoatings for tissue engineering*. *Colloids and Surfaces B: Biointerfaces*, 2014. **114**(0): p. 372-378.
- [52] Marsal, L.F., P. Formentín, R. Palacios, T. Trifonov, J. Ferré-Borrull, A. Rodríguez, J. Pallarès, and R. Alcubilla, *Polymer microfibers obtained using porous silicon templates*. *Physica Status Solidi A*, 2008. **205**(10): p. 2437-2440.
- [53] Aumailley, M. and B. Gayraud, *Structure and biological activity of the extracellular matrix*. *Journal of Molecular Medicine*, 1998. **76**(3-4): p. 253-265.
- [54] Foglia, M.L., D.E. Camporotondi, G.S. Alvarez, S. Heinemann, T. Hanke, C.J. Perez, L.E. Diaz, and M.F. Desimone, *A new method for the preparation of biocompatible silica coated-collagen hydrogels*. *Journal of Materials Chemistry B*, 2013. **1**(45): p. 6283-6290.
- [55] Yashiki, S., R. Umegaki, M. Kino-Oka, and M. Taya, *Evaluation of attachment and growth of anchorage-dependent cells on culture surfaces with type I collagen coating*. *Journal of Bioscience and Bioengineering*, 2001. **92**(4): p. 385-388.
- [56] Low, S.P., K.A. Williams, L.T. Canham, and N.H. Voelcker, *Evaluation of mammalian cell adhesion on surface-modified porous silicon*. *Biomaterials*, 2006. **27**(26): p. 4538-4546.
- [57] Celermajer, D.S., C.K. Chow, E. Marijon, N.M. Anstey, and K.S. Woo, *Cardiovascular Disease in the Developing World: Prevalences, Patterns, and*

- the Potential of Early Disease Detection*. Journal of the American College of Cardiology, 2012. **60**(14): p. 1207-1216.
- [58] Hansson, G.K., *Inflammation, Atherosclerosis, and Coronary Artery Disease*. New England Journal of Medicine, 2005. **352**(16): p. 1685-1695.
- [59] Wang, Z.-H. and G. Jin, *Covalent immobilization of proteins for the biosensor based on imaging ellipsometry*. Journal of Immunological Methods, 2004. **285**(2): p. 237-243.
- [60] Halliwell, C.M. and A.E.G. Cass, *A Factorial Analysis of Silanization Conditions for the Immobilization of Oligonucleotides on Glass Surfaces*. Analytical Chemistry, 2001. **73**(11): p. 2476-2483.
- [61] Fryxell, G.E., P.C. Rieke, L.L. Wood, M.H. Engelhard, R.E. Williford, G.L. Graff, A.A. Campbell, R.J. Wiacek, L. Lee, and A. Halverson, *Nucleophilic Displacements in Mixed Self-Assembled Monolayers*. Langmuir, 1996. **12**(21): p. 5064-5075.
- [62] Lehmann, V., *Macroporous Silicon*, in *Electrochemistry of Silicon*. 2002, Wiley-VCH Verlag GmbH. p. 183-205.
- [63] Schneider, C.A., W.S. Rasband, and K.W. Eliceiri, *NIH Image to ImageJ: 25 years of image analysis*. Nat Meth, 2012. **9**(7): p. 671-675.
- [64] Pasternack, R.M., S. Rivillon Amy, and Y.J. Chabal, *Attachment of 3-(Aminopropyl)triethoxysilane on Silicon Oxide Surfaces: Dependence on Solution Temperature*. Langmuir, 2008. **24**(22): p. 12963-12971.
- [65] Sniadecki, N.J., A. Anguelouch, M.T. Yang, C.M. Lamb, Z. Liu, S.B. Kirschner, Y. Liu, D.H. Reich, and C.S. Chen, *Magnetic microposts as an approach to apply forces to living cells*. Proceedings of the National Academy of Sciences, 2007. **104**(37): p. 14553-14558.
- [66] Schoen, I., W. Hu, E. Klotzsch, and V. Vogel, *Probing Cellular Traction Forces by Micropillar Arrays: Contribution of Substrate Warping to Pillar Deflection*. Nano Letters, 2010. **10**(5): p. 1823-1830.

UNIVERSITAT ROVIRA I VIRGILI

SILICON DIOXIDE MICROSTRUCTURES BASED ON MACROPOROUS SILICON FOR BIOMEDICAL APPLICATIONS.

María Alba Martín

Dipòsit Legal: T 153-2015

## ***Chapter 8***

---

### **Antibody-Functionalized SiO<sub>2</sub> Micropillars for Targeted Drug Delivery**

In the chemotherapy of cancer, its effectiveness is directly related to the treatment's ability to target and kill cancer while affecting as little as possible other healthy tissues. Thus, developing new, effective tumor-targeted drug delivery systems may be of high impact in the advance of tumor therapies.

In this chapter we present a multifunctional targeted drug delivery system that is developed from biocompatible silicon dioxide micropillars. The external surface and internal volume of the micropillars are available to be differently utilized: the hollow core is loaded with the hydrophobic anticancer drug camptothecin, thus micropillars become high-payload micropills; in the meantime, an antibody (anti-p75NTR) is conjugated to the external surface to actively target neuroblastoma cells. We assessed the ability of anti-p75NTR-functionalized micropillars to target neuroblastoma cells overexpressing p75NTR receptors compared to control cells. Cell viability assays were performed to demonstrate selective killing of neuroblastoma cells due to the targeting properties toward p75NTR receptor.

## 8.1 Introduction

Despite all the significant advances recently made in the chemotherapy of cancer, there are still many challenges that hamper treatment efficiency, such as poor therapeutic efficacy and deleterious side-effects. In this framework, target-specific drug delivery has emerged as an encouraging approach to enhance the uptake of the cytotoxic molecule in the specific tumor location. A broad palette of drug delivery systems have been explored for cancer therapy using specific targeting agents such as antibodies [1], peptides [2], aptamers [3] and vitamins (e.g. biotin [4] or folic acid [5]). The general idea is that the targeting moiety seeks and attaches to the cognate receptors overexpressed on the surface of the targeted cancer cells, resulting in the delivery of substantially higher fraction of the drug to the tumor site as opposed to healthy tissue. The drug delivery systems explored so far include polymeric micelles [6], liposomes [7], carbon nanotubes [8], quantum dots [9], gold nanoparticles [10] and iron oxide [11]. Drug carriers based on silicon and silicon oxide ( $\text{SiO}_2$ ) are of particular interest due to their biosafety [12] and tunable physico-chemical properties [13]. The ease to modify its surface chemistry for further coupling with biomolecules has also reinforced their use in biomedical sciences [14].

Nano- and micro-structures based on pSi have been explored for a number of therapeutic purposes including photothermal therapy [15], photodynamic therapy [16] and immunotherapy [17]. The available porous volume can be loaded with functional active agents such as antibiotics [18], enzymes [19] or siRNA [20]. In this context, in Chapter 6 we presented  $\text{SiO}_2$  micropillars as a non-targeted system for the pH-responsive delivery of an anticancer drug. Multifunctional pSi systems have been also investigated

for targeted drug delivery [17, 21]. Specifically, a pioneering drug delivery system based on pSi nanoparticles for the vectorization of drugs using specific antibody functionalization in cancer therapy has been recently proposed [1].

Microparticles with a well-controlled architecture promote the predictability of the drug delivery platform, which is crucial for improving the pharmacokinetics of the drug molecule carried and relevant to the pursuit of personalized chemotherapy regimens [22-24]. The combination of electrochemical etching and lithography enables the fabrication of monodispersed microparticles on the micrometer size scale with accurate control over geometry and dimension [25, 26]. Thus, the formation of tubular microparticles is easily scalable and can be performed in bulk on a single surface. The millions of resulting silicon microparticles have an identical shape and an ordered arrangement, in opposition to the polydisperse, low-aspect ratio microparticles obtained by ultrasonication or ball-milling of free-standing pSi films [27].

In addition to the versatile surface properties inherent to silicon dioxide [14], the unique architecture and particular disposition of SiO<sub>2</sub> micropillars allows the differential functionalization of the internal and external surfaces, as we have demonstrated in Chapter 5. Herein, we exploit this capability to develop a targeted drug delivery system. The chemically modifiable external surface can be selectively functionalized with targeting ligands to develop a site-specific drug delivery system and the large, hollow core can act as a reservoir for storing a substantial payload of anticancer or other drugs, thus creating targeted micropills. We attached anti-p75NTR to the external micropillar surface using an epoxy silane as a crosslinker to demonstrate the specific targeting of

neuroblastoma cells, which overexpress the p75 neurotrophin receptors (p75NTR) [28]. Subsequently, hollow cores of the micropillars were loaded with the anticancer drug camptothecin (CPT). CPT is a very powerful cytotoxic agent that targets a nuclear enzyme leading to growth inhibition and cell death [29]. However, CPT is a highly hydrophobic molecule and its delivery without inducing off-target adverse effects remains a challenge [30]. Hence, site-specific delivery of CPT using SiO<sub>2</sub> micropillars as biocompatible cargo carriers may lead a breakthrough in the chemotherapy of cancer.

## **8.2 Experimental methods**

### **8.2.1 Micropillars fabrication**

Firstly, macro-pSi was fabricated by electrochemical etching following the standard procedures outlined in Chapter 3, section 1.3. In order to obtain periodically arranged pores, we applied the lithographic and indentation process over a 6x6 mm<sup>2</sup> area, with 3 μm lattice constant. The sample was mounted in an electrochemical cell with the indented side exposed to the electrolyte, a solution 1:10 (v:v) of HF (40%, Sigma Aldrich) in DMF (Sigma Aldrich). Macropores were grown perpendicular to the surface by etching under galvanostatic conditions, applying a current density of 5 mA cm<sup>-2</sup>.

After straight, regular macropores were formed, an approximately 200 nm thick SiO<sub>2</sub> layer was grown by thermal oxidation at 1000 °C for 1.5 h in air. Then, the backside oxide layer was dissolved by BHF etch. Finally, the silicon bulk was anisotropically etched in aqueous TMAH (25%, Sigma Aldrich) at 85 °C. The oxide grown on the internal surface of the



macropores acted as TMAH etch stop and subsequently, the oxidized pore tips appeared protruding out of the wafer backside. This process was described in detail in Chapter 3, Section 2.1.

Macro-pSi samples and the subsequent silicon dioxide micropillars were morphologically characterized by scanning electron microscopy (SEM) using a FEI Quanta 600 environmental scanning electron microscope operating at an accelerating voltage between 15 and 25 kV. Micropillar structure was also characterized by transmission electron microscopy (TEM) using a JEOL 1011 operating in dark-field mode at 80 kV.

### **8.2.2 Modification of Outer Surface of Micropillars**

A sample pre-treatment in piranha solution for 2 h (2:1 mixture of  $\text{H}_2\text{SO}_4/\text{H}_2\text{O}_2$ ) was used for cleaning and increasing the number of available hydroxyl groups on the surface (Figure 8.1A). Subsequently, the surfaces were washed thoroughly with MilliQ water. After drying in an oven at 60 °C for 2 h, the outer surface of the substrates were modified by immersing pre-treated micropillars in a solution of 10% v/v (3-glycidyloxypropyl) trimethoxysilane (GOPS, Sigma-Aldrich) in anhydrous toluene for 30 min (Figure 8.1B) [31]. After rinsing with toluene several times, the modified micropillars were dried under a stream of nitrogen gas.

Anti-p75NTR antibodies were added at a concentration of 500  $\mu\text{g mL}^{-1}$  in sterile PBS (pH 7.4) on freshly epoxy-silane-coated micropillars then were stored at 4 °C for 16 h. Subsequently, to impede nonspecific attachment, modified micropillars were incubated in 5% BSA (Sigma Aldrich) in sterile PBS at pH 7 at 37 °C for 16 h (Figure 8.1C).

Freshly epoxy-silane-coated outer surface of micropillars were incubated with  $1 \text{ mg mL}^{-1}$  Dylight 549-conjugated mouse antihuman IgG (Abcam) for 16 h at  $4^\circ\text{C}$ . The outer surface of micropillars were then washed with sterile PBS (three times, 5 min each) to remove excessive and unattached antibodies. Micropillars were then examined using an inverted fluorescence microscope equipped appropriate filters (Nikon Eclipse Ti-S).

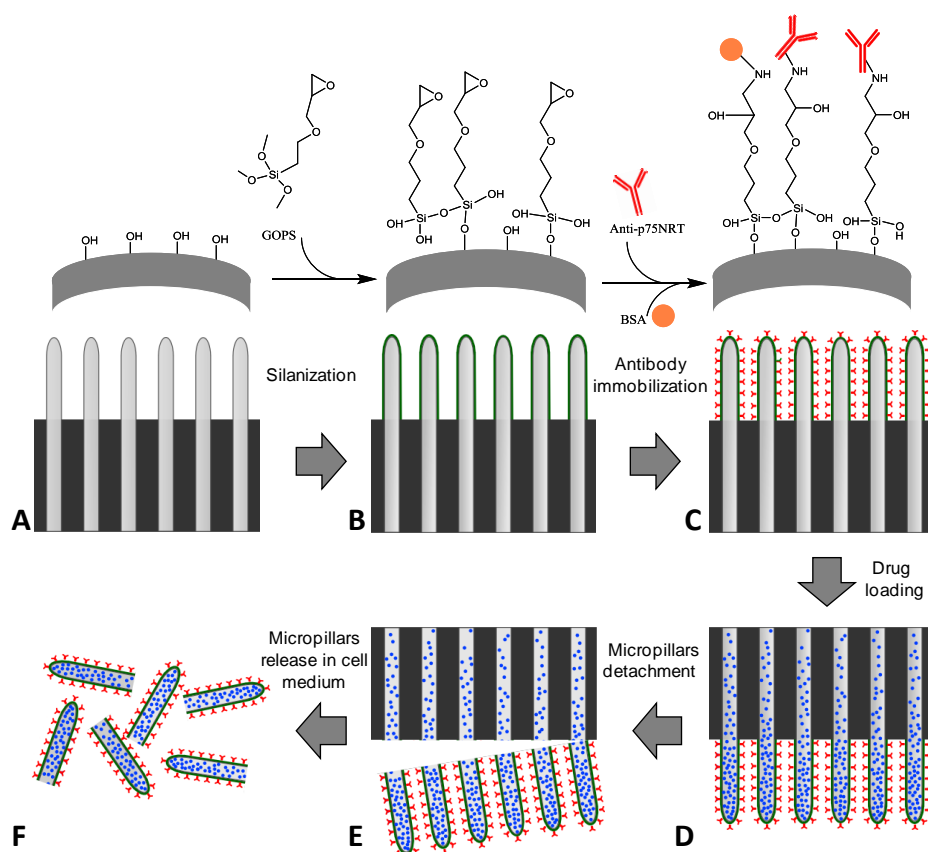


**Figure 8.1.** Schematic illustration of the method for the functionalization and drug loading of silicon dioxide micropillars. A) SiO<sub>2</sub> micropillars hydroxylation; B) GOPS silanization of the external surface; C) anti-p75NTR immobilization followed by BSA incubation to prevent nonspecific binding; D) CPT loading inside the micropillars; E) mechanical detachment of SiO<sub>2</sub> micropillars; F) micropillars release in the cell medium.

### **8.2.3 Fourier-Transform Infrared Spectroscopy**

Infrared investigation was performed with a Bruker Vertex 70 (Bruker Optics), using a DTGS detector and operating in air. Each spectrum is the average of 5212 scans, collected in transmission geometry and recorded over the range 360 – 4500  $\text{cm}^{-1}$  with resolution of 4  $\text{cm}^{-1}$ . All the absorbance spectra were calculated using the spectrum of the empty chamber as reference, and applying both the air compensation correction and a 13-points smoothing (Savitzky-Golay algorithm) available in OPUS software (Bruker Optics).

### **8.2.4 Loading of the Micropillars with Camptothecin**

After the silane grafting and anti-p75NRT immobilization on the external surface of  $\text{SiO}_2$  micropillars, the macropore side of the wafer was exposed and camptothecin (CPT) was drop loaded inside the macropores volume. CPT was dissolved in methanol to produce a 10  $\text{mg mL}^{-1}$  solution. The CPT solution was added drop wise 0.05  $\text{mL min}^{-1}$  into micropillars under laminar flow until the solvent was completely evaporated. This step was repeated 10-60 times depending on the length of the micropillars (Figure 8.1D).

The release experiments were performed by monitoring the fluorescence intensity of camptothecin in cell culture medium. The solution was excited at 350 nm, the fluorescence emission was monitored at 440 nm using a spectrofluorometer (PTI Quantmaster 40, Photon Technologies International, Edison, NJ, USA).

### **8.2.5 Cell Culture Procedures**

SH-SY5Y and BSR cells were seeded in wells of a 96-well plate at 10000 cells per well. After one day, cells were incubated with different CPT-loaded micropillar samples that were previously mechanically detached from the silicon substrate (Figures 8.1E, F). Cells were treated with the micropillars for 1 h at 50  $\mu\text{g mL}^{-1}$  concentration at 37 °C and 5% CO<sub>2</sub>. Following incubation, cells were washed with PBS to remove unattached micropillars and finally incubated in DMEM (10% FBS, 100 U mL<sup>-1</sup> penicillin and 100  $\mu\text{g/mL}$  streptomycin) in 5% CO<sub>2</sub> at 37 °C for 48 h to determine the effect of the micropillars treatment on cell viability by means of a LDH assay.

### **8.2.6 Cell Viability**

To determine the viability of micropillar treated cell cultures LDH released in culture supernatants was measured using an established assay (Abcam LDH-Cytotoxicity Assay Kit II) according to the manufacturer's instructions. After 48 h incubation with micropillar samples, 100  $\mu\text{L}$  of the cell suspension was centrifuged at 600 x g for 10 min, and the supernatant was transferred into a 96-well plate. To each well, 100  $\mu\text{L}$  LDH reaction mix was added, and after 30 min incubation at room temperature, the absorbance at 450 nm was measured. All experiments were repeated at least three times.

### **8.2.7 Laser Scanning Confocal Microscopy**

BSR cells and SH-SY5Y cells were grown on sterile coverslips at density of  $5 \times 10^4$  cells cm<sup>-2</sup>. After one day of incubation, cells were incubated with antibody- CPT loaded micropillars at 50  $\mu\text{g mL}^{-1}$  concentration for 1 h at 37 °C and 5% CO<sub>2</sub>. Cells were then washed with PBS, fixed for 10 min in a solution containing 4% paraformaldehyde EM grade (Electron Microscopy

Sciences), and subsequently permeabilized with 0.1% Triton X-100 (Sigma-Aldrich) for 5 min at room temperature. Nuclei of cells were stained with 1  $\mu\text{g}/\text{mL}$  Picogreen (Life Technologies) for 15 min at room temperature. The actin filaments in the cytoplasm were stained with 100  $\mu\text{M}$  TRITC-labeled phalloidin (Sigma-Aldrich) for 45 min. Finally, the coverslips were washed in PBS and mounted using fluoro-gel mounting reagent (ProSciTech). Stained cells were imaged using a confocal fluorescence microscope (Nikon A1) equipped with appropriate filters. An 405 nm argon laser was used as excitation source for CPT-loaded micropillars. Images shown are representative of at least three independent experiments and were obtained using identical sensitivity parameters.

### **8.2.8 Subcellular Localization of CPT and Imaging**

For CPT uptake by cells, SH-SY5Y cells were grown on sterile coverslips at density of  $5 \times 10^4$  cells  $\text{cm}^{-2}$ . After one day of incubation, antibody-CPT loaded micropillars at 50  $\mu\text{g mL}^{-1}$  concentration were incubated with cells for 1 h at 37 °C and 5%  $\text{CO}_2$ .

Following incubation, cells were washed with PBS for 5 min to remove unattached micropillars and finally incubated in DMEM (10% FBS, 100 U  $\text{mL}^{-1}$  penicillin and 100  $\mu\text{g mL}^{-1}$  streptomycin) in 5%  $\text{CO}_2$  at 37 °C for 30 min, 1 h, 2 h, 4 h and 8 h to determine CPT uptake by cells. Cells were then washed with PBS, fixed for 20 min in a solution containing 4% paraformaldehyde EM grade (Electron Microscopy Sciences), and subsequently permeabilized with 0.1% Triton X-100 (Sigma-Aldrich) for 1 min at room temperature. Nuclei of cells were stained with 2  $\mu\text{g mL}^{-1}$  Picogreen (Life Technologies) for 15 min at room temperature. The actin filaments in the cytoplasm were stained with 200  $\mu\text{M}$  TRITC-labeled phalloidin (Sigma-Aldrich) for 45 min. Finally, the coverslips were washed

in PBS and mounted using fluoro-gel mounting reagent (ProSciTech). Cells were imaged using a laser scanning confocal fluorescence microscopy (Nikon A1) with excitation at 405 nm for CPT.

### 8.3 Results and Discussion

High-aspect-ratio SiO<sub>2</sub> micropillars were obtained from ordered macro-pSi arrays [26, 32, 33]. These tubular macropores are prepared by electrochemical etching of lithographically pre-patterned silicon with a 3 μm lattice constant. SEM images in Figure 8.2A show the resulting SiO<sub>2</sub> micropillars with an external diameter of 1.8 μm. The pore size is given by the etching conditions, wafer resistivity and patterned lattice within a narrow range [34], but the length is highly tunable as is only dependent on the TMAH etching time, as described in Chapter 3. Micropillars of lengths ranging from 5 to 60 μm were used for this study. In Figure 8.2B we can observe micropillars mechanically detached from the substrate with a length of approximately 20 μm and a wall thickness of 200 nm.

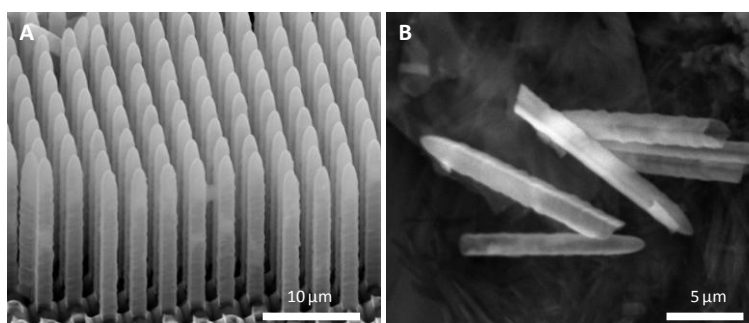


**Figure 8.2.** SEM micrographs of A) a tilted-view of ordered silicon dioxide micropillar arrays after TMAH etching of back side bulk silicon and B) detached micropillars.

The anti-p75NTR antibody was used in this study to target the p75NTR overexpressed receptor on SH-SY5Y neuroblastoma cells [28]. The BSR cell line was chosen as a negative control, which does not express p75NTR [28]. The immobilization of the antibodies was performed on the external side of the micropillars as schematically shown in Figure 8.1. Grafting between the SiO<sub>2</sub> surface and the specific antibody anti-P75NRT involved a silanization reaction with GOPS [31, 35]. Silanes can react with the surface hydroxyls present on the surface of the micropillar to form a covalent linkage through a condensation reaction. FT-IR spectroscopy was used to verify successful grafting of GOPS. Figure 8.3 shows the IR spectra of oxidized porous silicon before and after functionalization with GOPS. In the spectral region between 1200 and 1600 there are several bands related to CH<sub>x</sub> bending and scissoring modes, confirming the presence of the propylic chains, a motif within the GOPS molecule. In the CH<sub>x</sub> stretching region between 2800 and 3000 cm<sup>-1</sup> at least two bands appear centered at 2937 and 2877 cm<sup>-1</sup> which can be respectively assigned to the asymmetric and symmetric stretching modes of the C-H groups in the aliphatic chains. The spectra were collected in transmission mode in a nanoporous silicon sample hydroxylized and functionalized following the exact same procedures performed for the SiO<sub>2</sub> micropillars.

The anti-975NRT was immobilized onto the silanized outer side of micropillars via the covalent bond between the epoxy groups on the silane monolayer and the amine groups on lysine residues of the antibody [35]. The micropillars were incubated in 5% bovine serum albumin (BSA) to eliminate the residual binding capacity of GOPS. To confirm antibody grafting onto the silanized outer surface of the SiO<sub>2</sub> micropillars DyLight549-conjugated IgGs were incubated with GOPS-silanized and unsilanized micropillars and tubes were then dispersed in order to image

the outer walls of the tubes by fluorescence microscopy. As expected, binding of the red fluorescent DyLight549 IgG was observed only to the GOPS-silanized micropillars (Figure 8.4B).

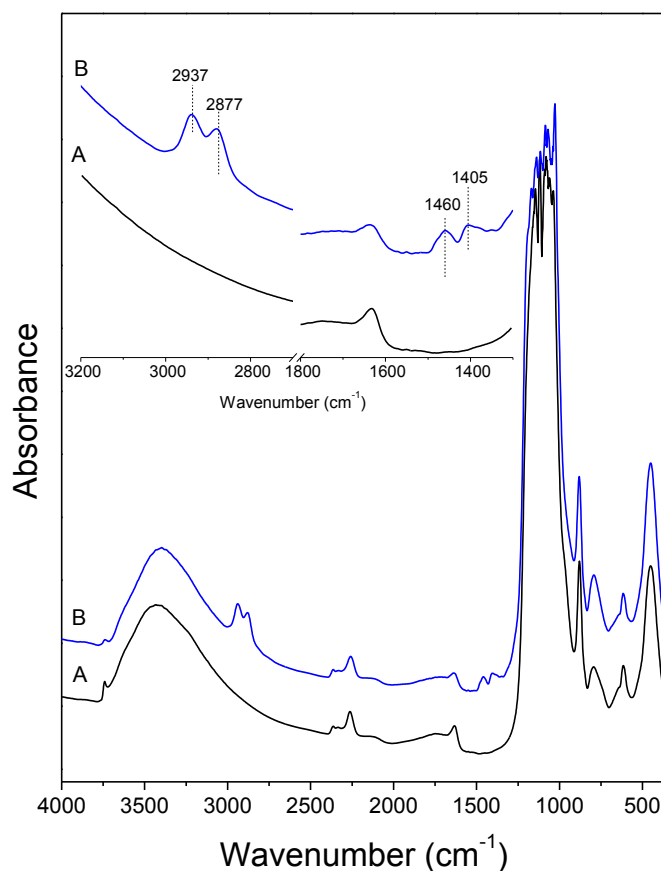


**Figure 8.3.** FT-IR of A) oxidized and B) GOPS-functionalized porous silicon.

Following the antibody immobilization, the internal volume of the micropillars was loaded with a CPT solution in methanol by drop coating at 0.05 mL min<sup>-1</sup>. Allowing the methanol to evaporate, the process was repeated 10-60 times to ensure a good filling and utilization of the hollow volume. CPT loading in the micropillars arrays was observed by fluorescence microscopy, exploiting the intrinsic luminescence of CPT at



405 nm. Figure 8.5A shows a pattern of blue dots that correspond with CPT-loaded micropillars arranged on the silicon substrate. The disparity in color intensity may reflect variation in the amount of CPT loaded between micropillars, due to blockages in CPT precipitation during loading. After CPT loading, the SiO<sub>2</sub> micropillars were detached from the wafer by mechanical scratching. This process does not affect the CPT loading in the micropillars (Figure 8.5B). Release kinetics of camptothecin from the loaded micropillars was obtained by monitoring the fluorescence intensity at 440 nm over time under excitation at 350 nm (Figure 8.6). The release experiments showed that 80% of the loaded CPT was released after 32 hours. After 5.5 h, 50% of the loaded CPT was released from the micropillars, rising to 80% after 32 h. These release kinetics are significantly slower than those described in previous experiments and are suitable for cancer targeting applications [1].

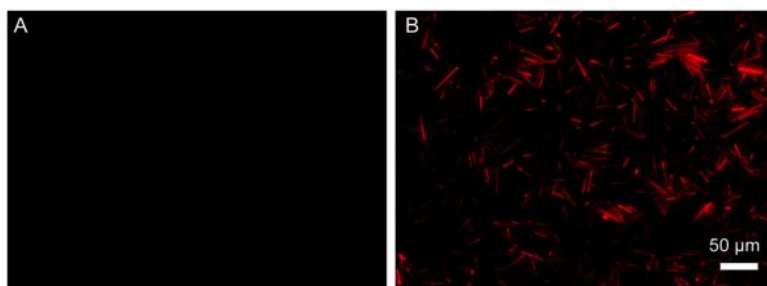


**Figure 8.4.** Binding of DyLight549-conjugated IgG to microtubules, analyzed by fluorescence microscopy. A) Native (unsilanized) microtubules and B) GOPS-silanized microtubules (control) were incubated with DyLight549-conjugated mouse antihuman IgG. The red chromophore ('DyLight549') indicates binding of IgG to the silanized microtubules.

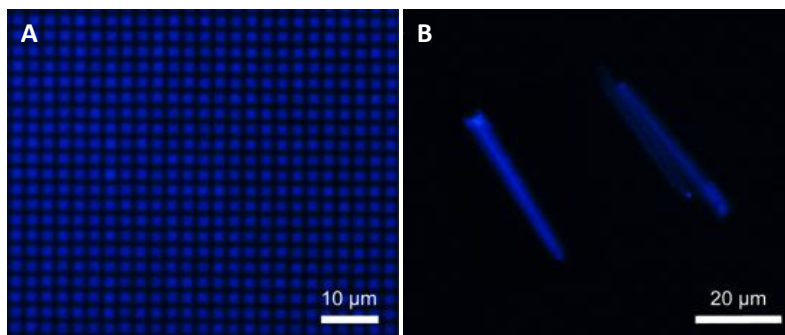


**Figure 8.5.** Fluorescence microscopy images of A) a top-view CPT-loaded SiO<sub>2</sub> micropillar arrays and B) individual SiO<sub>2</sub> micropillars loaded with CPT after mechanical detachment.

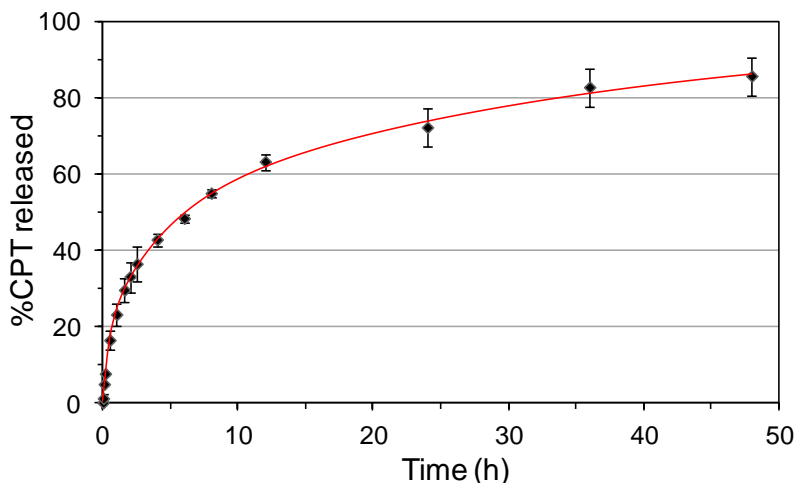


**Figure 8.6.** Release kinetics of CPT from loaded SiO<sub>2</sub> micropillars of 15 μm length.

The ability of the dispersed antibody-functionalized SiO<sub>2</sub> micropillars to target cancer cells was studied by incubating both SH-SY5Y neuroblastoma cells and BSR control cells for 1 h in cell medium supplemented with micropillars at 50 μg mL<sup>-1</sup> concentration. Cells were washed to remove any non-covalently attached micropillar and observed via microscopy. Note that this experiment was performed with non-drug-loaded SiO<sub>2</sub> micropillars. The majority of SH-SY5Y neuroblastoma cells

(60.2% of 431 counted cells) were associated with micropillars (Figure 8.7A), whereas not a single BSR cell was observed with micropillars attached (0% of 647 cells counted, Figure 8.7B). Hence, micropillar binding was verified to be specifically mediated by the anti-p75NTR antibody and not due to unspecific adsorption effects.

Finally, the ability of the antibody-functionalized micropillars loaded with CPT to target and kill cancer cells *in vitro* was investigated in neuroblastoma cells. SH-SY5Y and BSR cells were incubated with CPT-loaded micropillars at  $50 \mu\text{g mL}^{-1}$  concentration. After 1 h, the cell culture medium was replaced to remove unattached micropillars. This step ensures that CPT is not released to a significant extent into the cell culture medium from unattached micropillars. Washed cells were then incubated

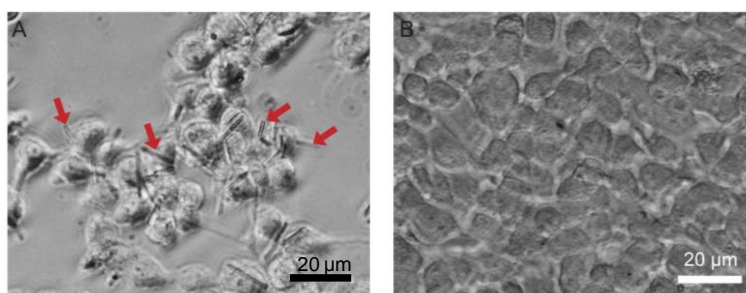


**Figure 8.7.** Antibody-functionalized  $\text{SiO}_2$  microtube attachment to cells. A) Brightfield microscopy image of SH-SY5Y cells after incubation with antibody-functionalized microtubes. The red arrows point to microtubes attached to cell membranes. B) Brightfield microscopy image of BSR cells after incubation with antibody-functionalized microtubes. No microtubes are visible.

for a further 48 h to determine the effect of the CPT release from anti-p75NTR-functionalized micropillars on cell viability by means of the LDH assay. The results are presented in Figure 8.8, micropillar preparations of different lengths were tested. These results clearly indicate that anti-

p75NTR-functionalized micropillars lacking CPT were non-toxic to the cells. Cell viability remains high for both SH-SY5Y cells and BSR cells after being exposed to the non-loaded anti-p75NTR-micropillars for 2 days, above 90% of untreated control measures. Upon incubation with anti-p75NTR-functionalized micropillars loaded with CPT, a reduction in viability to only 4-6% of untreated controls was observed after 2 days. In contrast, survival of BSR cells was unchanged after exposure to CPT loaded micropillars. Micropillar length was not found to influence the induction of cell death.

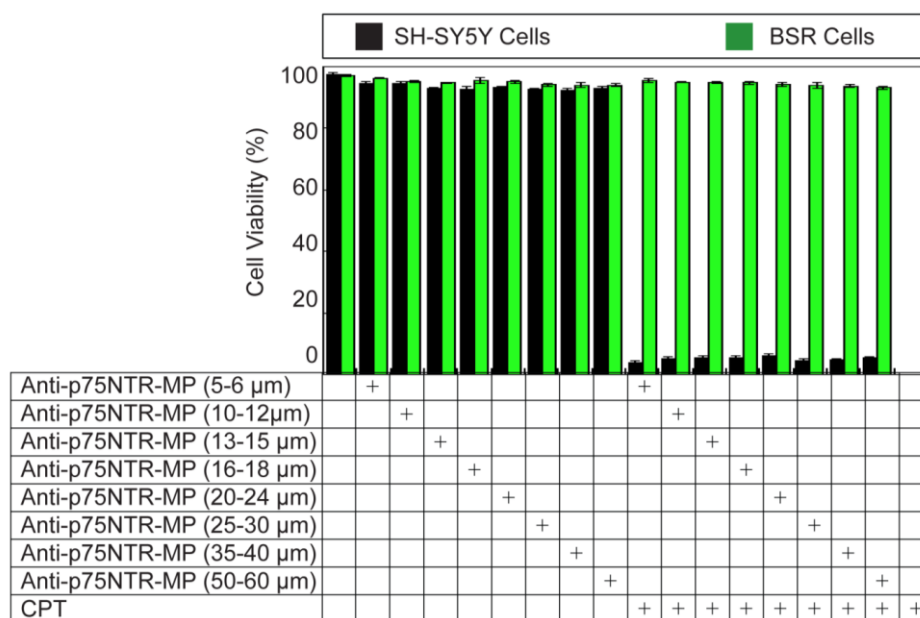


**Figure 8.8** Viability of SH-SY5Y and BSR cells after incubation with antibody-functionalized and CPT-loaded microtubes. Cells were incubated with anti-p75NTR-functionalized microtubes for 1 h. The medium was then replaced to remove unattached microtubes releasing CPT into the cell culture medium. For each sample, viability analysis was performed in triplicate. Microtubes were applied at a final concentration of  $50 \mu\text{g mL}^{-1}$ .

Confocal fluorescence microscopy revealed that anti-p75NTR-functionalized micropillars loaded with CPT readily attached to neuroblastoma cell surfaces and slowly released their cargo (Figure 8.9A). Over time CPT fluorescence inside of the micropillars weakened, and intracellular CPT fluorescence increased over the course of 8 h (Figure 8.10). Increasing incubation times led to accumulation of CPT in the cells. BSR cells incubated with anti-p75NTR-functionalized micropillars loaded with CPT were free of associated micropillars under the same incubation conditions (Figure 8.9B).

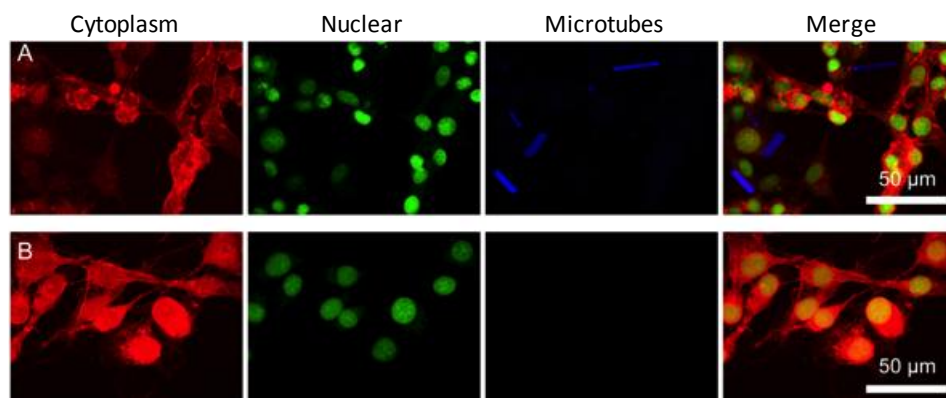


**Figure 8.9.** Interaction of anti-p75NTR-labelled micropillars with adherent cells. Confocal fluorescence microscopy image of SH-SY5Y neuroblastoma cells (A) and BSR cells (B). Red: actin filaments in the cytoplasm (phalloidin staining), green: nucleus (Picogreen staining), blue: micropillars (CPT fluorescence).

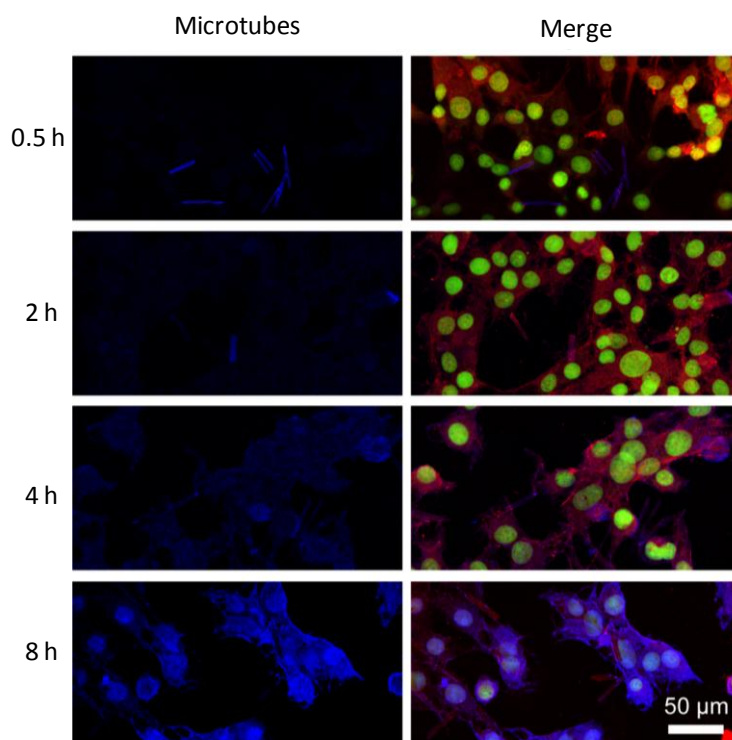


**Figure 8.10.** Time series of CPT uptake into SH-SY5Y neuroblastoma cells from CPT-loaded anti-p75NTR-labelled microtubes loaded with CPT by confocal fluorescence laser scanning microscopy. Left panels CPT fluorescence, right panels overlay (red: actin filaments in the cytoplasm (phalloidin staining), green: nucleus (Picogreen staining), blue: CPT fluorescence).

## 8.4 Conclusions

In summary, we designed a targeted micropill using engineered SiO<sub>2</sub> micropillars. The external and internal surfaces of SiO<sub>2</sub> micropillars were differentially functionalized. While the external surface displayed antibodies to target the corresponding overexpressed antigens on the tumor cell surface, the micropillars internal volume was used as cargo carrier for the hydrophobic anticancer drug CPT. Antibody-functionalized

micropillars attached to neuroblastoma cells within 1 h, whereas control cells that did not express the cognate receptors did not interact with the micropillars. The functionalized micropillars were demonstrated to be biocompatible as they do not induce toxicity in cells. CPT showed sustained release from cargo-loaded micropillars over the course of over 30 h. *In vitro* tests showed that the delivery of the anticancer drug led to efficient neuroblastoma cell killing. In contrast, cells which do not express the cognate receptor were unaffected when the micropillar-containing medium was replaced 1 h after incubation. We posit that deploying SiO<sub>2</sub> micropillars as cargo carriers for hydrophobic anticancer drugs is a promising strategy in chemotherapy. Furthermore, we argue that the ability to selectively functionalize the outer surface of the micropillars in the array with specific targeting molecules, whilst having independent access to the inside of the pillars a significant advantage of this particular architecture.

## 8.5 References

- [1] Secret, E., K. Smith, V. Dubljevic, E. Moore, P. Macardle, B. Delalat, M.L. Rogers, T.G. Johns, J.O. Durand, F. Cunin, and N.H. Voelcker, *Antibody-Functionalized Porous Silicon Nanoparticles for Vectorization of Hydrophobic Drugs*. *Advanced healthcare materials*, 2012. **2**(5): p. 718-727.
- [2] Pan, L., Q. He, J. Liu, Y. Chen, M. Ma, L. Zhang, and J. Shi, *Nuclear-Targeted Drug Delivery of TAT Peptide-Conjugated Monodisperse Mesoporous Silica Nanoparticles*. *Journal of the American Chemical Society*, 2012. **134**(13): p. 5722-5725.
- [3] Farokhzad, O.C., J. Cheng, B.A. Teply, I. Sherifi, S. Jon, P.W. Kantoff, J.P. Richie, and R. Langer, *Targeted nanoparticle-aptamer bioconjugates for cancer chemotherapy in vivo*. *Proceedings of the National Academy of Sciences*, 2006. **103**(16): p. 6315-6320.
- [4] Chen, J., S. Chen, X. Zhao, L.V. Kuznetsova, S.S. Wong, and I. Ojima, *Functionalized Single-Walled Carbon Nanotubes as Rationally Designed Vehicles for Tumor-Targeted Drug Delivery*. *Journal of the American Chemical Society*, 2008. **130**(49): p. 16778-16785.
- [5] Porta, F., G.E.M. Lamers, J. Morrhayim, A. Chatzopoulou, M. Schaaf, H. den Dulk, C. Backendorf, J.I. Zink, and A. Kros, *Folic Acid-Modified Mesoporous Silica Nanoparticles for Cellular and Nuclear Targeted Drug Delivery*. *Advanced Healthcare Materials*, 2013. **2**(2): p. 281-286.
- [6] Talelli, M. and W.E. Hennink, *Thermosensitive polymeric micelles for targeted drug delivery*. *Nanomedicine*, 2011. **6**(7): p. 1245-1255.
- [7] Wang, H., P. Zhao, X. Liang, X. Gong, T. Song, R. Niu, and J. Chang, *Folate-PEG coated cationic modified chitosan - Cholesterol liposomes for tumor-targeted drug delivery*. *Biomaterials*, 2010. **31**(14): p. 4129-4138.
- [8] Bhirde, A.A., V. Patel, J. Gavard, G. Zhang, A.A. Sousa, A. Masedunskas, R.D. Leapman, R. Weigert, J.S. Gutkind, and J.F. Rusling, *Targeted Killing of Cancer Cells in Vivo and in Vitro with EGF-Directed Carbon Nanotube-Based Drug Delivery*. *ACS Nano*, 2009. **3**(2): p. 307-316.
- [9] Muhammad, F., M. Guo, Y. Guo, W. Qi, F. Qu, F. Sun, H. Zhao, and G. Zhu, *Acid degradable ZnO quantum dots as a platform for targeted delivery of an anticancer drug*. *Journal of Materials Chemistry*, 2011. **21**(35): p. 13406-13412.
- [10] Cheng, Y., J.D. Meyers, R.S. Agnes, T.L. Doane, M.E. Kenney, A.-M. Broome, C. Burda, and J.P. Basilion, *Addressing Brain Tumors with Targeted Gold Nanoparticles: A New Gold Standard for Hydrophobic Drug Delivery?* *Small*, 2011. **7**(16): p. 2301-2306.
- [11] Chertok, B., A.E. David, and V.C. Yang, *Polyethyleneimine-modified iron oxide nanoparticles for brain tumor drug delivery using magnetic targeting and intra-carotid administration*. *Biomaterials*, 2010. **31**(24): p. 6317-6324.



- [12] Canham, L.T., *Bioactive silicon structure fabrication through nanoetching techniques*. *Advanced Materials*, 1995. **7**(12): p. 1033-1037.
- [13] Sailor, M.J., *Porous silicon in practice: preparation, characterization and applications*. 2012: John Wiley & Sons.
- [14] Biju, V., *Chemical modifications and bioconjugate reactions of nanomaterials for sensing, imaging, drug delivery and therapy*. *Chemical Society Reviews*, 2014. **43**(3): p. 744-764.
- [15] Shen, H., J. You, G. Zhang, A. Ziemys, Q. Li, L. Bai, X. Deng, D.R. Erm, X. Liu, C. Li, and M. Ferrari, *Cooperative, Nanoparticle-Enabled Thermal Therapy of Breast Cancer*. *Advanced Healthcare Materials*, 2012. **1**(1): p. 84-89.
- [16] Secret, E., M. Maynadier, A. Gallud, M. Gary-Bobo, A. Chaix, E. Belamie, P. Maillard, M.J. Sailor, M. Garcia, J.-O. Durand, and F. Cunin, *Anionic porphyrin-grafted porous silicon nanoparticles for photodynamic therapy*. *Chemical Communications*, 2013. **49**(39): p. 4202-4204.
- [17] Gu, L., J.-H. Park, K.H. Duong, E. Ruoslahti, and M.J. Sailor, *Magnetic Luminescent Porous Silicon Microparticles for Localized Delivery of Molecular Drug Payloads*. *Small*, 2010. **6**(22): p. 2546-2552.
- [18] Vale, N., E. Mäkilä, J. Salonen, P. Gomes, J. Hirvonen, and H.A. Santos, *New times, new trends for ethionamide: In vitro evaluation of drug-loaded thermally carbonized porous silicon microparticles*. *European Journal of Pharmaceutics and Biopharmaceutics*, 2012. **81**(2): p. 314-323.
- [19] DeLouise, L.A. and B.L. Miller, *Enzyme Immobilization in Porous Silicon: Quantitative Analysis of the Kinetic Parameters for Glutathione-S-transferases*. *Analytical Chemistry*, 2005. **77**(7): p. 1950-1956.
- [20] Wan, Y., S. Apostolou, R. Dronov, B. Kuss, and N.H. Voelcker, *Cancer-targeting siRNA delivery from porous silicon nanoparticles*. *Nanomedicine*, 2014: p. 1-13.
- [21] Zhang, H., D. Liu, M.-A. Shahbazi, E. Mäkilä, B. Herranz-Blanco, J. Salonen, J. Hirvonen, and H.A. Santos, *Fabrication of a Multifunctional Nano-in-micro Drug Delivery Platform by Microfluidic Templated Encapsulation of Porous Silicon in Polymer Matrix*. *Advanced Materials*, 2014. **26**(26): p. 4497-4503.
- [22] Chiappini, C., E. Tasciotti, J.R. Fakhoury, D. Fine, L. Pullan, Y.-C. Wang, L. Fu, X. Liu, and M. Ferrari, *Tailored Porous Silicon Microparticles: Fabrication and Properties*. *ChemPhysChem*, 2010. **11**(5): p. 1029-1035.
- [23] Smith, B.R., P. Kempen, D. Bouley, A. Xu, Z. Liu, N. Melosh, H. Dai, R. Sinclair, and S.S. Gambhir, *Shape Matters: Intravital Microscopy Reveals Surprising Geometrical Dependence for Nanoparticles in Tumor Models of Extravasation*. *Nano Letters*, 2012. **12**(7): p. 3369-3377.
- [24] Fine, D., A. Grattoni, R. Goodall, S.S. Bansal, C. Chiappini, S. Hosali, A.L. van de Ven, S. Srinivasan, X. Liu, B. Godin, L. Brousseau, I.K. Yazdi, J. Fernandez-Moure, E. Tasciotti, H.-J. Wu, Y. Hu, S. Klemm, and M. Ferrari, *Silicon Micro- and Nanofabrication for Medicine*. *Advanced Healthcare Materials*, 2013. **2**(5): p. 632-666.
- [25] Rodriguez, A., D. Molinero, E. Valera, T. Trifonov, L.F. Marsal, J. Pallares, and R. Alcubilla, *Fabrication of silicon oxide microneedles from*

- macroporous silicon*. Sensors and Actuators B-Chemical, 2005. **109**(1): p. 135-140.
- [26] Alba, M., E. Romano, P. Formentin, P.J. Eravuchira, J. Ferre-Borrull, J. Pallares, and L.F. Marsal, *Selective dual-side functionalization of hollow SiO<sub>2</sub> micropillar arrays for biotechnological applications*. RSC Advances, 2014. **4**(22): p. 11409-11416.
- [27] McInnes, S.J. and N.H. Voelcker, *Porous silicon-based nanostructured microparticles as degradable supports for solid-phase synthesis and release of oligonucleotides*. Nanoscale research letters, 2012. **7**(1): p. 1-10.
- [28] Rogers, M.-L., I. Atmosukarto, D.A. Berhanu, D. Matusica, P. Macardle, and R.A. Rush, *Functional monoclonal antibodies to p75 neurotrophin receptor raised in knockout mice*. Journal of Neuroscience Methods, 2006. **158**(1): p. 109-120.
- [29] Gallo, R.C., J. Whang-Peng, and R.H. Adamson, *Studies on the Antitumor Activity, Mechanism of Action, and Cell Cycle Effects of Camptothecin*. Journal of the National Cancer Institute, 1971. **46**(4): p. 789-795.
- [30] Gottlieb, J.A., A.M. Guarino, J.B. Call, V.T. Oliverio, and J.B. Block, *Preliminary pharmacologic and clinical evaluation of camptothecin sodium (NSC-100880)*. Cancer Chemother Rep, 1970. **54**(6): p. 461-70.
- [31] Rasi Ghaemi, S., F. Harding, B. Delalat, R. Vasani, and N.H. Voelcker, *Surface Engineering for Long-Term Culturing of Mesenchymal Stem Cell Microarrays*. Biomacromolecules, 2013. **14**(8): p. 2675-2683.
- [32] Müller, F., A. Birner, U. Gösele, V. Lehmann, S. Ottow, and H. Föll, *Structuring of Macroporous Silicon for Applications as Photonic Crystals*. Journal of Porous Materials, 2000. **7**(1-3): p. 201-204.
- [33] Trifonov, T., A. Rodriguez, F. Servera, L.F. Marsal, J. Pallares, and R. Alcubilla, *High-aspect-ratio silicon dioxide pillars*. Physica Status Solidi A, 2005. **202**(8): p. 1634-1638.
- [34] Lehmann, V. and U. Grüning, *The limits of macropore array fabrication*. Thin Solid Films, 1997. **297**(1-2): p. 13-17.
- [35] Corso, C.D., A. Dickherber, and W.D. Hunt, *An investigation of antibody immobilization methods employing organosilanes on planar ZnO surfaces for biosensor applications*. Biosensors and Bioelectronics, 2008. **24**(4): p. 805-811.

UNIVERSITAT ROVIRA I VIRGILI

SILICON DIOXIDE MICROSTRUCTURES BASED ON MACROPOROUS SILICON FOR BIOMEDICAL APPLICATIONS.

María Alba Martín

Dipòsit Legal: T 153-2015

## ***Chapter 9***

---

### Summary and Conclusions

This thesis has explored the fabrication of silicon oxide ( $\text{SiO}_2$ ) microstructures based on macroporous silicon (macro-pSi), with a focus on producing suitable architectures for application in biomedicine. The biocompatibility of  $\text{SiO}_2$  is generally accepted; nevertheless, a methodical study of the surface chemistry and its modification was performed by infrared (IR) spectroscopy to generate surfaces capable of biointerfacing with living cells. The particular architecture of these substrates allowed creating multifunctional particles with a selective dual functionality in nanometrically separated internal and external sides. We also foresaw these microstructured materials as drug carriers. Thus,  $\text{SiO}_2$  microparticles were proposed as pH-controlled drug delivery system when they are combined with pH-responsive polyelectrolytes. Finally, a dual-functionalization of the inner/outer sides was employed for creating multifunctional microparticles, which were demonstrated to be cancer-targeted in *in vitro* tests.

Chapter 3 described the methods to prepare macroporous silicon by the electrochemical etching of low doped p-type silicon. Both random and ordered silicon macropores were fabricated. The size distribution in random macro-pSi is highly dispersed and the nucleation sites undefined. A patterning lithography prior etching leads to an ordered nucleation of pores and a uniform size distribution. The optimal conditions for straight and stable pore growth were established considering the doping density, lattice constant and etching parameters. Macro-pSi substrates were used as precursor for producing random and ordered three-dimensional  $\text{SiO}_2$  structures. Hollow  $\text{SiO}_2$  micropillars essentially adopted the shape and arrangement of their preceding macropores. Thus, the interpore distance and diameter is mainly given by the anodization conditions in the formation of macro-pSi. However, the length is highly tunable as it depends

in the anisotropic etching time. Micropillars of lengths ranging from a few to several tens of micrometers were obtained. In the following chapters, micropillars were used as arrays in the silicon substrate and also as microparticles after mechanical detachment.

In the subsequent chapter, we described the functionalization methods towards bioligand conjugation for SiO<sub>2</sub> surfaces. Two different silanization reactions were studied and systematically characterized by infrared spectroscopy. We investigated the effect of acid and alkaline post-treatments on the hydrolysis and condensation of the lateral alkoxy chains, and on the terminal functionality of the silane layers. The protonation of the functional group in amino-terminated layers is of pivotal importance in subsequent crosslinker coupling towards bioligand conjugation. Our data showed that the covalent bond formed between amines and aldehydes is affected by the charge of the amino-functionalized layer. Results from these initial investigations determined the SiO<sub>2</sub> surface modification procedures and the reaction conditions used in subsequent chapters.

Following the surface chemistry investigation, in Chapter 5 we performed the dual-side functionalization of the interior and exterior sides of SiO<sub>2</sub> hollow micropillars. By alternating fabrication and chemical modification steps, the cross-contamination between the internal and external sides was avoided. Conjugation of fluorescent organic dyes to the differentially functionalized inner/outer surfaces allowed the investigation with confocal fluorescence microscopy. Fluorescent observation demonstrated successful immobilization of dual chemical species including the bioconjugation of the BSA protein. This approach enabled the independent chemical activation of two nanometrically separated surfaces, which can be simultaneously imaged. Results in this chapter led to

following investigations in the use of multifunctional micropillars as biointerfaces.

The first investigation towards biomedicine application was explored in Chapter 6, where  $\text{SiO}_2$  micropillars were internally coated with polyelectrolytes to create a hybrid organic/inorganic drug delivery system. A pH-responsive cationic/anionic polyelectrolyte multilayer (PME) was deposited by the layer-by-layer technique, and a model anticancer drug (doxorubicin, DOX) was successfully loaded into the PEM. The interaction between the PEM and DOX was appreciably dependent on the pH, thus the release rate at pH 5.2 was observed to be significantly higher than at pH 7.4. The effect of the number of layers was also investigated, being the drug loading capacity higher in those systems coated with PEM than in bare micropillars. This system was envisaged for pH-responsive drug delivery in localized therapy.

The use of three different  $\text{SiO}_2$ -based microstructured platforms for interfacing with living cells was explored in Chapter 7. A first evaluation performed on oxidized flat silicon showed an enhanced cell adhesion and growth on collagen functionalized surfaces. Then, human aortic endothelial cells (HAEC) were cultured on microstructures substrates, which were demonstrated to be biocompatible as they do not induce toxicity in the cells. The results highlighted the effect of the substrate topography on the cell adhesion, spreading and morphology of HAEC. Cell adhesion was found to be higher on ordered micropillar compared to all other substrates, including flat Si. The feasibility to induce different cell spreading and morphology behaviors was also tested. HAEC on macro-pSi showed a flat shape and the presence of pseudopods. A drastic impact in the nuclei and body shapes was induced by micropillar substrates. The results suggest

that patterned substrates generate cell patters that seem to mimic the pillar arrangement.

Finally, multifunctional monodispersed micropills based on SiO<sub>2</sub> micropillars were applied for targeted drug delivery. Following the differential functionalization scheme explored in Chapter 5, the external surface was conjugated with antibodies capable to target the corresponding overexpressed antigens on the tumor cell surface. Consecutively, the internal volume of the micropillars was loaded with the hydrophobic anticancer drug camptothecin (CPT). *In vitro* tests showed that neuroblastoma cells specifically attached to antibody-functionalized micropillars and the delivery of CPT led to efficient cell killing. Conversely, control cells that do not express the cognate receptor did not attach to micropillars and were unaffected when the micropillar-containing medium was replaced after 1 h incubation. We believe that employing multifunctional SiO<sub>2</sub> micropillars as cargo carriers for hydrophobic anticancer drugs is a promising strategy in cancer-target drug delivery chemotherapy.

The techniques herein presented for producing biocompatible SiO<sub>2</sub> structures from anodically formed macro-pSi open the door for the advancement of a range of biomedical and biotechnological systems. The technological and physico-chemical approaches that have been developed and the results that have been presented indicate the versatility and usefulness of these materials in the life sciences. We showed the feasibility and usefulness of using three-dimensional SiO<sub>2</sub> substrates for interfacing and interacting with living cells. The applicability of the micropillars for pH-controlled and targeted drug delivery has also been effectively proved. Altogether, we believe the technology, characterization and applications



presented in this thesis are rather encouraging and will provide a starting point for developing innovative smart systems that will find application in pharmaceutical, biotechnology and healthcare industries.

UNIVERSITAT ROVIRA I VIRGILI

SILICON DIOXIDE MICROSTRUCTURES BASED ON MACROPOROUS SILICON FOR BIOMEDICAL APPLICATIONS.

María Alba Martín

Dipòsit Legal: T 153-2015